Université de Lille

ED ENGSYS École doctorale Sciences de l'Ingénierie et des Systèmes

IEMN Institut d'électronique de microélectronique et de nanotechnologie

Thèse soutenue par Cécile HUEZ

Le 13 décembre 2022

Pour obtenir le grade de Docteure de l'université de Lille

Spécialité Electronique, microélectronique, nanoélectronique et micro-ondes

Nano-composants évolutifs à base d'oxydes moléculaires pour l'informatique non conventionnelle

Evolutive nanodevices based on molecular oxides for non-conventional computing

Devant un jury composé de :

Rapporteur	Jean Christophe Lacroix	Université de Paris cité Professeur
Rapporteure	Maria Luisa Della Rocca	Université de Paris cité Maître de conférence
Examinateur	Philippe Blanchard	MOLTECH Anjou Directeur de recherche CNRS
Examinateur	Michel Calame	Université de Bale Professeur
Invitée	Anna Proust	Sorbonne université Professeur
Co-directeur de thèse	Stéphane Lenfant	IEMN Directeur de recherche CNRS
Directeur de thèse	Dominique Vuillaume	IEMN Directeur de recherche CNRS

Acknowledgements

First of all, I would like to thank the CNRS through the 80|Prime program by financing my thesis. I would like to thank Thierry Melin, director of the 'Institut d'électronique, de microélectronique et de nanotechnologie', IEMN, for giving me the opportunity to work on the thesis in the laboratory.

Of course, I would like to express my sincere gratitude to my thesis supervisor Dominique Vuillaume and my co-supervisor Stephane Lenfant. Their optimistic insights, scientific discussions and leadership/group work skills have strengthened and advanced this study significantly. I will always be thankful for giving me this opportunity to really understand and like the fundamental science. I would like to thank Anna Proust and Florence Volatron for their collaboration, discussions, advices and indeed the great impact they added to this work.

I would like to thank David Guerin for the number of hours spend in the chemistry laboratory, Maxime Berthe and Dominique Deresmes for the help in the platform champ proche.

I thank all the members of the NCM team for the help and their daily presence. Especially Michel, Kirill, Hugo, Kamila and Corentin for their support. I would like to thank all the people I meet, exchange and work during these three years within the institute and the people of the ePOM team during my stay in their laboratory. I also thank Mickael Perrin for his time teaching me machine learning.

I desire to thank Jean Christophe Lacroix and Maria Luisa Della Rocca for accepting to report my thesis work and Philippe Blanchard, Michel Calame and Anna Proust to join the jury of my thesis defense.

Finally, I want to thank my friends and Jen for listening to me complain without understanding what I was doing and for changing my mind. Last but not least, I want to thank my parents and my siblings for always encouraging and pushing me to continue my studies till the Phd.

Résumé

Les polyoxométallates (POMs) sont des oxydes moléculaires nanométriques aux propriétés redox remarquables qui peuvent être explorées dans le cadre de composants avancés. Nous proposons de développer des fonctionnalités évolutives dans des nanomatériaux 2D à base de POMs (2D POM Network, 2D-PN) "programmables/switchables" à la demande grâce aux propriétés multifonctionnelles de ces molécules (par exemple, états redox multiples). Le premier objectif est de préparer une monocouche compacte et dense de POMs sur un substrat métallique afin d'évaluer leurs propriétés de transport d'électrons (ET). Ici, nous rapportons les propriétés de transport d'électrons de deux POMs dans leurs différents états redox en utilisant des monocouches auto-assemblées (SAM) et le C-AFM. Pour les deux molécules, nous avons clairement observé une augmentation d'un facteur 10 de la conductance pour les états réduits qui est liée à une diminution d'environ 0.3eV de l'énergie de l'orbitale moléculaire impliquée dans le transport à travers le métal/POM/métal. Ensuite, nous avons fabriqué un 2D-PN hybride multi-connecté (6 électrodes) avec deux POMs et des nanoparticules d'or et nous avons mesuré leur ET révélant une grande variabilité dans le 2D-PN. Des mesures de bruit à basse fréquence et de génération de hautes harmoniques sont utilisées pour discuter de l'utilisation possible de ces 2D-PN dans le cadre global de l'implémentation physique d'un système de calcul à réservoir neuromorphique avec des nano-objets (nanotubes de carbone nanoparticules, molécules, commutateurs atomiques). Nous synthétisons également des nanofils de $W_{18}O_{49}$ (environ quelques µm de long et quelques dizaines de nanomètres de diamètre) et nous mesurons leur conductivité avec un STM UHV 4 probes. Nous démontrons une conductivité très élevée allant jusqu'à 10^3S/cm le long du nanofil, qui surpasse les données de la littérature et une grande anisotropie de conductivité.

Mots clés: polyoxométallates ; jonction moléculaire ; C-AFM ; Reservoir Computing ; Nanofils $W_{18}O_{49}$

Abstract

Polyoxometalates (POMs) are nanometric molecular oxides with remarkable redox properties that can be explored in the context of advanced components. We propose to develop scalable functionalities in 2D nanomaterials based on POMs (2D POM Network, 2D-PN) "programmable/switchable" on demand thanks to the multifunctional properties of these molecules (e.g. multiredox states). The first objective is to prepare compact and dense monolayers of POMs on a metal substrate to assess their electron transport (ET) properties. Here, we report the ET properties of two POMs in their different redox states using self-assembled monolayers (SAM) and conductive-AFM. For both molecules, we clearly observed an increase of the conductance of a factor of 10 for the reduced states which is related to a decrease of the energy of about 0.3eV of the molecular orbital involved in the transport though the metal/POM/metal. Then, we successfully fabricated multi-connected (6 electrodes) hybrid 2D-PN with two POMs and Au nanoparticles and we measured their ET revealing large variability in the 2D-PN. Low-frequency noise and high-harmonic generation measurements will be used to discuss the possible use of these 2D-PN within the global framework of the physical implementation of a neuromorphic reservoir computing system with nano-objects (Carbon nanotubes, nanoparticles, molecules, atomic switches). We also synthesize $W_{18}O_{49}$ nanowires (about µm long and few tens of nanometers in diameter) and we measure their conductivity with a 4-probe UHV STM. We demonstrate a very high conductivity up to 10^3S/cm along the nanowire, which outperforms the literature data and a large conductivity anisotropy.

Key words: polyoxometalates; molecular junction; C-AFM; Reservoir Computing; $W_{18}O_{49}$ nanowires

List of main abbreviations in alphabetical order

AFM	Atomic Force Microscopy
C-AFM	Conductive- Atomic Force Microscopy
CD_3CN	Acetonitrile-d3
CV	Cyclic voltammetry
DC	Direct Current
E_F	Energy Fermi level
ET	Electron Transport
FN	Fowler-Nordheim
FTIR	Fourier transform infrared
HHG	High Harmonic Generation
HOMO	Highest Occupied Molecular Orbital
MJ	Molecular junctions
MO	Molecular Orbital
MTJ	Molecular transport junctions
NMR	Nuclear magnetic resonance
NND	Nearest Neighbour distance
NP	Nanoparticle
NW	Nanowire
NT	Nanotube
NPSAN	Nanoparticle self-assembled network
PBS	Phosphate Buffered Saline
PDMS	Polydimethylsiloxane
POM	Polyoxometalates
PSD	Power spectral density
RC	Reservoir Computing
RT	Room temperature
SAM	Self-assembly monolayer
SEM	Scanning electron microscopy
SCE	Saturated calomel electrode
SEL	One molecular level model or Single level model
STM	Scanning Tunneling Microscopy
^{TS}AU	Template-stripped gold surface
TBA	Tetrabutyl ammonium
TEM	Transmission Electron Microscopy
TLM	Transmission line method
TM-AFM	Tapping-Mode- Atomic Force Microscopy
TVS	Transition voltage spectroscopy
UHV	Ultra-high vacuum
UV-vis	Ultraviolet-visible
XPS	X-ray photoelectron spectroscopy
XRD	X-ray Diffraction

Contents of the manuscript

Acknowledgements 1
Résumé 3
Abstract 3
List of main abbreviations in alphabetical order 5
Contents of the manuscript 7
General introduction 11
Chapter 1 The polyoxometalates at the nanoscale 14
I. The field of molecular nanoelectronics 14
a) Molecular Junctions 14
b) Self-assembled monolayers 17
c) Electron transport in molecular junctions 19
II. Generalities about polyoxometalates 24
a) Chemistry of POMs 24
b) Electro-active molecules 27
c) Polyoxometalates in molecular devices 28
III. The development of reconfigurable and unconventional computing devices 33
a) Introduction to Reservoir Computing 33
b) At the molecular scale 35
IV. Conclusion of chapter 1 37
Chapter 2 Vertical nano-molecular junction 40
I. Fabrication of the molecular junctions and methods of electrical measurements 40
II. Redox-controlled conductance of PMo_{12} molecular junctions 42
a) Chemical synthesis of the POMs and physicochemical characterizations 42
b) Electron transport properties of C2 and C6 MJs 47
c) Electron transport properties of C2/PMo_{12} MJs 49
d) Electron transport properties of C6/PMo_{12} MJs 53
e) Discussion of the electron transport properties 67
f) Summary and outlook 71
III. Study of a second POM: P_5W_{30} 73
a) In-situ irradiation of KP_5W_{30} 73
b) Electron transport properties of C6/$TBAP_5W_{30}$ MJs 76
c) Exchange of the counterion 81

d) Influence of the counterion in the electron transport properties of C6/P_5W_{30} MJs 88
e) Summary and outlook ... 92
Chapter 3 Gold Nanoparticles - POMs network ... 95
I. Implementation of the Au NP-POM network ... 95
a) Homogeneous film of gold nanoparticles ... 96
b) Exchange of ligands ... 99
c) Reduction of the POMs ... 105
II. Electron transport dynamics of the NPSANs ... 108
a) IV measurements ... 108
b) Noise measurements ... 110
c) High harmonic generation measurements ... 117
d) Are polyoxometalates prone for Reservoir Computing? ... 119
Conclusion and outlook ... 120
Chapter 4 Another metal oxide structure: $W_{18}O_{49}$ nanowires ... 123
I. Introduction ... 123
II. Nanowires synthesis and characterization ... 126
III. Conductance of single nanowires ... 133
a) Electronic behaviour ... 133
b) Perpendicular conductance ... 138
c) Longitudinal conductance ... 139
IV. Conductance of a two-dimensional network of nanowires ... 147
Conclusion ... 153
General Conclusion and outlook ... 154
General Conclusion ... 154
Outlook ... 156
Annexes ... 158
Annexes of Chapter 2 ... 158
Annexe A2.1. Fabrication of the molecular junctions ... 158
Annexe A2.2. Methods of electrical measurements ... 160
Annexe A2.3. POM characterization ... 163
Annexe A2.4. Illumination setup ... 164
Annexe A2.5. Color switching of PMo12 ... 164
Annexe A2.6. Machine learning and clustering ... 164

Annexes of Chapter 3 168
Annexe A3.1. Device fabrication 168
Annexe A3.2. NPSAN characterization 168
Annexe A3.3. NPSAN electronic measurements 169
Annexe A3.4. NPSAN fragility 170
Annexe A3.5. LFN measurements with octanethiol and oleylamine at higher voltages 173
Annexe A3.6. High harmonic generation of $HPMo_{12}$ 175
Annexes of Chapter 4 176
Annexe A4.1. Synthesis and characterization of $W_{18}O_{49}$ 176
Annexe A4.2. Perpendicular conductance 180
Annexe A4.3. Longitudinal conductance 181
Annexe A4.4. Effect of e-beam exposure 186
Annexe A4.5. Activation energy calculated from TLM method 187
Publications & Oral communications 188
Publications 188
Oral communications 188
Bibliography 190

General introduction

The field of artificial intelligence has developed a lot in the last few years, both in software and hardware. Concerning hardware, a new interest in the design and fabrication of artificial neural networks and synapses with ultra-low power and energy consumption has taken hold. This is mainly referred to as neuromorphic systems. In this project, we propose to include self-assembled functional molecules for a subfield of neuromorphic computing, Reservoir Computing. These molecules are polyoxometalates, called POMs. They are particularly used in the field of catalysis, for their redox properties. Indeed, up to 24 electrons can reduce some POMs. The project of this thesis is to study the electron transport properties of different POMs at different redox levels in molecular junctions after optimization of the fabrication process.

This manuscript is organised in four chapters. **Chapter 1** will be devoted to a literature review on the scientific context in which the work of this thesis takes place.

One of the best methods to study the electron transport properties of POMs alone is to incorporate them into a molecular junction with a conductive AFM tip as one of the electrodes, this work is presented in **chapter 2**. A study on the conductance of POM as a function of its oxidation-reduction state will be presented and detailed through complementary machine learning analyses. A similar study will be carried out on another POM leading to the investigation of the influence of counterions on the latter.

Chapter 3 will present work on molecular junctions with a network of self-assembled nanoparticles, called NPSAN. The first part of this chapter will focus on the implementation of this monolayer network of gold nanoparticles and on the substitution of ligands by two POMs. The second part of this chapter will be a study of electrical measurements, in particular of 1/f noise, to try to answer the question of this thesis: are POMs good candidates for Reservoir Computing applications?

The last chapter, **chapter 4**, will not focus on POMs, but on another metal oxide, WO_{3-x} substochiometric nanowires. Their transport properties will also be discussed after having developed their synthesis and characterization. The conductivity will be calculated from single nanowires in "perpendicular" measurement via C-AFM and "longitudinal" measurement using an ultra-high vacuum STM coupled with a SEM. Finally, work on a dense network will be reported.

To end, we close this manuscript with a general conclusion and perspectives. **Annexes** are also provided for further explanation.

Contents of chapter 1

Chapter 1 : The polyoxometalates at the nanoscale 14

I. The field of molecular nanoelectronics 14

a) Molecular Junctions 14

b) Self-assembled monolayers 17

c) Electron transport in molecular junctions 19

II. Generalities about polyoxometalates 24

a) Chemistry of POMs 24

b) Electro-active molecules 27

c) Polyoxometalates in molecular devices 28

III. The development of reconfigurable and unconventional computing devices 33

a) Introduction to Reservoir Computing 33

b) At the molecular scale 35

IV. Conclusion of chapter 1 37

Chapter 1 The polyoxometalates at the nanoscale

The aim of this first chapter is to present in a general way the framework in which the work of this thesis is carried out, based on works and results reported in the literature. Some information, more specific to a particular chapter, will be developed in this particular one.

The first part describes an overview of the molecular nanoelectronic field, focused on the device I used during my thesis, mainly the molecular junction. The second one describes the main component of this junction: the polyoxometalate molecules. These molecules correspond to the main subject of this thesis, their electronic properties are presented in detail. The goal is to better understand the fundamental role of polyoxometalates in molecular nanoelectronics. The last part of this chapter is related to possible applications in neuromorphic devices and systems, placing this project at the frontiers of chemistry, physics and neuroscience.

I. The field of molecular nanoelectronics

a) Molecular Junctions

Mann and Kuhn measured for the first time the electrical properties of organic monolayers in 1971.[1] Then, Aviram and Ratner introduced in 1974 the theoretical concept of using a single organic molecule as a molecular rectifier (or molecular diode).[2] In 1977, Heeger, MacDiarmid and Shirakawa demonstrated that conducting polymers are the best conducting molecules (Nobel Prize in 2000).[3] It's the beginning of the molecular electronic field.

With the Moore's Law, research in the field of electronics has taken a new turn. The miniaturisation of technological devices that are more or at least as efficient as their predecessors has become a real international challenge. These devices are mainly composed of inorganic materials such as silicon. Their fabrication at the nanoscale has developed massively but has begun to reach the limits of classical physics with systems of few nanometers. One solution that some scientists have been looking at is the use of molecules to replace these materials and achieve ultimate device dimensions.

However, industrial applications seem unlikely because of the tradeoff between function and the implementation of the junction. Indeed, the fabrication of this molecular structure is sensitive to defects (e.g. problem of metallic filamentary conduction), hard to control and characterize, generating some reproducibility problem. Only OLED (organic light emitting diode) displays are already being commercialised. Still, the field of molecular electronics is very studied in the fundamental research in order to explore more about the electronic properties of molecule-based devices. The objectives are to find other functions or properties that can be difficult to reach with the mainstream technology as for example flexible, low cost or reconfigurable. Especially with the development of Scanning Probe Microscopy (SPM) techniques, like Scanning Tunneling Microscopy (STM) (Nobel Prize in 1986, invented by Binning, and Rohrer[4,5]) and Atomic Force Microscopy (AFM), it becomes easier to analyse the electric properties of this small element and these techniques are now widely used in lots of areas in nanosciences.

The field of molecular electronic encompasses all technologies using one or several molecules or molecular structures with a nanometric size (molecularly functionalized nanoparticles, molecular nanowires,…) in order to process an electronic function. We can talk about molecular nanoelectronics until the size of the device is less than few tens of nanometers (at larger size, it is referred as organic electronics).

Molecules have been connected between two electrodes forming the so-called molecular junctions (MJ), the main component of molecular nanoelectronics.[6] The MJ can be separate in two classes in function of the number of molecules inside:

- One or few molecules : single molecule junction
- Lots of molecules (~ >10) : large area junction

A junction can be formed by break-junction method, cross wire method, metal nanoparticles method, conductive probe atomic force microscope (C-AFM) and STM, nano-pore method and planar sandwich geometry... During my thesis, I used C-AFM (chapter 2), STM (chapter 4) and metal nanoparticles method (more details in chapter 3). Frequently, in a vertical junction, the first electrode is called the bottom electrode and the second one the top or the counter electrode.

Most of the time, the size of both the electrodes or the top electrode will define the number of molecules involved in the junction. As shown in the figure 1.1, in the break junction or STM, one or a few molecules are connected with the top electrode. Whereas in C-AFM, as the

conductive tip has a radius between 20 or 100 nanometers, we estimate the number of molecules between 50 and 1 000.

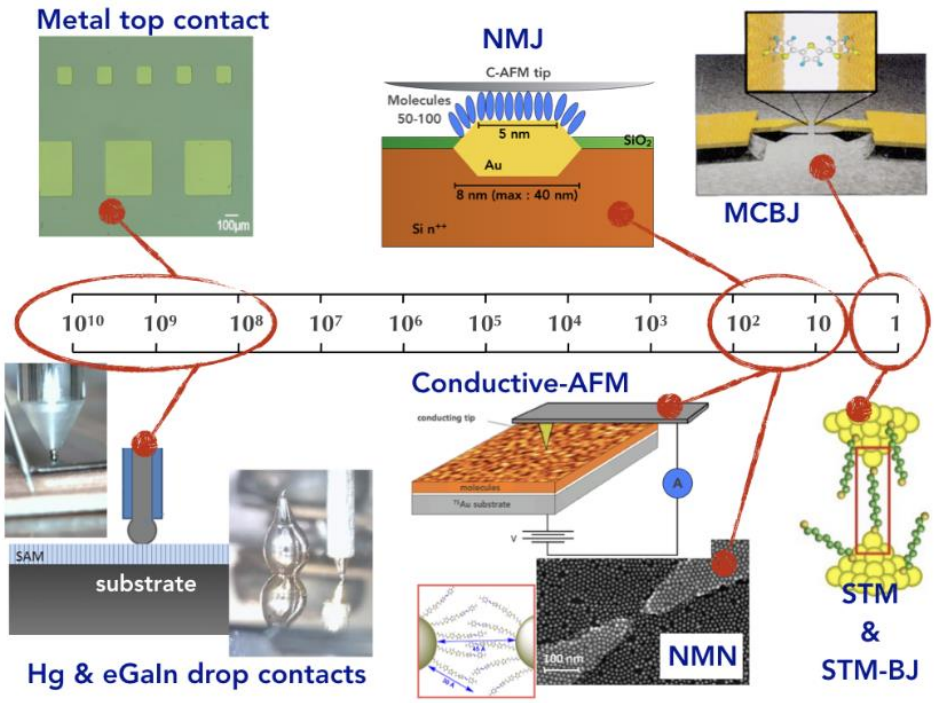

Figure 1.1. Overview of several types of molecular junctions (MJs) along a scale of the approximate number of molecules in the MJ: from "large area MJ" on the left to few molecules and single molecule junction on the right.[7]

To make these junctions, the bottom electrodes must have a low roughness to avoid spike effects that would generate short circuits. The bottom electrodes are usually made of gold, silver, silicon or carbon and cannot be damaged. The choice of metal electrodes is really important. The top electrode can be fabricated by metal evaporation. Most of the time, a protective layer, a highly conducting polymer (example PEDOT:PSS) is intercalated between the electrode and the molecules to avoid the formation of metallic filaments[8]. Another idea is the use of soft metal by transfer techniques[9–11] or by contacts as mercury drops[1,12] or eutectic GaIn drop contacts[13]. This development is limited by the liquid nature of this electrode, which is not compatible with commercial electronic systems.[14] The later one is combined with microfluidic systems for a better control and stability.[15]

Then, the molecules are attached to the bottom electrode. Not all molecules can be candidates to be inserted in such a device. The first important condition is the stability of the molecule in time. If the molecule does not support an electronic current and get damage automatically, it

cannot be integrated inside an electronic device that is supposed to have a long lifetime. The molecule must be stable during all the steps of the fabrication process and operation. Like molecular electronic is based on electron exchange, molecules should have a reversible behaviour during the electron transfer in purpose to repeat the function.[16]

The molecules are immobilised by a chemical function to form a self-assembled monolayer (SAM) – see next section, organic multilayers (Langmuir Blodgett[17],[18]), or layers deposited by electrochemical methods (electrografting of aryl diazonium salt[19]). The most widely used method in the literature is assembly by silane[20] on oxidized surface and thiols[21] for gold surface. It is in 1983, that Allara and Nuzzo produced the first gold-alkylthiolate monolayer at Bell laboratories.[22]

b) Self-assembled monolayers

According to J.-M. Lenn (Nobel prize in Chemistry, 1987), a definition of self-assembled monolayers is "systems capable of spontaneously generating well-defined supramolecular entities by self-assembly from their components in a given set of conditions".[23]

The components are composed of:[21]

- An anchoring function, a reactive group with an important affinity to the surface of the substrate in order to be chemisorbed on it (thiol for gold substrates, carboxylic acid and silane for oxidized silicium surface…).
- A spacer, for example an alkyl chain, with Van der Waals interactions between them. This allows a compact monolayer. The spacer also brings a specific function, alkyl will be used to insert an insulating molecule whereas an aromatic chain to obtain a more conductive layer.
- A end group or a surface group to add a function to the SAM (amine group, π-conjugated molecule …).

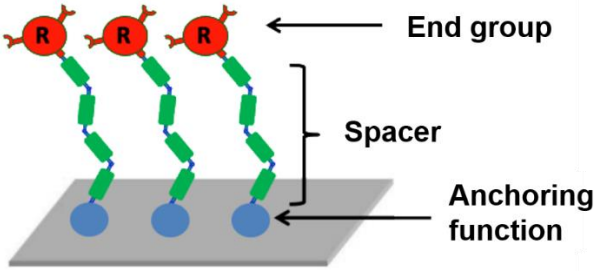

Figure 1.2. Scheme of self-assembled monolayers structure. Image adapted from reference[24]

As detailed in the review by Aswal et al.,[25] the quality of the SAM depends of some focused parameters:

- The thickness of the monolayer. Most of the time, the thickness is between 1 and 3 nm, depending on the size of the molecule. It can be measured by using ellipsometry technique.
- The molecular orientation and ordering. To study these two parameters, the Fourier-transform infrared (FTIR) spectroscopy is the most powerful tool. For example, in the case of alkyl chains, the peak positions of symmetric (ν_s) and asymmetric (ν_a) stretching modes of the CH_2 groups give the required information about the molecular order in the monolayers.[26]
- Uniformity and coverage. It is mainly controlled by the Van der Waals interactions between the molecules. Again, in the typical case of SAMs of alkyl chains, it may be assessed by ellispometry. The topography of the SAM (presence of pinholes, aggregates, uncovered areas….) can also be checked by AFM, and the SAM roughness can be estimated. We can also observe their organization phases by STM.[27] With the case of alkylsilane, even with AFM we can see in some case the molecules on the surface.[28]
- Chemical composition. X-ray photoelectron spectroscopy (XPS) is widely used to determine the elemental composition of the molecules inside the SAM. In other words, it helps us to know the stoichiometry and the correct bonding to the surface. Moreover, in case of redox molecules, this spectroscopy gives us access to their oxidation degree.[29]
- Thermal and chemical stability. Some SAMs (e.g. alkylthiol on Au, alkyl chains on Si and SiO_2) are very stable, they show no signature of degradation when stored in an airtight container for 18 months[30]. In a process, it is possible to heat the SAMs up to a certain limit (e.g. silane resist until 350°C).[31]

c) Electron transport in molecular junctions

In molecular junctions (MJs), when we apply a voltage between the electrodes, electrons are firstly injected into the molecules from one electrode and then collected at the second electrode. The basic measured characteristic is the current vs. voltage (I-V) curve.

An energy diagram of a MJ is illustrated in figure 1.3.[7] The electrodes are modelled by their Fermi energy ε_F and the molecule by their quantized energy levels. They are defined by their molecular orbitals (MO), mainly the highest occupied molecular orbital (HOMO, ε_H) and the lowest unoccupied molecular orbital (LUMO, ε_L). These two orbitals are playing the most important role in the charge transport and all energies are referred to the vacuum energy level. The interactions between the electron cloud in the electrodes and the electrons in the molecules also have some importance in the charge transport. It is called the coupling strength, i.e. the coupling parameters between the molecular orbitals and the density of states in the electrodes ($\Gamma_{1,2}$ or $\Gamma_{L,R}$).

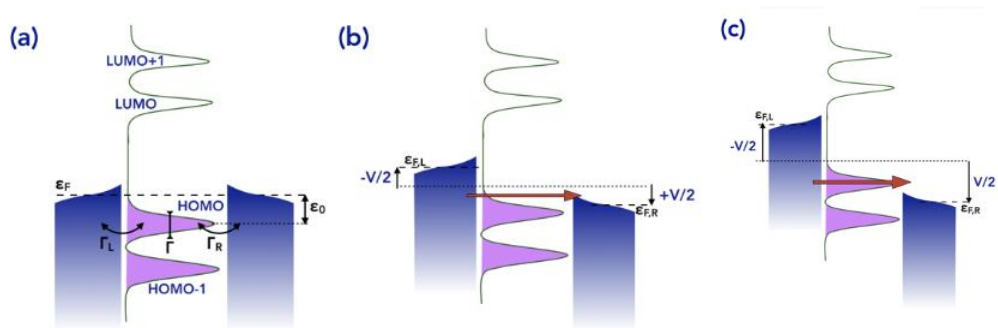

Figure 1.3. (a) Simplified energy diagram of a molecular junction. (b) Coherent, off-resonant, electron transport, $eV < 2\varepsilon_0$. (c) Coherent, resonant, electron transport, $eV \geq 2\varepsilon_0$.[7]

In general, at low voltage, the Fermi level is not aligned with the HOMO or LUMO of the molecules ($E_F \neq E_{LUMO \text{ or } HOMO}$). In other words, the energy eV= $|\varepsilon_{F,L} - \varepsilon_{F,R}|$ (with L and R respectively left and right electrodes), is lower than $2\varepsilon_0$, ε_0 being the energy position of the involved MO with respect to the Fermi energy of the electrodes. It is the off resonant transport (figure 1.3b). When we increase the voltage, we can reach the resonant transport. In contrast, this time the energy eV is larger than $2\varepsilon_0$ and the MO involved in the electron transport falls in the energy window defined by the energy difference of the Fermi levels (figure 1.3c).

It has already been shown that the stability of molecular devices, the coupling strength, and the charge transport mechanism can be directly controlled by the nature of the contact between the molecules and the electrodes.[32,33]

For the coupling strength, the nature of the interaction at the end of the molecules and the electrode plays an important role. We can talk about physisorption when the binding energy ranges from 10-100 meV (Van der Waals interactions). While, in chemisorption, it ranges from 1-10 eV (hydrogen, covalent and ionic bonds).[34]

Most of the time, a weak electronic coupling corresponds to a physisorption of the molecules on the surface of the electrodes due to weak Van der Waals interactions. On the opposite, in the case of chemisorption, strong covalent bonds between the molecule and the electrodes trend to a medium-strong electronic coupling. In some cases, molecules have intrinsic dipole. The interface formation can be modified because of interactions such as partial charge transfer, rearrangement of electron density or attraction through image forces.

That is why in electronic devices, the coupling between the electrode and the molecule must be clarified.

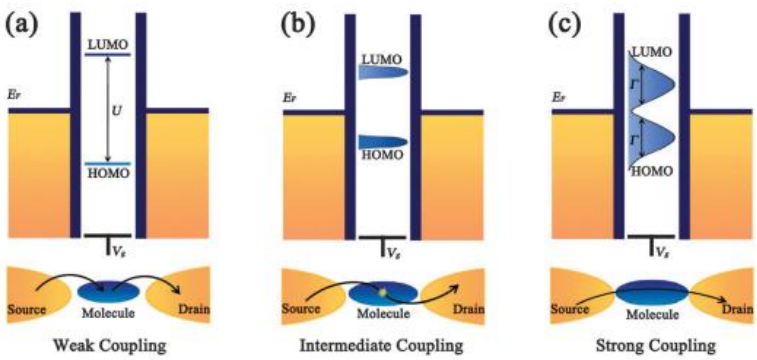

Figure 1.4. Scheme of the energy levels and electron transport processes of MJs with the different coupling strengths between the molecules and the electrodes (a) in the weak coupling regime (b) in the intermediate coupling regime and (c) in the strong coupling regime.[35]

With Γ the coupling parameters between the molecular orbitals and the density of states in the electrodes and U the addition energy , i.e. the energy necessary to add an electron to the LUMO or to remove one electron from the HOMO, we can define three regimes:[35]

- Γ << U: weak coupling regime
- Γ ~ U: intermediate coupling regime

- Γ >> U: strong coupling regime.

In case of a weak coupling, there is no strong perturbation of the electronic structure of the molecules in the solid-state molecular junction compared to the molecule in vacuum or gas phase. Furthermore, the electron transport properties in the junctions is mainly governed by the properties of the molecules and is described by a sequential transport electrode →molecule→electrode.

For the strong coupling, the electrodes and the electronic states of molecules are considerably overlapped and a charge transfer occurs at the interface. It leads to a large broadening of the energy levels of molecules. In this case, the electrons are efficiently transported from one electrode to the second one via an one-step coherent process (very rare phenomenon).

Finally, in the intermediate coupling regime, the molecular energy levels are partially broadened. The electrons on the molecule can affect the injected electrons during electron transport. The transport is usually coherent and is classified as off-resonant or resonant transport (see Fig. 1.3).

Some models are used to interpret the electronic properties of the junction and to describe the electronic conduction.

At low bias, the tunnelling mechanism is presented by a current of electrons who encounters a finite potential barrier (φ) at the metal molecule interface. Even though the energy of this barrier is higher than the one of the electrons, their wavefunctions do not disappear at the interface but fall off exponentially into the barrier.[36] This allows us to say that there is a finite probability that electrons from either of the electrodes are transferred through a small distance into the molecule despite the lack of allowed energy levels there.

In the direct tunnelling mechanism, Simmons[37] has shown that the theoretical relationship between direct tunneling current (I) and the applied voltage (V) for a trapezoidal energy barrier (figure 1.5a) is given by:

$$I(V) = S\,\frac{\mathrm{e}}{4\pi h d^2}\left[(2\varphi_T - \mathrm{eV})exp\left(-\frac{4\pi d\sqrt{m(2\varphi_T - \mathrm{eV})}}{h}\right) - (2\varphi_T + \mathrm{eV})exp\left(-\frac{4\pi d\sqrt{m(2\varphi_T + \mathrm{eV})}}{h}\right)\right] \qquad (1.1)$$

with e the electron charge, h the Planck constant, d the thickness of the tunneling barrier, φ_T the energy barrier height, V the voltage applied across the junction, m the effective mass of the electron, I the current and S the electrical

contact surface area. In MJ, φ is ascribed to the energy difference between the MOs and the Fermi energy.

This model is limited by his strong dependence of extracted parameters on the assumed contact area for transport. Moreover, it considers a linear variation of the electric field between the electrodes at applied voltage whereas, in MJs, we can consider the potential drops are mainly located at the molecule/electrode interface. This induces a deviation of experimental current-voltage data from the assumptions that underlie the Simmons model.[38] Now, this model is used as a simplify model transport and other models are used for describing the transport.

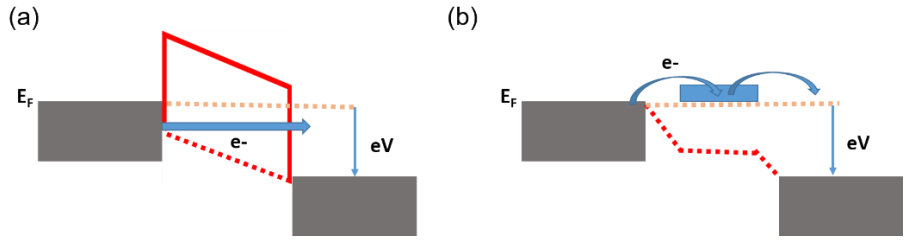

Figure 1.5. Simplified scheme showing at applied voltage (a) Simmons model with the trapezoidal barrier form and (b) Landauer formalism with a drop of potential located at the molecule/electrode interface.

Büttiker-Imry-Landauer formalism (figure 1.5b) describes the resonant transport through one of the molecular orbitals at higher voltages:

$$I(V) = \frac{2e}{h}\int T(E)\left[f\left(E,\varepsilon_{F,L}\right) - f\left(E,\varepsilon_{F,R}\right)\right]dE \qquad (1.2)$$

where T(E) is the transmission coefficient (electron transmission probability) through the molecule, f the Fermi-Dirac statistics $f(E,\varepsilon) = \left[1 + \exp\frac{E-\varepsilon}{k_B T}\right]^{-1}$ e the electron charge, k_B the Boltzmann constant, T the temperature, h the Planck constant and $\left|\varepsilon_{F,L} - \varepsilon_{F,R}\right| = eV$, V the applied voltage. To use these models, we pose three conditions: the electron transport is dominated by only one molecular orbital (MO), the voltage mainly drops at the molecule/electrode interface and Lorentzian or Breit-Wigner distribution describes the MO broadening. We obtain:

- The single-energy level (SEL) model[39,40]
- the transition voltage spectroscopy (TVS) method[41,42,43,44,45]

The I-V curves are fitted with the SEL model as illustrated in the figure 1.6, given by the equation:

$$I\,(V) = N * \frac{8e}{h} * \frac{\Gamma_1\,\Gamma_2}{\Gamma_1+\Gamma_2}\left[arctan\left(\frac{\varepsilon_{0-SEL}+\frac{\Gamma_1}{\Gamma_1+\Gamma_2}eV}{\Gamma_1+\Gamma_2}\right) - arctan\left(\frac{\varepsilon_{0-SEL}-\frac{\Gamma_1}{\Gamma_1+\Gamma_2}eV}{\Gamma_1+\Gamma_2}\right)\right] \quad (1.3)$$

with $\varepsilon_{0\text{-SEL}}$ the energy of the MO involved in the transport (with respect to the Fermi energy of the electrodes), Γ_1 and Γ_2 the electronic coupling energy between the MO and the electron clouds in the two electrodes, e the elementary electron charge, h the Planck constant and N the number of molecules contributing to the ET in the molecular junction (assuming independent molecules conducting in parallel, i.e. no intermolecular interaction[46,47,48]).

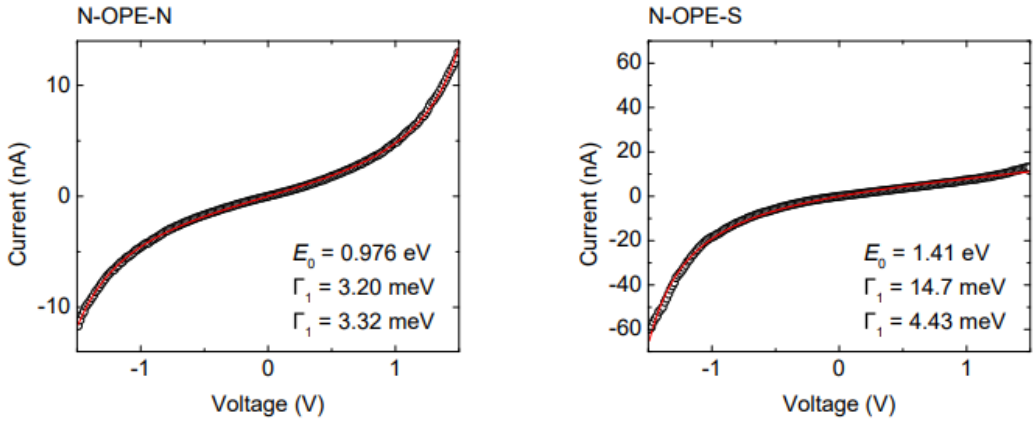

Figure 1.6. Typical examples of the fits of the SEL model on molecular junctions with symmetric anchoring groups N-OPE-N and asymmetric anchoring groups N-OPE-S (OPE : olygo(phenylene ethynylene) ; N and S refer to pyridine and thiol anchoring groups, respectively). The single molecule I(V) curves are measured by MCBJ (mechanically controlled break junction). After (Brunner, 2013).[49]

For the TVS method, we plot $|V^2/I| = f(V)$.[50] We note the transition voltages V_{T+} and V_{T-} for both voltage polarities at which the bell-shaped curve is maximum. This threshold voltage indicates the transition between off-resonant (below V_T) and resonant (above V_T) transport regime in the molecular junctions and can therefore be used to estimate the location of the energy level. The value of $\varepsilon_{0\text{-TVS}}$ is given by the equation:[45]

$$|\varepsilon_{0-TVS}| = 2 * \frac{e|V_T^+ + V_T^-|}{\sqrt{{V_T^+}^2 + \frac{10|V_T^+ V_T^-|}{3} + {V_T^-}^2}} \quad (1.4)$$

The electrode coupling energy Γ_{TVS} can also be determined by this relationship:[51,52]

$$G(0) = N * G_0 * \frac{{\Gamma_{TVS}}^2}{{\varepsilon_{0-TVS}}^2} \quad (1.5)$$

with G(0) the zero-bias conductance (value obtained by the 1st derivative of IV at V ~ 0V), G_0 the conductance quantum ($2e^2/h=7.75x10^{-5}$ S, e the electron charge, h the Planck's constant) and N the number of molecules in the junction. Γ_{TVS} is equivalent to the geometrical average of the SEL values $(\Gamma_1\Gamma_2)^{1/2}$.[51,52]

II. Generalities about polyoxometalates

a) Chemistry of POMs

The story of the polyoxometalates (POMs) begins with the discovery of the elements molybdenum (Mo) and tungsten (W) by C.W. Scheele in 1742-1786. Around one hundred years later, in 1862, Marignac discovered and characterized the first heteropolytungstates. The polyoxometalates have aroused great interest and, in 1930, hundreds of these compounds were described in the Gmelin volumes.[53,54,55]

It is in 1933, with the achievement of X-ray analysis that Keggin defines precisely the structure of the heteropoly acid $[H_3PW_{12}O_{40}].6H_2O$ with the arrangement of edge-shared polyhedra.[56] Then, in 1987 for example, 66 structures were published.[53]

POMs are anionic clusters of metal oxides. They are written in the form $X_xM_yO_z^{n-}$ with X a heteroatom and M a transition metal. Counter cations accompany the POM to make the total charge neutral. The counter cation can be a proton, an (organo)-ammonium cation, an alkaline or an organometallic complex. By consequence, the nature of this cation determines the solubility and acidity properties of the POM. POM clusters are soluble in many solvents, which makes them very popular. Like some reducing agents are soluble in only one kind of solvent, the counter cations can facilitate the capability of the POM to change its oxidation degrees. The use of alkylammonium cations allows to perform chemical reductions in non-aqueous solvents, while the presence of protons (or lithium ion Li^+) facilitate the reduction processes by proton-coupled electron transfers (PCET).

There are two main families of POMs, the isopolyoxometalates with the general formula $[M_xO_y]^{n-}$ and the heteropolyoxometalates of the general formula $[X_zM_xO_y]^{n-}$ which have one (or more) heteroatom(s) X in them. Because of the cationic radius size and the capability of π-bonding between metallic-d and oxygen-p orbitals, only Vanadium (V), Niobium (Nb),

Tantalum (Ta), Molybdenum (Mo) and Tungsten (W) can be at the basis of the POMs. They are well characterized and stable. Moreover, thanks to the accessibility of their empty d-orbitals for metal-oxygen bonding, Mo and W are the most used, in their highest oxidation states (d^0) as Mo(VI) and W(VI).

Several families of these POMs exist according to their geometric stacking such as Keggin, Dawson, Anderson or Preyssler structures (Figure 1.7):

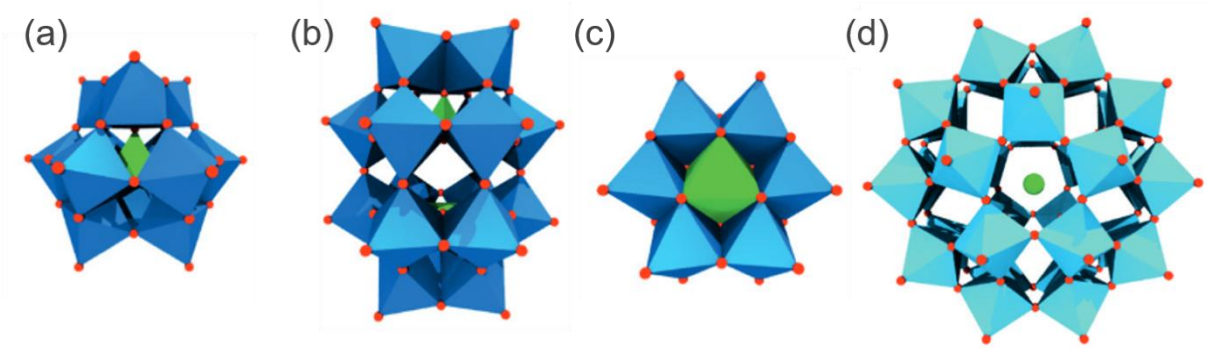

Figure 1.7. Polyhedral representation of POM a) Keggin $[XM_{12}O_{40}]^{n-}$, b) Dawson $[X_2M_{18}O_{62}]^{n-}$, c) Anderson $[XM_6O_{24}]^{n-}$ and d) Preyssler $[Na\subset P_5W_{30}O_{110}]^{14-}$ Blue polyhedral are$\{MO_6\}$(M=any addenda atom), light green polyhedral $\{XO_n\}$(X=heteroatom), light green spheres sodium light blue polyhedral $\{WO_6\}$, red spheres oxygen Image from the reference.[57]

The Keggin structure $[XM_{12}O_{40}]^{n-}$ is an assembly of one tetrahedral XO_4 (X = P, As, Si, B….) and twelve octahedral MO_6 $\{XM_{12}\}$. Four triads M_3O_{13} are built on edge-sharing octahedra. In the α-isomer, the four triads, assembled around the central heteroatom, are further linked through corners. This gives a T_d symmetry (tetrahedral group).

The Dawson structure $[X_2W_{18}O_{62}]^{n-}$ $\{X_2M_{18}\}$ can be viewed as resulting of the fusion of two trivacant Keggin structures $[XW_9O_{34}]^{p-}$, one on top of the other.

Meanwhile, the Anderson $[XMo_6O_{24}]^{n-}$, $\{XM_6\}$, displays a central XO_6 template (X being a metallic cation in that case Al(III), Cr(III), Mn(III), Ni(II), Zn(II), Te(VI) …). In this thesis we will also use the Preyssler anion $[Na\subset P_5W_{30}O_{110}]^{14-}$, which has the form of an ellipsoid. It is constituted of five PW_6 units, arranged in a crown and encapsulating a sodium cation or a lanthanide. That is why the whole anion has an internal fivefold symmetry axis. A PW_6 unit consists of two groups of three corner-shared WO_6 octahedra. Each one shares a vertex with the central PO_4 tetrahedron.[58]

The synthesis of the POMs starts by using a precursor of low nuclearity like $[MO_4]^{2-}$ (M = Mo, W) and a source of the heteroatom and by adding an acid for condensation. The synthesis conditions (pH, temperature, concentration, addition of another salt) of the reaction will allow us to obtain the POM type we want. Hereunder, the reaction (a) of $[PMo_{12}O_{40}]^{3-}$ condensation is given:[59]

$$12\ [MoO_4]^{2-} + HPO_4^{2-} + 23\ H^+ \rightarrow [PMo_{12}O_{40}]^{3-} + 12H_2O$$

In the formation of POMs, the more acidic the solution, the more the POM will be condensed. Conversely at higher pH or by adding a base to a complete POM, (multi)-vacant POMs, formally lacking one or several octahedra, are obtained, like $[PW_{11}O_{39}]^{7-}$ (mono-vacant) or $[PW_9O_{34}]^{9-}$ (tri-vacant). The charge is centralised on the phosphate PO_4^{3-} group.

By taking advantage of the coordination chemistry of vacant POMs, it is possible to get larger assemblies (until nano-object): for example $[H_{56}P_8W_{48}Fe_{28}O_{248}]^{28-}$ is composed of four hexavacant $[H_2P_2W_{12}O_{48}]^{12-}$ linked by 28 Fe^{3+} (Figure 1.8b). The nanometric blue-wheel $[Mo_{154}O_{462}H_{14}(H_2O)_{70}]^{14-}$ is formally composed of the assemblies of 14 $\{Mo_8\}$ building blocks generated in situ under reducing conditions by molybdenum dimers (in red on Figure 1.8c) and monomers (in yellow on Figure 1.8c). Organic-inorganic POM-based hybrids can also be obtained by condensation reactions involving the oxygens (Figure 1.8a).

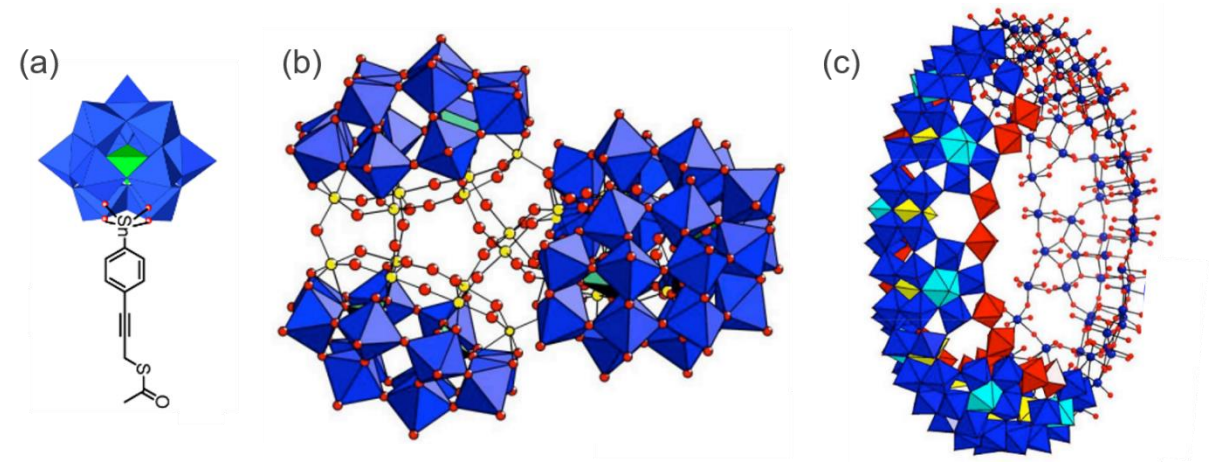

Figure 1.8. Examples of different sizes of POM by (a) adding a ligand to $[PW_{11}O_{39}]^{7-}$ and multiplying (b) the motif $[H_2P_{12}W_{12}O_{48}]^{12-}$ and (c) the pentagonal based {Mo8} motif to get the $\{Mo_{154}\}$ blue wheel. Images from the references.[60,61,62]

With simple POMs or bigger POMs, we can obtain an incredible number of POMs types. Those bulky anions have different sizes, shapes and charges. They induce different electronic and physical properties.

b) Electro-active molecules

An electro-active molecule is a molecule capable of accepting or giving one or several electrons by electron transfer during a chemical reaction called a redox reaction. POMs possess outstanding redox properties: most of them can successively and reversibly accept several electrons with minor structural rearrangement.[59,53,63] Only the counter-ions reorganize themselves around the polyanions when there is a supplementary charge. The POMs are called "electron reservoir". The Keggin one can accept up to 32 electrons. It is because the LUMO is predominantly composed of non-bonding metallic d-orbitals, with a very small antibonding participation of oxygens p orbitals, as shown by some DFT calculations (Figure 1.9).[64]

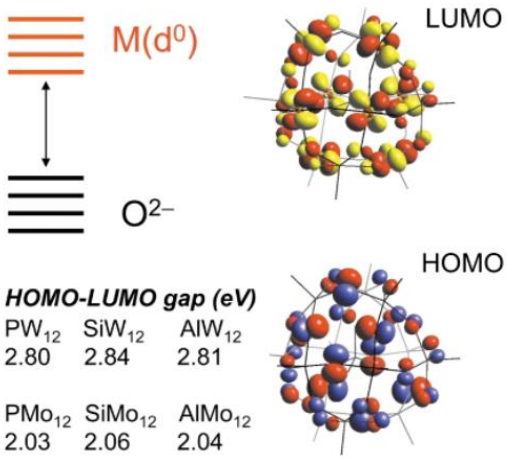

Figure 1.9. Molecular orbital scheme for $[SiW_{12}O_{40}]^{4-}$. LUMO is composed of 73% d-metal orbitals of tungsten atom. Images from the reference[64]

POMs are electron acceptors. At the oxidized state, POMs are white or yellow because of the ligand-to-metal charge transfer (LMCT) occurring in the UV part of the spectrum. When the POM is reduced, it changes to a blue color due to d-d transitions and metal-to-metal charge transfers (MMCT or IVCT intervalence charge transfer) in the visible-near IR. The electrochemistry signal is reversible in aqueous or non-aqueous medium (Figure 1.10). The

anion structure, charge and the nature of the metal atom are parameters which influence the redox potentials of the POMs. The more it is difficult to reduce, the more the redox potential will be negative.

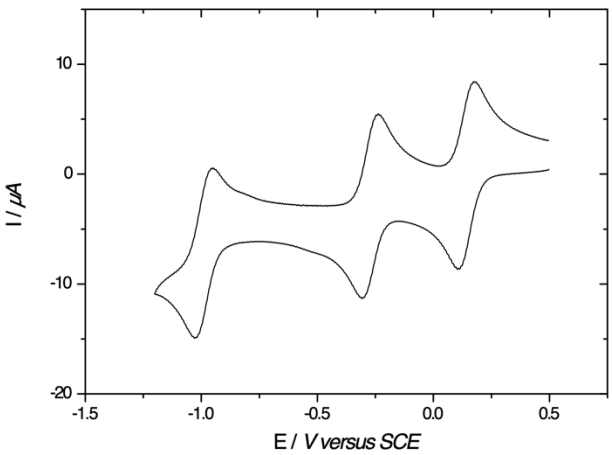

Figure 1.10. Cyclic voltammetry of 0.1 mM of $PMo_{12}O_{40}^{3-}$ in CH_3CN + 0.1M $TBAPF_6$ at a glassy carbon electrode; scan rate 0.1 $V.s^{-1}$

All these redox properties make the POM really interesting to catalysis applications. It is in this field that we find the most publications about POMs.[65] They have also applications in magnetic, photochemistry or biological field.[66] But POMs also have a great time and thermal stability and they are studied for possible applications in nanoelectronic devices.

c) Polyoxometalates in molecular devices

To be used in molecular devices, the POMs have three important advantages compared to other molecules. They have a highly defined morphology, a good solubility in aqueous and non-aqueous solvents and most of all, a rich redox activity. Thanks to these properties, many studies have been done with POMs combined with other electrically active materials for electronic devices. As enumerated in the recent review by Le Yang et al.[67], the charge transfer behaviors of POMs has been explored in POM-based devices. Indeed, several studies focussed on redox memory devices with the POMs embedded in a dielectric (insulating) layer, such as PMMA (poly(methyl methacrylate))[68,69] or stacked with other insulating materials like SiO_2, Ta_2O_5,

reduced graphene oxides in the gate dielectric of a silicon transistor or capacitance.[70–72] In these cases, it is difficult to establish a direct relationship between the redox state of the POMs and their electrical conductance.

In the other hand, it only exists few papers who studied/characterized the electronic transport properties of the POM alone inside a molecular junction. Figure 1.11 illustrates the results of one of this paper:[73]

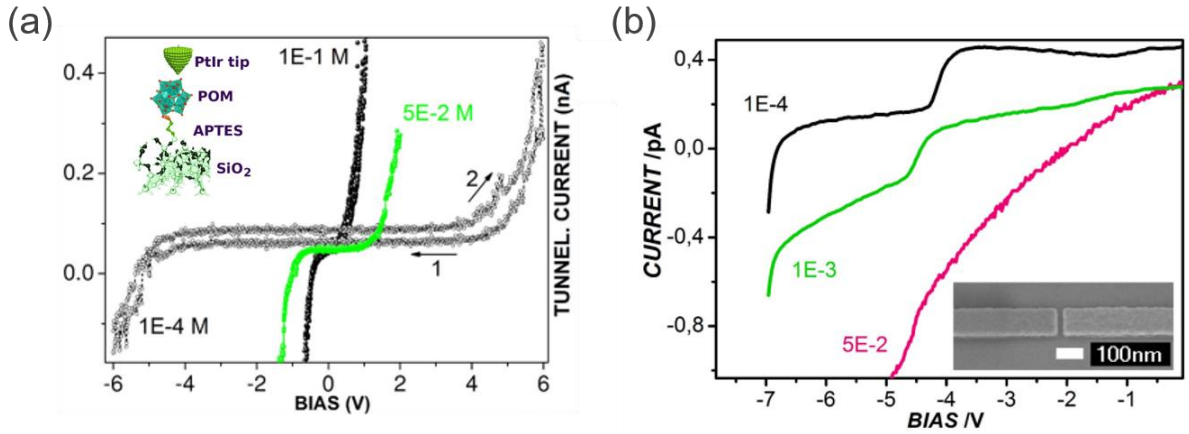

Figure 1.11. Examples of work on molecular junction with different concentrations of POMs by the team of Glezos (a) vertical molecular junction (b) planar molecular junction. Image adapted from the reference.[73]

Here, we see clusters of POMs ($H_3PW_{12}O_{40}$) deposited on SiO_2 surface by LbL (layer-by-layer, alternating anionic/cationic layers[74]). The size of clusters are adjusted by the POMs concentration in solution and a film of POM clusters is deposited between two lateral electrodes (few tens of nm) and STM. I-V curves obtained by STM on film, cross-plane transport, are shown in Figure 1.11a while transition from insulating behaviour (small clusters) to more highly conducting (large clusters, small gap) is shown in Figure 1.11b. In-plane transport, Fig. 1.11b illustrates Coulomb blockade (I-V staircase) for the smallest nanocluster (NC).

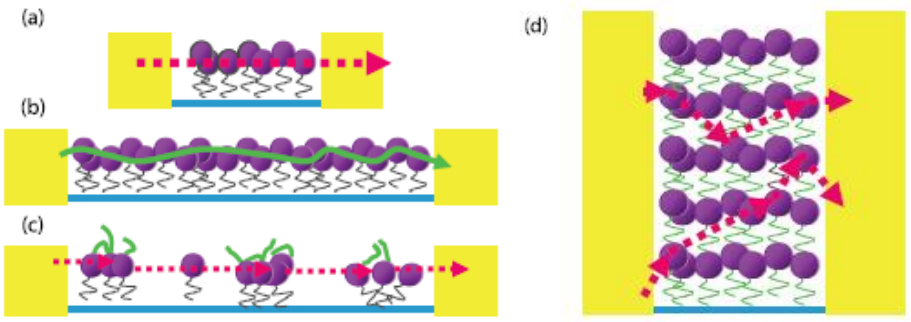

Figure 1.12. Schematic diagram of the transport mechanism model depending on the film types at the high-voltage regime (a) dense monolayer of POM in a short electrode gap (b) in a wide electrode gap (c) in a non-dense monolayer and (d) in a short electrode gap with several layers. Figures from Ref[75]

In another study, the same group has reported how the in-plane electron transport is related to the POM ($H_3PW_{12}O_{40}$) density.[75] Monolayers are formed by electrostatic deposition and multilayers by LbL. As shown in Figure 1.12, different transport mechanisms were identified at sufficient applied bias (i.e. typically electric field > 10^4 V/cm). In (a), in the case of the short electrode gap (< 50 nm) gap and the high density of the monolayer, the electrons can tunnel to the other electrode. By increasing the size of the electrode gap, 150 nm (b), electron tunnelling is no longer possible, and electron transport via percolation pathways dominates. By decreasing the density (c), electrons can tunnel between adjacent aggregates (variable range hopping transport). Finally, with more layers (d), electron transport is systematically observed even with the wide electrode gaps, due to multiple percolated electronic pathways.

The NCM team at IEMN and the e-POM group at IPCM have also studied the electronic properties of SAMs of various POMs deposited on Au or Si substrates (Figure 1.13). The electronic properties of these junctions were characterised by measuring the current-voltage curves, I-V, at several scales (large area junction with Hg electrodes and at the nanoscale by C-AFM). [76,77]

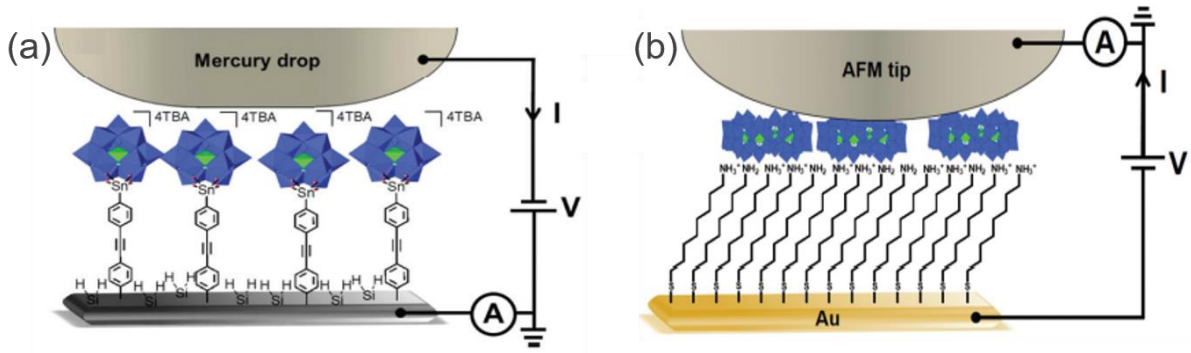

Figure 1.13. Scheme of the molecular junctions (a) Si-POM//Hg (b)Au-C8--POM//C-AFM tip.[76,77]

In one case, POMs ($TBA_3[PM_{11}O_{39}\{Sn(C_6H_4)C{\equiv}C(C_6H_4)N_2\}]$, M=W or Mo), which differ only by the transition metal, were covalently grafted onto a hydrogenated silicon (Si-H) surface via a diazonium salt reaction (Figure 1.13a).[38] The top electrode was a mercury drop. The main result was that the electronic structure of POMs in solution (i.e. a deeper LUMO for the Mo-based POM) is preserved in the solid-state molecular junction (Figure 1.14a). In a second study, a large POM $[H_7P_8W_{48}O_{184}]^{33-}$ was electrostatically deposited onto a positively charged 8-amino-1-octanethiol self-assembled monolayers and contacted by a conductive tip atomic force microscope (C-AFM) (Figure 1.13b). This work allowed to determine the optimal conditions to control the morphology and organization of the electrostatically deposited POM monolayer. From the analysis of the current-voltage curves with different models: electron tunneling though the SAMs (Simmons model), transition voltage spectroscopy (TVS) method or single molecular energy level mediated transport (Landauer equation), the authors concluded that the LUMOs of the alkyl spacer and the POM are energetically aligned probably due to dipole effects at the alkyl/POM interface (Figure 1.14b).

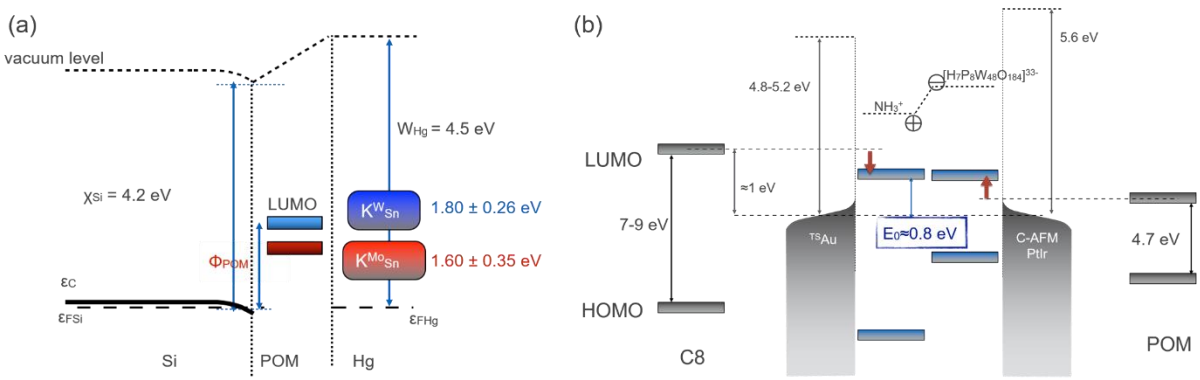

Figure 1.14. Energy diagrams of (a) POM with Mo or W and (b) alkyl/P_8W_{48} (images unpublished from the cited works above[76,77])

The electronic transport properties of POMs at different redox states have not been widely explored in the literature. Turo et al.[78] showed that the conductivity of single crystal, a metal-oxide-framework (MOF), of $[Na{\subset}P_5W_{30}O_{110}]^{14-}$ $\{P_5W30\}$ linked with $Co(H_2O)_4^{2+}$ is increased by a factor of ca. 440 upon photoreduction (UV light in anaerobic conditions) (Figure 1.15). It occurs because of the ability of the Preyssler POMs to accept up to 10 electrons without modification of the crystal structure. This MOF can stay indefinitely in the reduced state when

stored under inert conditions but go back to his oxidized state over few days when exposed to air.

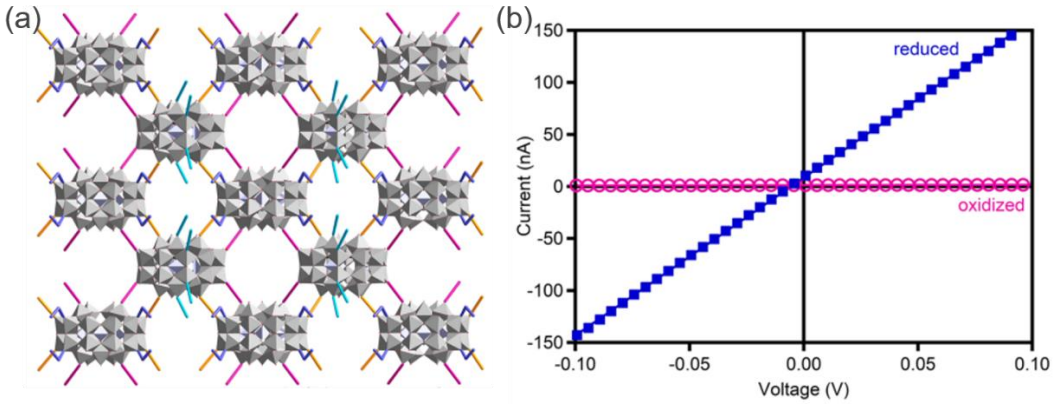

Figure 1.15. (a) Representation of the POM MOF and (b) I-V curves of a single crystal in the reduced and oxidized states with conductivity 9.2 × 10^{-5} and 2.1 × 10^{-7} S/cm respectively. Image adapted from the reference.[78]

Recently, using scanning tunneling microscopy, Linnenberg et al. demonstrated a step-by-step increase of a single POM $[V_6O_{13}\{(OCH_2)_3CCH_2SC_6H_5\}_2]^{2-}$ (Lindqvist-type V_6) conductance up to the 4-electron redox state (Figure 1.16).[79,80] In that case, DFT calculations[80] explained this behavior by the gradual filling of the vanadium d-levels in the projected density of states (PDOS).

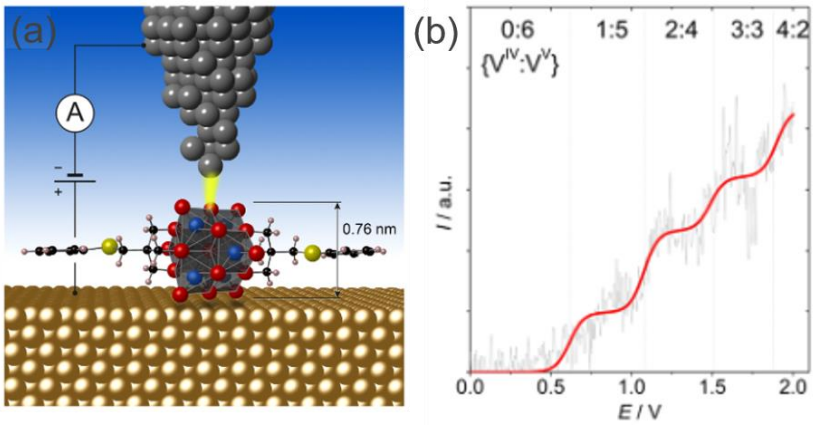

Figure 1.16. (a) Schematic representation of hexavanate single molecule in Au—POM STM tip configuration and (b) STM response showing four steps corresponding to the four redox state of the POM.[79]

These previous results prompted us to further study in detail the relationship between the electron transport in POM-based MJs and the redox state of the POMs. In the course of my

thesis, I studied POMs such as X = phosphorus (P) and M = molybdenum Mo (VI) or tungsten W(VI). More precisely, the main work was about POMs with the Keggin and Preyssler structures. Now, I present below a possible application.

III. The development of reconfigurable and unconventional computing devices

Neurons are the main components of the nervous system. When there is a stimulation of sufficient intensity, an electrical signal in the form of an action potential passes through the neuron, this is the nerve signal. Once in the synapse area, this signal is chemically transmitted from one neuron to the next one by neurotransmitters. The nerve signal is therefore an electrochemical signal and it is on this model that artificial neuromorphic systems are based.

The two main approaches to realise these systems are software and hardware, they are called "Artificial Neural Network" (ANN). In hardware, the ANN nanoarchitecture is built in the classical way using top-down or bottom-up methods.[81] Top down approach is based on the physics of silicon devices in order to reproduce the biophysics of nervous tissue[82] i.e. Si-CMOS (complementary metal oxide semiconductor) and trend to reach physical limitations. Emerging technologies using bottom-up approach with non-volatile memory (examples detailed in the review by Burr et al.[83]) become a good perspective to this field.[84]

A network of neuron-like processing units interconnected via synapse-like weighted links represents this approach. However, the limitations of these architectures prevent a good distinction of signals and a good adaptation to noise levels in the environment.[85] To best mimic the function of the brain, and to overcome these difficulties[86] Reservoir Computing (RC) has been proposed.

a) Introduction to Reservoir Computing

The research field of Reservoir Computing emerged in the years 2001-2002 with two seminal publications of Jaeger et al.[87] and Maass et al.[88] RCs are part of the Recurrent Neural Network (RNN) framework and are appropriate for temporal/sequential information processes.[89]

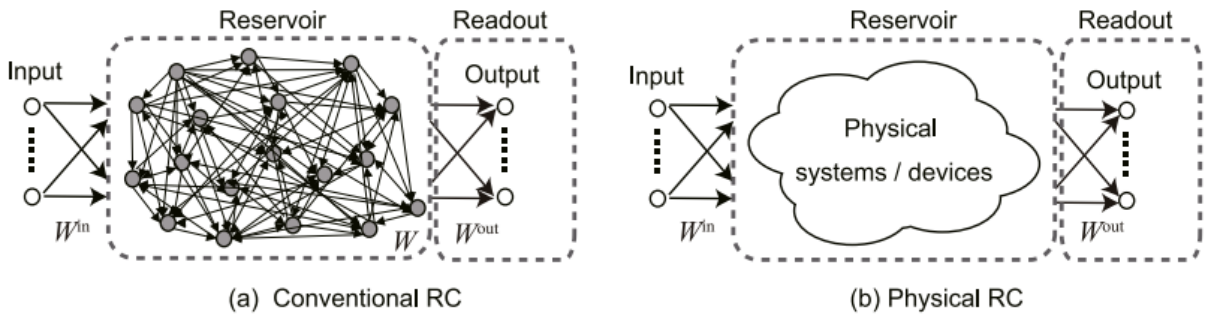

Figure 1.17. Reservoir Computing with W = Weight (a) Software realisation and (b) hardware realisation.[90]

In the RC approach, the input signals excite a reservoir with complex dynamics and highly non-linear properties composed of nodes and links. The signals propagate between nodes that are interconnected by links with random "weights" (high variability) (Figure 1.17). In the reservoir, the input signals are projected into a higher-dimensional representation space. The signals of some output nodes are read by an output layer, a simple algorithm for supervised learning of binary classifiers called a perceptron[91], which is trained to perform a given information processing task. That is to say, only the readout weights are trained with a learning algorithm and not the input weight and the weight of the recurrent connections in the reservoir.

RC systems could be seen as attractive learning machine. They are easy to construct and optimize (few parameters, less computational requirements). When the perceptron is trained properly, they are efficiently robust to input and state noise. They are not sensible to some variations in their internal parameters, due to random fabrication of reservoirs. Moreover, it is possible to use the same reservoir for different tasks simultaneously. Finally, RC shows competitive performances in a variety of temporal signal processing tasks.[92] All these elements make RC a really low-cost approach compared to a standard RNN.

Of course, these advantages must be tempered by the all-important criterion of technological maturity, which will enable the transfer of neuromorphic technologies to the industrial level.

The physical implementations can be dynamic system models, such as electronic, photonic, spintronic, mechanical, biological and more recently molecular (cf. review by Tanaka[90]). In electronics, CMOS components were used in these systems but their identical electronic character does not satisfy the wide variability conditions. The wide dispersion of transport properties in molecular electronics could lead to a more efficient RC.

b) At the molecular scale

Components based on polyelectrolyte, notably Organic Electrochemical Transistors (OECT), have been implanted in these RCs, allowing new advances in bioelectronics.[93–96]

In a wider approach, systems based on nano-objects (nanoparticles, nanowires, nanotubes, molecules,…) are also prone to be used to implement unconventional computing devices. They represent an example of the so-called research field "evolution-in-materio (EIM)". Briefly, EIM deals with the manipulation of physical systems by computer-controlled evolution, exploitable at the molecular level.[97,98] For example, Bose et al.,[99] proposed a system with nanoparticles (NP) surrounded by octanethiol, connected between several electrodes (Fig. 1.18). Each NP act as a nonlinear single-electron transistor and electron transport is dominated by Coulomb blockade. The disordered network, combined with a genetic algorithm (GA), is prone to various logic gates reconfigured and some Boolean functions as AND, OR, XOR were demonstrated. All this work has been done at 5K.

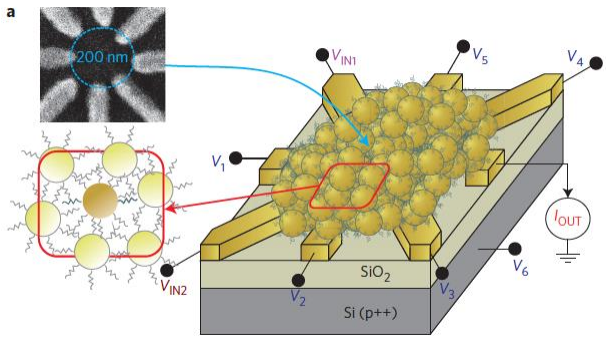

Figure 1.18. Schematic of the device layout of reconfigurable logic.[99]

Bose with the team of Simon A. Brown have also done similar work with atomic switch network (ASN) using simulations and experiments.[98-100] ASN has been proven to generate network level dynamics that resemble those observed in biological neural networks. Indeed, atomic switches induce high non-linear and variable electronic switching behaviours. They have optimised a self-assembled ASN with Sn NP and succeeded to fabricate tunnelling-percolating devices. This process facilitates critical avalanches of signals (quantitatively the same as the one in cortical tissue), promising good advanced in brain-like networks.[100–102] The teams of Gimzewski and Aono has also use ASN, this time with disordered sulfurized silver (Ag_2S) nanowires to introduce a RC.[79,101-103] The fabrication of such component creates some hazardous/random interconnections between these nanowires who act as the links and the

interconnections between them are the nodes. The input signal can follow different pathways through the network and the output electrodes and the perceptron is trained to reconstruct three signals with well defined waveforms (sinus, square and triangle).[81,103–105]

Another example included POM at room temperature. Indeed, molecular neuromorphic devices, composed of a dynamic dense network of single-walled carbon nanotubes (SWNTs) complexed with POMs, generates spontaneous spikes and noise. Simulation has been done to know if this organic material can be inserted into the reservoir of the RC by pushing the redox properties of the POMs. It turned out that we can pass progressively from a charging and discharging, respectively due to reduction and oxidation reactions (figure 1.19a). This arises the advantage of inherent non-linear dynamics.[106] Banerjee et al.[107,108] extended this simulation to experiment by adding porphyrins to the complex. They success to reconstruct six Boolean functions via supervised training of linear voltage readouts at room temperature. Finally, they demonstrated the implementation and integration of this RC at the hardware level (Figure 1.19b). These results show promising role of porphyrin-$[SW_{10}V_2O_{40}]^{4-}$ in RC and in our work, we will explore this capability using the POM alone.

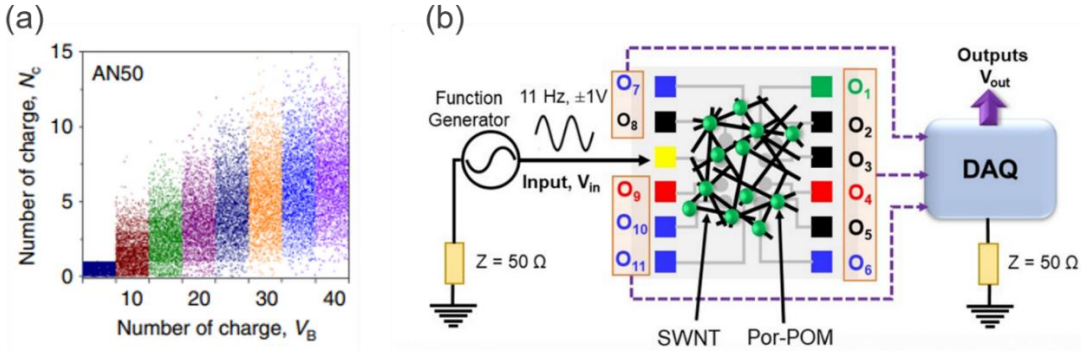

Figure 1.19. SWNT/POM network (a) Noise generation in the base current at each cycle for stepwise increments of V_B and (b) full circuit schematic of the outputs obtained from different electrode pads when a sine wave of 11 Hz, ±1 V is applied at the yellow-colored electrode pad connected to the SWNT (black line)/Por– POM film (green circle). A function generator is used where the output from one pole is fed as the input signal, whereas the other pole is grounded via a 50 Ω resistor (z value, orange box). All outputs are then taken from the data acquisition (DAQ) system which is grounded via a similar 50 Ω resistor, to complete the full circuitry.[106,108]

Finally, Viero et al.[109] proposed another implementation (Figure 1.20a): the nodes are gold nanoparticles and the molecules capping the NPs, azobenzene-bithiophene-alkylthiol (AzBT), are the links. Thanks to their photoswitch properties, they obtain a light-control reconfigurable logic (e.g. follower gate with the AzBTs in the trans configuration to AND gate in the cis

configuration). They show evidence of (i) increase of non-linearity and complex dynamics from frequency harmonic generation, (ii) more peaks in the FFT of sinusoidal input signals due to the increase of the harmonic, interharmonic and intermodulation distorsions (Figure 1.20b,c). All these parameters play a role for the applications in RC. The team has also published a work with a similar implementation (Au NP/molecule) by playing with the redox properties of EDOT to propose reconfigurable logic functions.[110]

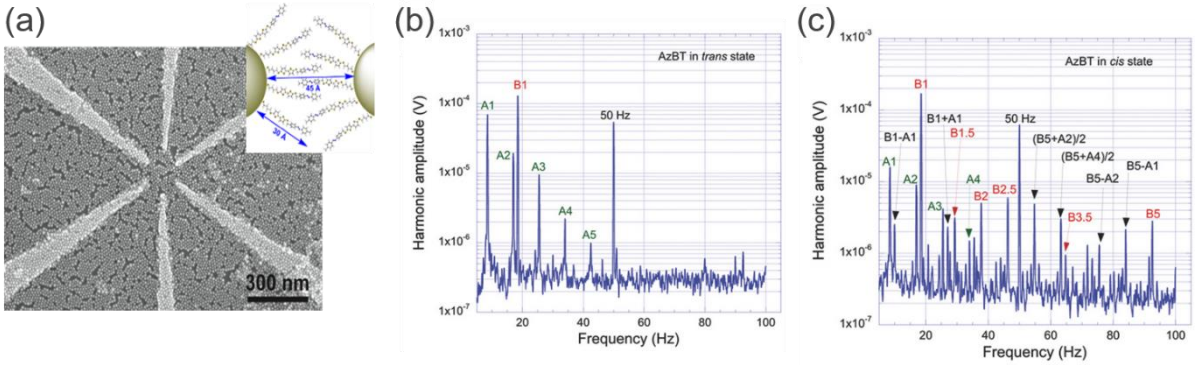

Figure 1.20. (a) SEM images of the representation of the nano-objet Au-AzBt who can be studied at a reservoir base for RC, and Signal frequency spectra for the same NPSAN output when b) the AzBT molecules are in the trans state and c) in the cis state showing Intermodulation distorsion (IMD) and interharmonics. The HHG peaks are labeled as Ai (i = 1 for the fundamental, i = 2 for the second harmonic, etc.) and Bi for harmonics corresponding to the A and B input signals, respectively. IMD peaks are labeled by a combination of Ai and Bi. Interharmonics are labeled with noninteger i values.[109]

IV. Conclusion of chapter 1

To conclude, in this chapter, the basic concepts were introduced and the key words of the work were discussed. The chapter 2 will be focused on vertical molecular junctions with the C-AFM tip as the top electrode. They are made of two polyoxometalates, $[PMo_{12}O_{40}]^{3-}$ and $[Na{\subset}P_5W_{30}O_{110}]^{14-}$, monolayers self-assembled on ultra-flat Au electrodes. The electron transport properties at different redox states and the influence of the counter-cations will be detailed. The chapter 3 will present the study of some planar molecular junctions made of a two-dimensional network of Au nanoparticles (NPs) and POMs. They are called 2D-PNs: 2D POM networks. Several assembly processes were studied and optimized, they will be described and some electronic properties will be explored. Finally, the last chapter will not be based on POMs but a material close to, the metal oxide nanowires $W_{18}O_{49}$. The choice of this type of nanowires will be explained later in the chapter 4 as well as their synthesis, the electronic properties of a single nanowire and 2D networks of them.

Contents of chapter 2

Chapter 2 Vertical nano-molecular junction 40

I. Fabrication of the molecular junctions and methods of electrical measurements..... 40

II. Redox-controlled conductance of PMo_{12} molecular junctions..... 42

a) Chemical synthesis of the POMs and physicochemical characterizations 42

b) Electron transport properties of C2 and C6 MJs..... 47

c) Electron transport properties of C2/PMo_{12} MJs..... 49

d) Electron transport properties of C6/PMo_{12} MJs..... 53

e) Discussion of the electron transport properties..... 67

f) Summary and outlook..... 71

III. Study of a second POM: P_5W_{30}..... 73

a) In-situ irradiation of KP_5W_{30} 73

b) Electron transport properties of C6/TBAP_5W_{30} MJs 76

c) Exchange of the counterion..... 81

d) Influence of the counterion in the electron transport properties of C6/P_5W_{30} MJs 88

e) Summary and outlook 92

Chapter 2 Vertical nano-molecular junction

The goal of this chapter is to discuss the electronic properties of polyoxometalate-based molecular junctions with an ultra-flat gold surface as the bottom electrode and the conductive – AFM tip as the top one. The structure of the molecular junction is the same during this entire chapter.

I. Fabrication of the molecular junctions and methods of electrical measurements

The detailed protocol is explained in annexe A2.1.

- **Bottom electrode**

To obtain a flat surface of the electrode, we used template-stripped gold surfaces (^{TS}Au).[111,112] The gold thickness is around 400 nm and the Ti around 40nm. Briefly, an Au film is evaporated by sputtering on a flat silicon wafer, transferred to a glued clean glass piece, mechanically stripped with the gold film attached on the glass piece (figure 2.1 (a)).

- **Monolayer**

The POMs are inserted in the MJ by electrostatic interaction using SAMs. The first step consists of adding some charge to the surface of the electrode by using an aminoalkylthiol SAM. The electrode is dipped in a solution at 10^{-3}M of aminoalkylthiol in ethanol overnight, then immersed in Phosphate Buffered Saline (PBS) to obtain a SAM surface with a low roughness. Indeed, it has been proven that this PBS treatment optimizes the of NH_3^+/NH_2 ratio on the surface and consequently removes the formation of aggregates on the aminoalkylthiol SAMs and avoids clustering of POMs during the electrostatic deposition.[76]

For the following, we will write CX with X the number of CH_2 in the alkyl chain. In this work, we used C2 and C6 SAMs. Once at the surface, there will be some positive charges due to the partial protonation of the terminal group: NH_3^+ (~ 30 – 50%)[113–116]. By immersion of the functionalized substrate in a solution at 10^{-3}M of POMs in solvent (H_2O or acetonitrile) during few hours, one monolayer of POMs is electrostatically deposited (whatever the immersion

time). To be sure that the monolayer is grafted, at each step, ellipsometry measurements were done (annexe A2.1). Moreover, the roughness of the modified substrate has been also determined by using the tapping mode of AFM (annexe A2.1).

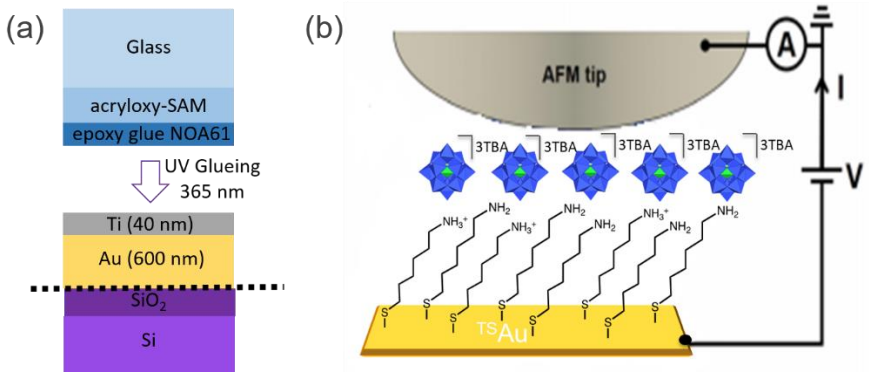

Figure 2.1. (a) Preparation of the template-stripped gold electrode with the black dashed line symbolizing the detachment of the superior part of the bottom electrode and (b) structure of the molecular junction.

- **Top electrode**

The top electrode is a C-AFM tip in full metal, the platinum (purchased from Rocky Mountain Nanotechnology, model 12PT400B, k=0.3N/m). This tip is chosen because of the good aptitude to contact the surface and to use a low loading force. The loading force is around 6 – 11 nN. By fixing the force, we also control the number of molecules connected in the MJ (larger the loading force, larger the tip contact area and the number of molecules).

We will note ^{TS}Au-Cx/POM//Pt the short name of the MJ with "-" a chemical bond, "/" an electrostatic bond and "//" a mechanical contact.

- **Electrical measurements**

The current-voltage (IV) curves of the MJs were acquired by C-AFM (ICON, Bruker) operated in ambient conditions in an air-conditioned laboratory (at room temperature RT=22°C and 35-40% of relative humidity), the C-AFM tip is grounded, and the voltage is applied to the substrate from -1.5V to +1.5V (typically). Once the loading force is calibrated, 100 current-voltage (IV) traces are recorded with back and forth voltage sweeps and at three different zones (Figure 2.1b), thus given a dataset of 600 I-Vs for each sample (see details in annexe A2.2). After cleaning the dataset (see details in annexe A2.2), these IVs are plotted as a 2D histogram (or heat map) in a semi-log scale to obtain an overview of the current, and dispersion, involved during the measurement. 1D histogram of log(|current|) at a known voltage are also given to further analysis. Then, the electronic structure (e.g. energy position of the MOs, electronic

coupling to electrodes,…) is estimated with the SEL model and TVS method (see Section Ic in Chap. 1). The fit of the SEL model is combined with the TVS method and we limited the fits of the SEL model to an optimized voltage window to obtain the best determination of ε_0 (see details in annexe A2.2). Sometimes, the number of molecules contributing to the electron transport (ET) in the MJ can be estimated using mechanical models of the tip/SAM interface when the Young modulus of the SAM is reasonably known.[117–121] This is not the case here for the POM/alkyl SAM system, the Young modulus has not been determined. That is why we use N=1 all along this chapter. The exact value of N does not change significantly the fitted parameter ε_0.

II. Redox-controlled conductance of PMo_{12} molecular junctions

The main objective is to examine the repercussion of adding one electron (i.e. reduction) to the POM on the conduction mechanism of the MJ. Here, the work has been done with phosphomolybdate $[PMo_{12}O_{40}]^{3-}$ with a tetrabutyl ammonium salt ($N(C_4H_9)_4^+$ or TBA) counterion, the pristine POM is $[PMo^{VI}_{12}O_{40}]^{3-}$ ($PMo_{12}(0)$) and the reduced one is $[PMo^{VI}_{11}Mo^{V}_{1}O_{40}]^{4-}$ ($PMo_{12}(I)$).

We have chosen this POM because its synthesis is well known in the literature as well as its reduction reaction.[122,123]

a) Chemical synthesis of the POMs and physicochemical characterizations

The chemical synthesis and physicochemical characterizations were done by Kelly Trinh in collaboration with Florence Volatron and Anna Proust (ePOM team, Institut Parisien de Chimie Moléculaire, CNRS and Sorbonne University, Paris).

$PMo_{12}(0)$ and $PMo_{12}(I)$ have been synthesized according to previously published procedures.[122,123]

To synthesize the $PMo_{12}(0)$, 60 mL of a 1M solution of sodium molybdate dihydrate $Na_2[MoO_4].2H_2O$ was added to 9 mL of nitric acid HNO_3 and 50 mL of 1,4-dioxane. Then, 5 mL of a 1 M solution of orthophosphoric acid H_3PO_4 and 5g of tetrabutylammonium bromide

NBu_4Br (TBABr) are added under stirring. After filtration, the yellow heavy solid is immersed in 50 mL of boiling water and stirred, filtered again and washed with 50 mL of water, 100 mL of ethanol and diethyl ether until obtaining of a yellow powder. It is finally recrystallized in hot acetone (30 mL of hot acetone for 1 g of powder). After three days in the refrigerator, the mixture is filtered and yellow crystals are collected, dried under vacuum several days at 60°C. Note that during the experiment, the POM was handled with glass spatula/material to avoid its reduction.

The redox properties of the POM were checked by cyclic voltammetry (CV). Figure 2.2 shows the CV of 1mM solution of $(TBA)_3[PMo^{VI}_{12}O_{40}]$ in 0.1 M $TBAPF_6$ in CH_3CN. Three reversible waves are observed corresponding to three monoelectronic processes with midpoint potentials at +0.142, -0.272 and -0.991 V/SCE ($E_{1/2}=0.5(E_{pa}-E_{pc})$; Epa: anodic peak potential; Epc cathodic peak potential).

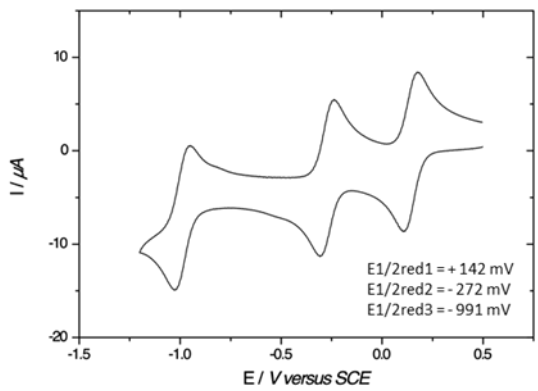

Figure 2.2. Cyclic voltammetry showing reduction of the PMo_{12} up to 3 electrons.

The LUMO energy position is calculated by $E_{LUMO} = -(E_{1/2red}+E_{ref/ESH})-4.44$, with $E_{ref/ESH}=0.308$ eV for the saturated calomel electrode (SCE) with CH_3CN.[124] With $E_{1/2red}=0.14$ V/SCE for the one-electron reduction, we get E_{LUMO} = -4.89 eV with respect to the vacuum level.

Here, we process to one mono-electronic reduction by reaction with phenyllithium in acetonitrile:

$$(TBA)_3[P\mathbf{Mo}^{\mathbf{VI}}_{12}O_{40}] + LiC_6H_5 + TBABr \rightarrow (TBA)_4[P\mathbf{Mo}^{\mathbf{VI}}_{11}\mathbf{Mo}^{\mathbf{V}}_{1}O_{40}] + LiBr + {}^{1}/_{2}C_{12}H_{10}$$

Precisely, 100 mg of $(TBA)_3[PMo_{12}O_{40}]$ is dissolved in a minimum volume of dry acetonitrile (~6 mL) in a dry Schlenk tube containing a magnetic stir bar, under argon. Under stirring, few

drops of phenyllithium are added to the $PMo_{12}(0)$ solution until the solution displays a blue color. 15 mg of NBu_4Br is added to the solution followed by the addition of ~ 15 mL of diethylether, leading to the formation of a blue precipitate. The suspension is filtered on a cellulose membrane. The blue solid is subsequently washed with 10 mL of tetrahydrofuran and 10 mL of methanol. It is finally dried under vacuum, in the dark.

The first indication of the oxidation degree change is that the POM powder passes from yellow to a blue color. Then, we have successively characterized the composition of the product by ^{31}P NMR, solution UV-vis spectra and XPS on powder (technical details in annexe A2.3).

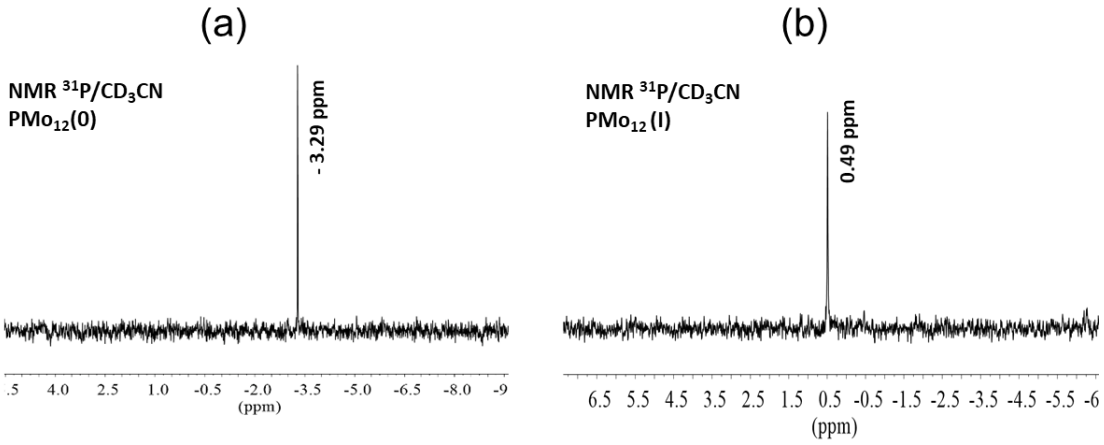

Figure 2.3. NMR ^{31}P of (a)$PMo_{12}(0)$ and (b) $PMo_{12}(I)$

The ^{31P} NMR of PMo_{12} is done in solution with CD_3CN (Figure 2.3). The initial singlet is at -3.29 ppm and shifts to 0.49 ppm after adding phenyllithium. Once the reaction is over and we get the dry powder, we proceed to UV-vis spectroscopy and XPS (Figure 2.4).

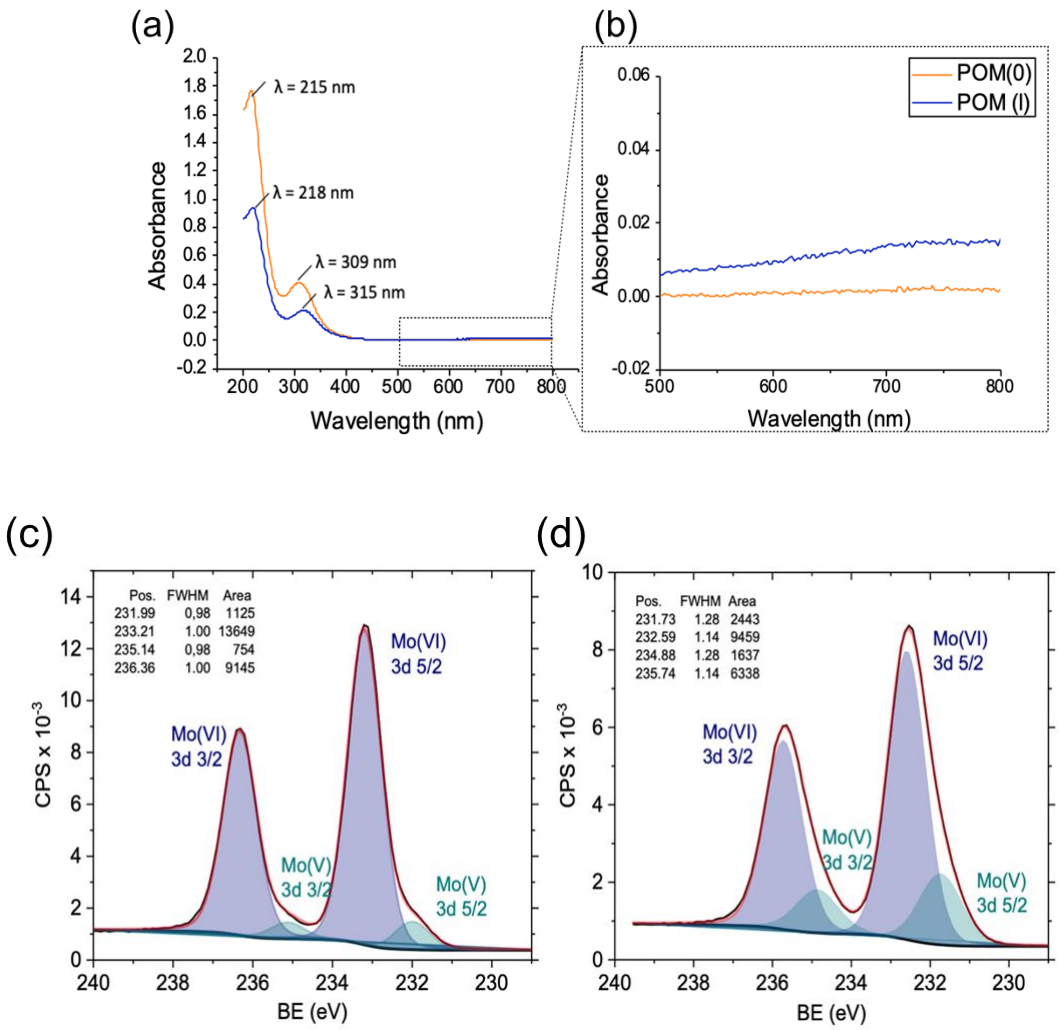

Figure 2.4. (a) and (b) UV-vis spectra of $PMo_{12}(0)$ and $PMo_{12}(I)$ and Mo_{3d} XPS spectra of (c) $PMo_{12}(0)$ and (d) $PMo_{12}(I)$

For the UV-vis spectroscopy (Figure 2.4 a and b), POMs were diluted in solution with CH_2Cl_2 (~ µm). For the reduced POM, we clearly see a shift of the ligand-to-metal charge transfer (LMCT) band (309 → 315 nm). Also, an intervalence charge transfer (IVCT) band between Mo(V) and Mo(VI) appears at around 750 nm. The XPS measurements were done on powder of $PMo_{12}(0)$ and $PMo_{12}(I)$ deposited on Si/SiO_2 functionalized with aminopropyltriethoxysilane (APTES) that give a better uniform deposition of the powder than on Au functionalized with aminoalkylthiol. Figure 2.4 (c and d) shows the Mo_{3d} spectra. The energy splitting between the $3d_{3/2}$ and $3d_{5/2}$ peaks is fixed to 3.15 eV with an amplitude ratio of 0.67. From the peak areas, we calculate the Mo(VI)/Mo(V) ratios of 12.1 for $PMo_{12}(0)$ and 3.9 for $PMo_{12}(I)$.

The $PMo_{12}(0)$ and the $PMo_{12}(I)$ (respectively short name for the pristine and reduced to one electron POM) have been inserted in the MJ with short alkyl chain (C2) and long alkyl chain (C6) aminoalkylthiol SAM as described in the previous part (Chapter 2_I).

- **Ellipsometry and topography**

The thickness and the roughness of the layer have been checked after the deposit of the alkyl chain alone and with the POM (Table 2.1) by ellipsometry and TM-AFM (technical details in annexe A2.1). Figure 2.5 shows the TM-AFM image of the layers.

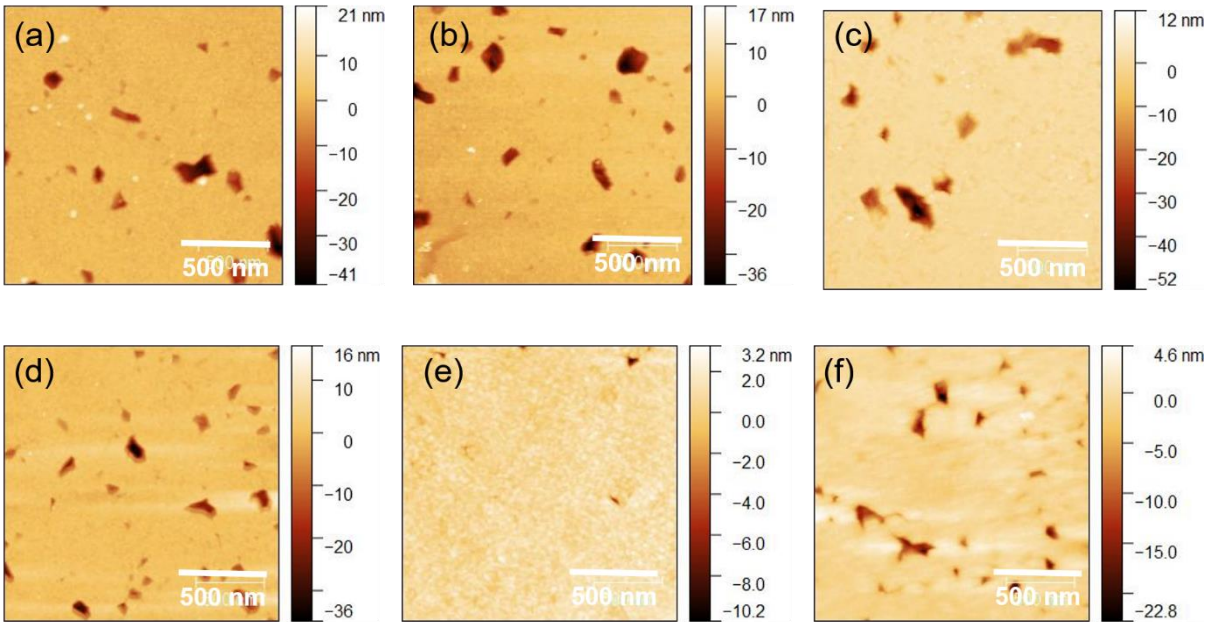

Figure 2.5. Tapping-Mode AFM images of (a) ^{TS}Au-C2 SAM, (b) ^{TS}Au-C2/$PMo_{12}(0)$, (c) ^{TS}Au-C2/$PMo_{12}(I)$, (d) ^{TS}Au-C6 SAM, (e) ^{TS}Au-C6/$PMo_{12}(0)$, (f) ^{TS}Au-C6/$PMo_{12}(I)$. The dark spots are defects (pinholes) in the underlying Au substrate and they are masked for the roughness analysis.

Table 2.1. Overview of average values of the thickness of the SAM and SAM+POM determined by ellispometry measurement and the RMS roughness analysed from TM-AFM images.

		Thickness (± 2) (Å)	RMS roughness (nm)
C2		4	~ 0.85
C2 + POM	$PMo_{12}(0)$	12	~ 0.86
	$PMo_{12}(I)$	12	~0.88

C6		10	~ 0.65
C6 + POM	$PMo_{12}(0)$	18	~ 0.56
	$PMo_{12}(I)$	18	~ 0.73

As expected, the thickness of the C2 SAM is almost twice thinner than with the C6 molecules. The thickness of the PMo_{12} alone is around 8 Å in the four configurations. Concerning the rms roughness, the reference of ^{TS}Au is 0.3-0.4nm.[111,112] On the TM-AFM images (Figure 2.5), we can see some dark spots due to pinholes in the underlying Au substrate. They are masked for the analysis. With a short or long aminoalkylthiol SAMs, we notice that the deposition of the POM does not have an important impact on the roughness and the surface is still featureless. With the short SAM, the roughness is a bit larger, in agreement with the known feature that shorter alkyl chains lead to more disordered SAMs.[17]

In theory, the PMo_{12} size (diameter) is supposed to be 10 Å. Here, the thickness of the POM SAM can be a little smaller due to the voids in a close-packed monolayer of spheres.[125] Still, in the four monolayers, we can conclude that the POM coverage is almost complete.

b) Electron transport properties of C2 and C6 MJs

Firstly, the electronic properties of the SAM C2 (Figure 2.6) and C6 (Figure 2.7) alone have been controlled and are presented here.

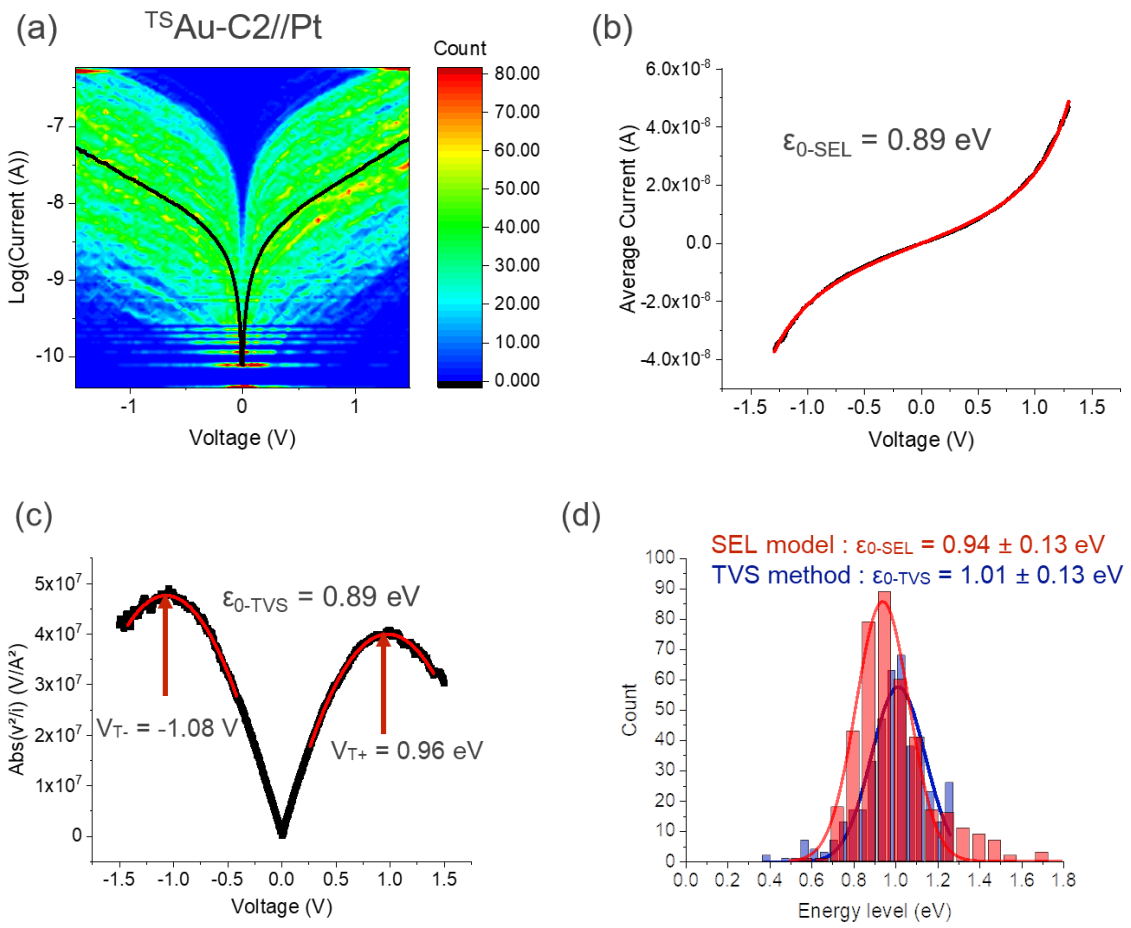

Figure 2.6. (a) 2D histograms (heat maps) of I-Vs (~ 8 nN) in a semi-log$_{10}$ plot for (a) ^{TS}Au-C2//Pt, the solid black line is the mean $\bar{I}$-V curve. (b) SEL fit of the $\bar{I}$ -V curve, (c) TVS method with t the $\bar{I}$ -V curve and (d) The histograms of the SEL model (red bars) and TVS method (blue bars) and fits by a normal distribution (the fitted mean value ± standard deviation is indicated on the panels).

After cleaning the dataset, 424 IVs are selected and shown in the 2D histograms (Figure 2.6a). The mean curve is calculated from the histogram (black line) and then, fitted with the SEL model (equation 1.3 in Chapter 1; on the range ± 1.3V as discussed in annexe A2.3 to avoid some artefacts of the model, Figure 2.6b) and analysed by the TVS method (equation 1.4 in Chapter 1; Figure 2.6c). We find a value ε_0 of 0.89 eV in both cases. Finally, the two methods have been applied to the 424 IVs and from the statistical distribution, we obtained a mean $\varepsilon_{0\text{-SEL}}$ value around 0.94 eV with SEL model and $\varepsilon_{0\text{-TVS}}$ around 1.01 eV with TVS method (Figure 2.6d). The same results are presented with the SAM C6 (Figure 2.7).

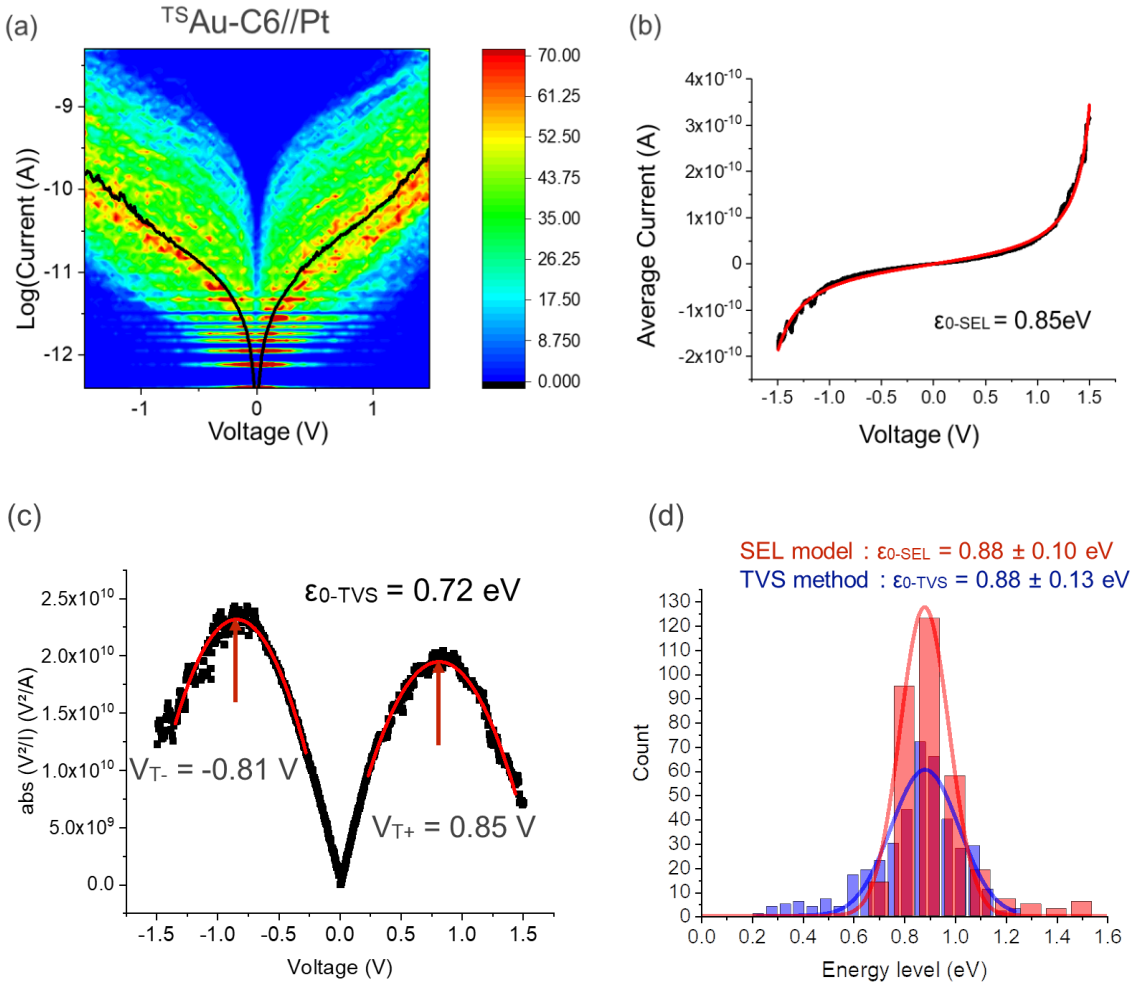

Figure 2.7. (a) 2D histograms (heat maps) of I-Vs (~ 8 nN) in a semi-log$_{10}$ plot for (a) ^{TS}Au-C6//Pt, the solid black line is the mean Ī-V curve. (b) SEL fit of the Ī -V curve, (c) TVS method with t the Ī -V curve and (d) The histograms of the SEL model (red bars) and TVS method (blue bars) and fits by a normal distribution (the fitted mean value ± standard deviation is indicated on the panels).

Here, 415 cleaned IVs are shown in the 2D histogram (Figure 2.7a). As previously, by extracted the mean Ī-V curve, we obtain a value $\varepsilon_{0\text{-SEL}}$ of 0.85 eV with the SEL model (fit on ± 1.5V, Figure 2.7b) and $\varepsilon_{0\text{-TVS}} \approx 0.72$ eV with the TVS method (Figure 2.7c). From both methods, we observe the same mean value of 0.88 eV from the statistical analysis.

These datasets are the reference for the ET properties of SAM/POMs MJs.

c) Electron transport properties of C2/PMo$_{12}$ MJs

We first present the electron transport properties of the PMo_{12} deposited on a C2 SAM.

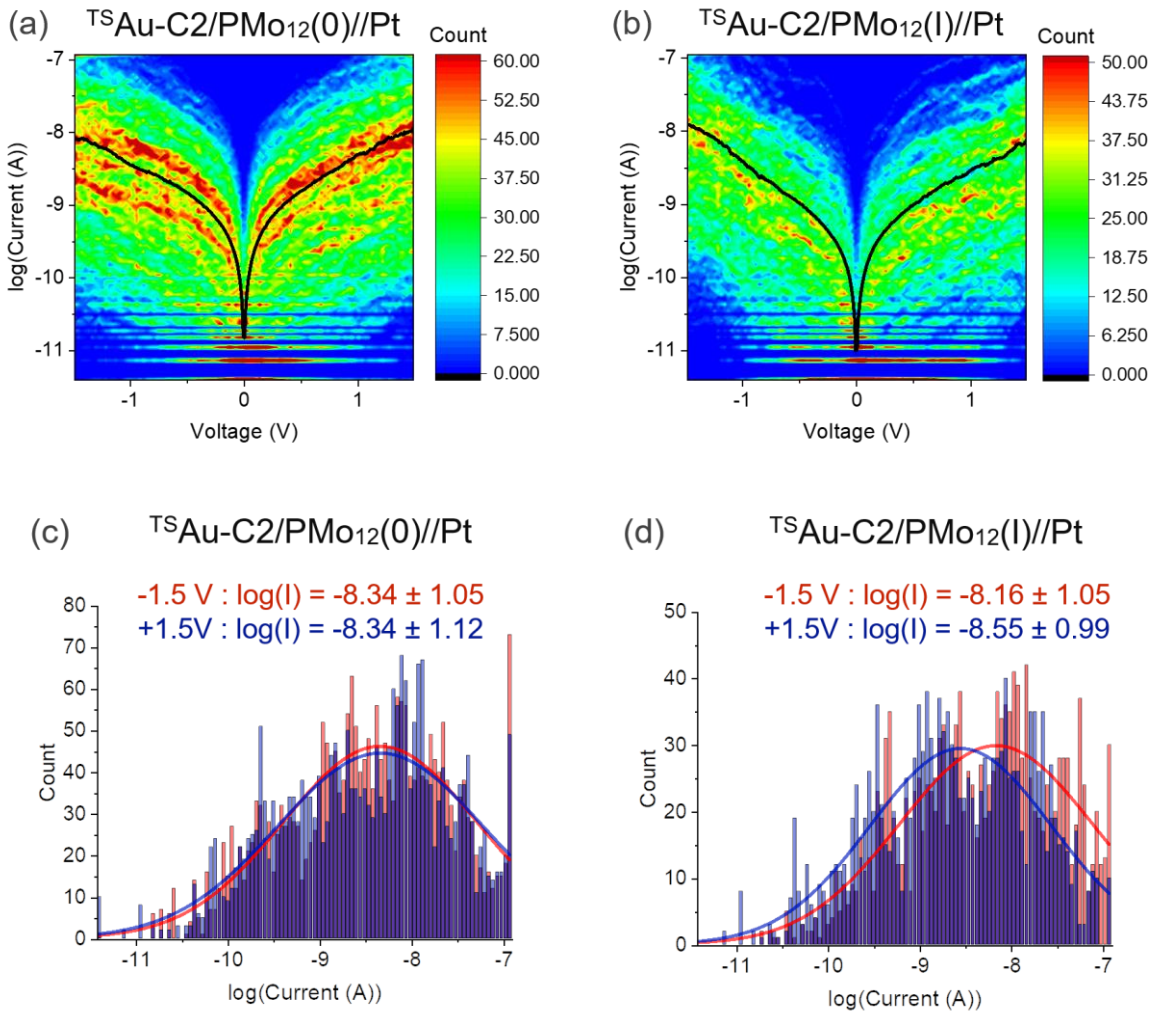

Figure 2.8. 2D histograms (heat maps) of I-Vs (loading force ~ 6 nN) in a semi-log_{10} plot for (a) ^{TS}Au-C2/PMo_{12}(0)//Pt and (b) ^{TS}Au-C2/PMo_{12}(I)//Pt. The solid black lines are the mean Ī-V curves. (c) and (d) The histograms of the currents at -1.5 V (red bars) and +1.5 V (blue bars) and fits by a log-normal distribution (the fitted log-mean value ± log-standard deviation is indicated on the panels).

In Figure 2.8, (a) and (b), we present the heat maps of the MJ with the short SAM and the PMo_{12} prepared in the two different reduced states. In total, there is 491 IV curves presented here for both states of the PMo_{12}. By comparing the 2D histograms, no difference is observed. The statistical distribution of the currents and the mean Ī-V curves (black lines) are quite similar. Pushing the analysis further, by comparing the log(current) histogram at ± 1.5V (Fig. 2.8(c) and (d)), we see a small difference. Indeed, for the PMo_{12}(0), we obtain the same mean value at positive and negative voltages. For the PMo_{12}(I), there is a little deviation with a mean value of current slightly higher at negative voltage. The asymmetry ratio R^{-} = I(-1.5V)/I(1.5V) is around 2.5.

To analyze the electronic structure in more detail, both the TVS method and SEL model (Equations 1.3 and 1.4 in Chapter 1) are first used on the mean Ī-V curves (Figure 2.9) and then for the complete data set (Figure 2.10). The SEL model is fitted in the range ± 1.0V.

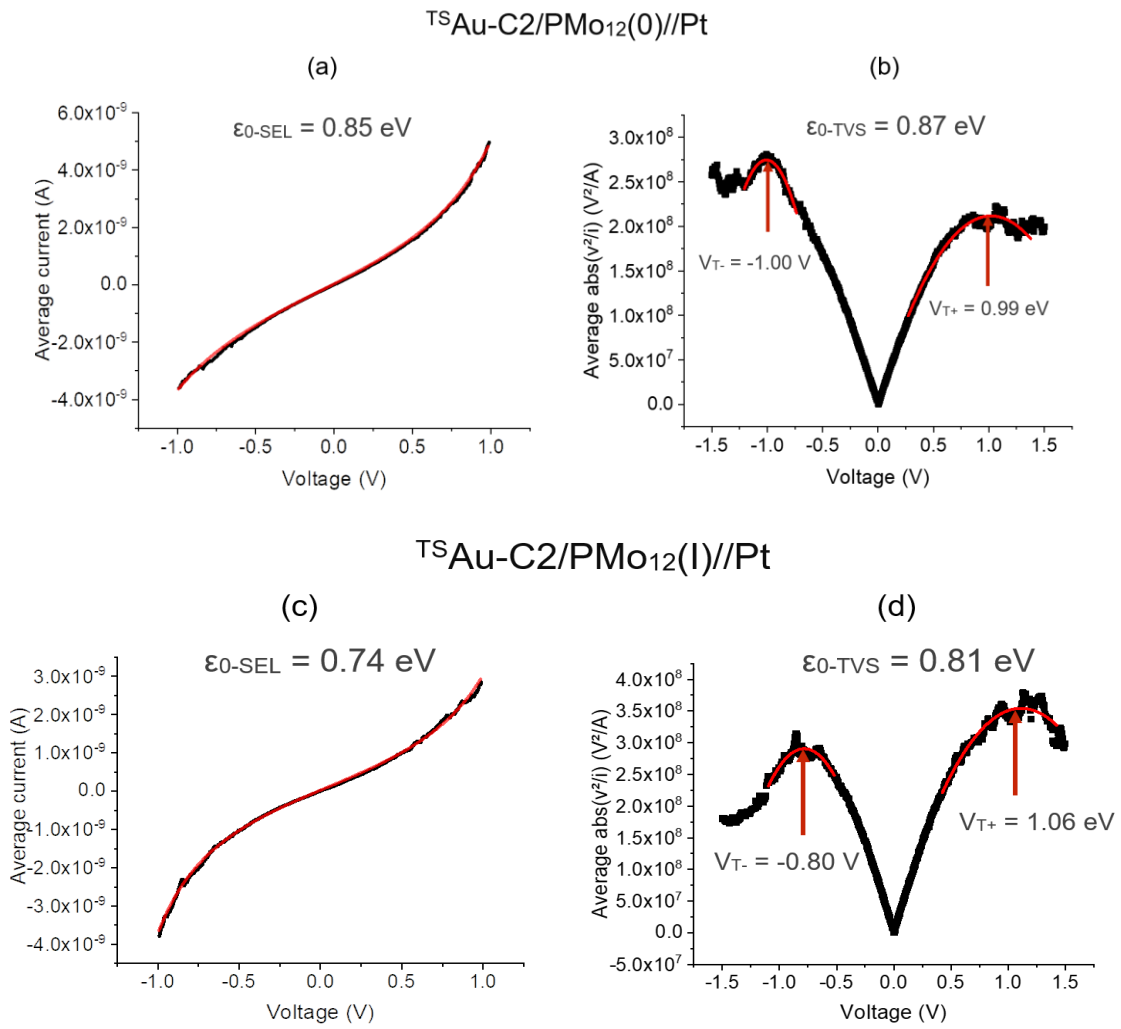

Figure 2.9. Mean Ī-V curves for ^{TS}Au-C2/PMo$_{12}$(0)//Pt fitted with (a) SEL model and (b) TVS method and for ^{TS}Au-C2/PMo$_{12}$(I)//Pt fitted with (c) SEL model and (d) TVS method.

For the ^{TS}Au-C2/PMo$_{12}$(0)//Pt, the average ε_0 values are 0.85 and 0.87 eV with SEL model and TVS respectively. For the ^{TS}Au-C2/PMo$_{12}$(I)//Pt, the average ε_0 values are slightly lower at 0.74 and 0.81 eV respectively.

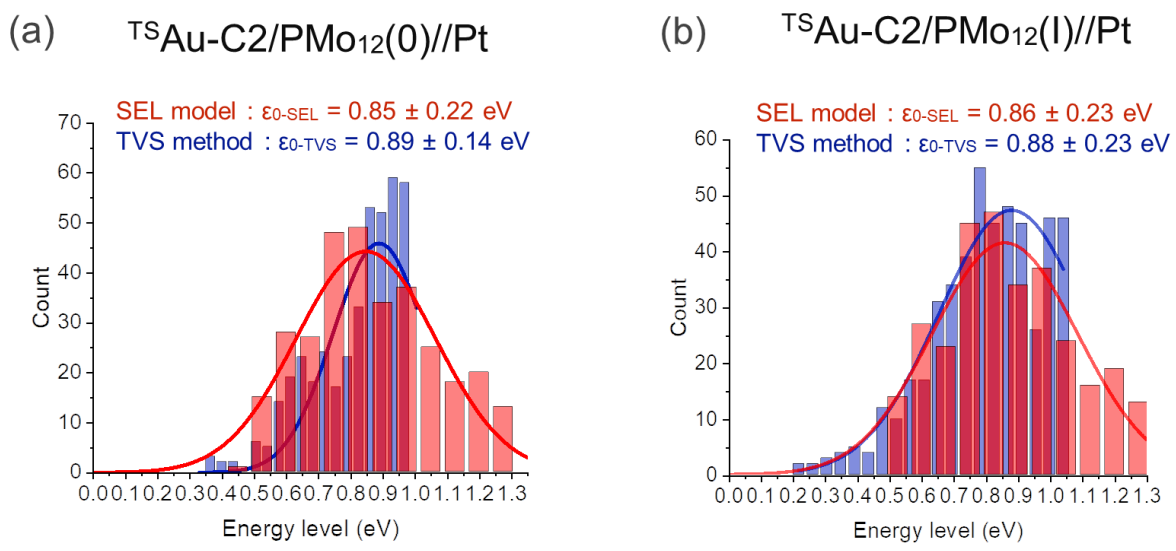

Figure 2.10. Statistical distribution of the energy level (SEL model and TVS method) involved in the ET properties for (a) ^{TS}Au-C2/PMo$_{12}$(0)//Pt and (b) ^{TS}Au-C2/PMo$_{12}$(I)//Pt. The solid lines are the fits by a Gaussian distribution with the mean value ± standard deviation indicated in the panels.

Figure 2.10 shows the statistical distribution of the energy levels $\varepsilon_{0\text{-SEL}}$ and $\varepsilon_{0\text{-TVS}}$ obtained on the datasets shown in Figure 2.8, and the fits by a Gaussian distribution. We obtain the same results for the PMo$_{12}$(0) and PMo$_{12}$(I) MJs. The electronic coupling energies to the electrodes, Γ_1 and Γ_2, have been also determined from the mean Ī-V curves in both cases (Figure 2.9) and also by the statistical method with the SEL model (Figure 2.11).

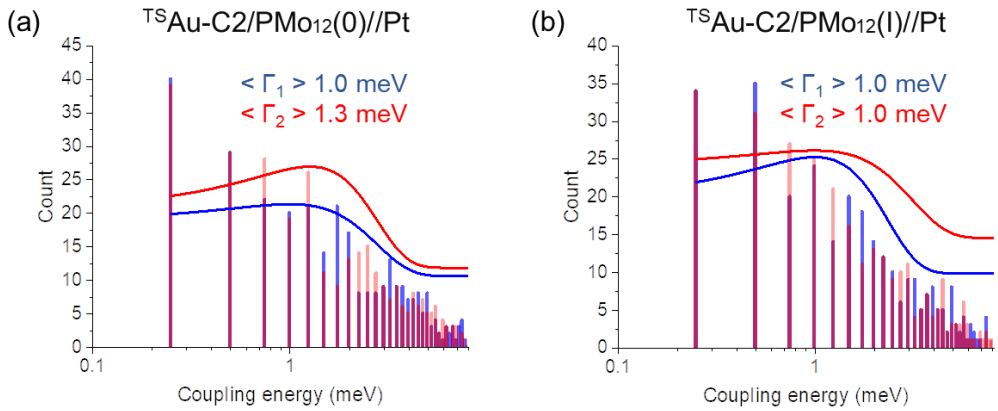

Figure 2.11. Histogram of coupling parameters Γ_1 (blue bars) and Γ_2 (red bars) for (a) ^{TS}Au-C2/PMo$_{12}$(0)//Pt and (b) ^{TS}Au-C2/PMo$_{12}$(I)//Pt . The Γ values are fitted by a log-normal distribution leading to the geometric mean given in the figure

A large dispersion is observed for the coupling parameter, mainly in the range 0.1 – 4 meV with both POMs (Figure 2.11). As we took N = 1 to apply the SEL model, here the coupling parameters are "effective" parameters and they are used only for a relative comparison between two states of the same samples measured in similar conditions (e.g. same tip, same loading force,…). For the Γ_{TVS}, we use the equation 1.5 given in Chapter 1 from the mean I-V curves only.

All these parameters are summarized in the Table 2.2 below:

Table 2.2. Parameters of the Gaussian fits of the molecular energy level ε_0 for the TVS method and the SEL model (Fig. 2.10) and of the electrode coupling energies. For the electronic coupling to the electrodes (Γ_{TVS}, Γ_1 and Γ_2) the values are given from the analysis of the mean $\bar{I}$-V curves, mainly due to a large dispersion of Γ_1 and Γ_2.

		^{TS}Au-C2/PMo$_{12}$(0)//Pt	**^{TS}Au-C2/PMo$_{12}$(I)//Pt**
TVS	**$\varepsilon_{0\text{-TVS}}$ (eV)**	0.89 ± 0.14	0.88 ± 0.23
	Γ_{TVS} (meV)	5.21	3.91
SEL	**$\varepsilon_{0\text{-SEL}}$ (eV)**	0.85 ± 0.22	0.86 ± 0.23
	Γ_1 (meV)	1.93	1.54
	Γ_2 (meV)	2.25	1.40

The coupling values are around few meV and again no significant difference is observed between the two states of the PMo$_{12}$ junctions.

The same experiment has been done with a longer aminoalkylthiol SAM: the C6.

d) Electron transport properties of C6/PMo$_{12}$ MJs

Figures 2.12(a) and (b) present the 2D histograms for the ^{TS}Au-C6/PMo$_{12}$(0)//Pt and (b) ^{TS}Au-C6/PMo$_{12}$(I)//Pt junctions. We first note that the currents are globally lower by a factor up to ~100 than with the C2 SAM as expected knowing the well-established length dependence behaviour of alkyl chain MJs.[17,126]

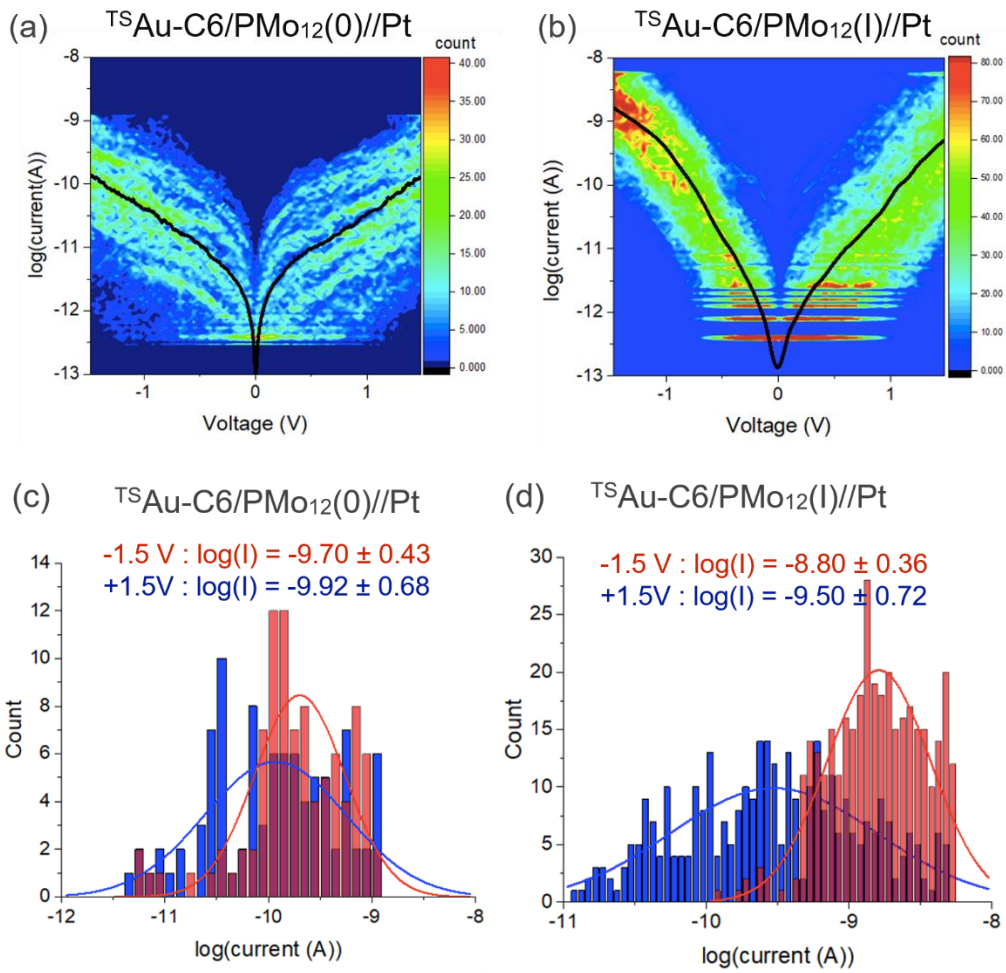

Figure 2.12. 2D histograms (heat maps) of I-Vs (loading force ~ 6 nN) in a semi-log$_{10}$ plot for (a) ^{TS}Au-C6/PMo$_{12}$(0)//Pt and (b) ^{TS}Au-C6/PMo$_{12}$(I)//Pt. The solid black lines are the mean $\bar{I}$-V curves. (c) and (d) The histograms of the currents at -1.5 V (red bars) and +1.5 V (blue bars) and fits by a log-normal distribution (the fitted log-mean value ±log- standard deviation is indicated on the panels).

94 IV curves have been selected for the MJ with the PMo$_{12}$(0) and 356 IV curves for the MJ with the PMo$_{12}$(I) (see methodology in annexe A2.3). There is less curves with the PMo$_{12}$(0) because current is lower and a high transimpedance gain (100 pA/V) is used on the C-AFM equipment, and many IVs are really noisy and are removed to avoid distorting of the statistic (see annexe A2.3). Indeed, by comparing the 2D histograms of both the junctions, we can clearly see a difference of level of the currents. Looking in more details, the mean current at –1.5V is a factor ~10 lower for the PMo$_{12}$(0) than for PMo$_{12}$(I). With the PMo$_{12}$(0), no current asymmetry ratio is observed, contrary to the MJs with the PMo$_{12}$(I) for which R^- is around 5.5 (Fig. 2.12(d)).

To compare the difference of the current with the long and short SAMs, we notice that with a longer SAM, the oxidation state of the POM has an influence on the current: adding one electron

to the structure gives a factor 10 increase of the current. In addition, the asymmetry behavior of the IVs for the $PMo_{12}(I)$ is clearly more important with the C6 SAM.

- **In-situ UV irradiation**

As it implies that we can electronically recognize a ^{TS}Au-C6/$PMo_{12}(0)$//Pt to a ^{TS}Au-C6/$PMo_{12}(I)$//Pt, we then follow in-situ the reversible reduction/re-oxidation of the POMs in the SAMs by C-AFM. This is possible because excitation of a POM in the UV-range indeed results in oxygen-to-metal charge transfer transitions, increasing its oxidising character.[127,128] The reducer can be less powerful than in a classical chemistry reaction and we suppose here the sacrificial reducer is the amine function of the SAM (see also discussion section below). Previous examples, as mentioned in Chapter 1_IIc with Preyssler crystal, exist but have never been observed at the molecular level in MJs.

Starting from a ^{TS}Au-C6/$PMo_{12}(0)$//Pt, we measure a dataset of I-Vs (Figure 2.13). Secondly, the POM layer is irradiated under UV light at 302 nm (analytikjena lamp, power ~ 0.5mW/cm², details annexe A2.4). The kinetic of reduction is slow in this way (for example, 2 hours in solution) so we irradiated the MJs during few hours. As soon as we turn off the UV light, we process of the second measure of the IVs. The kinetic of the re-oxidation state of the POM is also slow, letting the time to do the second round of C-AFM measurements. Then, we let the POM layer in ambient air either at room temperature (overnight) or under a moderate heating (2h at 80°C on a hotplate in air). A third time of IV measurement is done and all this process is repeated twice.

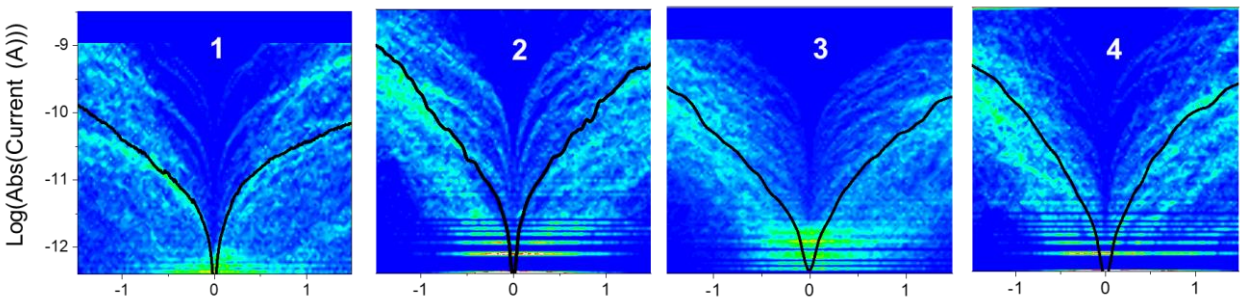

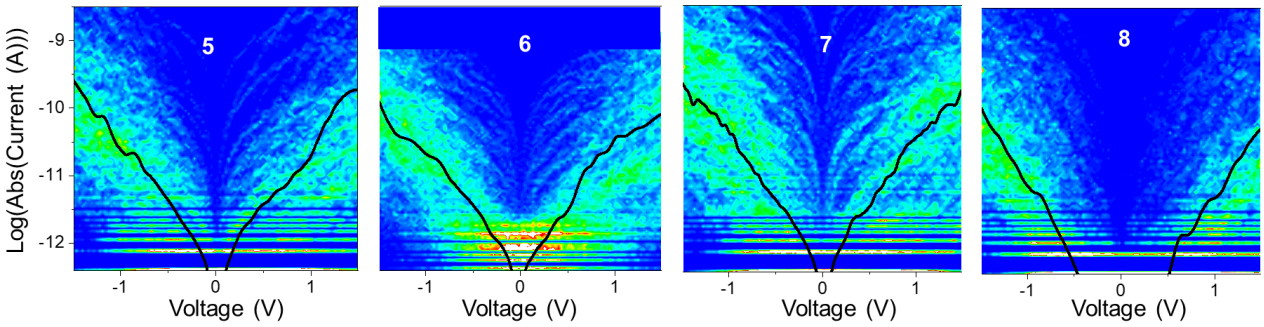

Figure 2.13. The whole IV dataset of the irradiation/relaxation cycles for: 1) pristine, 2) UV 5.5h, 3) RT 14.5h, 4) UV 4h, 5) 80°C 2h, 6) RT 24h, 7) UV 3.5h, 8) 80°C 2h.

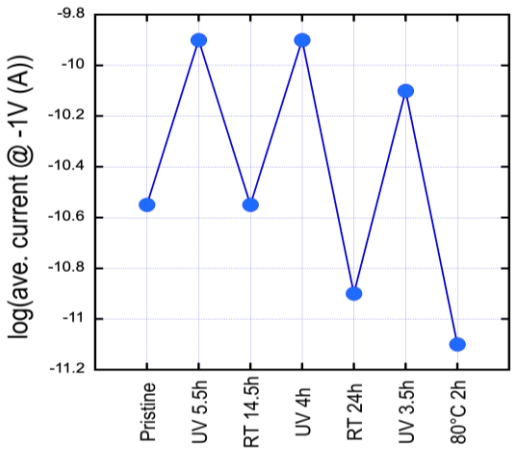

Figure 2.14. Evolution of the mean current log(|Ī|) at -1V for 3 cycles of reduction/oxidation. The currents measured during the last cycle are lower, possibly due to some degradation of the sample or the tip or a drift of the C-AFM loading force.

The figure 2.14 shows the evolution of the mean current recorded at -1V during this 3 irradiation/relaxation cycles. We observe a clear increase in the conductance upon UV irradiation, followed by a return to a state of lower conductance after stopping the irradiation. From the previous experiments of the MJs directly prepared with the POMs in their $PMo_{12}(0)$ and $PMo_{12}(I)$ states, we can deduce that the $PMo_{12}(0)$ monolayer is *in-situ* photo-reduced at one electron and subsequently air re-oxidized. This is coherent with photochromic materials applications due to their photochemical reduction.[129] This behaviour was also verified on a drop cast film of $PMo_{12}(0)$ on a glass substrate in reproducible condition (more important thickness

but visual change of colour, see annexe A2.5). Thus, we demonstrate that it is possible to change the redox state of PMo_{12} *in-situ* at the monolayer scale.

- **Electronic structure of the molecular junctions**

To push the analysis further and to understand better the difference of electron transport between the two oxidation states, the determination of the energy position of the MOs has also been studied with the average curves (Figure 2.15) and in a statistical way (Figure 2.16) as explain previously. This time, TVS is applied to the two oxidation/reduction states but the SEL model is only applied to the C6-PMo_{12}(0) (in the range ± 1.0V). Indeed, the SEL model is valid as long as the applied voltage does not drive the MO near the Fermi energy of the electrodes (*i.e.* ET in the off-resonance situation). When it is not the case, the model is not well fitted (Figure 2.15c) so it cannot be used and the analysis is only done by TVS method.

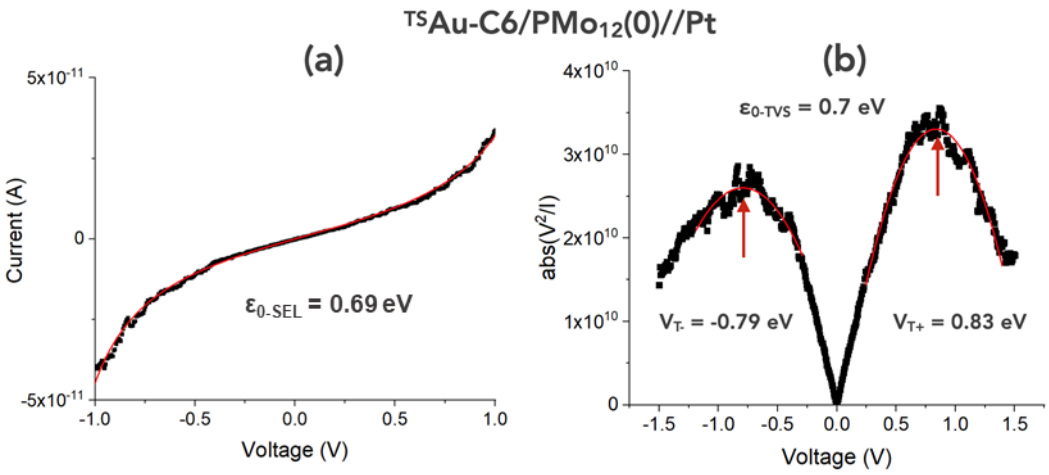

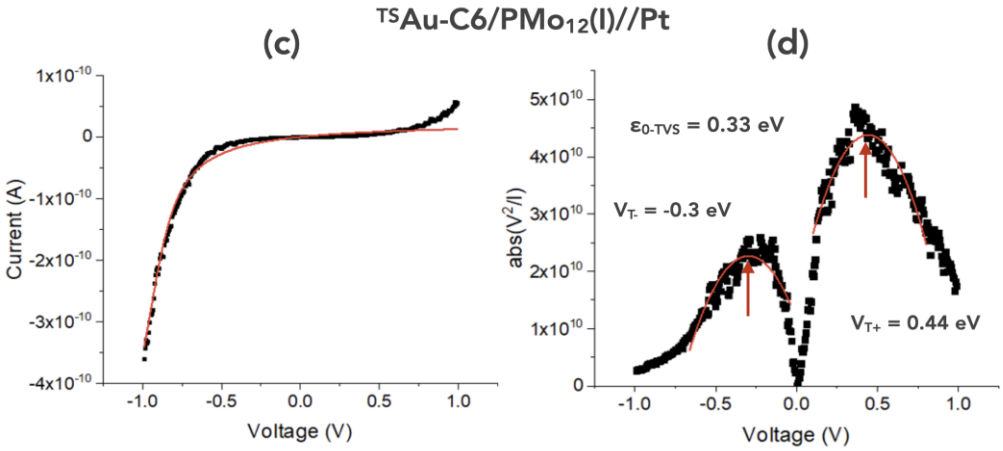

Figure 2.15. mean Ī-V curves of for ^{TS}Au-C6/PMo$_{12}$(0)//Pt fitted with (a) SEL model and (b) TVS method and for ^{TS}Au-C6/PMo$_{12}$(I)//Pt fitted with (c) SEL model and (d) TVS method.

For the ^{TS}Au-C6/PMo$_{12}$(0)//Pt, the average ε_0 values are 0.69 and 0.70 eV with SEL model and TVS respectively. For the ^{TS}Au-C6/PMo$_{12}$(I)//Pt, the average ε_0 value is lower, 0.33 eV.

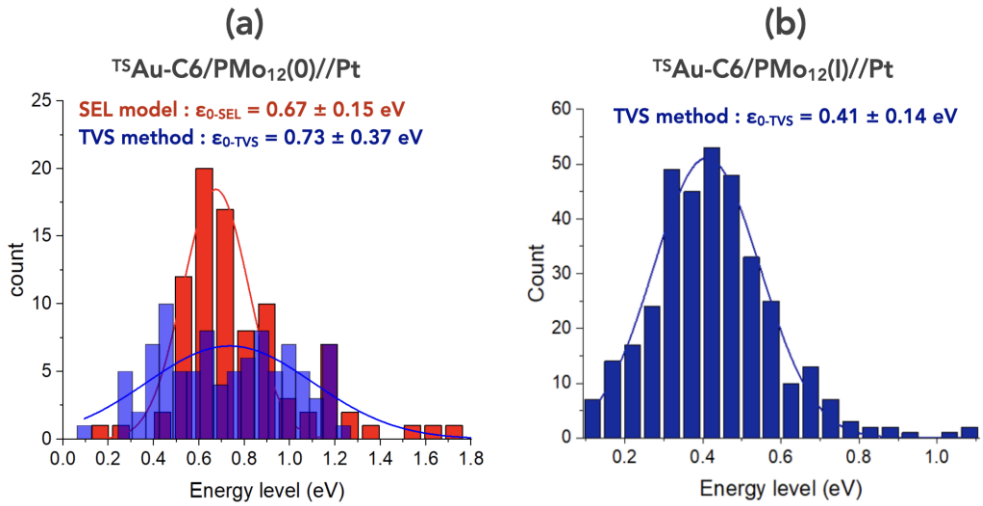

Figure 2.16. Statistical distribution of the energy level (SEL model and TVS method) involved in the ET properties for (a) ^{TS}Au-C6/PMo$_{12}$(0)//Pt and (b) ^{TS}Au-C6/PMo$_{12}$(I)//Pt. The solid lines are the fits by a Gaussian distribution with the mean value ± standard deviation indicated in the panels.

From the statistical distributions of the ^{TS}Au-C6/PMo$_{12}$(0)//Pt, the ε_0 values given by the two approaches are quite close with an average value around 0.7 eV. This energy value is relatively much higher than for the ^{TS}Au-C6/PMo$_{12}$(I)//Pt of 0.41 eV. This difference is in a good

agreement with the clear difference of current between both the junctions (higher the energy position of the MOs with respect of the electrode Fermi energy, lower the current in the MJ).

Again, the electronic coupling energies, Γ_1 and Γ_2, to the electrodes have been also determined from the mean $\bar{I}$-V curves (Figure 2.15) of both junctions and in a statistic way for the $PMo_{12}(0)$ with SEL model (Figure 2.17).

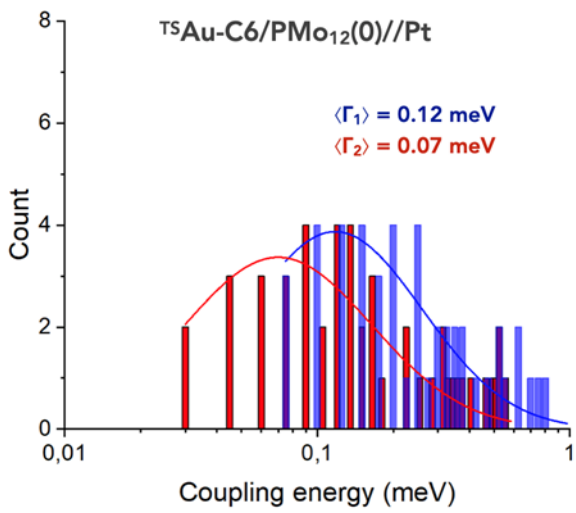

Figure 2.17. Histogram of coupling parameters Γ_1 (blue bars) and Γ_2 (red bars) for ^{TS}Au-C6/PMo$_{12}$(0)//Pt. The Γ values are fitted by a log-normal distribution leading to the geometric mean given in the figure.

The values are dispersed in the range 0.05-0.15 meV for Γ_1 and 0.08-1 meV for Γ_2. All these parameters are summarized in the Table 2.3 below:

Table 2.3. Parameters of the Gaussian fits of the molecular energy level ε_0 for the TVS method and the SEL model (Fig. 2.16) and of the electrode coupling energies. For the electronic coupling to the electrodes (Γ_{TVS}, Γ_1 and Γ_2) the values are given by the analysis of the mean $\bar{I}$-V curves, mainly due to a large dispersion of Γ_1 and Γ_2

		^{TS}Au-C6/PMo$_{12}$(0)//Pt	^{TS}Au-C6/PMo$_{12}$(I)//Pt
TVS	**$\varepsilon_{0\text{-TVS}}$ (eV)**	0.73 ± 0.37	0.41 ± 0.14
	Γ_{TVS} (meV)	0.32	0.1
SEL	**$\varepsilon_{0\text{-SEL}}$ (eV)**	0.67 ± 0.15	n.a.
	Γ_1 (meV)	0.14	
	Γ_2 (meV)	0.13	

- **Machine Learning and clustering**

Since the datasets are largely dispersed, we also used a clustering method to separate the data in different clusters. This analysis has been done in collaboration with M.L. Perrin and M. Calame (Transport at nanoscale interfaces laboratory, EMPA, Dübendorf, Switzerland). We applied machine learning (ML) and classified all the individual I-V curves according to common characteristic parameters (pattern recognition), e.g. shape of the I-V (linear, sigmoidal, presence of negative-differential resistance peaks, current level, etc…).[130–133] More precisely, we used an unsupervised, reference-free tool developed by the team of M.L Perrin.[130,131] Following the benchmark reported in ref. 131, we used:

- UMAP(cos.) (uniform manifold approximation and projection with a cosine distance metric) for feature space construction
- GAL (graph average linkage) for the clustering algorithm with an optimal number of 5 clusters (the choice of 5 clusters is justified in annexe A2.6).

For this study, the whole dataset of the I-Vs is used. Figure 2.18 illustrates the feature space obtained for the C6-PMo_{12}(0) MJ dataset and the 5 clusters mean Ī-V. The same data are presented for C6-PMo_{12}(I) in the next two panels of the figure.

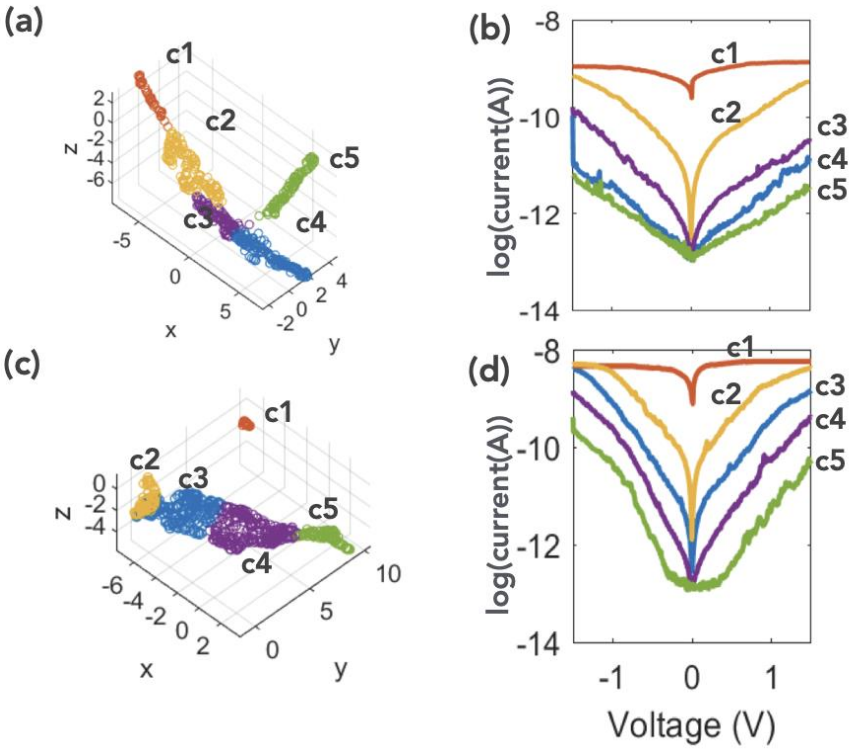

Figure 2.18. (a) Feature space and (b) mean Ī-V for each cluster c1 to c5 for the ^{TS}Au-C6-PMo_{12}(0)//Pt junctions. (c) Feature space and (d) mean Ī-V for each cluster c1 to c5 for the ^{TS}Au-C6-PMo_{12}(I)//Pt junctions.

Cluster 1 for both the junctions correspond to I-Vs saturating during the measurements (7.7% of the dataset with the C6-PMo_{12}(0) and 2.8% with PMo_{12}(I)) so they are not taken into account for the analysis. Clusters 2 to 5 mean Ī-V curves and each curve are analysed with the SEL model for the C6-PMo_{12}(0) and the TVS method is used in both the cases.

- **With ^{TS}Au-C6-PMo_{12}(0)//Pt**

Successively, we present the mean IV curves fitted with SEL model (Figure 2.19) and with the TVS method (Figure 2.20) for each cluster. Then, we illustrate the 2D histograms (Figure 2.21), the statistics of the asymmetry ratio R^- (Figure 2.22) and finally the statistical distribution of the energy level (Figure 2.23). All the figures are discussed below.

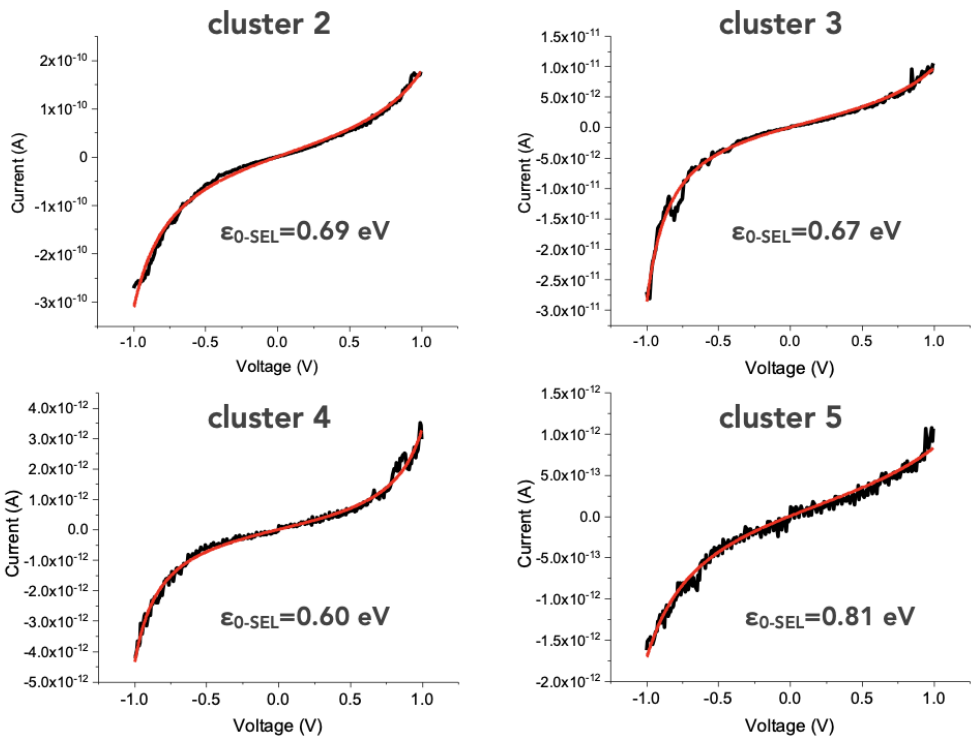

Figure 2.19. Mean Ī-V curves fitted with SEL model for ^{TS}Au-C6/PMo_{12}(0)//Pt clusters (a) 2, (b) 3, (c) 4 and (d) 5.

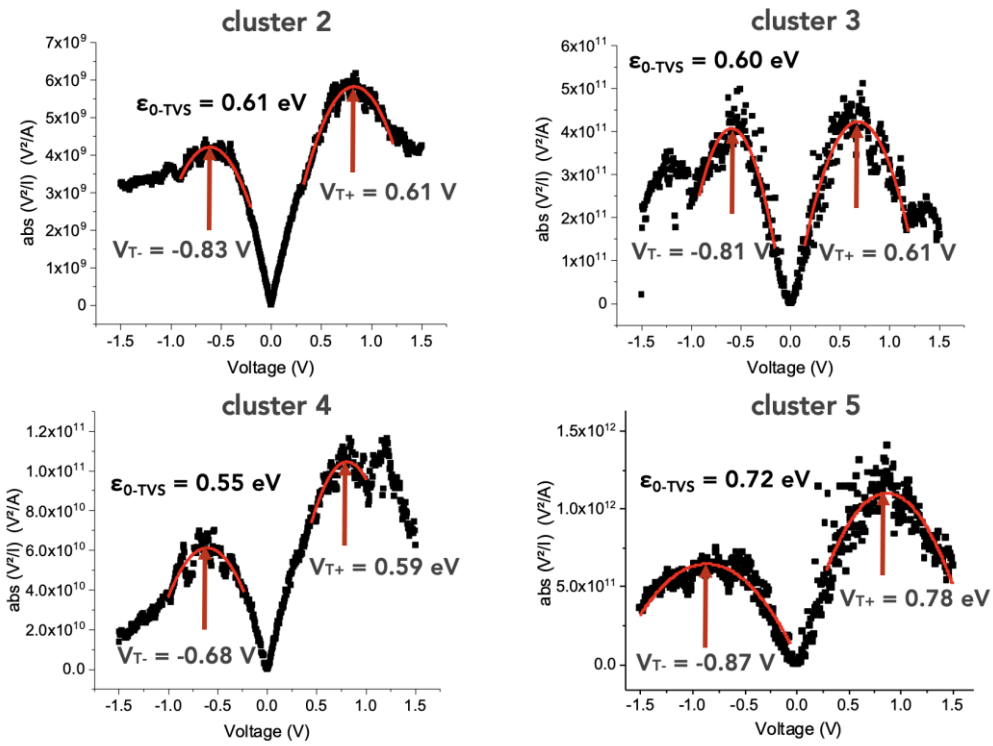

Figure 2.20. Mean Ī-V curves analysed with the TVS method for ^{TS}Au-C6/PMo$_{12}$(0)//Pt clusters (a) 2, (b) 3, (c) 4 and (d) 5.

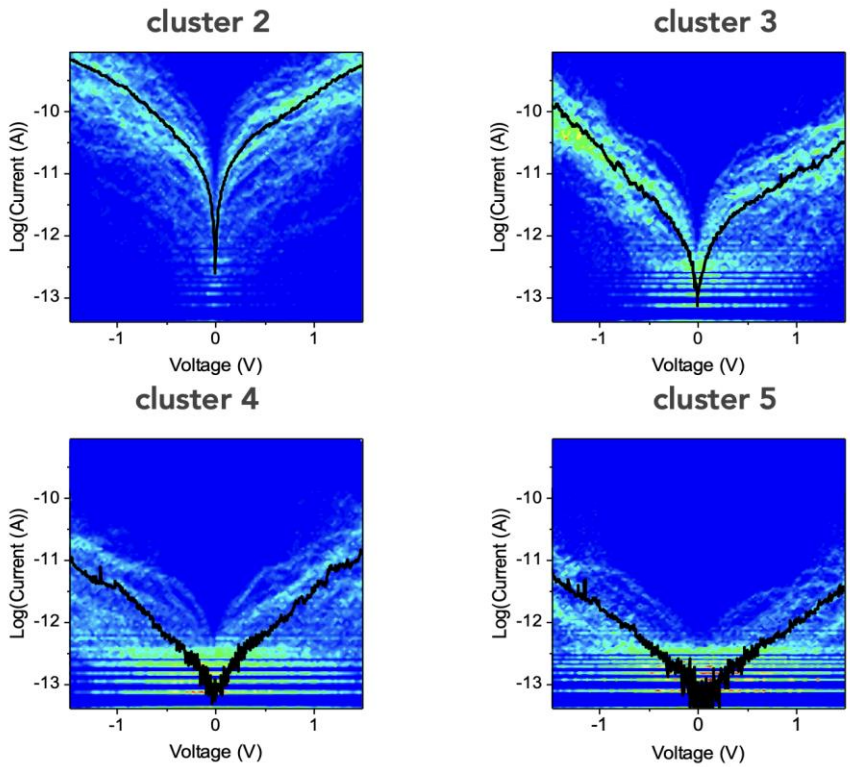

Figure 2.21. 2D histogram and mean Ī-V curves for ^{TS}Au-C6/PMo$_{12}$(0)//Pt clusters (a) 2, (b) 3, (c) 4 and (d) 5.

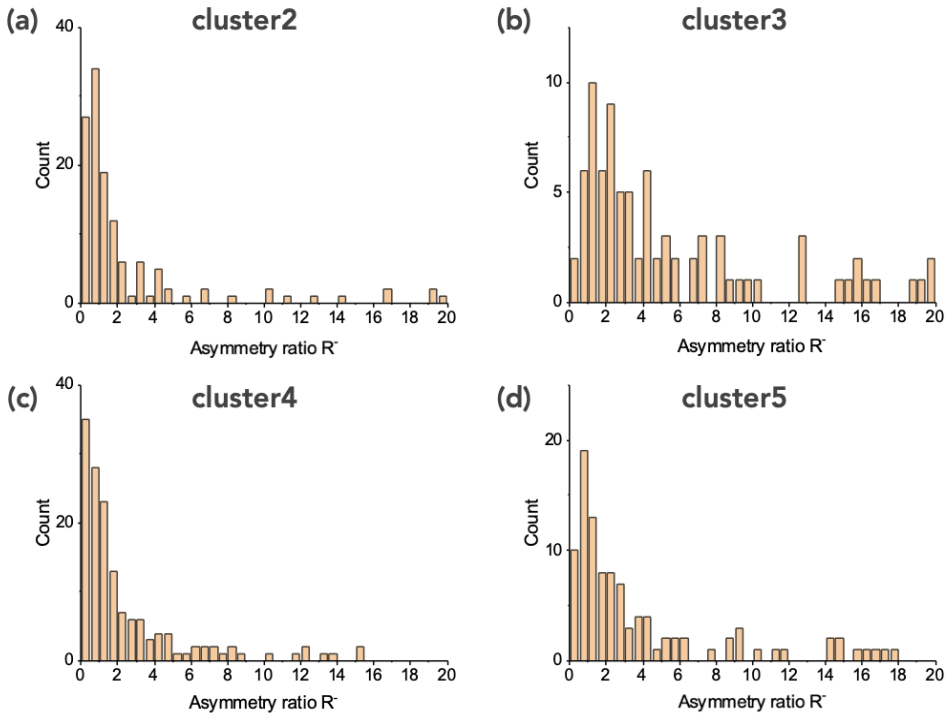

Figure 2.22. Asymmetry ratio R⁻ for ^{TS}Au-C6/PMo$_{12}$(0)//Pt clusters (a) 2, (b) 3, (c) 4 and (d) 5 at V± 1.5 V

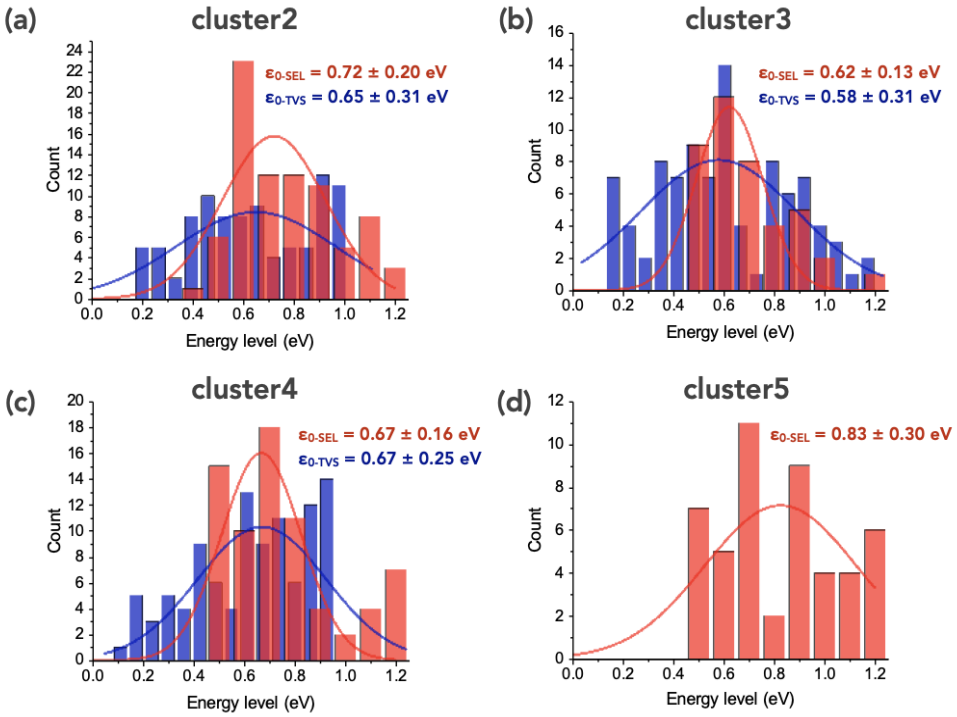

Figure 2.23. Statistical distribution of the energy level (SEL model and TVS method) involved in the ET properties for ^{TS}Au-C6/PMo$_{12}$(0)//Pt clusters (a) 2, (b) 3, (c) 4 and (d) 5 (distribution with TVS method is not shown because of the too large dispersion). The solid lines are the fits by a Gaussian distribution with the mean value ± standard deviation indicated in the panels.

For the ^{TS}Au-C6-PMo$_{12}$(0)//Pt junctions, the same ε_0 values (0.60-0.61 eV by TVS, 0.67-0.69 eV by SEL, Figures 2.19 and 2.20) characterize the cluster 2 (24.6% of the IVs in the dataset) and cluster 3 (18.8%). We find a higher electronic coupling to the electrodes for cluster 2 ($\Gamma_{TVS}\approx$0.63 meV; $\Gamma_1\approx$0.44 meV and $\Gamma_2\approx$0.37 meV by SEL) compared to cluster 3 ($\Gamma_{TVS}\approx$0.14 meV; $\Gamma_1\approx$0.11 meV and $\Gamma_2\approx$0.083 meV by SEL), data summarized in Table 2.4 at the end. Finally, cluster 4 (29.2%) and cluster 5 (19.7%) show the lowest current and almost similar mean $\bar{I}$-V traces (Figures 2.19 and 2.20). However, these clusters are characterized by slightly different couple of the ε_0 and Γ_{TVS} parameters (larger ε_0 for cluster 5 with a better electrode coupling : $\varepsilon_{0\text{-}TVS} \approx$ 0.72 eV, $\Gamma_{TVS} \approx$ 0.28 meV for cluster 5 vs. $\varepsilon_{0\text{-}TVS} \approx$ 0.55 eV, $\Gamma_{TVS} \approx$ 0.054 meV for cluster 4 (Table 2.4) (same behavior for the data obtained by SEL, Table 2.4). This results counterbalance each other. Indeed, a larger ε_0, i.e. a MO far away from the Fermi energy of the electrodes tends to decrease the current, while a better electrode coupling energy tends to increase the current. We also observe that clusters 2, 4 and 5 display almost symmetric mean $\bar{I}$-Vs (with $R^- = \bar{I}(-1.5\text{ V})/(1.5\text{ V}) < 2$), while a slight negative asymmetry is noticed for cluster 3 with $R^- \approx 2.8$ (Table 2.4). This trend is confirmed by a statistical analysis on all the I-Vs belonging to each cluster as shown above (Figures 2.21, 2.22 and 2.23).

- **With ^{TS}Au-C6-PMo$_{12}$(I)//Pt**

The same methodology is applied with this MJ.

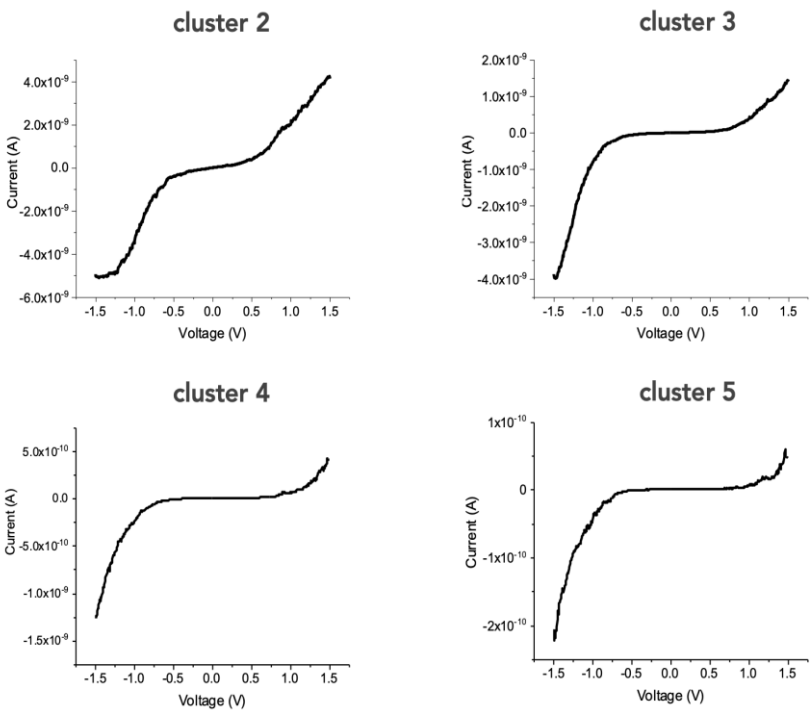

Figure 2.24. Mean $\bar{I}$-V curves of ^{TS}Au-C6/PMo$_{12}$(I)//Pt clusters (a) 2, (b) 3, (c) 4 and (d) 5.

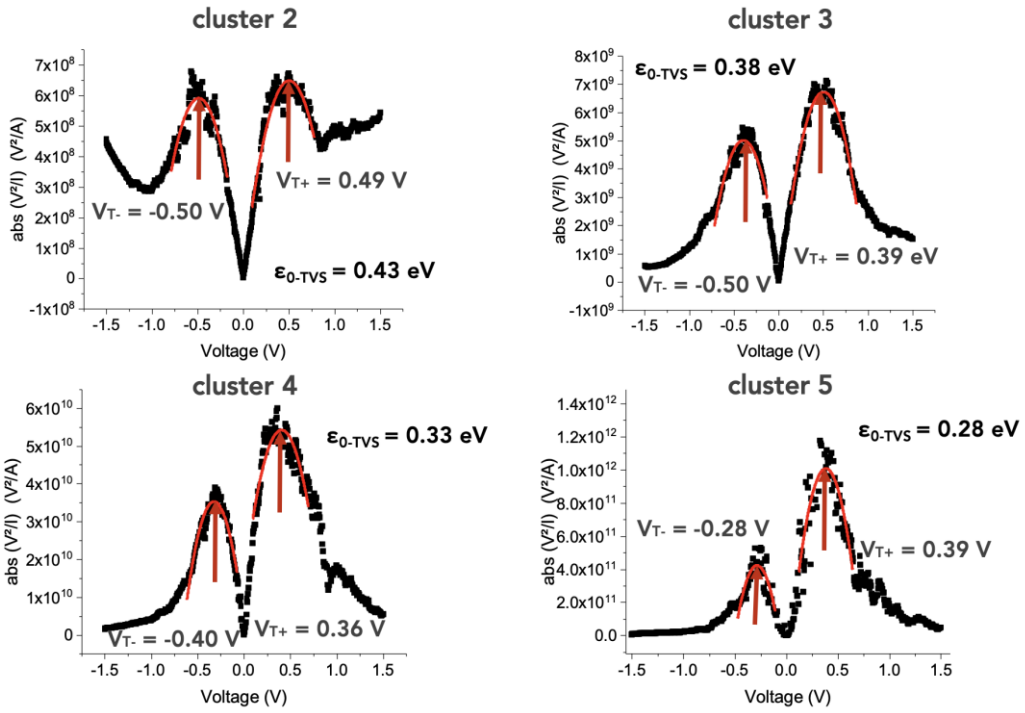

Figure 2.25. Mean Ī-V curves transformed with TVS method for ^{TS}Au-C6/PMo$_{12}$(I)//Pt clusters (a) 2, (b) 3, (c) 4 and (d) 5.

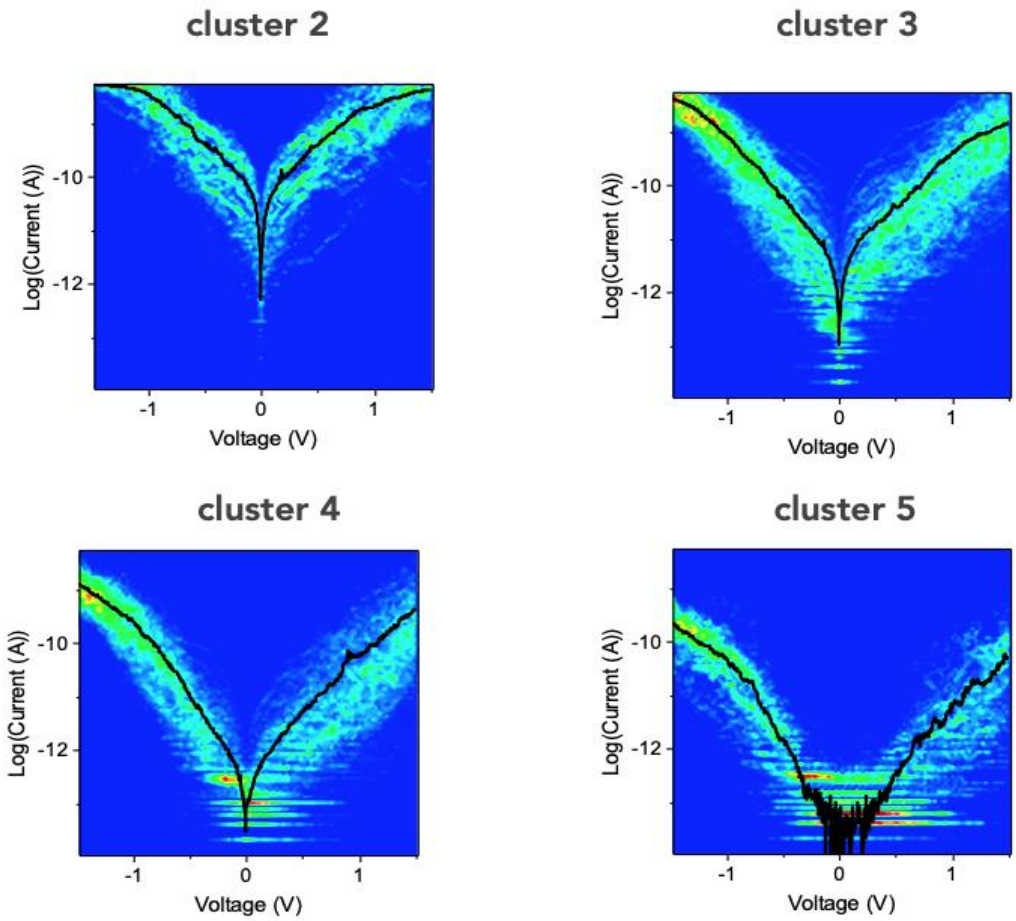

Figure 2.26. 2D histogram and mean Ī-V curves for ^{TS}Au-C6/PMo$_{12}$(I)//Pt clusters (a) 2, (b) 3, (c) 4 and (d) 5.

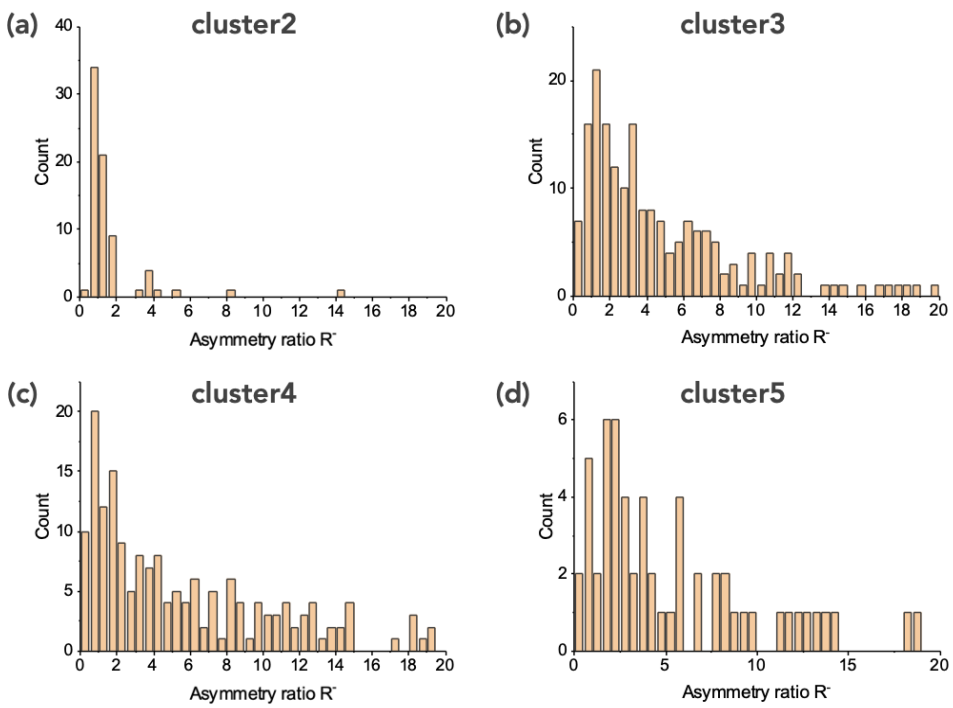

Figure 2.27. Asymmetry ratio R^- for ^{TS}Au-C6/PMo$_{12}$(I)//Pt clusters (a) 2, (b) 3, (c) 4 and (d) 5 at ±1.5 V.

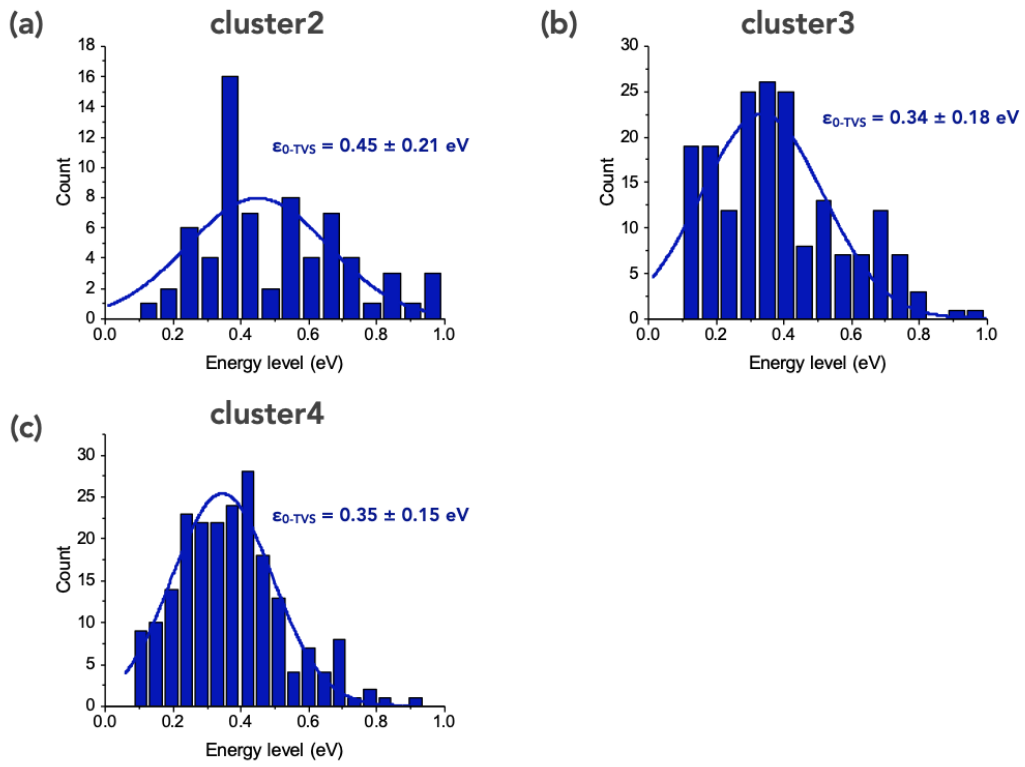

Figure 2.28. Statistical distribution of the energy level (TVS method) involved in the ET properties for ^{TS}Au-C6/PMo$_{12}$(I)//Pt clusters (a) 2, (b) 3, (c) 4 (distribution with TVS method for cluster 5 is not shown because of the too large dispersion) The solid lines are the fits by a Gaussian distribution with the mean value ± standard deviation indicated in the panels.

For the ^{TS}Au-C6-PMo$_{12}$(I)//Pt junctions, $\varepsilon_{0\text{-TVS}}$ value around 0.4 eV and Γ_{TVS} 0.35 - 1.1 meV (Figure 2.25, Table 2.4), characterize the clusters 2 and 3. Whereas clusters 4 and 5 have a lower $\varepsilon_{0\text{-TVS}}$ around 0.3 eV (Fig. 2.25) but also a lower Γ_{TVS} (0.068-0.094 meV). With the reduced POM, we notice again that all the mean Ī-Vs traces are asymmetric with the clusters 4 and 5 displaying the highest R^- values (5-8, Table 2.4). Again, this trend is confirmed by a statistical analysis on all the I-Vs belonging to each cluster (Figures 2.26, 2.27 and 2.28).

*Table 2.4. Parameters of the molecular energy level ε_0 for the TVS method and the SEL model of the mean Ī-V curves belonging to the different clusters (Figs. 39, 40 and 45) and of the electrode coupling energies. R^- is the asymmetry ratio, $R^- = \bar{I}(-1.5\ V)/\bar{I}(1.5\ V)$, calculated from the mean Ī-Vs of each cluster. * stands for underestimated value since the current saturates below around -1V in that case.*

	^{TS}Au-C6/PMo$_{12}$(0)//Pt				**^{TS}Au-C6/PMo$_{12}$(I)//Pt**			
cluster	C2 (24.6%)	C3 (18.8%)	C4 (29.2%)	C5 (19.7%)	C2 (12.5%)	C3 (35.7%)	C4 (35.5%)	C5 (13.5%)
$\varepsilon_{0\text{-TVS}}$ (eV)	0.61	0.60	0.55	0.72	0.43	0.38	0.33	0.28
Γ_{TVS} (meV)	0.63	0.14	0.054	0.28	1.1	0.35	0.094	0.068
$\varepsilon_{0\text{-SEL}}$ (eV)	0.69	0.67	0.60	0.81	n.a.			
Γ_1 (meV)	0.44	0.11	0.038	0.046				
Γ_2 (meV)	0.37	0.083	0.036	0.032				
$(\Gamma_1.\Gamma_2)^{1/2}$	0.40	0.096	0.037	0.038				
R^-	≈1.7	≈2.8	≈1.1	≈1.5	≈2*	≈2.6	≈5	≈8

e) Discussion of the electron transport properties

- **C6/PMo$_{12}$ MJs**

Thanks to the global analysis including the mean Ī-V and statistical analysis, we suggest the energy scheme shown in Figure 2.29 for the ^{TS}Au-C6-PMo$_{12}$(0)//Pt and the ^{TS}Au-C6-PMo$_{12}$(I)//Pt junctions.

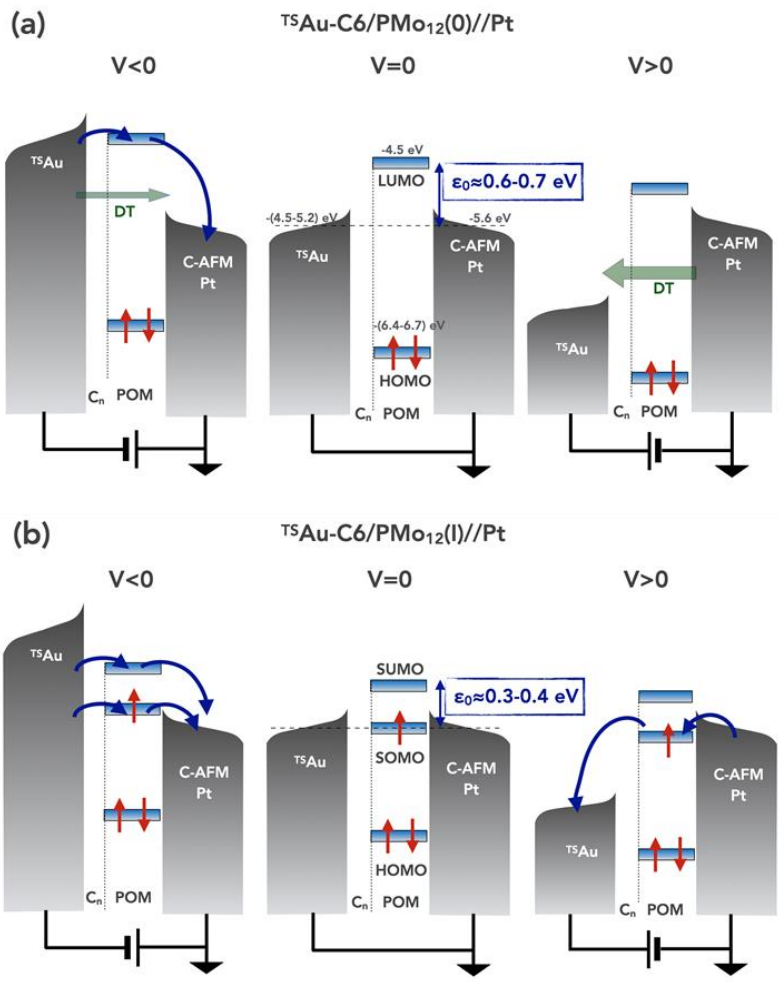

Figure 2.29. Hypothesized schemes of the energy diagrams: (a) ^{TS}Au-C6/PMo$_{12}$(0)//Pt and (b) ^{TS}Au-C6/PMo$_{12}$(I)//Pt junctions at a negative, null and positive bias applied on the ^{TS}Au substrate (the C-AFM tip grounded). The blue arrows indicate the MO-mediated electron transport and the green arrows show the direct tunneling (the wider the arrow, the larger the tunneling current). The MO energies (vs. vacuum energy) are given as reported from calculations (see text) and the ε_0 values are taken from our experiments (Figs. 2.12 and 2.16, Table 2.3).

For the C6-PMo$_{12}$(0), the electron transport occurs through the LUMO, that is at about 0.7eV above the Fermi level ($\varepsilon_{0\text{-SEL}}$= 0.67 ± 0.15 eV, $\varepsilon_{0\text{-TVS}}$ = 0.73 ± 0.37 eV, Table 2.3), as determined by the SEL and TVS analysis of the I-V measurements (Fig. 2.10). This value is in a good agreement with a LUMO at -4.5 eV (*vs.* vacuum energy, theory)[134] and work functions (WF) of Au (≈4.8-5.2 eV) and Pt (≈5.6 eV). The interface dipole and the details of the molecule/metal contact dictate the exact alignment of the MOs with the Fermi energy of the electrodes.[135–137] Here, some ab-initio calculations are in progress[138] and cannot be unveiled at the time of writing this PhD thesis (collaboration with L. Vila-Nadal and V.P. Georgiev, Glasgow University). This LUMO energy level is also consistent with the cyclic voltammetry measurements (LUMO

at -4.9 eV, Figure 2.2). According to previous reports, the HOMO-LUMO gap is around 1.9-2.2eV[134,138,139] and the HOMO is not involved in the ET property of the MJ.

For the C6-PMo_{12}(I), the additional electron involves a new MO, the SOMO (Single Occupied Molecular Orbital). This SOMO is located near to the electrode Fermi level, as also noticed when open-shell radicals are implemented in MJ.[140–145] The calculated SOMO-SUMO gap is reduced to around 0.4eV[138] and both orbitals can now contribute to ET in the junctions. This leads to the experimentally observed increase in current.

The experimental value of $\varepsilon_{0\text{-TVS}} = 0.41 \pm 0.14$ eV (Table 2.3) is attributed to the SUMO level, in accordance with preliminary calculations.[138] The SOMO stay close to the Fermi energy. This result highlights the good stability of the open-shell structure of the C6-PMo_{12}(I) molecules at room temperature when inserted in the MJ. Indeed, the SOMO is localized on the Mo atoms and therefore it is integrated into the molecule. Like this, it is partly protected from a too strong interaction with the electrodes that can result in a rapid return to the PMo_{12}(0) state. A similar result has been recently demonstrated using a verdazyl radical, stable in the same conditions (stable in its open-shell configuration at RT in a MJ).[143]

We obtain a higher value $\varepsilon_0 \approx 0.9$ eV for the reference sample without the POMs, so ^{TS}Au-C6//Pt junctions (*vide supra*). This value is consistent with what we can find in the literature about the LUMO position of alkyl chains SAMs on Au.[43,146] Consequently, the C6 playing the role of a thin tunnel barrier between the bottom electrode and the POM and so, the determined values of ε_0 discussed above can be entirely attributed to the POM MOs.

Moreover, the different shape of the I-Vs can also be related to the difference of the electron transport through C6/PMo_{12}(0) and C6/PMo_{12}(I). For a reminder, we observed almost symmetric IVs for the pristine POM and asymmetric IVs for the reduced one.

On closer inspection of the energy diagram (Fig. 2.29), the ^{TS}Au-C6/PMo_{12}(0)//Pt, we see that the LUMO is near the grounded Pt electrode and can induce an asymmetry. Indeed, when we applied a negative voltage, the Fermi level of the ^{TS}Au electrode is moved upward and so the LUMO of the POM is between the Fermi levels of the two electrodes. In contrast, by applying a positive voltage, the LUMO level stay higher than the levels of the two electrodes.[147–150] In this case, this MO cannot be involved in the ET. We conclude that at negative bias, we have a MO-mediated ET (blue arrow, fig. 2.29(a)) and at positive bias, a direct tunnelling (green arrow). However, the lower work function for Au than Pt can favour a positive asymmetry. It means we can have more direct tunnelling current for a positive voltage applied on the electrode with the lowest WF, Au (larger green arrow in Fig. 2.29(a)). We illustrate the same phenomena

with the C6 SAMs for which we observed a slight positive asymmetry (Fig. 2.7). Since the ^{TS}Au-C6/PMo_{12}(0)//Pt and the ^{TS}Au-C6//Pt junctions display current levels of the same order of magnitude (Fig. 2.7 and 2.12), these two effects of opposite behaviour can counterbalance each other, leading to the observed almost symmetric I-V behaviour for the ^{TS}Au-C6/PMo_{12}(0)//Pt molecular junction.

On the opposite, we notice an asymmetric IV shape for all the dataset for the ^{TS}Au-C6/PMo_{12}(I)//Pt junctions. The SOMO and SUMO are closer to the Fermi energy of the electrodes than in the previous case (HOMO-LUMO for the C6-PMo_{12}(0)). Consequently, we hypothesize that when we applied a negative bias, the two MOs are between the Fermi level of the two electrodes (Fig. 2.9(b) and so, the two MOs can be involved in the ET. At positive bias, the Au Fermi level is lowered and only the SOMO is involved (like almost aligned with Pt Fermi level). Finally, since the current of PMo_{12}(I) MJs is larger than for the C6 SAM alone, the direct tunnelling current mentioned before is negligible. To conclude, the asymmetric behaviour derives from the fact that two MOs are involved at negative voltage instead of one for positive voltage.

These hypotheses must be confirmed by ab-initio calculations. The IV behaviour is dependent on the shift of the MOs (Stark effect) and likely on the dipoles (*e.g.* between $(PMo_{12})^{4-}$ and NH_3^+, $(PMo_{12})^{4-}$ and TBA^+, charge transfer at the electrodes) who can change the junction energy landscape.[151] Finally, the change of the shape of the IV curves (symmetric vs. asymmetric) has also been recently illustrated when switching a molecule between closed-shell and open-shell (radical) configurations.[143,145]

The above discussion is the result of the global overview of the dataset. Now, the ML and clustering methods help us to distinguish different behaviours inside the large dispersion of the IV dataset.

For the ^{TS}Au-C6/PMo_{12}(0)//Pt, we notice two clusters with high current level (#2 and #3, 0.1 - 1 nA at +/- 1.5V). They have the same LUMO energy (≈ 0.6 eV), in agreement with the average value deduced from statistics on the full dataset (Figure 2.7). Their electronic coupling to the electrodes is different (a factor about 4.5) but we can explain it as the consequences of C-AFM tip contact on the C6/PMo_{12}(0) fluctuations. The two other clusters at lowest current (#4 and #5, ≈ 10 pA at +/- 1.5 V) have more dispersed LUMO values (Fig. 2.20). However, the current level is near the sensitivity limit of the current-voltage preamplifier so the I-V curves are really noisy. What is important to notice is that the cluster 3 is the only one to display a slight asymmetric shape of the I-V curves (Table 2.3).

For the ^{TS}Au-C6/PMo_{12}(I)//Pt, we can also determine two series of two clusters each. As previously, the first one includes the clusters with the highest currents (≈ 10 nA at +/- 1.5 V). They are characterized by a MO level around 0.4 eV, as also found in the Figure 2.8, with the largest electronic coupling to the electrodes (0.35-1.1 meV). Unlike in a second series, the energy level is slightly lower (≈ 0.3 eV), as well as the electrode coupling (0.07-0.1 meV). These elements lead to the lowest current level (≈ 10-100 pA et +/- 1.5 V). The distinction of the two series may be due to different configurations of the PMo_{12}(I) between the C6 SAM and the C-AFM tip, as well as fluctuations of the SAM/Pt tip contact. Here, compared to the PMo_{12}(0) case, all the clusters display asymmetric shape (with the largest one for clusters 4 and 5, Table 2.3).

To summarise, the ML and clustering methods show us that asymmetric feature can be considered as a fingerprint of the reduced POM and so the PMo_{12}(0) cluster 3 would correspond to the fact that a small fraction of reduced Mo (≈ 19%) in the pristine PMo_{12} product as observed from XPS (Figure 2.4).

- **C2/PMo_{12} MJs**

The analysis of the ^{TS}Au-C2/PMo_{12}//Pt has not been pushed further since we observed the same behaviour with the pristine and reduced POM.

First, this time, we have more current with the C2 SAM alone than for the C2- PMo_{12} (Figure 2.6 and 2.8). The coupling energy with a C2 is 10 times bigger than with a C6, probably due to the better insulating character of C6. As C2 is very thin, this alkyl chain could be not efficient enough to isolate the reduced POM from the electrode. During the deposition, the added electron can spontaneously and rapidly go back to the bottom electrode and maybe we observe each time an oxidized POM. To conclude, a hypothesis could be the possibility of a "spontaneous" back to the pristine form.

f) Summary and outlook

To summarise, in this part, we have shown that the monolayer PMo_{12} is stable enough to do some electronic measurements at room temperature condition with the molecule in the pristine (oxidized) or one-electron reduced state. If the PMo_{12} molecules are "decoupled" from the underlying metal electrode by an alkyl chain of a sufficient length (6 carbon atoms), we have demonstrated several results by combining: i) electron transport measurements at the nanoscale

(C-AFM on self-assembled monolayers), ii) analytical models statistically applied on large current-voltage datasets and iii) unsupervised machine learning and clustering algorithms.

1.We demonstrated a reversible redox switching triggered *in-situ* by UV photoreduction.

2. The one-electron reduced PMo_{12} (open-shell state) is stable in the molecular junctions in air and at room temperature, the spontaneous return to its oxidized state laps for several hours to days.

3. The reduced PMo_{12} molecular junctions are characterized by an increase of the conductance (a factor ~ 10) and asymmetric current-voltage curves.

4. The electron transport in the pristine PMo_{12} junctions is controlled by the LUMO located at ~ 0.6-0.7 eV above the Fermi energy of the electrodes, with 25% of the junction dataset characterized by a better electronic coupling to the electrodes.

5. The electron transport in the reduced PMo_{12} junctions and the asymmetric current-voltage behavior is ascribed to a combined electron transmission through energetically closed (0.3-0.4 eV) SOMO and SUMO levels near resonance with the Fermi energy of the electrodes.

These results have been published in the journal Nanoscale.[152]

We were wondering if we can obtain similar results with another POM or if it is proper at this one.

III. Study of a second POM: P_5W_{30}

We have chosen to work with the Preyssler anion, $[Na\subset P_5W_{30}O_{110}]^{14-}$ (Figure 2.30) because it can be easily reduced at several electrons.[58,78,153] In this report, we will call it P_5W_{30}. We started by a study of the in-situ reduction of this POM.

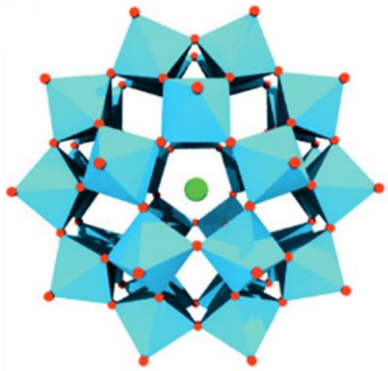

Figure 2.30. Polyhedral representation of Preyssler $[Na\subset P_5W_{30}O_{110}]^{14-}$. Light green sphere sodium, light blue polyhedra $\{WO_6\}$ and red spheres oxygens. Image from the reference.[57]

a) In-situ irradiation of KP_5W_{30}

We proceed to the irradiation of $((NH_4)^+K_{13}^+)\,[Na\subset P_5W^{VI}_{30}O_{110}]^{14-}$, for short KP_5W_{30}. This POM has been synthetized and characterized by the ePOM team and its synthesis is not developed here. The molecular junctions have been fabricated as indicated above (Chapter2_I) with a C6 SAM. The measured size of the POM layer is 9Å by ellipsometry. The KP_5W_{30} POM has a crown shape molecular structure with a 5-fold symmetry, an external diameter of about 18 Å and a height of about 13 Å. Probably, in this configuration, the POM is deposited with the long axis parallel to the C6 SAM surface. First, we measured by C-AFM the I-Vs with the KP_5W_{30} at the oxidized state. Then, the sample is irradiated under UV-light at 302 nm (analytikjena lamp, power ~ 0.5mW/cm²) in a solution of methanol during few hours. Methanol plays the role of the sacrificial reducer by following this reaction:[128]

$$((NH_4)^+K_{13}^+)\,[Na\subset P_5W^{VI}_{30}O_{110}]^{14-} + {}^{x}/_{2}\ CH_3OH \rightarrow ((NH_4)^+K_{13}^+H_x^+)\,[Na\subset P_5W^{VI}_{(30-x)}W^{V}_{x}O_{110}]^{(14+x)-} + {}^{x}/_{2}\ HC(O)H$$

By trying to reduce this way, we cannot know how many electrons this POM is reduced so we call it $KP_5W_{30}(x)$. We obtain the 2D histograms shown in Figure 2.31 below.

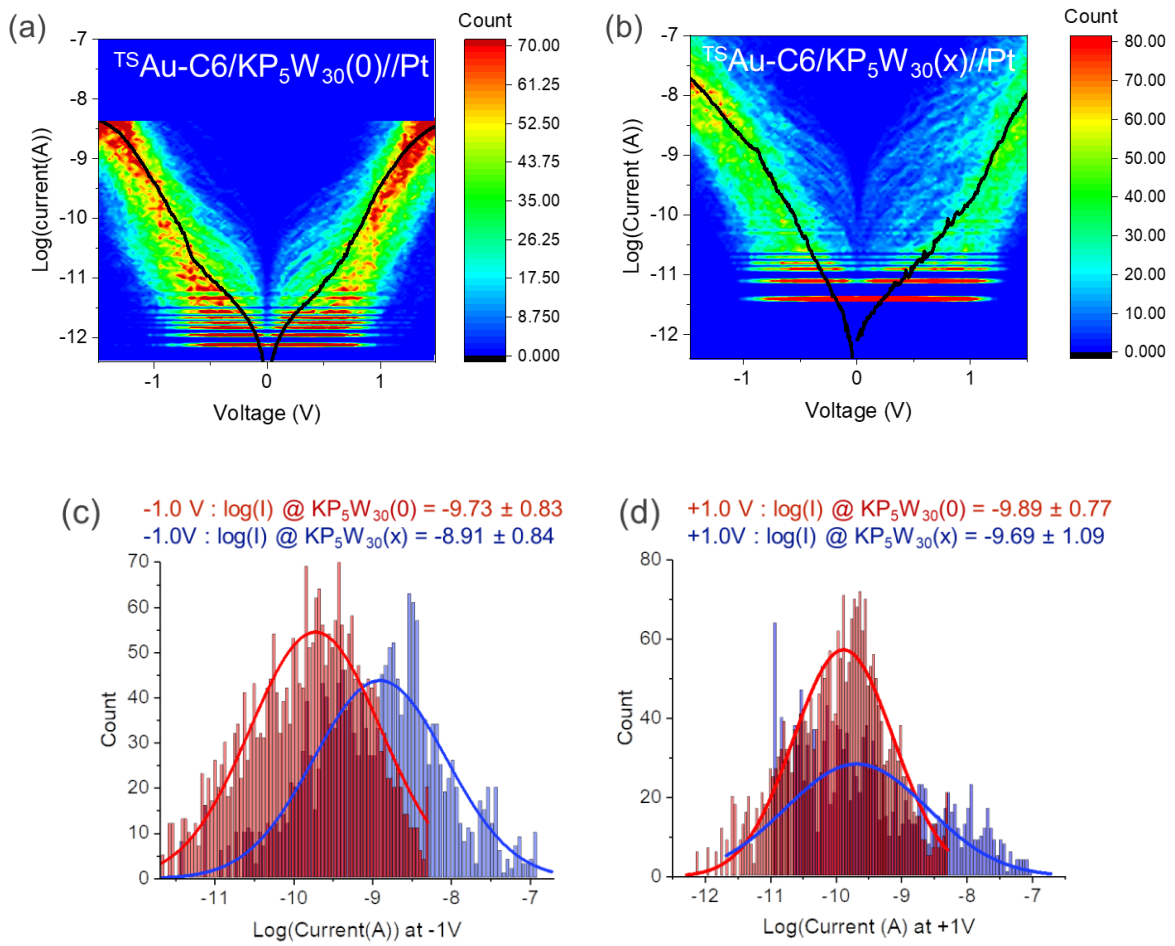

Figure 2.31. 2D histograms (heat maps) of I-Vs (loading force = 7.5 nN) in a semi-log$_{10}$ plot for (a) ^{TS}Au-C6/KP_5W_{30}(0)//Pt and (b) ^{TS}Au-C6/KP_5W_{30}(x)//Pt. The solid black lines are the mean $\bar{I}$-V curves. Histograms of the currents at (c) -1.0 V and (d) +1.0 V for the pristine (red bars) and reduced POM (blue bars) and fits by a log-normal distribution (the fitted log-mean value ± log-standard deviation is indicated on the panels).

In both junctions, there are 444 curves. It seems that in the 2D histograms there is a trend to an increase of the current upon reduction. Comparing the evolution of the current histograms after irradiation at -1V, we notice that we pass from a log-mean(I) value at -9.73 ($\bar{I} = 1.9\text{x}10^{-10}$ A) to -8.91 ($\bar{I} = 1.2\text{x}10^{-9}$ A), which represent an increase factor around 8. At +1V, we obtain a mean value -9.98 ($\bar{I} = 1.0\text{x}10^{-10}$ A) for the pristine POM and -9.69 ($\bar{I} = 2.0\text{x}10^{-10}$ A) for the irradiated one, which corresponds to a slight increase (factor ~ 2), negligible compared to the large current dispersion.

This preliminary result seems less relevant than with the PMo_{12} but still showing the same trend.

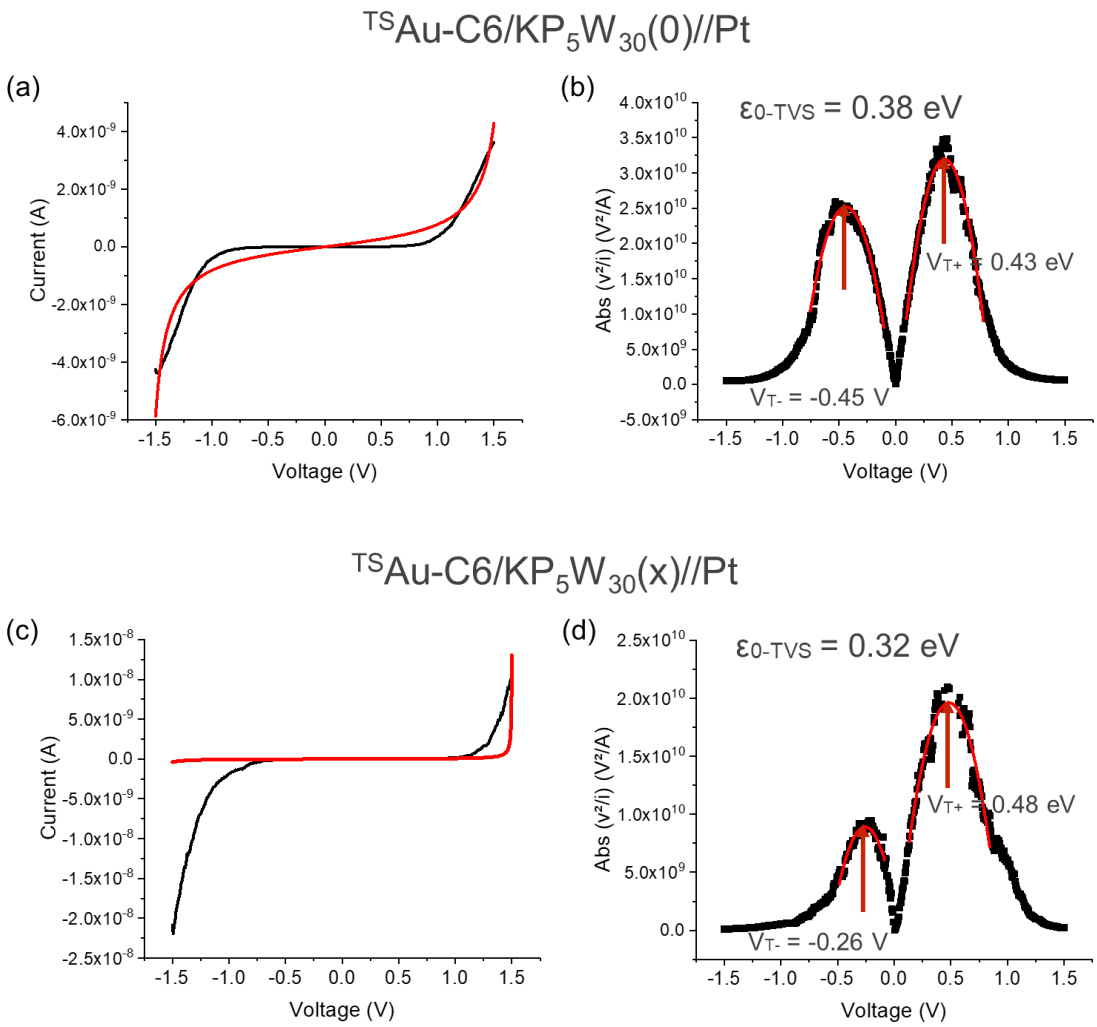

Figure 2.32. (a) Mean Ī-V curve fitted with SEL model and (b) with TVS method for ^{TS}Au-C6/KP$_5$W$_{30}$(0)//Pt and (c) Mean Ī-V curve fitted with SEL model and (d) with TVS method for ^{TS}Au-C6/KP$_5$W$_{30}$(x)//Pt.

Figure 2.32 (a) and (c) shows the average Ī-V curves obtained with the two junctions. The shape of the Ī-V, as also observed in the log scale (Figure 2.31 a and b), is not usual. We observe some shoulder and the data are not well fitted by the SEL model (red line on Figure 2.32a and c, even after reducing the fitted range), thus we do not used this model. We use the TVS method with these two junctions and we obtain $\varepsilon_{0\text{-TVS}}$ = 0.38 eV for the pristine POM and 0.32 eV for the irradiated POM. These two values are quite similar.

Note: This shoulder let us think that maybe two channels of conduction co-exist. During some measurements, electrons can pass by one of these two channels. One is predominating before the shoulder and the second one after. The two channels can be two MO of the P_5W_{30}, the LUMO and the LUMO +1. Another hypothesis is as at small voltage, the IV looks similar to

the IV of the SAM C6, dominated by tunnel transport. Maybe in this case, tunnel transport co-exist with a MO channel. SEL do not fit well because IV could be a mix of two SEL. This supposition must be confirmed with theory.

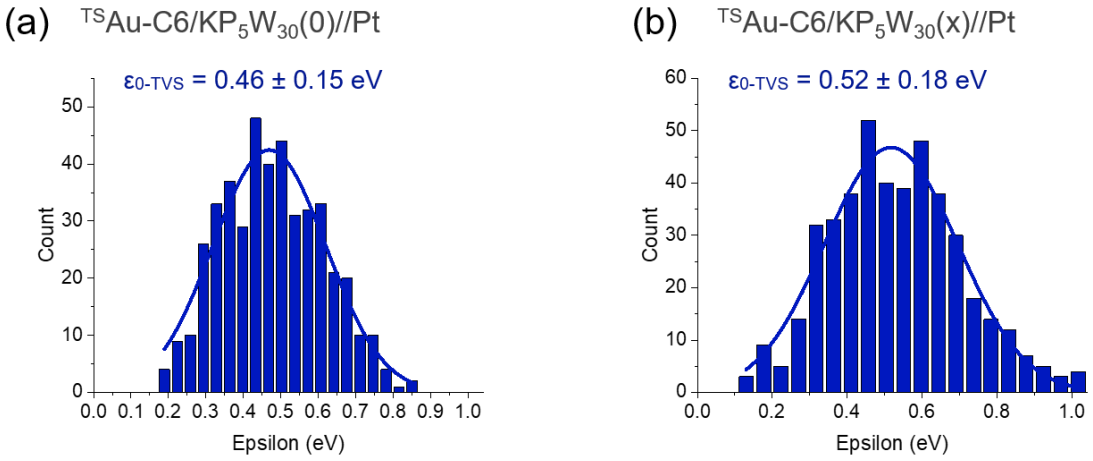

Figure 2.33. Statistical distribution of the energy level (TVS method) involved in the ET properties for (a) ^{TS}Au-C6/KP_5W_{30}(0)//Pt and (b) ^{TS}Au-C6/ KP_5W_{30}(0//Pt. The solid lines are the fits by a Gaussian distribution with the mean value ± standard deviation indicated in the panels.

Figure 2.33 shows the statistical distribution of $\varepsilon_{0\text{-TVS}}$. We find value a bit higher than with the mean Ī-V (Figure 2.32 b and d) but still similar, i.e. 0.46 and 0.52 eV for the pristine POM and after irradiation respectively. From these values, we calculated the coupling parameters Γ_{TVS} 0.14 and 0.48 meV.

b) Electron transport properties of C6/TBAP_5W_{30} MJs

Since we observe only a weak effect by UV photoreduction, we decided to start with a strongly reduced P_5W_{30} (3 electrons) and measure the ET properties to establish a "reference".

To process to the reduction of this POM, we use a $(TBA)_{10}H_4P_5W_{30}$ (synthesis detailed in IIIc) with a short name TBAP_5W_{30}. The reduction was made by Maxime Decker during his Bachelor L3 internship in the ePOM team.

- **Synthesis and titration of $TBANaP_5W_{30}$(III)**

The reduction of $TBA_{10}H_4[Na\subset P_5W_{30}O_{110}].24H_2O$, dissolved in degassed water and maintained under a dinitrogen flow, by successive additions of solid sodium dithionite ($Na_2S_2O_4$) was first monitored by the growing of the IVCT band at about 700 nm by UV-vis spectroscopy (Annexe A2.7). The absorbance maximum was reached after addition of 11 equivalents of $Na_2S_2O_4$ (ε = 26 000 $cm^{-1}.M^{-1}$). Because of competitive redox reactions, like the disproportionation of the dithionite itself, sodium dithionite should be added in great excess.

1.03 g of $TBAP_5W_{30}$ (i.e. 10^{-4} mol) is introduced into a 100 mL flask and dissolved in 20 mL of a mixture of degassed aqueous saturated TBABr (14 mL) and H_2O (6 mL). The solution is heated up to 70°C to facilitate the dissolution of the POM and 11 equivalents of sodium dithionite ($Na_2S_2O_4$) is added under control atmosphere. Then, we close the flask under argon flow. After cooling the solution, we observe a blue precipitate. This precipitate was filtered and washed with ethanol (rapidly) and diethylether (first crop 232 mg, second crop 74 mg). It is characterized by ^{31}P NMR by a rather sharp signal at -8.23 ppm (Annexe A2.7).

- **Determination of the reduction degree**

As sodium dithionite is instable in H_2O, 11 equivalents do not mean the POM is reduced to 22 electrons. To know to how many electrons the POM is reduced, 25.9 mg of this powder is dissolved in 5 mL of degassed acetonitrile and titrated with cerium (IV) in degassed ACN ($5x10^{-3}$ M for $(NH_4)_4Ce(SO_4)_4.2H_2O$). The colorimetric equivalence (from blue to yellow solution) is obtained after addition of V_{eq}=1.6 mL of the Ce(IV) solution.

To go further and determine the reduction degree of the POM, we need its molecular weight (MW), which depends on the nature and number of the counter-cations, also related to the reduction degree. It is thus quite intricate. The experimental observations are:

- ε_{max} = 26 000 $cm^{-1}. M^{-1}$: according to Pope and coll.[58], this could correspond to a POM reduced with 3 electrons (reported value ε_{max} = 24 700 $cm^{-1}. M^{-1}$)
- Observation of a rather sharp signal in the ^{31}P NMR spectrum: it goes in the direction of a diamagnetic species rather than a paramagnetic, so a POM reduced to 4 electrons
- ATD/ATG analysis give a loss of water molecules corresponding to 9.15% of the total mass

- The elemental analysis (C 7.01 %, H 1.91 % and N 0.64%) reveals that the number of TBA cations is lower than expected and probably replaced by Na^+ (introduced with the dithionite). This explains the limited solubility of the reduced POM in CH_3CN. There is no elemental analysis of Na due to the low quantity of isolated compound.

We made two simulations considering only TBA^+ and Na^+ as possible counterions and with a number of added electrons n (reduction degree) equal 3 or 4.

- **First hypothesis, n= 4:**

- An agreement with the elemental analysis and without considering the number of water molecules of crystallization x is $(TBA)_4Na_{14}[Na\subset P_5W_{30}O_{110}]$. This formula in turn allows calculating x = 49 and a molecular weight for $(TBA)_4Na_{14}[Na\subset P_5W_{30}O_{110}].49H_2O$ of 9627.79 $g.mol^{-1}$. The final calculated % values become C 7.98%, H 2.53% and N 0.58% and can be coherent with the previous elemental analysis because of the partial loss of water.
- Using this calculated molecular weight, a volume V_{eq}= 2.15 mL of the Ce(IV) solution would be expected for the titration.

- **Second hypothesis, n = 3:**

- This time, the closest agreement with the elemental analysis and without considering the number of water molecules of crystallization x is $(TBA)_3Na_{14}[Na\subset P_5W_{30}O_{110}]$. It in turn allows calculating x = 47 and a molecular weight for $(TBA)_3Na_{14}[Na\subset P_5W_{30}O_{110}].47\ H_2O$ of 9349.29 $g.mol^{-1}$. The final calculated % values are C 6.17%, H 2.18% and N 0.45%. Again, the partial loss of water can justify the little difference.
- Under this hypothesis, a volume V_{eq}= 1.66 mL of the Ce(IV) solution would be expected.

We obtained a better agreement of the equivalent volume with the second hypothesis; it lets us suppose that the POM is reduced to 3 electrons and the isolated compound labelled $TBANaP_5W_{30}$(III) (for $(TBA)_3Na_{14}[Na\subset P_5W_{30}O_{110}].47\ H_2O$). Finally, a UV-vis spectrum was recorded after isolation and redissolution of the reduced compound in degassed ACN. The calculated value for ε_{max}, 20 340 cm^{-1}. M^{-1} was lower than in the preparative monitoring, but the compound is very sensitive to reoxidation.

- **ET properties of C6/TBAP$_5$W$_{30}$(0) C6/TBAP$_5$W$_{30}$(III) MJs**

The MJ with C6/TBAP$_5$W$_{30}$(0) has been prepared as following in section I, in solution with acetonitrile and propan-2-ol (POM thickness ~ 14Å). As TBANaP$_5$W$_{30}$(III) is very air sensitive, once the SAM C6 were grafted on the ^{TS}Au substrate, we passed in the glovebox to deposit the POM from solution in degassed ACN. The functionalised substrate was then directly measured with the C-AFM in RT (measures were done in 25 minutes).

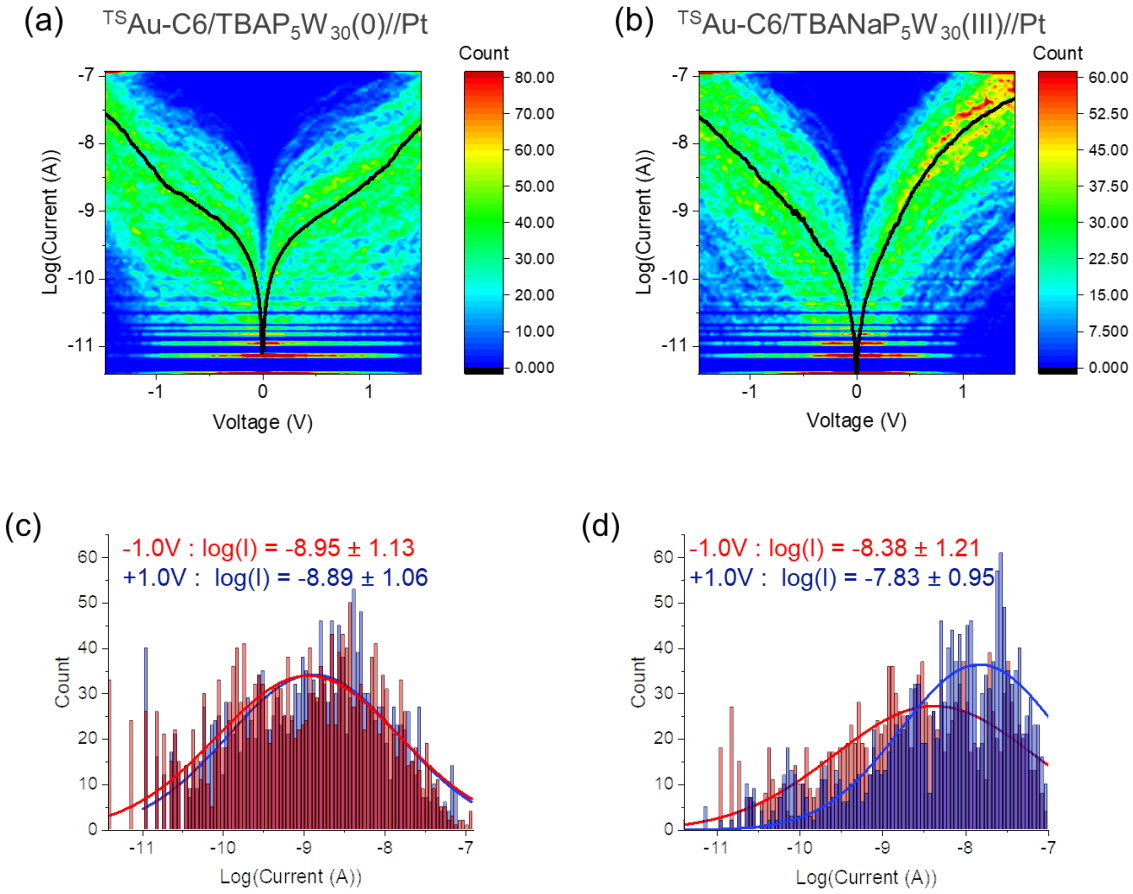

Figure 2.34. 2D histograms (heat maps) of I-Vs (loading force ~ 9 nN) in a semi-log$_{10}$ plot for (a) ^{TS}Au-C6/TBAP$_5$W$_{30}$(0)//Pt and (b) ^{TS}Au-C6/TBANaP$_5$W$_{30}$(III)//Pt. The solid black lines are the mean Ī-V curves. (c) and (d) The histograms of the currents at -1.0 V (red bars) and +1.0 V (blue bars) and fits by a log-normal distribution (the fitted log-mean value ± log- standard deviation is indicated on the panels).

After cleaning these datasets, 409 IV curves are shown in Figure 2.34a and 340 in Figure 2.34b. By looking at the 2D histograms, we notice that the two junctions present the same level of current. Nevertheless, the shape is different for the reduced one, we do not see a shoulder. One consequence of this difference is that the current does not evolve the same way with the voltage and we see more currents with the reduced POM at ± 1.0V, increasing from log I = -8.95 (I =

1.1×10^{-9} A) to log I = -8.38 (I = 4.1×10^{-9} A) at negative bias (factor ~ 4) and from log I = -8.89 (I = 1.3×10^{-9} A) to log I = -7.83 (I = 1.5×10^{-8} A) at positive voltage (factor ~ 11). Moreover, no asymmetry is observed with the C6/$TBAP_5W_{30}$(0) and one appears with C6/$TBANaP_5W_{30}$(III) (R^+ ~ 3.5).

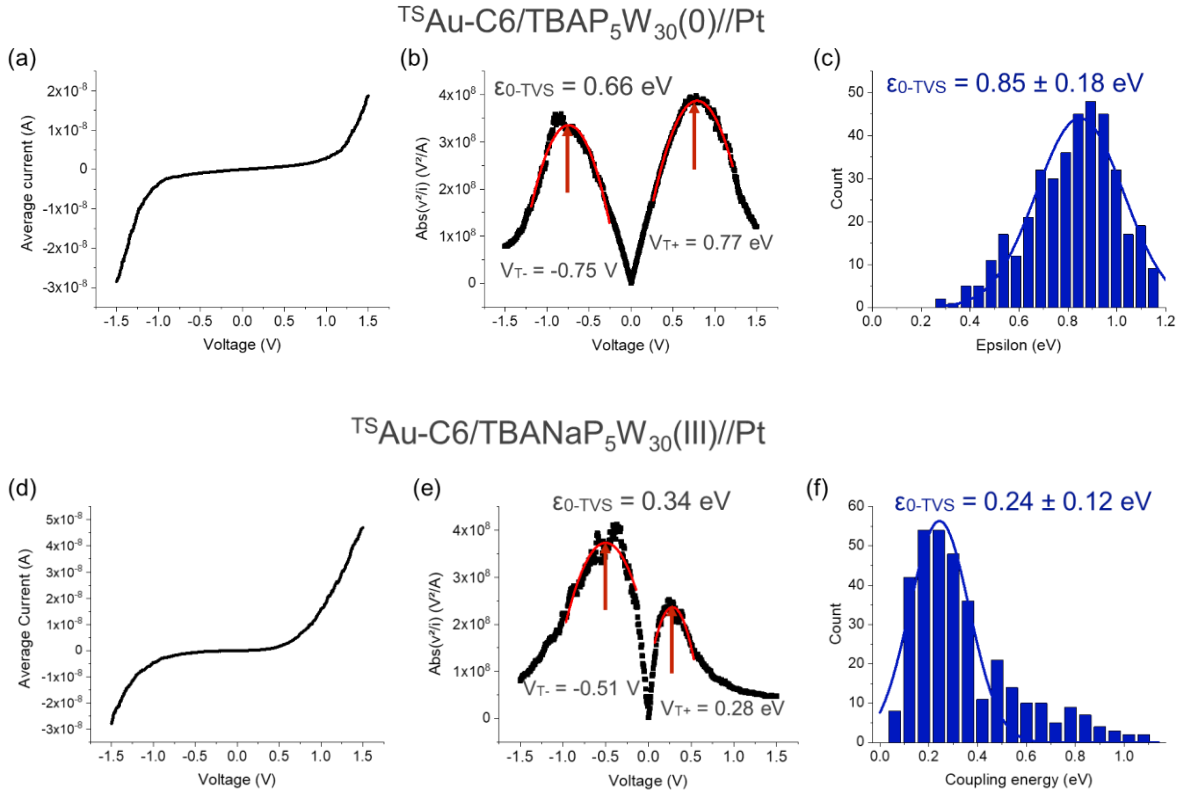

Figure 2.35. (a) and (c) Mean Ī-V curves, (b) and (e) with TVS method and (c) and (f) statistical distribution of the energy level (TVS method) involved in the ET properties for ^{TS}Au-C6/$TBAP_5W_{30}$(0)//Pt and ^{TS}Au-C6/ $TBANaP_5W_{30}$(III)//Pt, respectively. The solid lines are the fits by a Gaussian distribution with the mean value ± standard deviation indicated in the panels.

In comparison with the 2D histogram (Figure 2.34 a and b), the mean curves are in a good agreement with the fact that the junctions have almost the same level of current (± 3×10^{-8} A) but with a totally different shape (Figure 2.35 a and d). The mean ε_0 value calculated with the TVS method falls by a factor 2 with the reduction (0.66 → 0.34 eV, Figure 2.35 b and e) and the statistical epsilon value falls by a factor 3.5 (0.85 → 0.24, Figure 2.35 c and f). Concerning the coupling parameters Γ_{TVS}, we have calculated 3.7 meV with $TBAP_5W_{30}$(0) and 0.7 meV with $TBANaP_5W_{30}$(III).

- **Discussion**

The ePOM team succeeded in reducing this POM at 3 electrons as described. This new POM is really air sensitive and all the preparation of functionalisation of surfaces have been done in glovebox. Nevertheless, the electronic measurements have been done with the same AFM at RT and we did not observe a large current increase compared to the oxidized POM but some changes in the I-V shape that translate into changes in the electronic structure. However, we cannot exclude that the POMs get re-oxidized between the exit of the glovebox and the end of the measurement. The perspective of this investigation is to realise the study of the electron transport properties with an ultra-high vacuum C-AFM.

As two pristine P_5W_{30} with two different counterions have been already presented, we will continue to analyse this POM by doing a second study: the influence of the counterion on the ET properties of the POM.

c) Exchange of the counterion

- **Introduction**

It has already been proved that we cannot ignore the influence of the counter anion on the electron transport inside a molecular junction. For example, it has been experimentally demonstrated that the position of the ions in the MJs (i.e. close to the bottom or top electrode) can reversibly switch the IV behaviour from a symmetric to an asymmetric shape.[154] In the case of $[W_{18}O_{54}(SO_3)_2]^{4-}$-based MJs, DFT-NEGF calculations showed that the presence of the counterion (whatever its nature, here tetramethylamonium (TMA) vs. Cs^+) moves the LUMO closer to the Fermi energy of the electrodes (~0.08 eV above E_F in both the cases). Albeit this position of the LUMO, the computed I-V curves showed slight differences of the shape (more asymmetric I-V for Cs^+). [155] The authors suggested that this feature might be due to small differences in the amplitude of calculated transmission coefficient T(E), clearly calling to more joint experimental and theoretical works. They also noted that the presence of the counterions does not create additional new conduction channels in the MJs, but rather that they modify the potential landscape "viewed" by the POMs that transmit the electrons through the junction.

Thus, we synthesised a series of P_5W_{30} based MJs with different counterions to study this issue in more details.

When we have proceeded to the reduction of the Preyssler anion chemically, i.e. to reduce some W(VI) centers to W(V), we decided to switch to a tetrabutylammonium salt (TBA^+) to make the POM soluble in acetonitrile. The first intention was indeed to use organic reducing agents. The Preyssler anion is usually accompanied by K^+ and Na^+ cations, so the main goal was to exchange these cations with TBA^+. When it appeared that the cation exchange was incomplete and that we got a mixed TBA^+/H^+ salt, we came back to the reduction in an aqueous medium.

- **Synthesis of $K_{12,5}Na_{1,5}[Na\subset P_5W_{30}O_{110}]$**

The POM we used was a by-product of the synthesis of $K_6[\alpha\text{-}P_2W_{18}O_{62}]$ prepared in the e-POM team. In that case, contamination with NH_4^+ cation is possible, as revealed by IR spectroscopy and elemental analysis. It can also be directly prepared under hydrothermal conditions.[156]

To 33g of $Na_2WO_4.2H_2O$ dissolved in 30mL of water are added 26.5mL of H_3PO_4 (85%). This mixture is placed in a solvothermal synthesis bomb (Parr Model 4748), heated to 120°C overnight. Once the yellow solution has cooled to room temperature, 15mL of H_2O is added followed by 10g of KCl. The precipitate was membrane filtered and washed with 2M potassium acetate and methanol. Recrystallization in hot water is necessary to purify the product (with a pause time < 2h to avoid the formation of crystals of $[\alpha\text{–}P_2W_{18}O_{62}]^{6-}$). About 8g of crystals are then collected. A second recrystallization can be performed if the product still contains impurities.

For each step, the compound is characterised by phosphorus-31 NMR (annexe A2.3), which indicates the type of POM and its purity. The NMR of this POM is shown below (Figure 2.36). Note that all the NMR spectra have been recorded by dissolving a small amount of product with a solvent in a NMR tube.

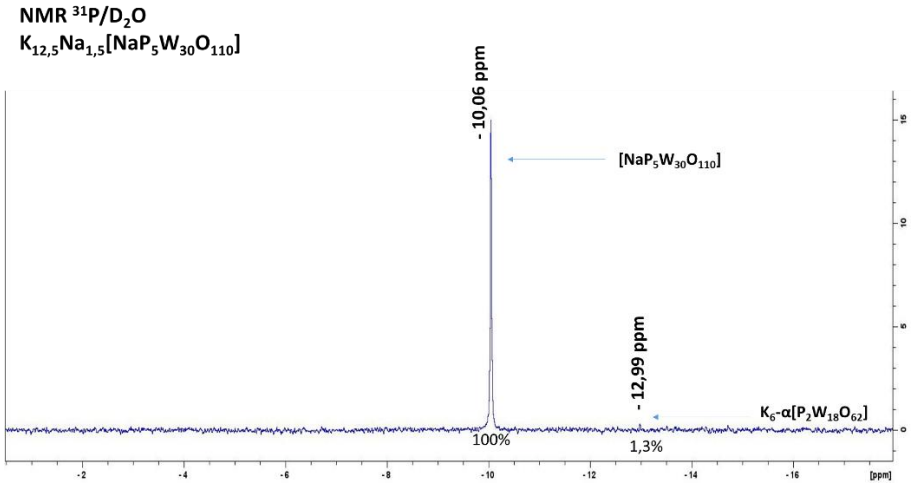

Figure 2.36. ^{31}P NMR spectra of $K_{12,5}Na_{1,5}[Na\subset P_5W_{30}O_{110}]$ in D_2O showing the main component at -10.06ppm.

The NMR spectrum shows the purity of the obtained product. The quantity of the reagent is negligible. The IR spectrum supports the composition of the POM (Figure 2.37, technical protocol annexe A2.3).

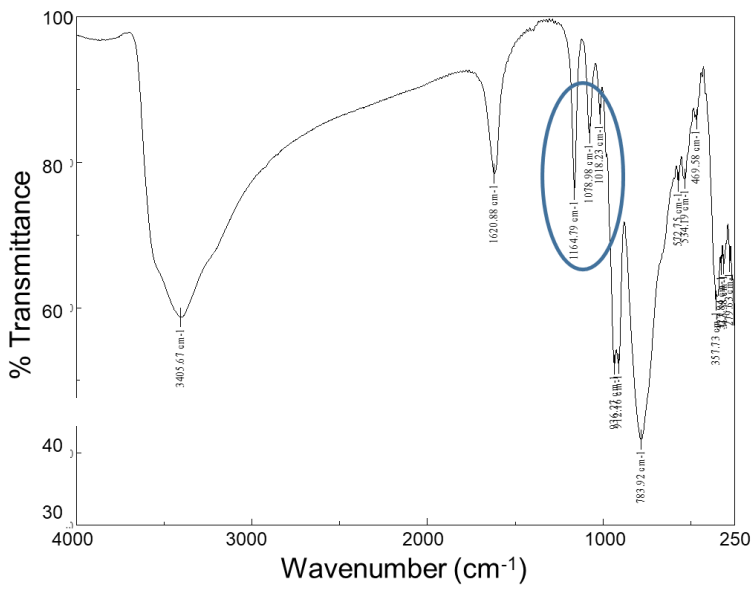

Figure 2.37. IR spectrum of $K_{12,5}Na_{1,5}[Na\subset P_5W_{30}O_{110}]$.

IR spectra were recorded from KBr pellets. The three bands between 1000 and 1150 cm^{-1} (blue circled) are specific to P-O vibrations and related to the local Cs symmetry (no axis of symmetry but a plane) for the PO_4 groups due to the internal Na^+.[58]

Complementary elemental analysis has been investigated to know the exact nomenclature of the POM. Inductively coupled plasma optical atomic emission spectrometry (ICP-OES) at Crealins (Lyon) and Synapse (Versailles) (results in annexe A2.8) have been used to know the composition of the counter ions. Thermogravimetric analysis (ATD/ADTG) has been done at ePOM to assess the quantity of water molecules and the exact molar mass of the POM.

Here, we have obtained a POM with formula: $\mathbf{K_{13,3}Na_{0,7}[Na\subset P_5W_{30}O_{110}].27H_2O}$ (MW = 8475.07 g mol^{-1}).

We have tried to directly pass from the potassium counter anion to the TBA one but we figure out that one intermediate step is necessary, passing by the protoned POM.

- **Exchange of alkali cations by H^+ then by TBA^+**

Sadakane's team[157] investigated the cation exchange of this Preyssler anion to TBA^+ via H^+.

  - **Exchange of cations K^+ and Na^+ by H^+ synthesis of $H_{14}[Na\subset P_5W_{30}O_{110}]$**

First, we prepare the Dowex column 50W-X8. This resin is charged with excess protons, where the hydronium ion is the counterion to the functional groups.

In a beaker, the very fine particles of the resin were separated from the mass by successive sedimentations and decantations in distilled water. Then, on the sintered material, an acid wash (1M HCl) was used to remove any residual metal traces. The resin was washed with distilled water until the orange coloration resulting from the degradation of the polymer disappeared. Finally, this resin was placed in a column (diameter 1.5 cm, length 40 cm), washed three times with the dead volume of the resin (~ 20 mL) and rinsed with water until a pH for the eluent identical to that of the water was obtained.[158] The pH increased very slowly to 4.8 (addition of 1L of H_2O) and finally water was left overnight in the column, the next day until to obtain pH 5.4.

On a second time, we pass the POM on the resin:

In a beaker, 8.2g of $K_{13,3}Na_{0,7}[Na\subset P_5W_{30}O_{110}].27H_2O$ is dissolved in 160 mL of H_2O. The solution is transferred to the column and passed through the resin at a rate of one drop per second, all the eluent is collected. Water is then passed through to ensure that all the products are collected. As long as the pH is acidic, some Preyssler anion remains (an addition of 40mL of H_2O is sufficient to collect all the product).

The eluent is evaporated at a temperature of around 60-65°C. The recovered product (mass 7.8g) is yellower and stickier, it is crushed twice with ethanol, then dried with diethylether and analysed by NMR (Figure 2.38). According to ATD/ATG, 44 water molecules are present leading to the general formula **$H_{14}[Na\subset P_5W_{30}O_{110}].44H_2O$** with a molar weight of 8260.08 g mol^{-1} (Annexe A2.8).

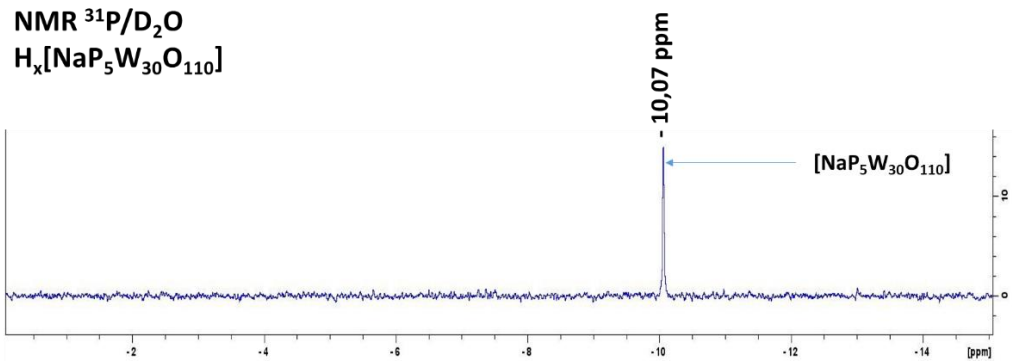

Figure 2.38. ^{31}P NMR spectrum of the $H_{14}[Na\subset P_5W_{30}O_{110}]$.

The peak observed in this NMR spectrum did not move compared to the one shown in Figure 2.36. This NMR spectrum confirms that the product is still pure and the polyanion is intact.

To complete these studies, the electrochemical signature of these POMs was studied.

- **Electrochemistry of $H_{14}[Na\subset P_5W_{30}O_{110}]$**

In a 10mL electrochemical cell, 1mM $H_{14}[Na\subset P_5W_{30}O_{110}].44H_2O$ (m=75mg) is added with 0.1M tetrabutylammonium hexafluorophosphate ($TBAPF_6$) electrolyte in acetonitrile. The solution was mixed and degassed for about 20 minutes. After total solubilisation, the electrochemical parameters give the cyclic voltammetry (CV) below (Figure 2.39):

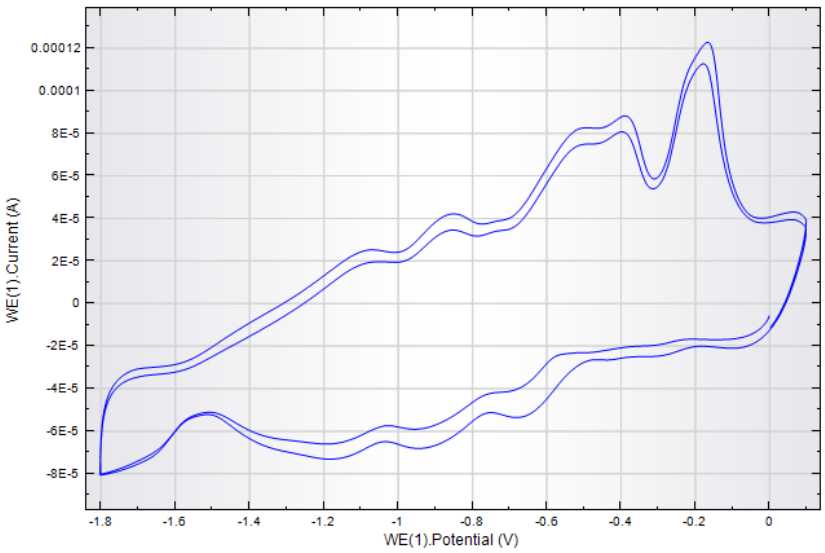

Figure 2.39. CV of $H_xP_5W_{30}$ 1mM, ACN, $TBAPF_6$ 0.1 M, 0.1 $V.s^{-1}$.

Several redox waves are observed but the processes are complex (especially in the reverse direction) and it is difficult to separate and attribute them. The presence of protons facilitates the reduction, so multi-electron processes are frequently observed in POM chemistry.

- **Exchange of H^+ by TBA^+ preparation of $TBA_{10}H_4[Na\subset P_5W_{30}O_{110}]$**

This exchange of cations takes place according to an acid-base reaction:[157]

$$H_{14}[Na\subset P_5W_{30}O_{110}].44H_2O + 14\ TBA\text{-}OH \rightarrow TBA_{14}[Na\subset P_5W_{30}O_{110}] + 14\ H_2O$$

In a bicol flask, 6.0 g of POM is dissolved in 100 mL of distilled water (MM = 8259.78 $g.mol^{-1}$; n = $7.27x10^{-4}$ mol), 2 drops of phenolphthalein are added to clearly see the turning point, and the solution is degassed in order to measure only the protons from the POM and not those from the dissolved CO_2 (H_2CO_3). The solution is titrated with a 1.54 M TBAOH solution and the titration is monitored with a pH electrode under nitrogen flow. The titrant solution is added slowly to the syringe, the solution becomes milky very quickly but can become clear again (shortly before the turning point).

The equivalent volume is 4.8 mL + 0.1 mL of TBAOH 0.308 M, the solution becomes slightly pinkish, the solution is evaporated under vacuum. During the evaporation, a discoloration of the solution is observed which shows that the pH decreases, the evaporation is stopped and an

addition of TBAOH is made. The phenomenon was repeated 3 times bringing the equivalent volume to Veq = 5 mL. The product was dried with 2x10 mL absolute ethanol and 10 mL ether.

The experimental equivalent volume is lower than the theoretical volume (0.76 eq), if we assume that all the TBA introduced at equivalence were exchanged with the protons of the POM, then we have a mixed salt with 10 TBA per POM i.e. $(TBA)_{10}H_4[NaP_5W_{30}O_{110}]$. The TBAOH could be a base that is not strong enough to pull out these last protons.

According to ATD/ATG, 24 water molecules are present leading to the general formula **$TBA_{10}H_4[Na\subset P_5W_{30}O_{110}].24H_2O$** (MW = 10314.41 g.mol^{-1}, Annexe A2.8). Our supposition is confirmed by the elemental analysis.

The IR spectrum has also been done to characterize the product (Figure 2.40).

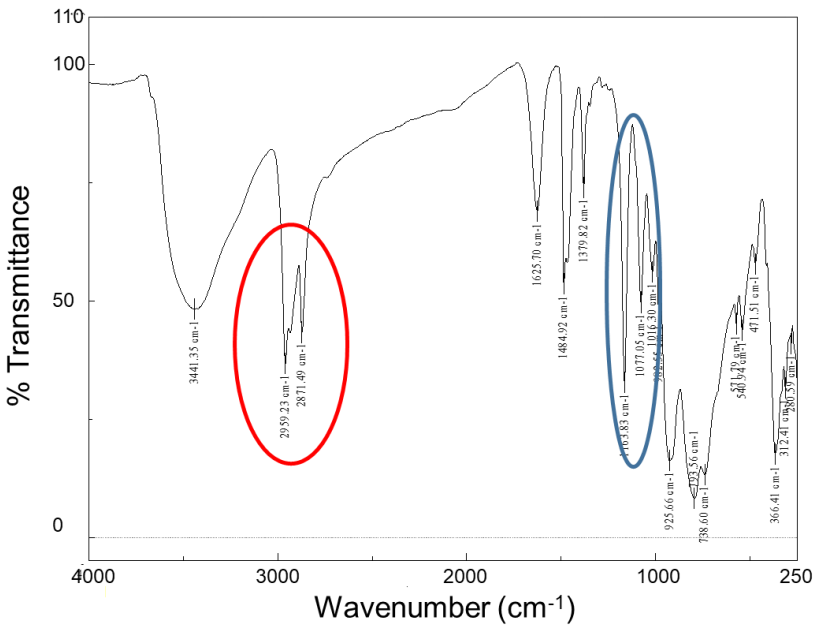

Figure 2.40. IR spectrum after exchange of counterion.

We observe two new bands (red circle) on this spectrum at 3959 and 2871 cm^{-1} (CH stretching modes) and also at 1485 and 1380 cm^{-1} (C-H bending modes). These bands represent the signature of the TBA. The signature of the P_5W_{30} did not change (blue circle).

To conclude, this multi-step process gives us three different P_5W_{30} with K, H and TBA as counterions:

- $K_{13,3}Na_{0,7}[Na\subset P_5W_{30}O_{110}].27H_2O$ (short name: KP_5W_{30})
- $H_{14}[Na\subset P_5W_{30}O_{110}].44H_2O$ (short name: HP_5W_{30})
- $TBA_{10}H_4[Na\subset P_5W_{30}O_{110}].24H_2O$ (short name: $TBAP_5W_{30}$)

A similar KP_5W_{30} has already been studied (III_a) and the results on $TBAP_5W_{30}$ were presented in III_b. For the influence of counterion, we will use these previous results, and, on the next part, we will focussed on HP_5W_{30} and another POM, $NH_4P_5W_{30}$, not linked to this multi-step process but prepared directly.[159] *Note that the HP_5W_{30} used for the electric measurement is derived from the first synthesis of this multi-process and the general formula was $H_{13}Na_1[Na\subset P_5W_{30}O_{110}].54H_2O$ (MW = 8 461.07g.mol^{-1}).*

d) Influence of the counterion in the electron transport properties of C6/P_5W_{30} MJs

The results for the MJs with the potassium counterion (KP_5W_{30}) and the tetrabutylammonium counterion ($TBAP_5W_{30}$) were already presented in section IIIa and IIIb respectively. The study of the influence of the counterion of the POM Preyssler has been continued with cations H described above (section III_c) and also NH_4 (synthesis done by ePOM and only use for this study, not detailed here). These POMs have been inserted inside a molecular junction as described in the chapter 2-I: the $NH_4P_5W_{30}$ POM from solution with H_2O and the HP_5W_{30} POM from solutions with ACN/ISO. The thicknesses of the POM monolayers measured by ellipsometry are 9Å and 10Å (±2Å) respectively.

It could mean that these POMs have the same orientation on the C6 SAM: $NH_4P_5W_{30}$ and HP_5W_{30} can be parallel along the C6 SAM ($TBAP_5W_{30}$ thickness is 14Å, could be standing upright, or the size of the cations influence the total thickness of the layer). Figure 2.41 shows the IV curves obtained with these C6/$NH_4P_5W_{30}$ and C6/HP_5W_{30} junctions:

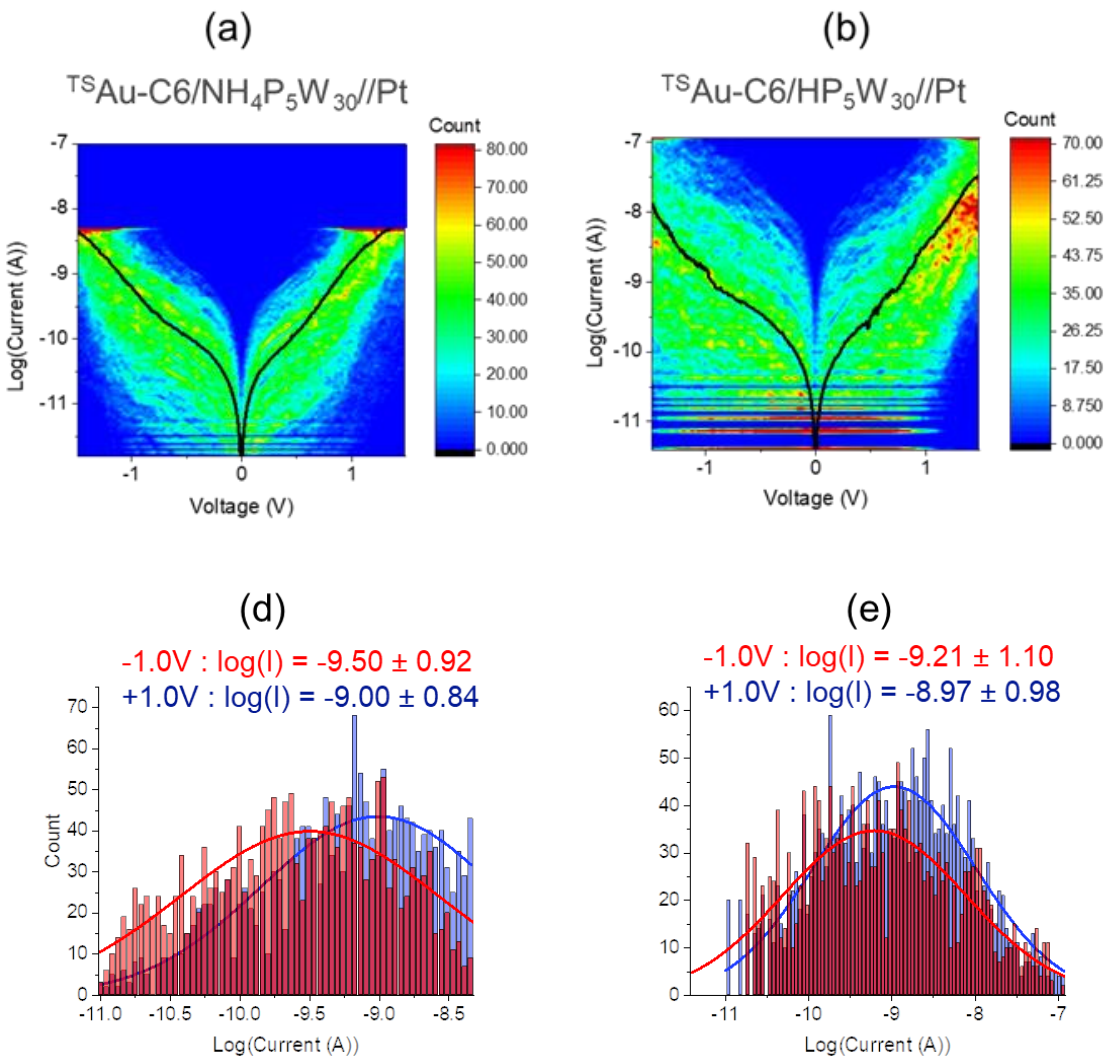

Figure 2.41. 2D histograms (heat maps) of I-Vs (loading force= 9 nN) in a semi-log_{10} plot for (a) ^{TS}Au-C6/($NH_4P_5W_{30}$//Pt, (b) ^{TS}Au-C6/HP_5W_{30}//Pt. The solid black lines are the mean $\bar{I}$-V curves. (d) and (e) The histograms of the currents at ±1.0 V (blue bars) and fits by a log-normal distribution (the fitted log-mean value ± log-standard deviation is indicated on the panels).

409 IV curves are treated for the MJ with $NH_4P_5W_{30}$ and 477 for the MJ with HP_5W_{30}. At a first glance, the 2D current histograms have quite a similar level of currents. More precisely, from the current histograms +1.0V, we notice a mean current of log I = -9.00 (I = 10^{-9} A) and log I = -8.97 (I = $1.1x10^{-9}$ A) for the two junctions (Figure 2.41d-e) (-9.89 ($1.3x10^{-10}$A) with K, Figure 2.31 and -8.89 ($1.3x10^{-9}$ A) with TBA, Figure 2.44). These values are almost the same. At -1V, the variation between the values is more important, but still in the same range: log I = -9.50 (I = $3.2x10^{-10}$ A) with NH_4 (Figure 2.41c) and log I = -9.21 (I = $6.2x10^{-10}$ A) with H (Figure 2.41d) (log I =-9.73 (I = $1.9x10^{-10}$ A) with K (Figure 2.31) and log I = -8.95 (I = 1.1x10^{-}

[9] A) with TBA, Figure 2.34). At first glance, we can suppose that there is no significant influence of the counter anion on the level of current with the P_5W_{30}.

- **Discussion**

The electronic structure of these junctions have been studied only by TVS method using the mean Ī-V curve (Figure 2.42) and the statistical analysis (Figure 2.43).

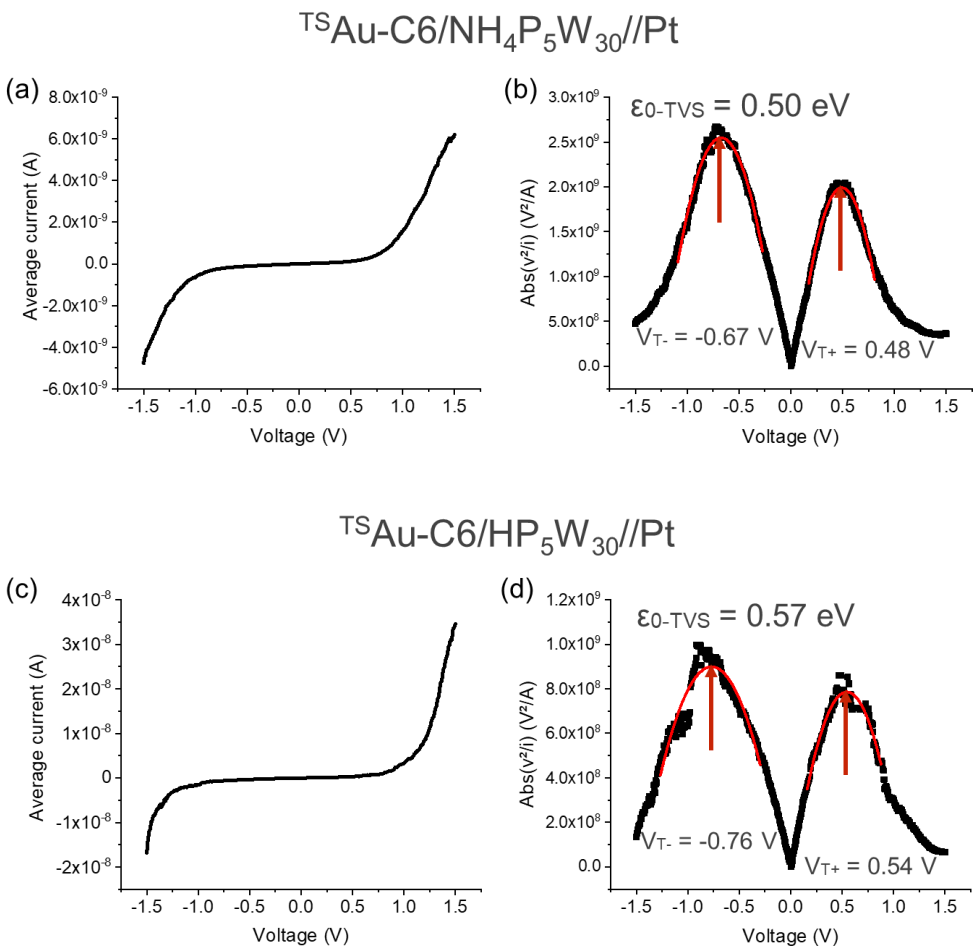

Figure 2.42. (a) Mean Ī-V curve and (b) with TVS method for ^{TS}Au-C6/$NH_4P_5W_{30}$//Pt and (c) Mean Ī-V curve and (d) with TVS method for ^{TS}Au-C6/HP_5W_{30}//Pt.

From the mean Ī-V curves, we have calculated $\varepsilon_{0\text{-TVS}}$ values of 0.50 eV for the C6/$NH_4P_5W_{30}$ MJ and 0.57 eV with the HP_5W_{30} (Figure 2.42). For the statistics, we also replot (Figure 2.43)

the histograms with KP_5W_{30} and $TBAP_5W_{30}$ to facilitate the comparison (from Figures 2.33 and 2.35) and we recapitulate all the data in the Table 2.6.

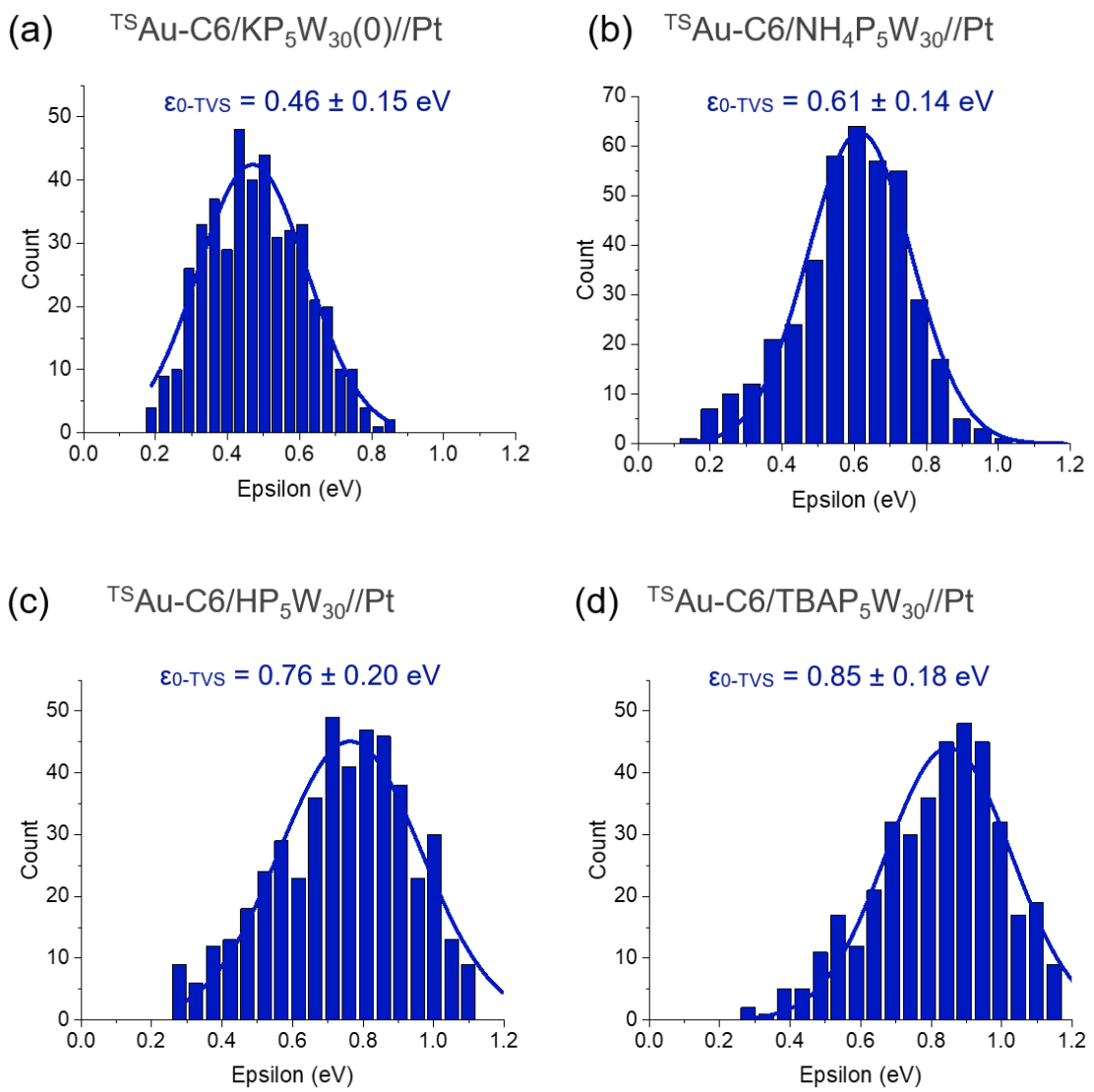

Figure 2.43. Statistical distribution of the energy level (TVS method) involved in the ET properties for (a) ^{TS}Au-C6/KP_5W_{30}//Pt, (b) ^{TS}Au-C6/$NH_4P_5W_{30}$//Pt, (c) ^{TS}Au-C6/HP_5W_{30}//Pt and (d) ^{TS}Au-C6/$TBAP_5W_{30}$//Pt. The solid lines are the fits by a Gaussian distribution with the mean value ± standard deviation indicated in the panels.

Using statistics, we obtain $\varepsilon_{0\text{-TVS}}$ = 0.61 eV (Γ_{TVS} ~ 0.95 meV) with $NH_4P_5W_{30}$ and 0.76 eV (Γ_{TVS} ~ 2.04 meV) with HP_5W_{30}. These values are slightly larger than the values from the mean Ī-V but the same gap is noticed.

Table 2.6. Summarize of the current values and electronic structure of the four P_5W_{30}.

POM	Log(I) at -1V	I at -1V (A)	Log(I) at +1V	I at +1V (A)	ε0 by TVS method (eV)	Γ_{TVS} (meV)
KP_5W_{30} (0)	-9.73 ± 0.83	$-1.9x10^{-10}$	-9.89 ± 0.77	$1.3x10^{-10}$	0.46 ± 0.15	0.14
$NH_4P_5W_{30}$	-9.50 ± 0.92	$-3.2x10^{-10}$	-9.00 ± 0.84	$1.0x10^{-9}$	0.61 ± 0.14	0.95
HP_5W_{30}	-9.21 ± 1.10	$-6.2x10^{-10}$	-8.97 ± 0.98	$1.1x10^{-9}$	0.76 ± 0.20	2.04
$TBAP_5W_{30}$(0)	-8.95 ± 1.13	$-1.1x10^{-9}$	-8.89 ± 1.06	$1.3x10^{-9}$	0.85 ± 0.18	3.68

The position of the MO involved in the ET is different for all the POMs. We observed a gradual increase of LUMO position (w. /E_F) from K<NH_4<H<TBA, passing from 0.46 eV with K to 0.85 eV with TBA. This increase is counterbalanced by an increase of the electronic coupling (from 0.14 meV to 3.68 meV) (Table 2.6).

Another important point is the structural detail of the POM/electrode interface and how the molecule is connected to the electrode. P_5W_{30}, unlike PMo_{12}, is an ellipsoid and anisotropic molecule. In Ref. 155, the electronic properties of another ellipsoidal POM have been calculated. It was shown that positioned in a "vertical" orientation (w. /electrode substrate) it leads to a higher conductance than a "horizontal" orientation (if the same number/nature of chemical bonds are considered). With less "chemical contact bonds", the LUMO shifted higher compared to Fermi level. According to ellipsometry, K, NH_4 and H could have likely "horizontal" orientation whereas TBA could have a "vertical" one, which may be consistent with the larger measured value of ε_0. Thus, the POM orientation could also play a role. However, at this stage of our work, it stays difficult to conclude and a comparison with simulations are required.

e) Summary and outlook

To summarize this section III, we have started by doing a similar study than the one with PMo_{12} (section II). We proceed to the reduction of P_5W_{30}, first in-situ by UV irradiation and then, with the POM directly chemically reduced. We succeed in passing from $TBAP_5W_{30}$(0) probably to $TBANaP_5W_{30}$(III), so a P_5W_{30} reduced to 3 electrons. Unlike in the C6/PMo_{12} MJs, we

observed a weak effect of reduction in the C6/P_5W_{30} MJs. Interestingly, we found almost the same level of current but with different parameters of the electronic structure (MO energy levels and electronic coupling to the electrodes). The kinetic of oxidation/reduction is much faster with this last POM and probably we were confronted to stability issues. A perspective of this work is to use UHV C-AFM.

Then, we have worked on the effect of the counterions on the electron transport properties. No clear significant difference on the IVs appears, we found more or less same current amplitude and same statistics. But, using TVS method to analysis the electronic structure, we figure out that MJ parameters (LUMO/E_f and electrode coupling) increase from 0.46 to 0.85 eV and from 0.14 to 3.7 meV, respectively, in the order K, NH_4, H, TBA.

Whether for the electronic transport properties with reduction or with counterion, we notice no relevant difference in the value of currents but a more important one for the electronic structure. These results call for more joint experiment and theory works.

Contents of chapter 3

Chapter 3 : Gold Nanoparticles - POMs network 95

I. Implementation of the Au NP-POM network 95

a) Homogeneous film of gold nanoparticles 96

b) Exchange of ligands 99

c) Reduction of the POMs 105

II. Electron transport dynamics of the NPSANs 108

a) IV measurements 108

b) Noise measurements 110

c) High harmonic generation measurements 117

d) Are polyoxometalates prone for Reservoir Computing? 119

Conclusion and outlook 120

Chapter 3 Gold Nanoparticles - POMs network

In this chapter, we report on the fabrication and study of two-dimensional (2D) networks of molecular junctions. This device is constituted of a 2D POM network where the POMs surround gold nanoparticles (NPs). This network is deposited under the form of a monolayer at the surface of SiO_2 on which some motifs are lithographed and consisted of six concentric electrodes (Figure 3.1 a and b and annexe A3.1). Hereafter, this network of molecularly functionalized metal nanoparticles is called nanoparticle self-assembled network (NPSAN) (Figure 3.1_c). Having six electrodes allows studying the electron transport (ET) properties between different connexions inside the network, the purpose being to assess the ET variability inside the NPSANs and check if they are prone to be a part of reservoir computing, as described in the Chapter 1-III. Gold NPs play the role of artificial nodes and the POMs the connexions between them. The NCM team has already done similar work with NP/azobenzene NPSANs[160] and our goal is to study if similar results can be obtained with POMs.

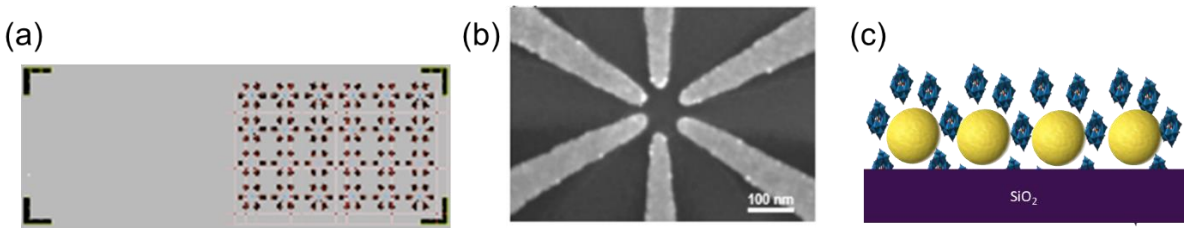

Figure 3.1. (a) Schematic image of one component with a matrix of 6 x 4 NPSANs, (b) SEM image of one NPSAN motif with six electrodes and (c) schematic representation of NPSAN with Au NP-POM

We will first present the synthesis and characterization of these networks and in a second time, we will discuss their electronic properties, in particular focusing on noise measurements, as a tool to reveal ET dynamics.

I. Implementation of the Au NP-POM network

This implementation contains two fabrication steps. The first step consists to obtain a homogeneous and monolayer compact film of gold nanoparticles and the second one is to exchange the ligands passivating the NPs by the POMs.

a) Homogeneous film of gold nanoparticles

To synthesize gold nanoparticles, two methods in the literature are well known. The Turkevich method[161,162] gives the advantage to obtain gold nanoparticles with a controlled and homogeneous size. The NPs are surrounded by citrate ligands (Figure 3.2a). They are negatively charged (Coulomb repulsion) and water-soluble. Thus, it is impossible to make a floating Langmuir film on a water subphase. The Wang et al. method[163] gives gold NPs surrounded by oleylamine ($C_{18}H_{35}$-NH_2) (Figure 3.2b). The advantage is that the NPs are coated with hydrophobic ligands suitable for assembling by Van der Walls interactions, so it is easier to form a Langmuir film (*vide infra*). We combine the two methods, i.e., starting by citrate capped Au NPs then substituted with oleylamine in order to benefit of the two advantages.[164–166]

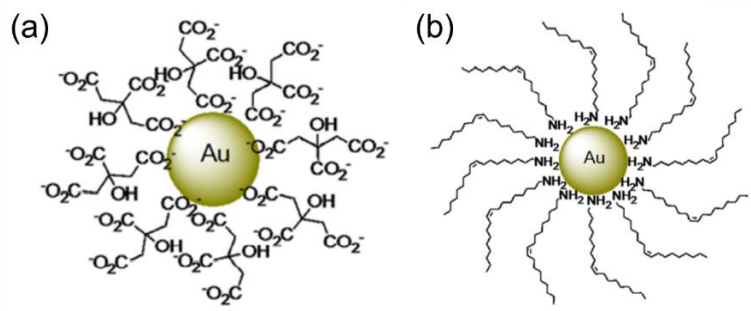

Figure 3.2. (a) citrate capped AuNP and (b) oleylamine capped AuNP

- **Synthesis of 8 nm oleylamine-coated AuNPs**

In a flask, 1 mL of trihydrated tetrachloroauric acid ($HAuCl_4.3H_2O$, 1%) is added to 79 mL of H_2O. We add quickly 20 mL of a reducer solution (4 mL of the trisodium salt of citric acid (1%) with 80 µL of tannic acid 1% in 16 mL of H_2O) under stirring at 60 °C. After boiling for 10 minutes and cooling down to room temperature, we obtained a solution containing citrate-AuNPs.[167] Then, this 100 mL of citrate-AuNPs solution is extracted with 20 mL of hexane containing 0.2 mL of oleylamine. After vigorous stirring, in a separatory funnel, the organic phase is isolated and washed twice with electrodeionized water (EDI). The dark red suspension is distributed in centrifuge tubes and then added with 50 to 70% ethanol until agglomeration begins (shift into purple). After centrifugation at 7000 rpm for 5 min, the precipitate was washed with absolute ethanol and then redispersed in hexane. The washing of the NPs by precipitation with ethanol then redispersion in hexane was repeated twice in order to eliminate the traces of

excess oleylamine and citrate. The NPs suspension is stable in hexane or toluene. It is stored in the refrigerator.

- **Langmuir film**

In order to obtain a film of NPs, we must form a network of this solution at the surface of a solvent, non-miscible and non-volatile and with a higher density than the solution of the NPs. H_2O and ethylene glycol meet these criteria but we have obtained better quality films with ethylene glycol. We use the Santhanam method[168] to form a Langmuir film. In a crystallizer, we put a pierced Teflon petri dish (hole diameter: 2 cm) upside down. We add ethylene glycol (EG) until we form a meniscus on the hole and then we spread some drops of the solution of NPs. We protect the assembly by covering with a crystallizer and wait around 10 minutes that the solvent evaporates and the film is self-organized on the EG surface (Figure 3.3).

Figure 3.3. Picture of the spontaneous film of gold nanoparticles at the surface of ethylene glycol

Once the film is formed, we use a polydimethylsiloxane (PDMS) stamp to collect it and print it on the surface of the SiO_2/electrode substrate, following the Langmuir–Schaefer technique.[169] We delicately put the PDMS stamp at the surface of the meniscus, dry the stamp under nitrogen flow and we recover the SiO_2/electrode substrate with this modified stamp. We take it out after a few seconds to be sure it is well printed and we rinsed quickly with ethanol the new functionalized substrate. The film peels off easily from the PDMS tab. Then, we check the homogeneity and organization of the film by scanning electron microscopy (SEM, Figure 3.4, annexe A3.2).

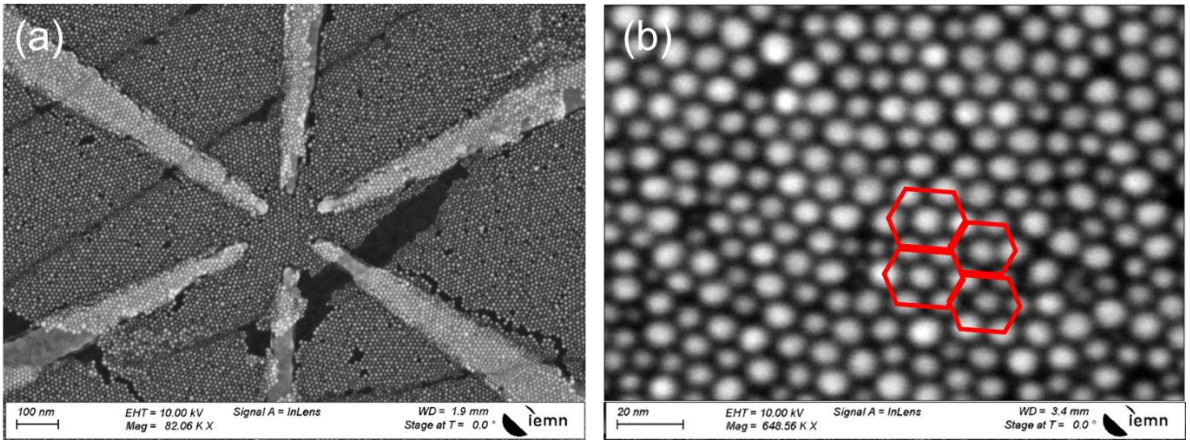

Figure 3.4. SEM images of NPSAN with oleylamine (a) with the six electrodes and (b) large image enlargement with hexagonal arrangement (in red)

Figure 4 shows the SEM images of the NPSAN with the six electrodes and a zoom of the NPs. We observe a monolayer with mainly a hexagonal arrangement of the NPs and an almost homogeneous size of NPs. The zoom image is treated with ImageJ[170] (Annexe A3.2) to give us statistical data on the NP sizes and inter NP distances.

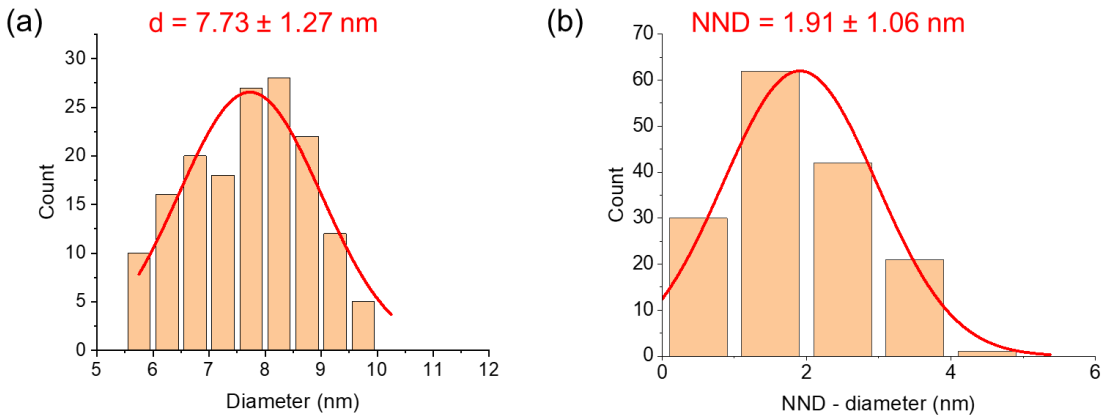

Figure 3.5. 1D histogram of (a) diameter of NPs and (b) Nearest Neighbor distance for oleylamine NPSAN. The solid red lines are the fits by a Gaussian distribution with the mean value ± standard deviation indicated in the panels.

Figure 3.5a shows the distribution of the diameter of the NPs, the mean diameter is around 8 nm as expected due to the initial condition.[161,165] The spacing between two neighbour NPs, i.e. the nearest neighbour distance is around 19 Å. The length of the oleylamine is ~20 Å.[171] It means the ligands are strongly interdigitated. These parameters will help us to know if the exchange of ligands went well.

b) Exchange of ligands

We process to the exchange of ligands by POMs using $(H^+)_3\,[PMo_{12}O_{40}]^{3-}$ (Figure 3.6a), short name $HPMo_{12}$ and $(TBA^+)_3[PW_{11}O_{40}(SiC_3H_6SH)_2]^{3-}$ (Figure 3.6b), short name $TBAPW_{11}SH$. These two POMs have been synthesized and characterized by the ePOM team and will not be developed here.[59,172] The processes of POM-decorated nanoparticles are already known in the literature.[173] We choose $HPMo_{12}$ because of its affinity with gold surface[174] and $TBAPW_{11}SH$ because the thiolate group forms covalent bond with Au, destabilizes the amine and avoids reduction of the POM.[175,176]

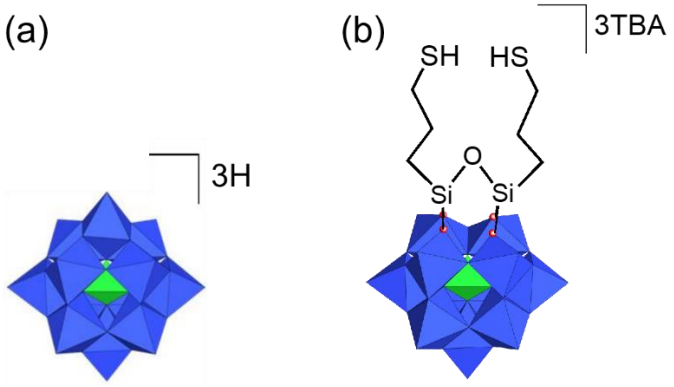

Figure 3.6. Keggin structure (a) $(H^+)_3\,[PMo_{12}O_{40}]^{3-}$ and (b) $(TBA^+)_3\,[PW_{11}O_{40}(SiC_3H_6SH)_2]^{3-}$

- **Exchange with $HPMo_{12}$**

We optimized the condition of exchange by immersing the predeposited film on the substrate (SiO_2/electrode for SEM images and Ge crystal for infrared analysis) for one hour in a solution of 10^{-3}M $HPMo_{12}$ in a mixture of EtOH/H_2O 50-50%. We rinse delicately with ethanol. Then, we characterized the film by FTIR in the attenuated total reflection (ATR) configuration (Annexe A3.2).

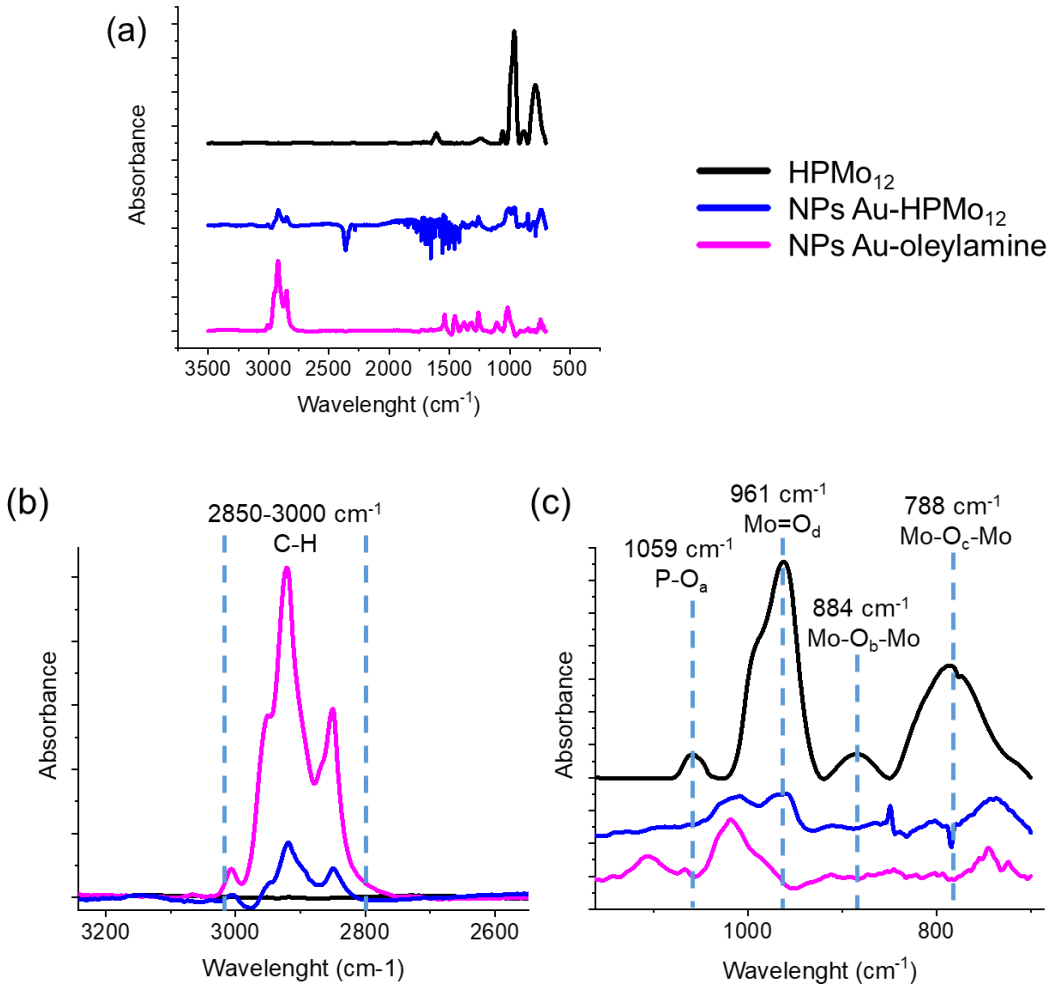

Figure 3.7. IR spectra measured on germanium ATR crystal (a) full spectra, (b) and (c) zoom on the bands of the C-H region and PMo_{12} region, respectively.

50 scans were accumulated from 700 to 3500 cm^{-1} using a crystal of germanium. We use a germanium crystal because its limit of detection is around 700 cm^{-1} instead of 1500 cm^{-1} for the silicon one. To obtain a reference spectrum, we have directly deposited the $HPMo_{12}$ powder on the crystal (using ethanol to stick it) and also the NPSAN using the same protocol as the deposition on SiO_2. Another advantage of this Ge ATR crystal is its large dimension (few cm), so that we can deposit all along the NPSANs and increase the signal due to multi-reflexion without deposit multilayers due to a large number of internal reflections. Figure 3.7a shows the spectra for NPSANs deposited on the ATR Ge crystal for the oleylamine NPSAN before and after exchange with $HPMo_{12}$, as well as a reference spectrum for the $HPMo_{12}$ powder. Figure 3.7b puts in evidence the peak of oleylamines, with the signal of the C-H stretching vibrations from 2850-3000 cm^{-1}.[177] The intensity of the signal clearly decreases after the POM exchange

indicating a partial exchange of the oleylamines by the POMs. From the reference spectrum, the POM is characterized by four peaks (black curve, Figure 3.7c). At 1059 cm^{-1}, the band is related to the stretching of the P-O_a bonds and the bands at 961, 884 and 788 cm^{-1}, respectively assigned to the Mo=O_d, Mo-O_b-Mo and Mo-O_c-Mo stretching modes *(O_a is the central oxygen; O_d is the terminal oxygen of the POM Keggin; O_b is the bridging oxygen that links two corner-sharing octahedra; O_c is the bridging oxygen that links two edge-sharing octahedra*).[122] Detecting a signal from a monolayer is not simple because the quantity of matter is low compared to the powder. We just see the apparition of one of these four peaks for the NPs Au-$HPMo_{12}$, the more intense one at 961 cm^{-1}, which is not present in the oleylamine NPSAN. These three spectra let us suppose that there is a partial exchange between the two ligands.

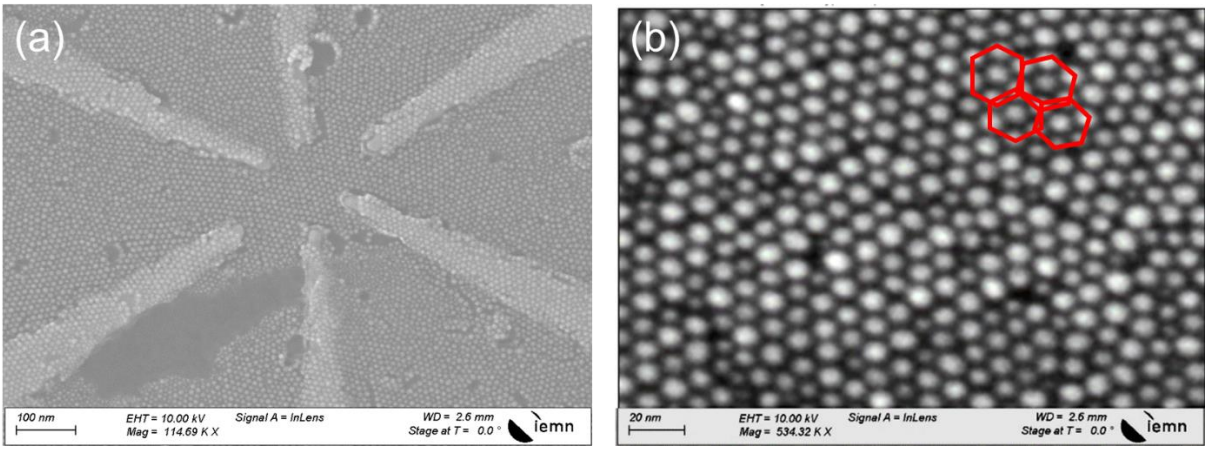

Figure 3.8. SEM images after exchange of ligands by $HPMo_{12}$ (a) NPSAN with the six electrodes (b) large image enlargement with hexagonal arrangement (in red)

From the SEM images (Figure 3.8), the organization in the film of NPs looks not disturbed by the exchange. As previously, the image was analysed with ImageJ.[170]

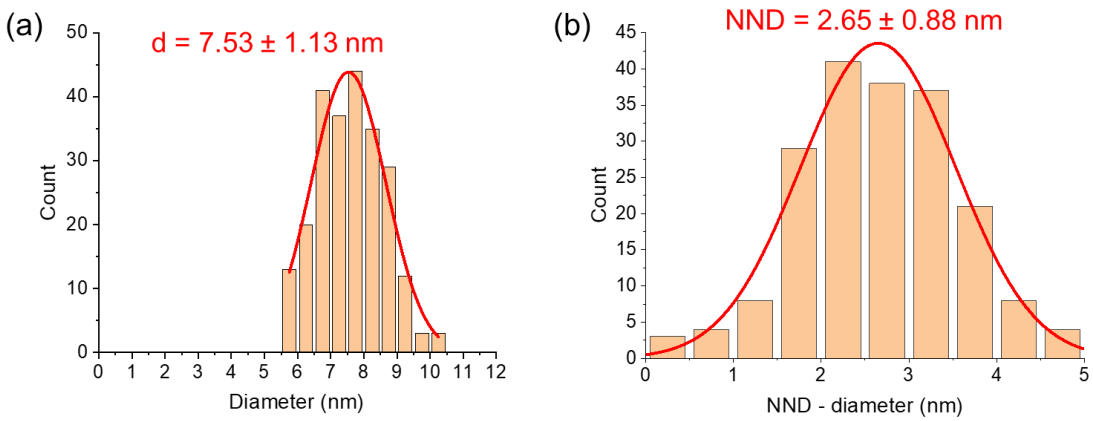

Figure 3.9. 1D histogram of (a) diameter of NPs and (b) Nearest Neighbor distance for $HPMo_{12}$ NPSAN. The solid red lines are the fits by a Gaussian distribution with the mean value ± standard deviation indicated in the panels.

The size of the NP did not change (~ 8 nm, Figure 3.9a) and the NND is a little bit higher, from 19 to 27 Å (Figure 3.9b). The size of $HPMo_{12}$ (ca. 1 nm in diameter) is smaller than the size of oleylamines (2 nm in length), but unlike oleylamine, $HPMo_{12}$ molecules cannot be interdigitated. The NND is close to the size of two-three POMs in average.

- **Exchange with $TBAPW_{11}SH$**

To exchange the oleylamine ligands with this thiolate POM (thiol-ligand exchange already demonstrated elsewhere[178,179]), we immerse the functionalized substrate (SiO_2/electrode for SEM images and Au for infrared) in a 10^{-3} M solution of $TBAPW_{11}SH$ in acetonitrile during 5-10 minutes. Then, we rinse quickly with acetonitrile. We have first characterized the film by FTIR in specular reflexion (Annexe A3.2).

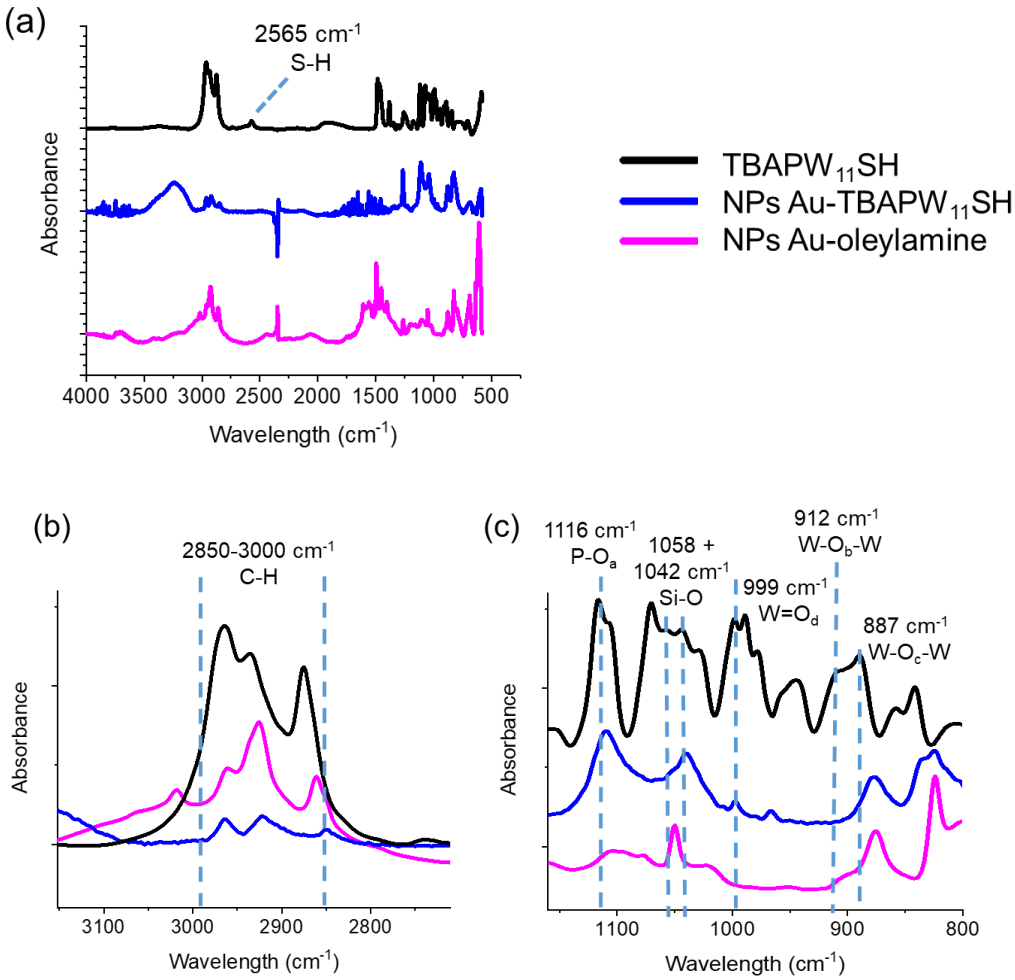

Figure 3.10. IR spectra done in specular reflexion (a) full spectra, (b) and (c) zoom on the peak of the C-H region and PMo_{12} region, respectively.

Here, we use specular reflexion mode because we have succeeded in having enough IR signal with the monolayer and to avoid the use of germanium crystal, hard to clean and expensive. The FTIR spectrum of $TBAPW_{11}SH$ powder (stick with ACN on Au surface) has many peaks with one signal at 2564 cm^{-1}, due to the S-H bond (Figure 3.10a). We see that the signals of the C-H stretching vibrations of the TBA are mixed with the ones of oleylamine from 2850 to 3000 cm^{-1} (Figure 3.10b). By consequence, we cannot use these signals to detect if the exchange of ligand has been successful. From 850 to 1150 cm^{-1}, we see six bands on the reference spectrum for $TBAPW_{11}SH$, assigned to the P-O_a, W=O_d, W-O_b-Wand W-O_c-W vibrations and two related to the Si-O bonds (Figure 3.10c).[180] New peaks appear after the exchange of ligands around 1000 cm^{-1}, at the same wavenumbers as some bands of the POM (~ 999 and 1116 cm^{-1}, blue line Figure 3.10c). We can do the hypothesis that there is a partial exchange.

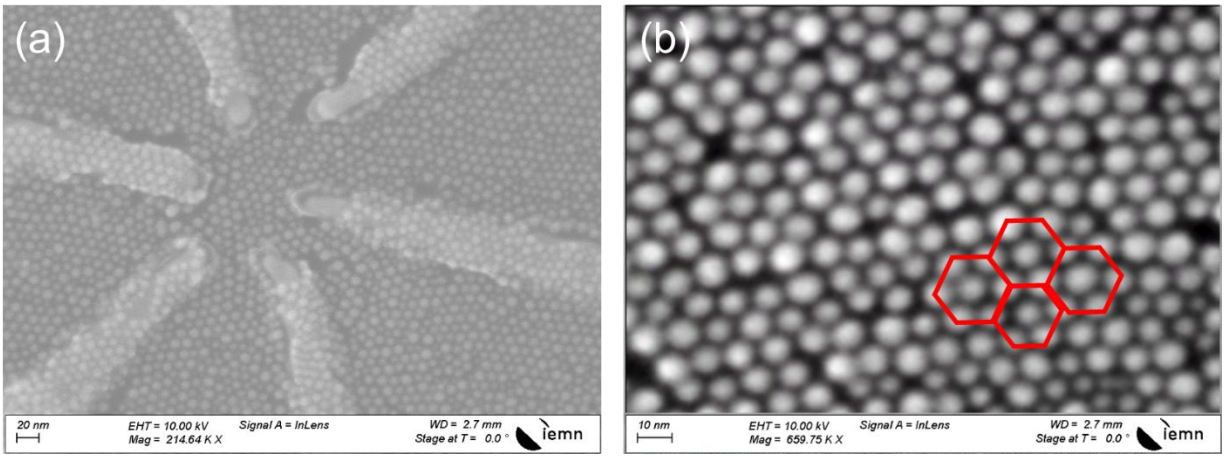

Figure 3.11. SEM images after exchange of ligands by TBAPW_{11}SH (a) NPSAN with the six electrodes (b) large image enlargement with hexagonal arrangement (in red)

From the SEM images (Figure 3.11), the organization of the NPs looks stable after the exchange as well; we still see some hexagonal arrangement. Figure 3.11b was analysed by ImageJ:[170]

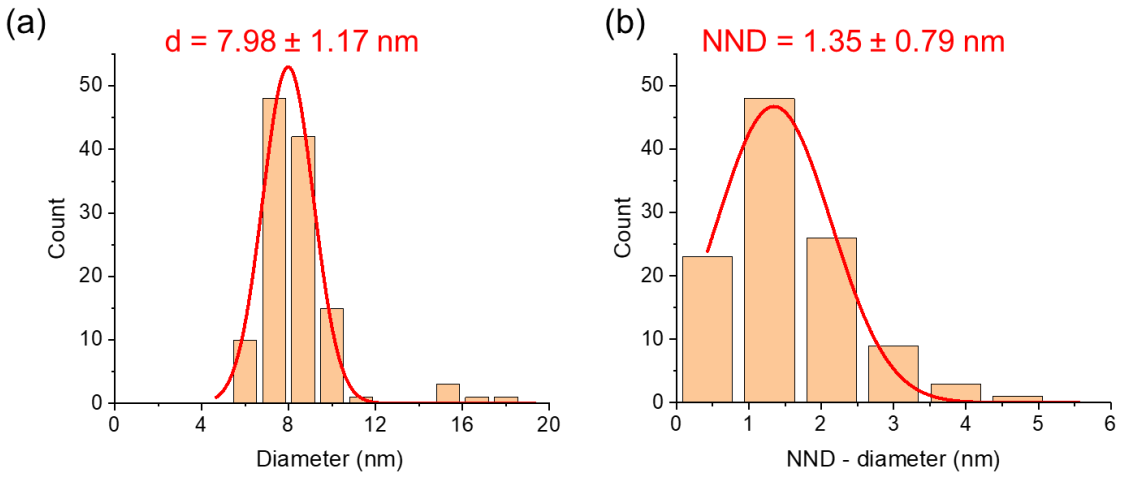

Figure 3.12. 1D histogram of (a) diameter of NPs and (b) Nearest Neighbor distance for TBAPW_{11}SH NPSAN. The solid red lines are the fits by a Gaussian distribution with the mean value ± standard deviation indicated in the panels.

From the image analysis (Figure 3.12), the mean diameter is still around 8 nm and the distances between two NPs slightly decrease (from 19 to 14 Å). This POM is covalently bonded to the Au NP thanks to the thiol group and no interdigitation is possible. Its diameter is ~ 1nm, the NND is close to the size of one POM.

c) Reduction of the POMs

Once the exchange of the POMs was done, we tried to reduce in situ these POMs. The NPSANs with $HPMo_{12}$ are reduced during 3-4 hours under UV light (same condition than in Chapter-II, see annexe A2.4) in solution with ethanolamine (some drops of acetonitrile are added until the solution do not be viscous anymore) because of the POMs solubility in ethanol. The NPSANs with $TBAPW_{11}SH$ are also reduced during 3-4 hours under UV light but in solution with degassed ethanol in glovebox. Once the irradiation is done, NPSANs are quickly rinsed with acetonitrile and ethanol respectively and dried under nitrogen flow. We check by SEM images taken before and after reduction if the networks have been disorganized or damaged.

- **$HPMo_{12}$ reduction**

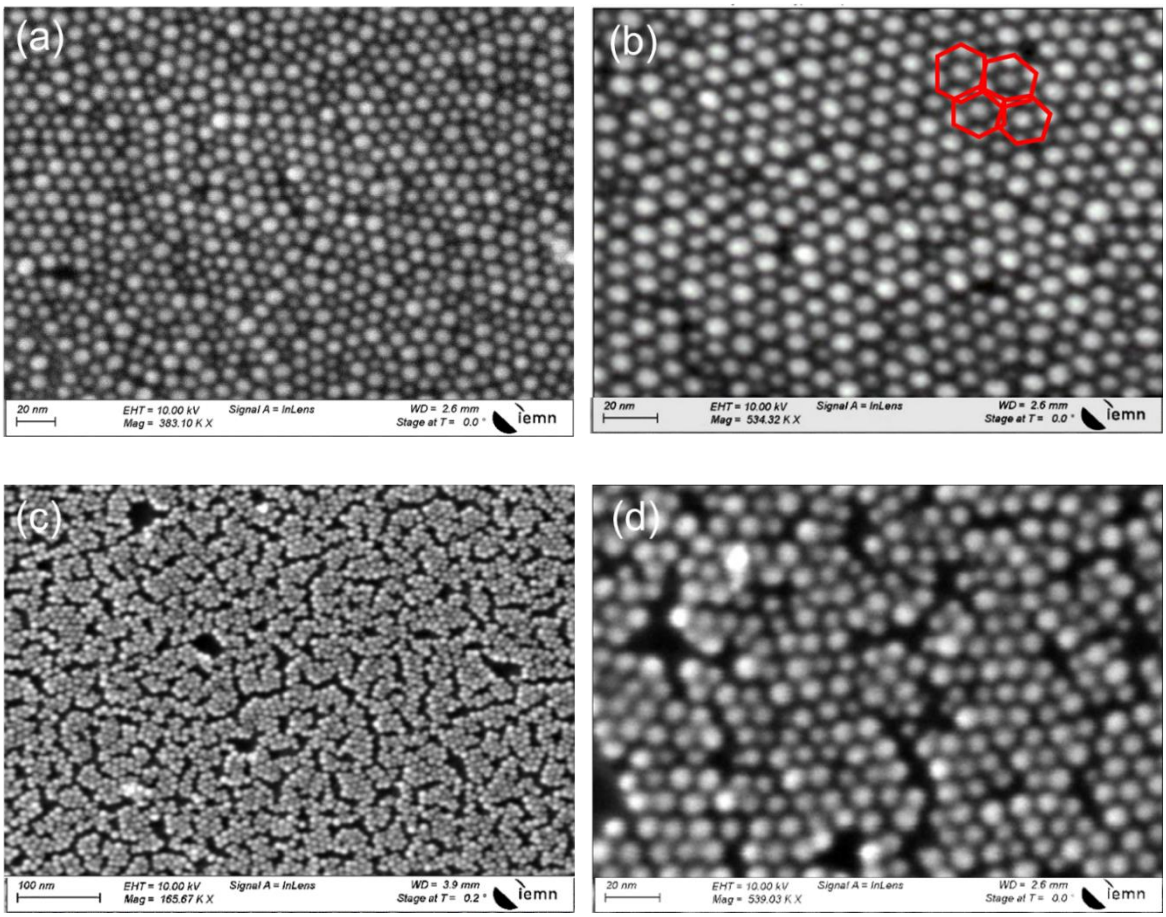

Figure 3.13. SEM images (a-b) before and after (c-d) irradiation of $HPMo_{12}$. Note that (a) and (c) are not at the same magnification

From the Figure 3.13, we see that the organization of NPs in the network was modified after irradiation, with areas where the NPs are closer to each other, leaving some holes on the surface. On the zoom image (Figure 3.13d), we notice that the NPs arrangement is no longer hexagonal. Nevertheless, no agglomerates seem to be appearing, individual NPs are still clearly distinguishable. We confirm these suppositions by the analysis with ImageJ.

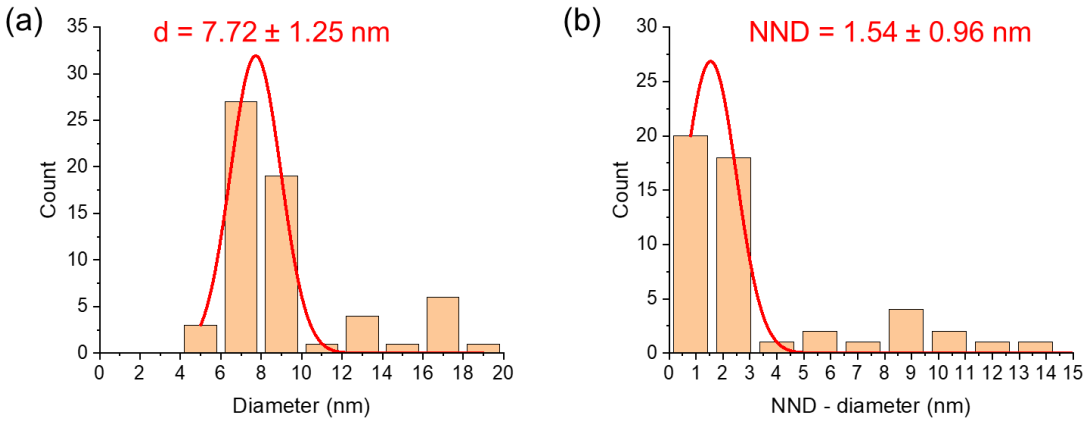

Figure 3.14. 1D histogram of (a) diameter of NPs and (b) Nearest Neighbor distance for irradiated $HPMo_{12}$ NPSAN. The solid red lines are the fits by a Gaussian distribution with the mean value ± standard deviation indicated in the panels.

The diameter of the NP is still around 8 nm (Figure 3.14a). Nevertheless, we observe a bigger dispersion until 20 nm, letting us suppose that some NPs are aggregated. The NND has passed from 26 to 15 Å (Figure 3.14b). We also see a bigger dispersion with distance between two NPs reaching 14 nm. We can conclude that the surface has been modified, maybe due to a side effect of the solvent, but we still observe some NPs surrounded by the reduced POMs.

- **$TBAPW_{11}SH$ reduction**

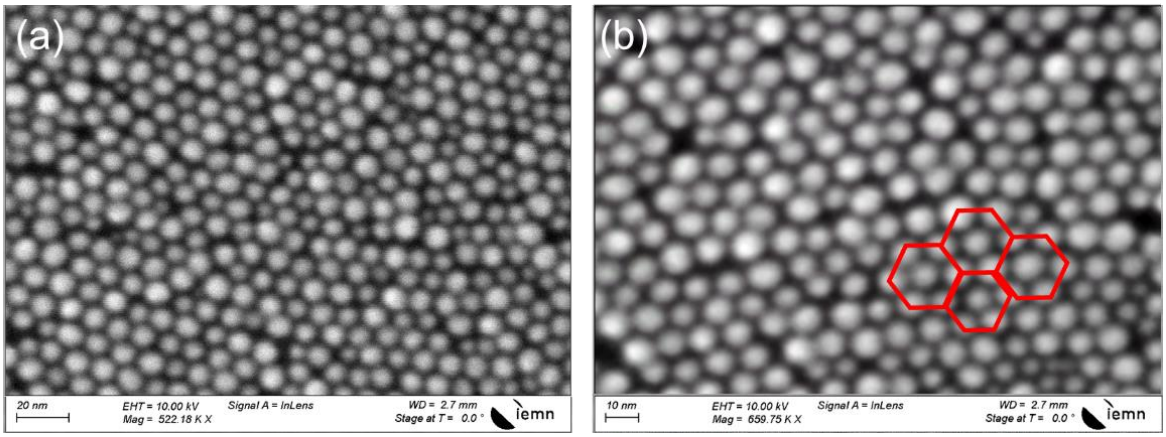

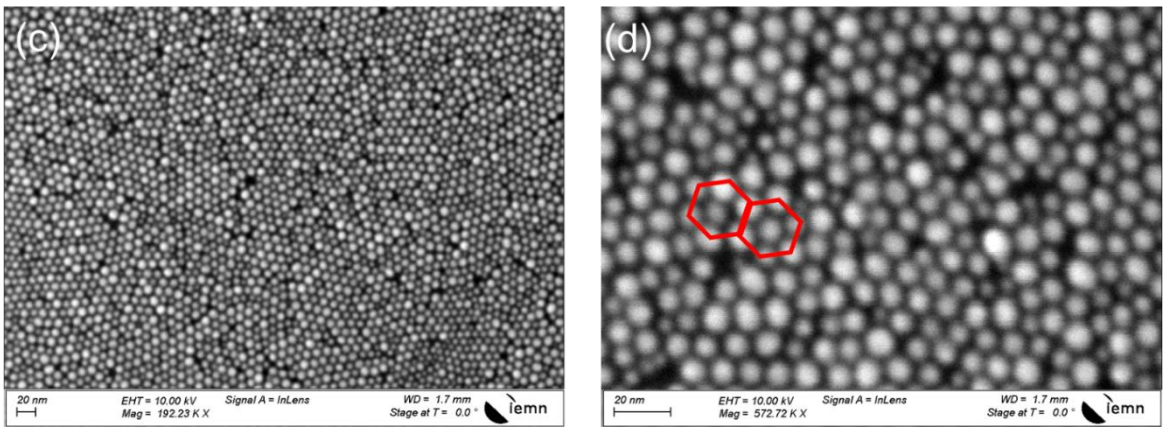

Figure 3.15. SEM images (a-b) before and (c-d) after irradiation of TBAPW$_{11}$SH. Note that (a) and (c) are not at the same magnification.

The comparison of the SEM images (Figure 3.15) shows that the network looks to be intact after reduction of the POMs. We still have a film with one monolayer. On the zoomed image (Figure 3.15d), we still see some hexagonal arrangements.

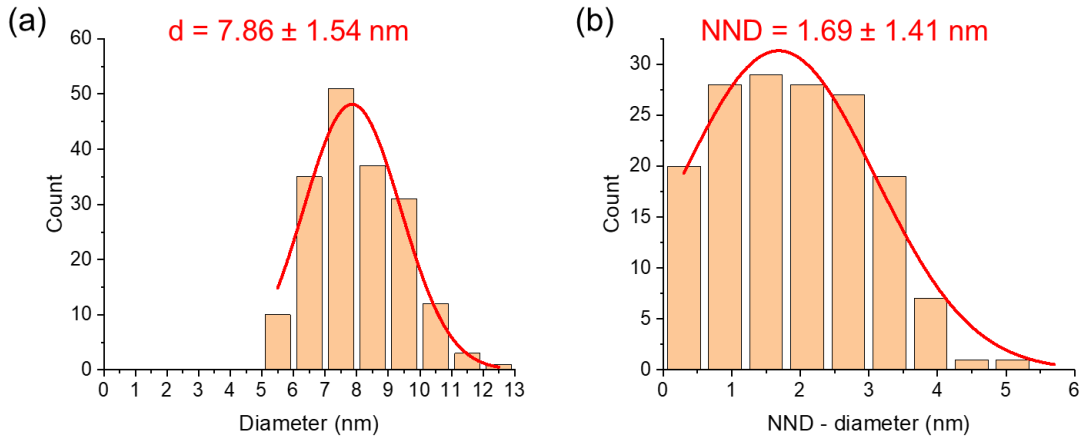

Figure 3.16. 1D histogram of (a) diameter of NPs and (b) Nearest Neighbor distance for irradiated TBAPW$_{11}$SH NPSAN. The solid red lines are the fits by a Gaussian distribution with the mean value ± standard deviation indicated in the panels.

After analysing the image in Figure 3.15d, we obtain a diameter ~ 8 nm with no important dispersion (Figure 3.16a), the NPs are intact. Concerning the distance between two neighbour particles, it passes from 14 to 17 Å after irradiation (Figure 3.16b). This slight increase is negligible (compared to the data dispersion); the manipulation did not modify the organization of the network.

To conclude, we have fabricated NPSANs with oleylamine, POMs and reduced POMs. We did not observe the same NND or modification of the network with the two POMs probably because $HPMo_{12}$ is electrostatically inserted between the NPs whereas $TBAPW_{11}SH$ is covalently bonded to Au. At this monolayer scale, it is not obvious to surely conclude that there is an exchange and reduction of the ligands. However, the FTIR spectra and the change of the distance between two nearest neighbour AuNP let us suppose that a partial exchange happened. The reduction of a POM by in situ irradiation has already been demonstrated in Chapter2-IId and will be strengthened by the electrical measurement in the next part. Indeed, all these samples have been studied and electronically characterized. The goal is to study the dynamic behaviours of ET in these NPSANs.

II. Electron transport dynamics of the NPSANs

a) IV measurements

We first evaluate the static ET behaviour of the NPSANs, recording the classic dc current versus voltage, IV measurements (Keysight B2901A SMU source/measure unit device, Annexe A3.3). The sample is placed in a glovebox, connected with a probe station and around 10 IVs from 0 to 1 V are acquired by randomly selecting 2 electrodes out of the six electrodes in the pattern. We have decided to stay at low voltages because of the instability of the NPSANs with the POMs when submitted to higher voltages (annexe A3.4).

- **NPSAN with $HPMo_{12}$**

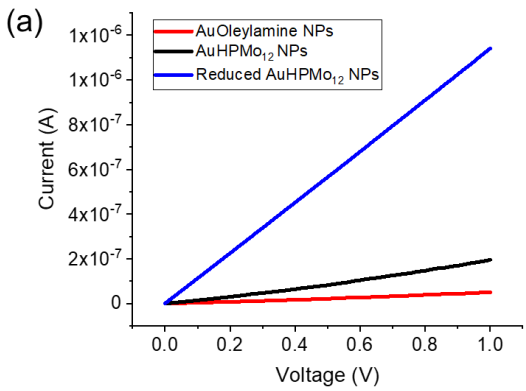

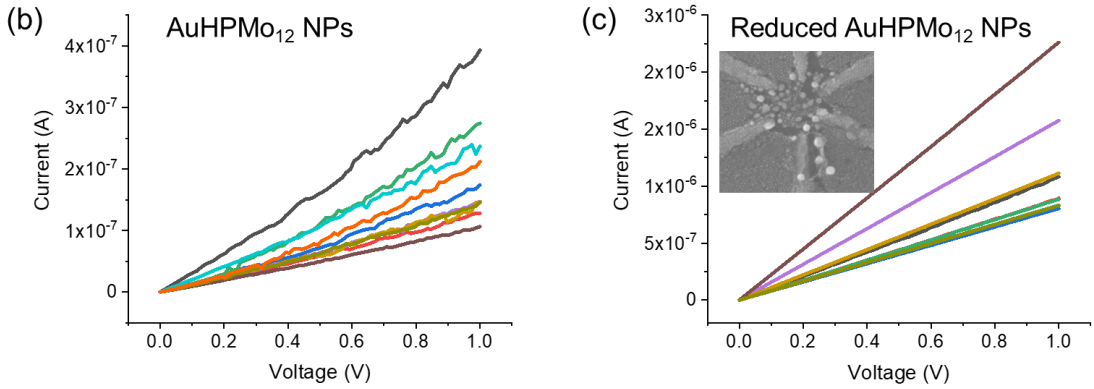

Figure 3.17. (a) Mean IV curves of NPSAN with oleylamine, $HPMo_{12}$ and reduced $HPMo_{12}$, (b) 10 IV curves of the pattern with $HPMo_{12}$ and (c)10 IV curves of the pattern with reduced $HPMo_{12}$. Inset: control SEM image taken at the end of the electrical measurements.

Figure 3.17a illustrates the mean IV curves of the same NPSAN pattern for the three cases (oleylamine, POM and reduced POM). First, we see an increase of the current (factor ~ 4) after the substitution of the oleylamine ligands by the POMs. This information also reinforces the previous conclusion that the substitution went well, since the conductance of PMo_{12} is larger than long alkyl chains (see Ch. 2-II). When the POM is reduced, the mean current increases by about 10, as also observed in SAM junctions (Ch. 2-IIc). Figure 3.17b shows the dispersion of the 10 measured IV curves for the $HPMo_{12}$ NPSANs, the currents vary from $1x10^{-7}$ A to $4x10^{-7}$ A at 1V approximately. This variability is sought after in the field of reservoir computing (Chapter 1-III). After UV irradiation, where the POMs are supposed to be reduced, the currents vary from $5x10^{-7}$ A to $3x10^{-6}$ A at 1V approximately (Figure 3.17c). Nevertheless, after measurement, a control SEM image was done, revealing that the network was strongly damaged (inset Figure 3.17c), so these NPSANs with reduced $HPMo_{12}$ POM were no longer electrically characterized.

- **NPSAN with $TBAPW_{11}SH$**

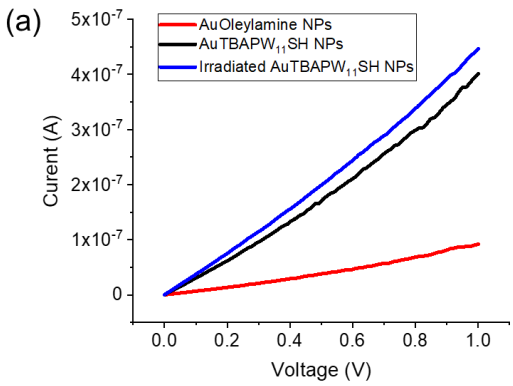

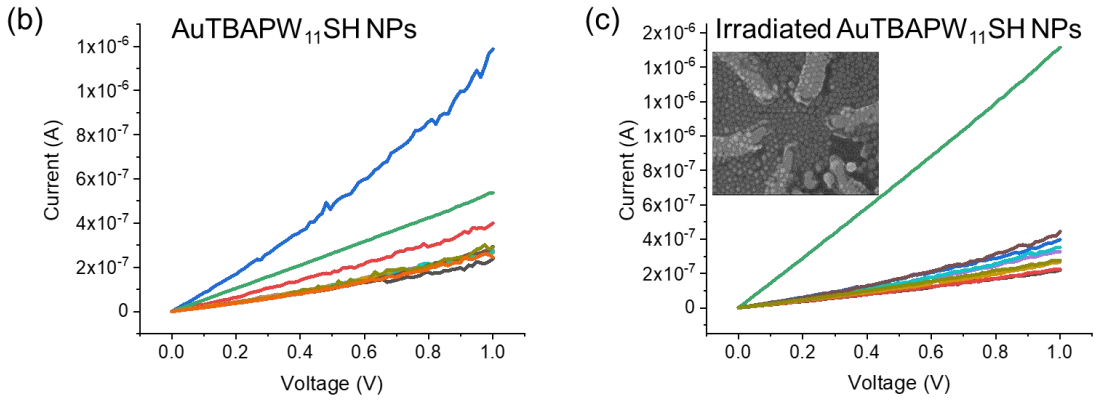

Figure 3.18. (a) Mean IV curves of NPSAN with oleylamine, $TBAPW_{11}SH$ and irradiated $TBAPW_{11}SH$, (b) 10 IV curves of the pattern with $TBAPW_{11}SH$ and (c) 10 IV curves of the pattern with reduced $TBAPW_{11}SH$. Inset: control SEM image taken at the end of the electrical measurements.

The same series of IV measurements were performed on the $TBAPW_{11}SH$ NPSAN. With the $TBAPW_{11}SH$ ligands, we clearly see an increase of the mean current by a factor ~ 4 compared to oleylamine NPSAN (Figure 3.18a). After irradiation, the change of level of mean current is weak (factor 1.1, Figure 3.18a). At +1V, the currents vary between $2x10^{-7}$ and $1x10^{-6}$ A with the pristine POM (Figure 3.18b). We observe the same range of currents once the POMs are UV irradiated, leaving us in doubt about the reduction (Figure 3.18c). After these electrical measurements, the control SEM image (Figure 3.18c) shows that the network inside the electrodes is still intact (the green curve corresponds to the measure between the two exterior electrodes, where the morphology is little damaged).

b) Noise measurements

Recently, origins of the current fluctuations in molecular junctions have started to be studied. More precisely, several studies on electronic noise spectroscopy have been reported in the last decade (see review in Ref. 181). They can provide important information about hidden dynamic electronic phenomena, which are undetectable in conventional DC current-voltage measurements.[181] The charge transport properties in molecular junctions can be perturbed by noise from many external and internal interference sources. For the internal noise, the current in electronic devices can be written as $I(t) = \langle I \rangle + \delta I(t)$, where $\langle I \rangle$ is the mean current and $\delta I(t)$ is the current fluctuation. Typically, the noise is characterized in the frequency domain, which

is converted from the time domain measurements via Fourier transformation.[182] The power spectral density (PSD) of the current fluctuation is given by:

$$PSD(f) = \langle \delta I_{f,\Delta f}(t)^2 \rangle / \Delta f \tag{3.1}$$

where $\langle \delta I_{f,\Delta f}(t)^2 \rangle$ is the variance of a band-pass filtered time-dependent noise in a bandwidth (Δf) at frequency (f).[183] Here, we will focus on one type of internal noise: the flicker noise or 1/f noise (Figure 3.19b). In this case, PSD is proportional to $1/f^n$, with n close to 1, but possibly between 0.5 and 2 depending on the details of the physical origins of the current fluctuations. In materials and macroscopic solid-state devices, the number fluctuation (i.e. fluctuations of the number of charges carrying the electrical current) and the mobility fluctuation models are the main explanation of this noise. Briefly, number fluctuation is due to trapping/detrapping processes in materials and devices (e.g. by traps and defects)[182] and the mobility fluctuation is related to charge scattering by phonons, impurities for example.[184,185] In a molecular-scale junction, these phenomena translate into, respectively:

- Two-level conductance fluctuations (also known as RTS, random telegraph noise, Figure 3.19c) as observed by several groups in single molecule junctions[186–189] and attributed to dynamic rearrangements of the molecule-electrode bonds. In large area molecular junctions (i.e. SAMs), the coexistence of a large number of RTS events leads to 1/f noise as experimentally observed.[190,191]
- Fluctuations of the transit time through the molecular junctions, albeit in this latter case, this noise is likely to occur at high frequency given the short transit time in molecular junctions (< ns).[192]

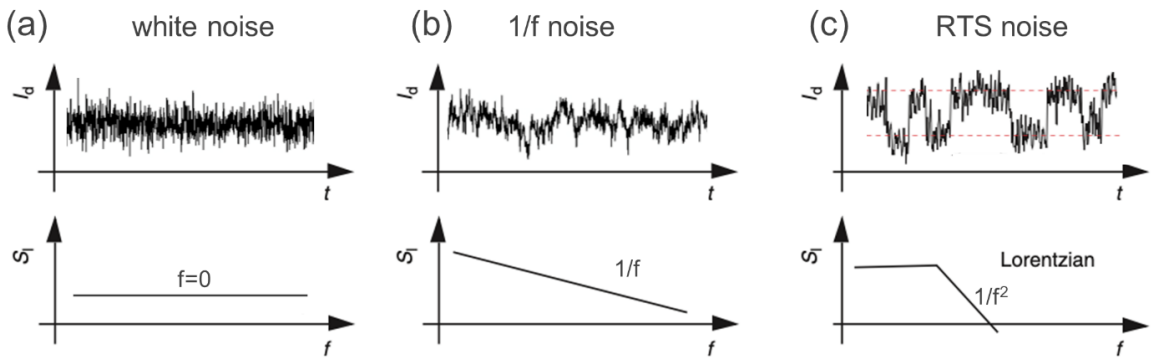

Figure 3.19. Graphic representation of (a) white (thermal) noise, (b) 1/f noise and (c) RTS noise. The upper panels show typical time fluctuations I(t) and the lower panels show the corresponding PSD vs. f behaviours.

In this part, we study the flicker noise in the NPSANs with oleylamine and with the two POMs. The objective is to observe any change in the dynamic ET behaviours (i.e. change in the value of the frequency exponent n) with the nature of the molecules and also if there is a difference before and after irradiation of $TBAPW_{11}SH$.

The noise measurements were performed on the same NPSAN for all the configurations (oleylamine, POMs and reduced POMs). To process to the PSD measurements, we apply a DC voltage (from 0 to 1V) on one electrode and we measure the current on two others in parallel (electrodes #2 and #3) and we accumulate 50 scans from 1 to 100 Hz (Figure 3.20, more detailed annexe A3.3). We plot PSD vs. f in a log-log scale and we determined the slope that represents n (from f^n). At a given frequency, we also plot PSD vs. DC current I in a log-log scale to check if the PSD is proportional to I^2 as expected from the number fluctuation and mobility fluctuation models (*vide supra*), albeit proportionality to (dI/dV) and $(dI/dV)^2$ was sometime also observed in molecular junctions.[188,190]

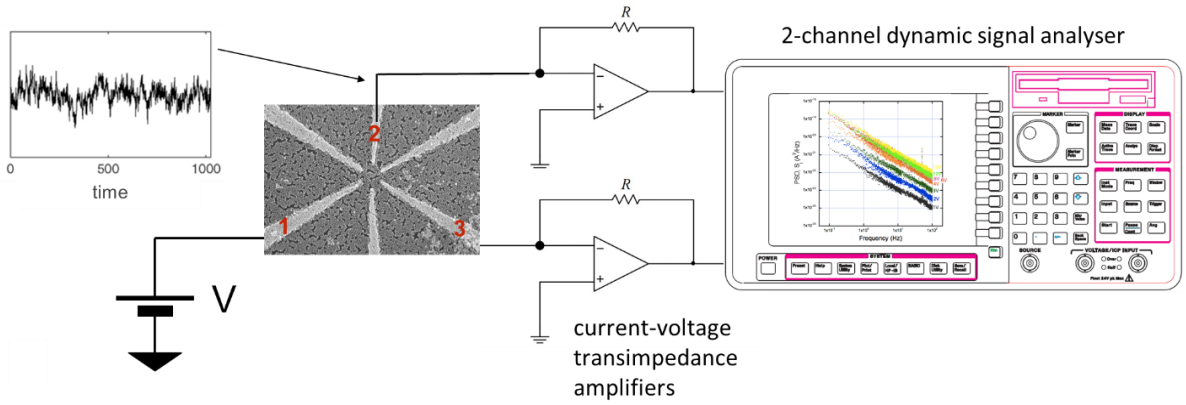

Figure 3.20. 1/f noise setup

- **Au-oleylamine NPs**

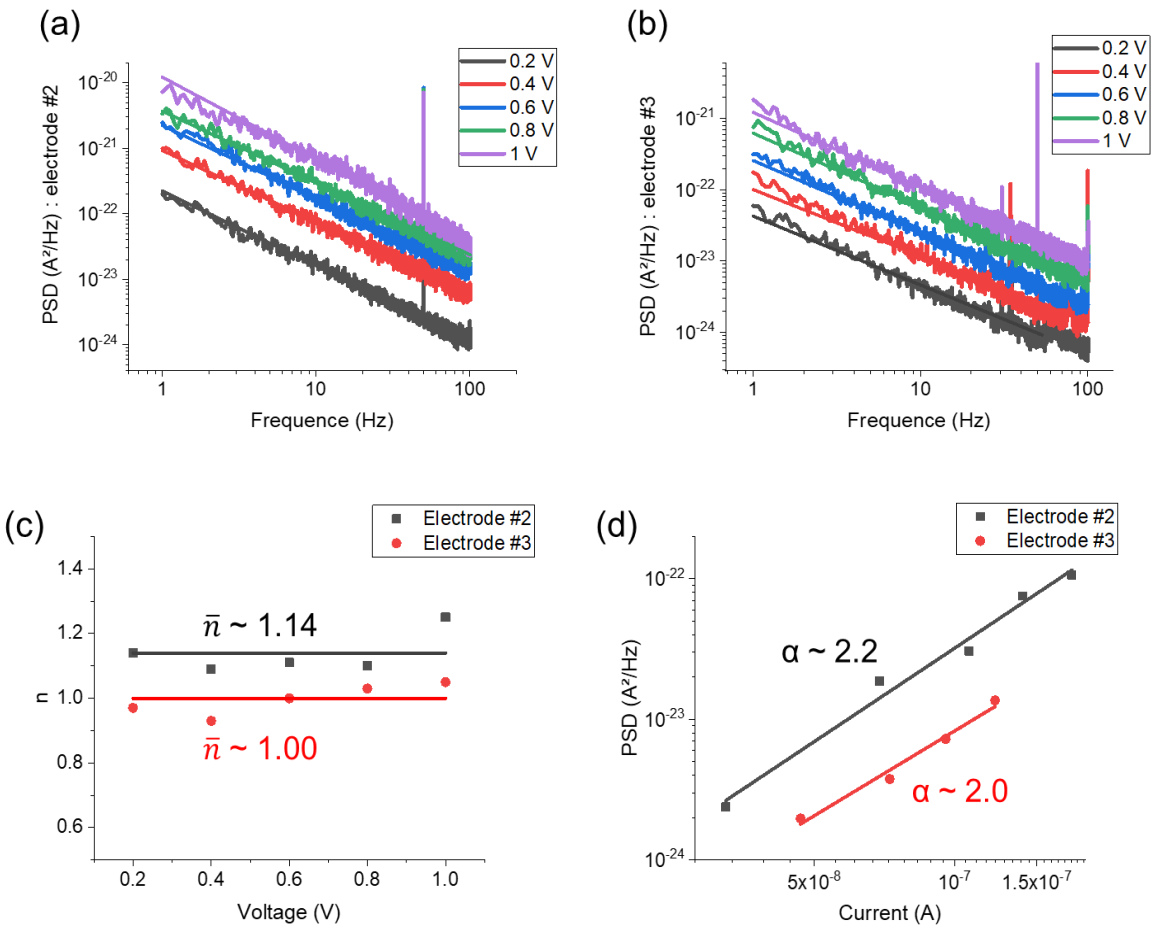

Figure 3.21. Graph of PSD at different voltages versus frequency for (a) electrode #2 and (b) electrode #3, (c) graph of the frequency exponent at each voltage with $\bar{n}$ the mean value of n and (d) graph of PSD (at 30 Hz) versus DC current for NPSAN with oleylamines

Figure 3.21a and b show the log-log plot of the PSD vs. frequency measured at different DC voltages for two electrodes. The $1/f^n$ curves have the same frequency exponent with a mean value n around n 1.1 (black symbols) and n 1.0 (red symbols) (Figure 3.21c)). Figure 3.21d shows that the PSD is almost proportional to I^2. An exponent close to 1 and a proportionality to I^2 is expected for a long alkyl chain, as also observed with alkythiols[193] and measured in wider voltage range (until 13 V) for this molecule and octanethiol (see annexe A3.5).

- **Au-HPMo$_{12}$ NPs**

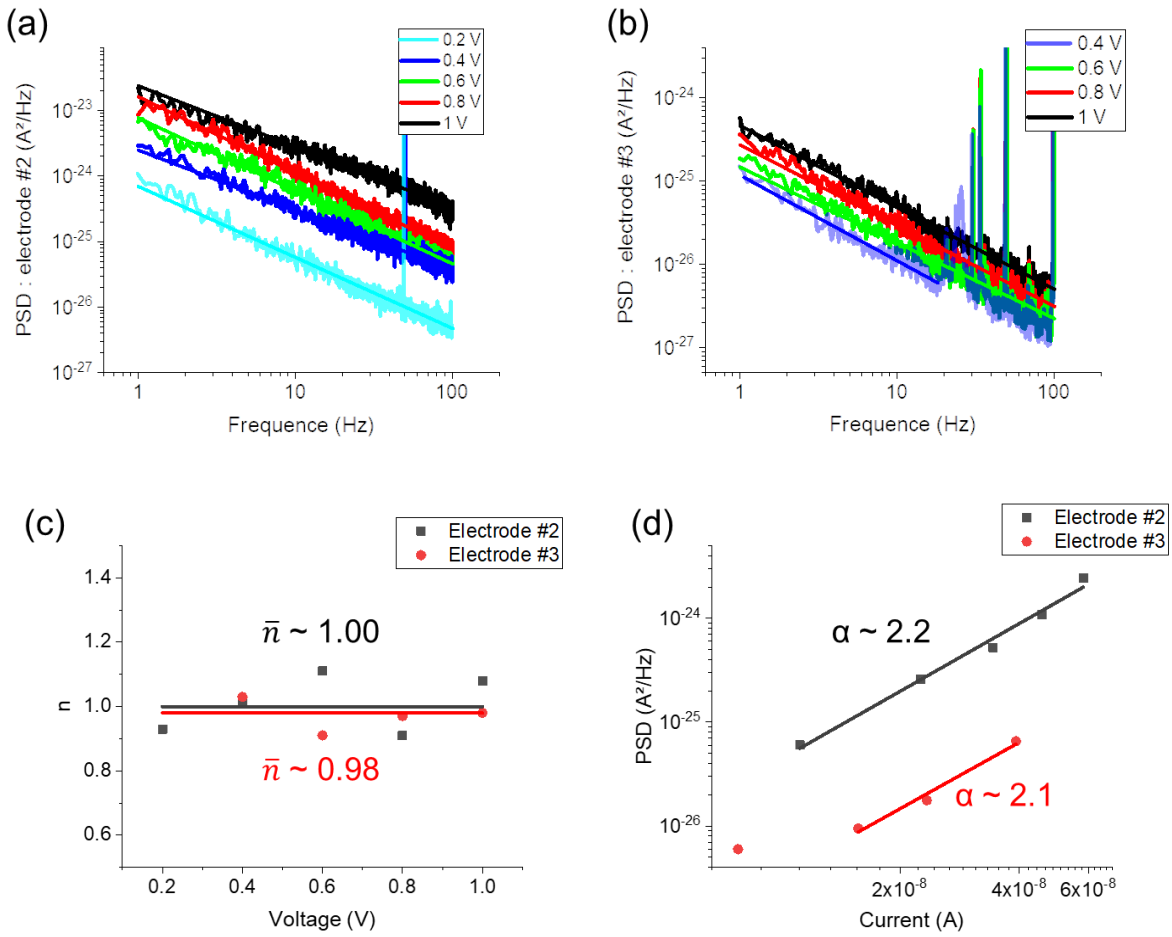

Figure 3.22. Graph of PSD at different voltages versus frequency for (a) electrode #2 and (b) electrode #3, (c) graph of the frequency exponent at each voltage with $\bar{n}$ the mean value of n and (d) graph of PSD (at 40 Hz) versus DC current for NPSAN with HPMo$_{12}$ ligands

Figure 3.22a and b show the log-log plot of the PSD vs. frequency measured at different voltages for the NPSANs with HPMo$_{12}$ ligands. We start to see instability of the network at low voltage, which is why there is no graph at 0.2 V presented in Figure 3.22b. In this case, we observe a mean $\bar{n}$ value equals to 1 in both cases but with large variations (Figure 3.22c). It is likely due to instabilities in the NPSANs under the application of the voltage since the POMs inserted between the NPs are only physisorbed. Here, the PSD is also proportional to I^2 (Figure 3.22d).

- **Au-TBAPW$_{11}$SH NPs**

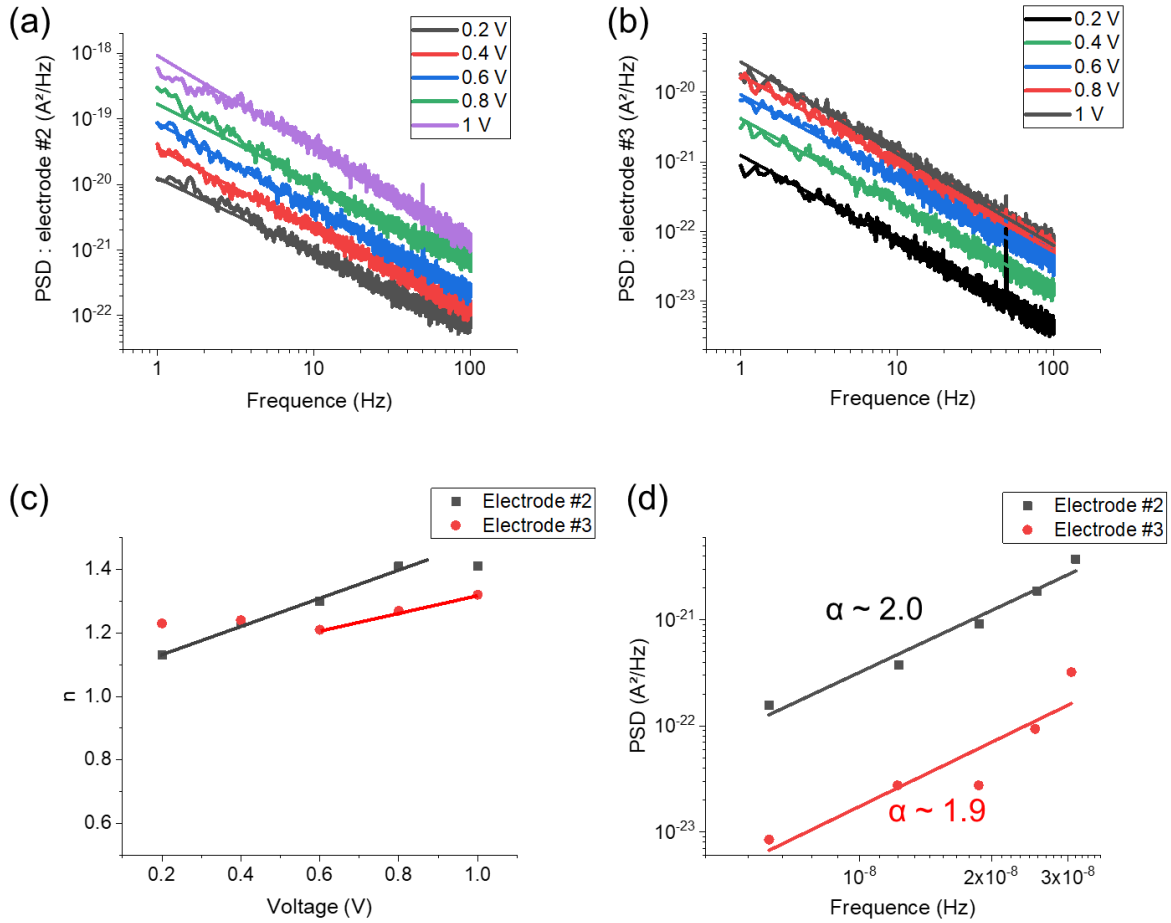

Figure 3.23. Graph of PSD at different voltages versus frequency for (a) electrode #2 and (b) electrode #3, (c) graph of the frequency exponent at each voltage ($\bar{n}$ value no pertinent here) and (d) graph of PSD (at 40 Hz) versus DC current for NPSAN with TBAPW$_{11}$SH ligands

Figure 3.23a and b show the log-log plot of PSD vs. frequency at different voltages with ligands TBAPW$_{11}$SH for the signals from two electrodes. In this case, the flicker noise $1/f^n$ depends on the voltage and we observe a slight increase of n with the voltage from 1.1 to 1.4 (Figure 3.23c). This behaviour is markedly different from the ones for NPSAN previously observed, with NPs functionalized by alkyl chains and HPMo$_{12}$, but similar to NPSANs with azobenzene derivatives (see Annexe A3.5). Here also, PSD is also almost proportional to I^2 (Figure 3.23d).

- **Irradiated Au-TBAPW$_{11}$SH NPs**

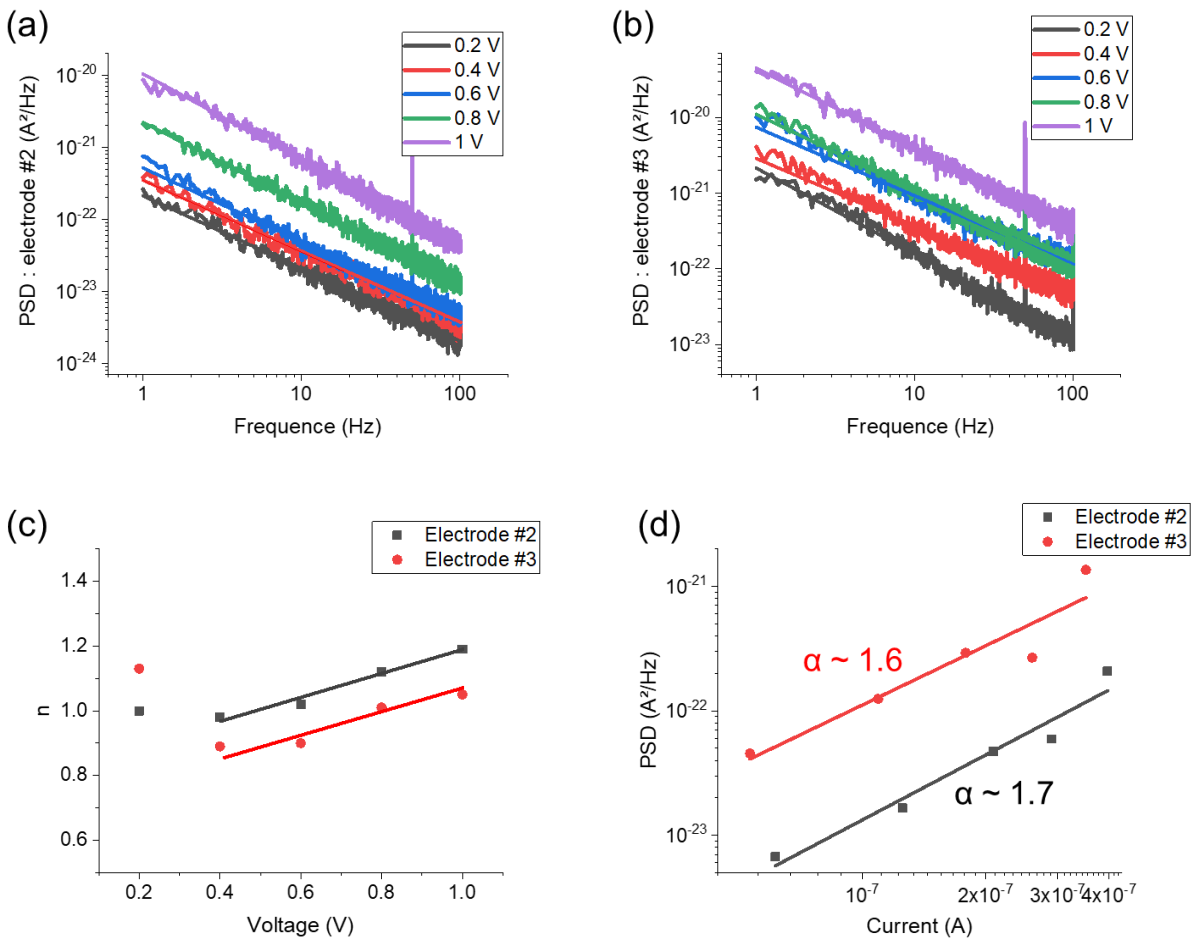

Figure 3.24. Graph of PSD at different voltages versus frequency for (a) electrode #2 and (b) electrode #3, (c) graph of the frequency exponent at each voltage ($\bar{n}$ value no pertinent here) and (d) graph of PSD (at 40 Hz) versus DC current for NPSAN with irradiated TBAPW$_{11}$SH ligands

Figure 3.24a and b show the PSD at different voltages with ligands TBAPW$_{11}$SH after UV irradiation for two electrodes. We do not observe the same slope as before irradiation but we still see a slight increase of n when V > 0.4 V from 0.9 to 1.2 this time (Figure 3.24c). Here also the flicker noise $1/f^n$ depends on the voltage, albeit the frequency exponent has decreased for the NPSANs with the irradiated POMs. PSD remains proportional to I^2 (Figure 3.24d).

- **Summary**

In summary, we observe a usual 1/f behaviour for NPSANs with alkyl chains i.e. the octanethiol and oleylamine ligands. For the $HPMo_{12}$ NPSANs, we also observe a n value constant around 1 but with lots of fluctuations in function of the voltage. Finally, we notice that n increase with the voltage for $TBAPW_{11}SH$ NPSANs, both with pristine and irradiated POM. Likely voltage or current are driven the fluctuations. The important difference between the POM NPSANs is the physisorption vs the chemisorption between Au NPs and POM. At this stage of this work, physical mechanisms remain to be identified.

c) High harmonic generation measurements

The measurement of High Harmonic Generation (HHG) is a tool for helping us to examine the dynamic behaviour of the ET in NPSANs when we apply sinusoidal signals instead of a DC voltage. In brief, we apply an input signal at one given frequency f and we recover an output signal that contains also signals at higher frequencies generated by nonlinearity and time fluctuations in the system. Those new signals are classified between:[194,195]

- harmonic generation: $f_i = nf$ with n integer, caused by nonlinearities in the transfer function of the devices
- interharmonic generation: $f_i = nf$ with n non-integer, caused by non-periodic changes in current and voltage (e.g. stochastic/random noise)
- inter-modulation distortion with two input signals (IMD) $f_n = a_1f_1+a_2f_2$, caused by nonlinearities or time variance in the device.

Here, the purpose is to observe if the complex nonlinearities and dynamics electron transport occurring inside the POM and NP network itself are modified when we pass from the pristine to reduced state. This phenomenon has already been seen by the team, using NPSAN with azobenzene derivatives when switched from *cis* to *trans* state,[109] as presented in Chapter1-IIIc. As the NPSAN with $HPMo_{12}$ is not stable when this one is reduced, we will present here the study of NPSAN with $TBAPW_{11}SH$ only (see Annexe A3.6 for the HHG of $HPMo_{12}$).

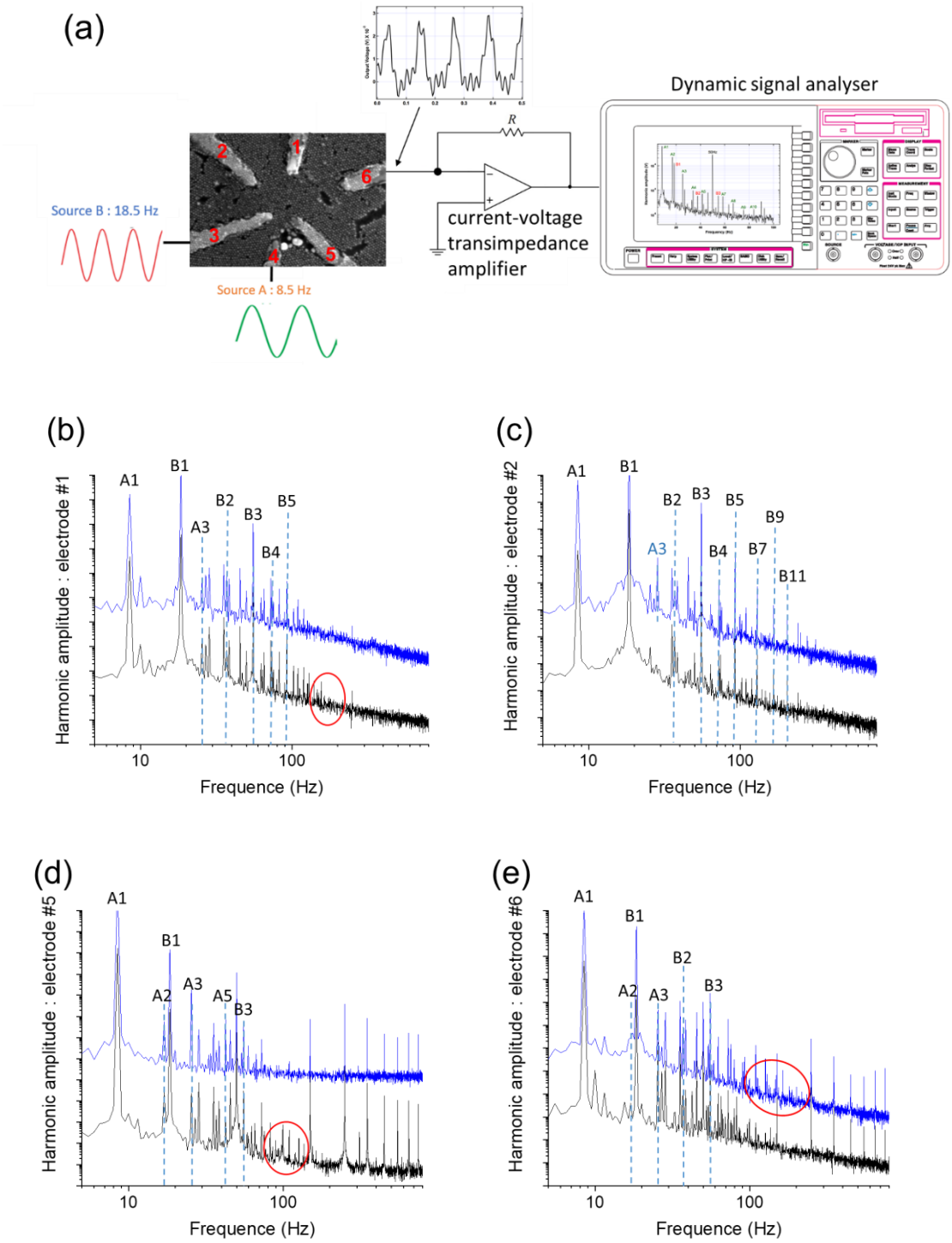

Figure 3.25. a) Typical configuration for HHG experiments. Two sinusoidal signals, signal A at 8.5 Hz and signal B at 18.5 Hz (peak-to-peak amplitude VPP = 2 V for both) are applied at electrodes 3 and 4, respectively. (b–e) The four output currents are measured by the dynamic signal analyzer (FFT). HHG peaks are normalized. The HHG peaks are labelled as Ai (i = 1 for the fundamental, i = 2 for the second harmonic, etc.) and Bi for harmonics corresponding to the A and B input signals, respectively (written in black when it is common to the two signals and in blue when it is just in irradiated POM signal) . Black lines correspond to the measurement with the pristine POM and blue lines with the irradiated POM. Red circles show the difference between the two spectra.

We apply two frequencies at 8.5 Hz and 18.5 Hz (Figure 3.25a and annexe A3.3) on two randomly selected electrodes and we compare the harmonic spectra on the four other electrodes of the NPSAN pattern (Figure 3.25b-e). On the HHG spectra, we have labelled some of the main harmonics (integer multiple of the input signal). We do not observe difference between the two states of the POM in the four configurations (except A3 in Figure 3.25c) but we notice different numbers of harmonic signals for the four electrodes (Figure 3.25b-e). The peaks in between can be attributed to either interharmonic or IMD, they were not identified at this stage of the work (time constraint). We only note that the presence of these peaks reveals a complex dynamic behaviour, beyond simple non-linearity effects. By looking at the signals from the four electrodes in their entirety, we note that:

- We see heterogeneous harmonic responses. They give us a large variability of signals, due to different topology of the conduction pathways into the NPSANs and the variability of the non-linear IV of the NP-molecule-NP building blocks.
- There is no large difference between pristine and irradiated POM. Only few more peaks appear/disappear (red circles). This is not surprising because the current-voltage curves are similar before and after irradiation (Figure 3.18). The complex nonlinearities and dynamics electron transport occurring inside the POM and NP network itself does not switch when we pass from the pristine to irradiated POM.

d) Are polyoxometalates prone for Reservoir Computing?

A molecule is prone for RC if the final dynamic reservoir include variability, complex dynamics and non-linearity.

For both the NPSAN with pristine POMs, $HPMo_{12}$ and $TBAPW_{11}SH$, we observe large variability with the DC IVs and HHG measurement. We also note the rich complex dynamics with the rich harmonic response (many peaks from harmonic, interharmonic and intermodulation distortion). In addition, we observe an unusual $1/f^n$ with n a function of V as for AzBT NPSAN with $TBAPW_{11}SH$ NPSAN only.

The NPSAN prepared with $HPMo_{12}$ are only stable with the POM at the pristine state. We cannot discuss about reconfigurable RC in this case because we cannot switch the molecule from oxidized to reduced state. However, when we irradiated the NPSAN with $TBAPW_{11}SH$,

we do not observe a large difference of noise and HHG compared to the pristine NPSAN. The molecular junction conductance switching is too low (about a factor 1.1) compared to about 10^3 for AzBT molecular junctions.

To conclude, these two POMs are not prone for reconfigurable RC but they are prone for classical Reservoir Computing.

Conclusion and outlook

In this chapter, we have presented results of NPSANs with POMs. We have optimized the protocols to fabricate NPSAN with two different POMs in their oxidized and reduced states. Despite the easy damage of the NPSAN pattern, we have succeeded in doing some electronic measurements to assess whether these NPSANs are reliable to implement reservoir computing. A large ET variability in the NPSANs has been demonstrated both from DC current-voltage and HHG measurements, while low-frequency noise and HHG measurements on $TBAPW_{11}SH$ NPSANs demonstrate a rich ET dynamics in these devices, albeit without significant difference between the oxidized and irradiated states of the POMs in the NPSANs.

Contents of chapter 4

Chapter 4 Another metal oxide structure: $W_{18}O_{49}$ nanowires 123

I. Introduction 123

II. Nanowires synthesis and characterization 126

III. Conductance of single nanowires 133

a) Electronic behaviour 133

b) Perpendicular conductance 138

c) Longitudinal conductance 139

IV. Conductance of a two-dimensional network of nanowires 147

Conclusion 153

Chapter 4 Another metal oxide structure: $W_{18}O_{49}$ nanowires

I. Introduction

Nanowires (NWs) are wires with a diameter between 1 and 100 nm. The formation of this nanostructure relies on crystallization, involving two fundamental steps, nucleation and growth. For this purpose, gas phase and solution phase methods can be used to synthesize NWs in large quantities. Nowadays, the semiconductor nanowire field of research has become one of the most active research areas within the community of nanoscience. These NWs have found applications in biology, energy conversion and storage, photonics or electronics. Indeed, they are used a lot in nanoelectronic because with their small dimension, they can be easily integrated in devices such as field-effect transistors as a channel between the source and drain terminals, for example. Some material compositions include nitrides (InGaN), phosphides (GaP), chalcogenides (CdSe), silicon or metal oxides (TiO_2, WO_3).[196–198]

Tungsten oxides (WO_3) are considered as one of the key materials for electrochromic (EC) devices. WO_3-based EC "smart windows" have become a viable commercial product. The EC properties are explained by the presence of oxygen vacancies (V_0), which can trap electrons and induce an optical transition due to the change of the energy gap as illustrated in the paper of Satyen K. Deb (Figure 4.1):[199]

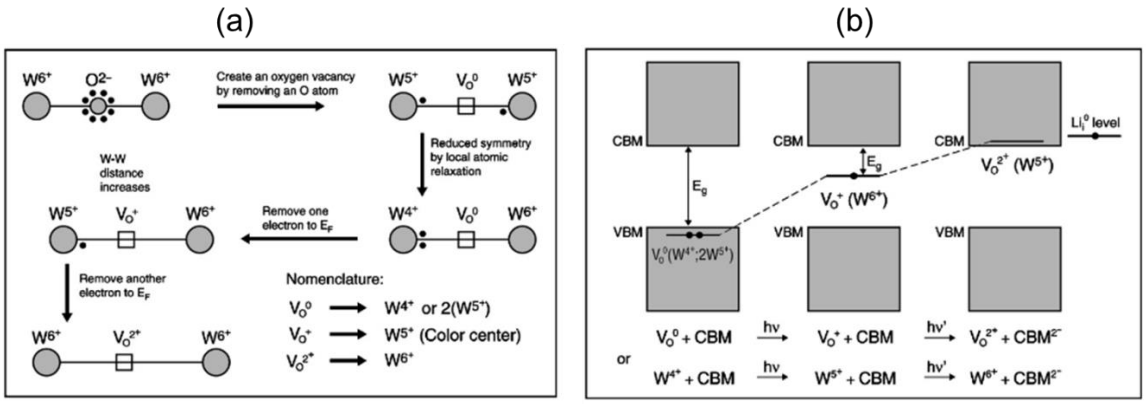

Figure 4.1. Hypothesis of a model for coloration in $LiWO_3$ involving oxygen vacancies[199]

Under electric stimulus, the apparitions of V_0^+ and V_0^{2+} induce a new optical transition at lower energy, modifying the coloration.

Another application of WO_3 is the Reservoir Computing. WO_3 is based-memristor and can propose a dynamic reservoir with internal and short-term memory effects. Indeed, this oxide is used as active material for memory applications because it offers a high degree of compatibility and ease of processing within the overall integrated circuit. The implementation of this oxide-memristor has already been validated and demonstrated for use as handwritten digit recognition or to solve a second-order nonlinear task.[200,201]

It exists many suboxides of WO_3, labelled WO_{3-x} as $W_{19}O_{55}$ ($WO_{2.89}$) or $W_{18}O_{49}$ ($WO_{2.72}$) for example.[202] Nanowires $W_{18}O_{49}$ that are composed of 18 WO_3 bonded together (W-O-W) with five oxygen vacancies have aroused particular interest. These nanowires are substochiometric tungsten oxide semiconductors (bandgap < 3.0 eV).[203,204]

One approach to synthesize these nanowires is done at high temperature. On a quartz tube in a furnace is posed an alumina boat loaded with tungsten (W) powder. Some H_2O vapour flows on the tube while the furnace is heated up to 600°C for 30 minutes. After cooling, nanocrystals are obtained under the form of nanowires with several micrometers lengths (Figure 4.2a). Some electric measurements have been done showing a temperature dependence, proper to a semiconductor behaviour (Figure 4.2b).[205] Another method of synthesis at high temperature consists to use pyrolysis-H_2 process at H_2 flow rates ~ 10 l/h to reduce a tungsten oxide, $(NH_4)_2WO_4$, around 650°C during two hours. The size of obtained nanorods (few micrometers) confirms that with high temperature we form crystals (Figure 4.2c). In this case, conductivity has been calculated and reached 15 S/cm (Figure 4.2d).[206]

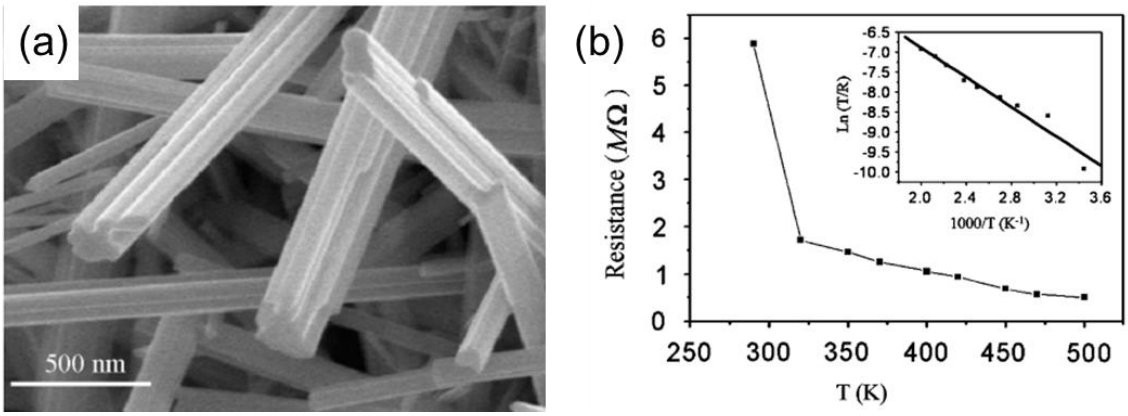

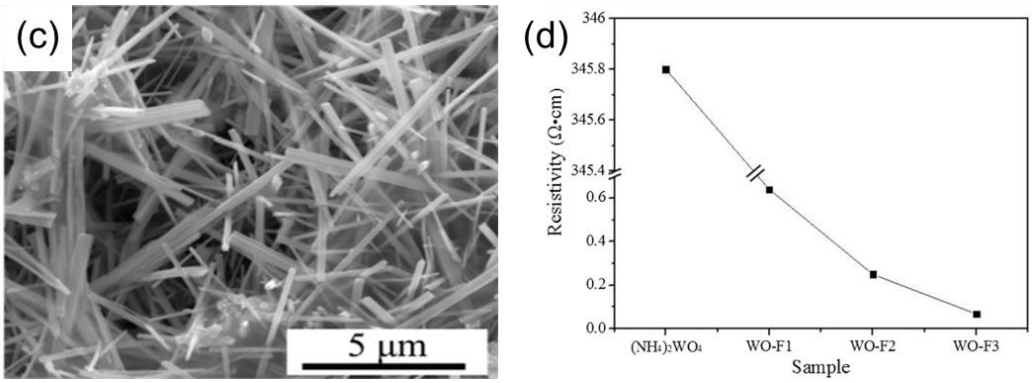

Figure 4.2. (a) SEM image showing nanowire bundles and (b) plot of resistance versus temperature. The relation of ln(T/R) versus 1000/T plotted in the inset shows an activation energy of 0.26eV. Images from the reference 205. (c) SEM images of nanorods heated at 700°C and (d) Resistivity variation curve of samples who differ by the H_2 flow rate. Images from the reference 206.

A second approach is the solvothermal synthesis at high pressure. A tungsten precursor is mixed with a solvent during days in an autoclave. With this method, temperature does not reach 200°C and smaller nanowires are obtained with diameter less than 100 nm as well as length inferior or close to one micrometer (Figure 4.3a-b).[207,208] Xi et al. has noticed that most of the time the synthesis give bundles of nanowires, and in their case nanowires have diameters below 1 nm.[209] As no electrical measurements have been reported from this kind of synthesis, we will focus on this protocol and develop it in the next session to probe their electrical behavior.

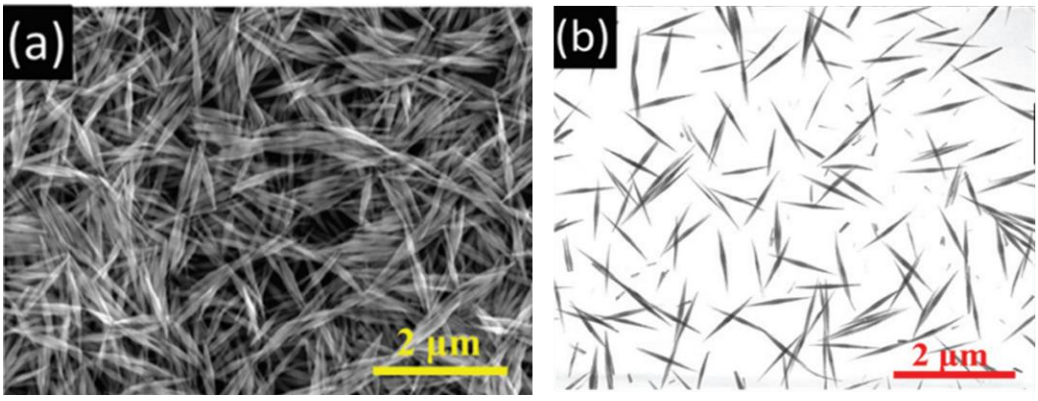

Figure 4.3. (a) SEM image and (b) TEM image of $W_{18}O_{49}$ nanowire. Images from the reference 207.

As the polyoxometalates, $W_{18}O_{49}$ nanowires possess a metal oxide structure but the density of one nanowire is higher than POMs grafted next to each other on surfaces. With the new interest of 2D network of conductor/semi-conductor NWs for the Reservoir Computing,[103] we figure out that it can be interesting to investigate the conductance of this NW oxide.

II. Nanowires synthesis and characterization

To synthesize these nanowires, we based our approach on Guo and al.[207] protocol. Briefly, we did several solvothermal syntheses using WCl_6 as a precursor in different sizes of Teflon box and various concentrations as summarized in Table 4.1. We took care during the experiments to avoid (or minimize) exposure to air.

Table 4.1. Examples of synthesis parameters with corresponding TEM images shown in Figure 4.5. Other syntheses with ethanol are shown in annexe A4.1.

Trials	Mass WCl_6 (mg)	Solvent	Volume (mL)	Concentration (mM)	Final mass product $W_{18}O_{49}$ (mg)	Colour
#1	103.9	Propanol	20	13.1	26	Blue - grey
#2	52	Propanol	10	13.1	16	Blue
#3	250	Propanol	60	10.5	150	Dark blue
#4	276.5	Propanol	60	11.6	110	Dark blue

WCl_6 was weighed into the Teflon box of the autoclave in the glove box and then the solvent was added under an argon flow funnel (the total volume of the Teflon box is 45 mL (#1), 23 mL (#2) and 125 mL (#3 and #4)). The solution was mixed and then sealed in the autoclave. Then, the same solvothermal conditions were applied. We started by 10 minutes at 25°C, 1h to reach 180°C and stayed 24h at this temperature. Finally, the solution was slowly cooled at 25 °C during 18h. The product was decanted with a plastic pipette in centrifugation tube (previously purged). We centrifuged first at 5000 rpm-5 min and then we proceed to two washes with H_2O (6000 rpm- 6min and 9000 rpm- 10min). We finished by a third wash with ethanol 9000 rpm-10 min. All the solvents were also previously purged. We dried under vacuum at 50-60 °C during a few hours and let under vacuum without heating the whole night. We obtained blue powders.

To characterize the nanowires, the product (trial #4) has been analysed by RAMAN spectroscopy, X-ray Diffraction (XRD) (see details in annexe A4.1) and XPS (details and methods in annexe A2.3) (Figure 4.4).

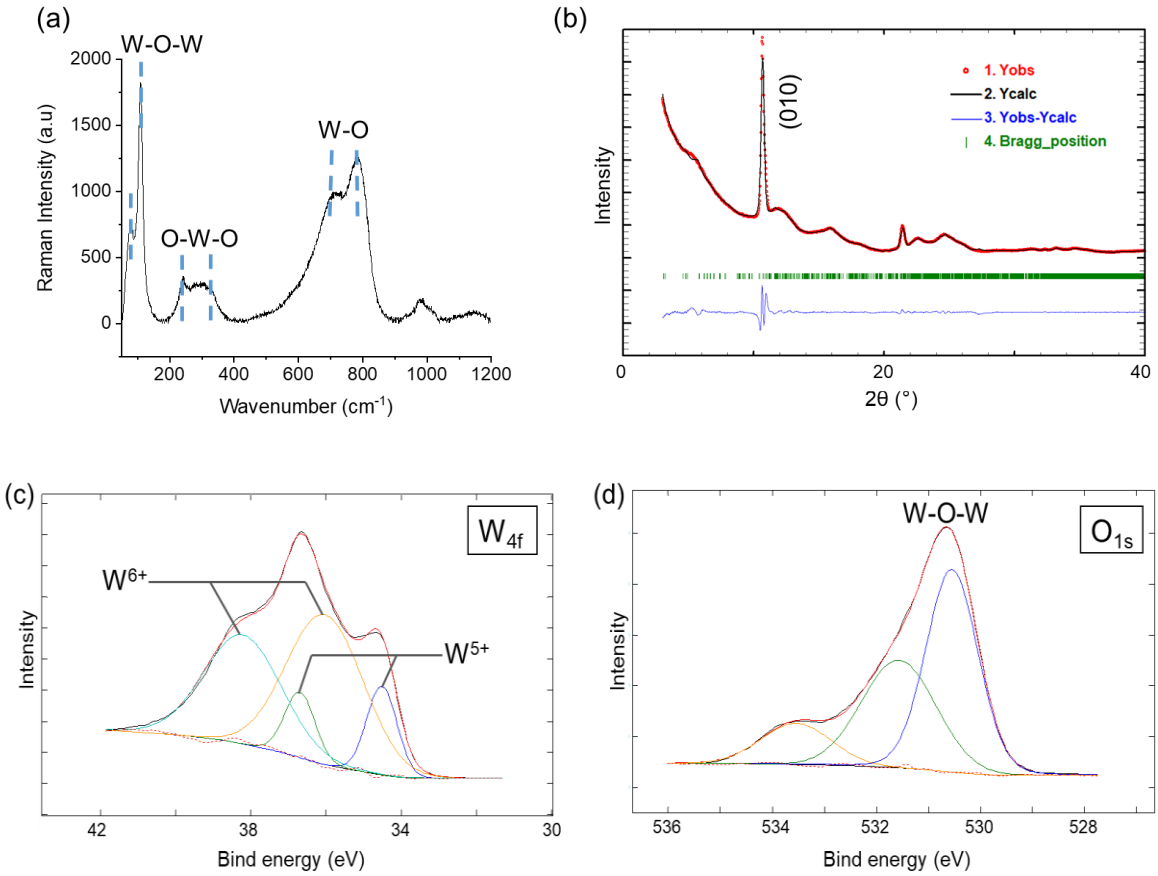

Figure 4.4. (a) Raman, (b) XRD and (c,d) XPS of NWs obtained in trial #4

The Raman spectrum (Figure 4.4a) displays the characteristic peaks of tungsten suboxide. Three bands are observable at 73 and 122 cm^{-1} (W-O-W bending modes), 218 and 345 cm^{-1} (O-W-O bending modes), 674 and 803 cm^{-1} (W-O stretching modes).[206–208,210] On the XRD pattern (Figure 4.4b) is represented the measured (Y_{obs}, red line) and calculated ((Y_{calc}, fit with the reference JCPDS712450, black line) X-Ray diffraction data, their difference (Y_{obs} - Y_{calc}, blue line), as well as the expected Bragg reflection positions for a perfect $W_{18}O_{49}$ lattice (Bragg_position, green line) following the Le Bail method.[211] These data show the expected large peaks of the monoclinic phase (010) in good agreement with the previous reports on the structural characterization of $W_{18}O_{49}$ NWs.[206–208] The large peak defines nano-object structure, in good agreement with our nanowires. Nevertheless, this peak of monoclinic phase and the other peaks with less intensity are also observed on other tungsten suboxide, like $W_{19}O_{55}$

($WO_{2.89}$) or $WO_{2.90}$.[202] This spectrum just tell us that we have a monoclinic phase with a lattice parameter b = 0.382 nm, consistent with the literature, but it is not enough to know which suboxide we have synthesized. Finally, the XPS spectrum can be decomposed into two W $4f_{5/2}$-$4f_{7/2}$ doublets (Figure 4.4c), one for the W^{6+} oxidation state (38.2 and 36.1 eV) and the other one for the W^{5+} oxidation state (36.7 and 34.5 eV). Unlike previously reported results for $W_{18}O_{49}$,[206–208] here we do not observe any weak signal for W^{4+}. The O1s photopeak (Figure 4.4d) shows a broad main peak (at 530.6 eV) associated to W-O bonds with additional weak peaks at higher binding energies, likely associated to two residual types of contamination (C-O bonds in contaminants…).[207] From the integrated peak areas, we deduced the stoichiometry of our final compound. The ratio of W_{6+}:W_{5+} is 1:0.23 and the deduced chemical formula is $W_{0.814}{}^{6+}W_{0.186}{}^{5+}O_{2.91}$. The ideal $W_{18}O_{49}$ phase is equivalent to $WO_{2.72}$, some slight difference indicating superficial oxygen enrichment on the nanowire surfaces has also been reported.[208] Here, the difference is a little bit more important and let us conclude that we have synthesized another tungsten suboxide: $W_{18}O_{52.4}$. However, by sake of simplicity, for the rest of this chapter, we will still labelled our nanowires $W_{18}O_{49}$.

Then, we have imaged by Transmission Electron Microscopy (TEM, annexe A4.1) the NWs obtained in all the trials (Figure 4.5).

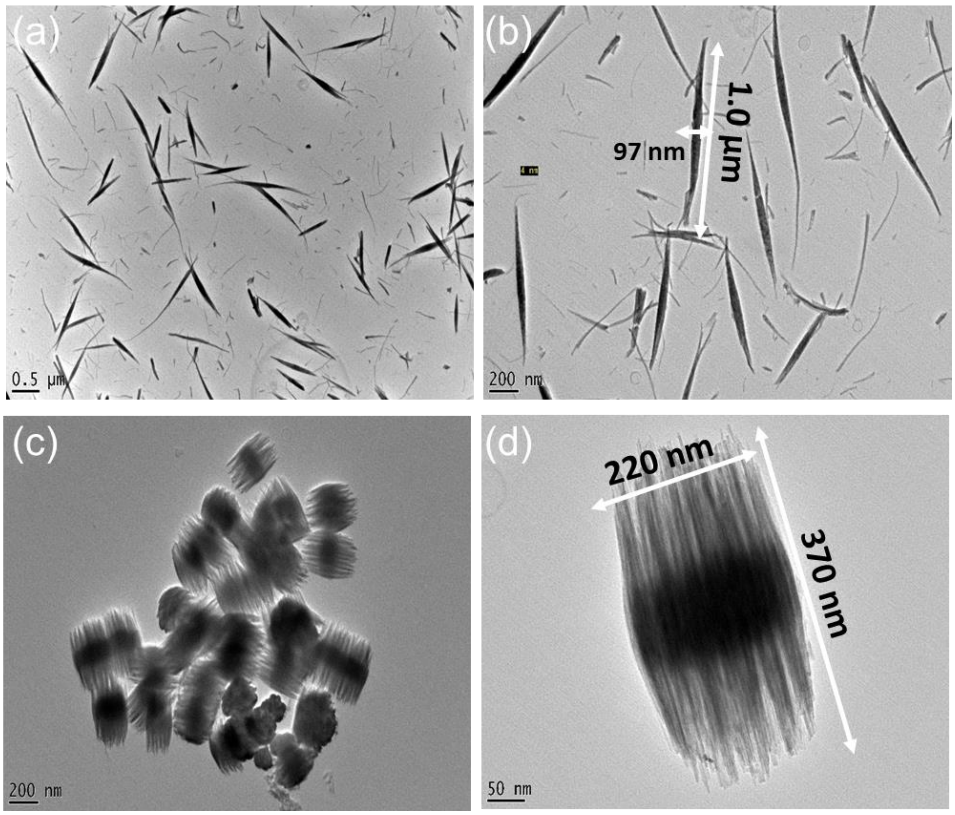

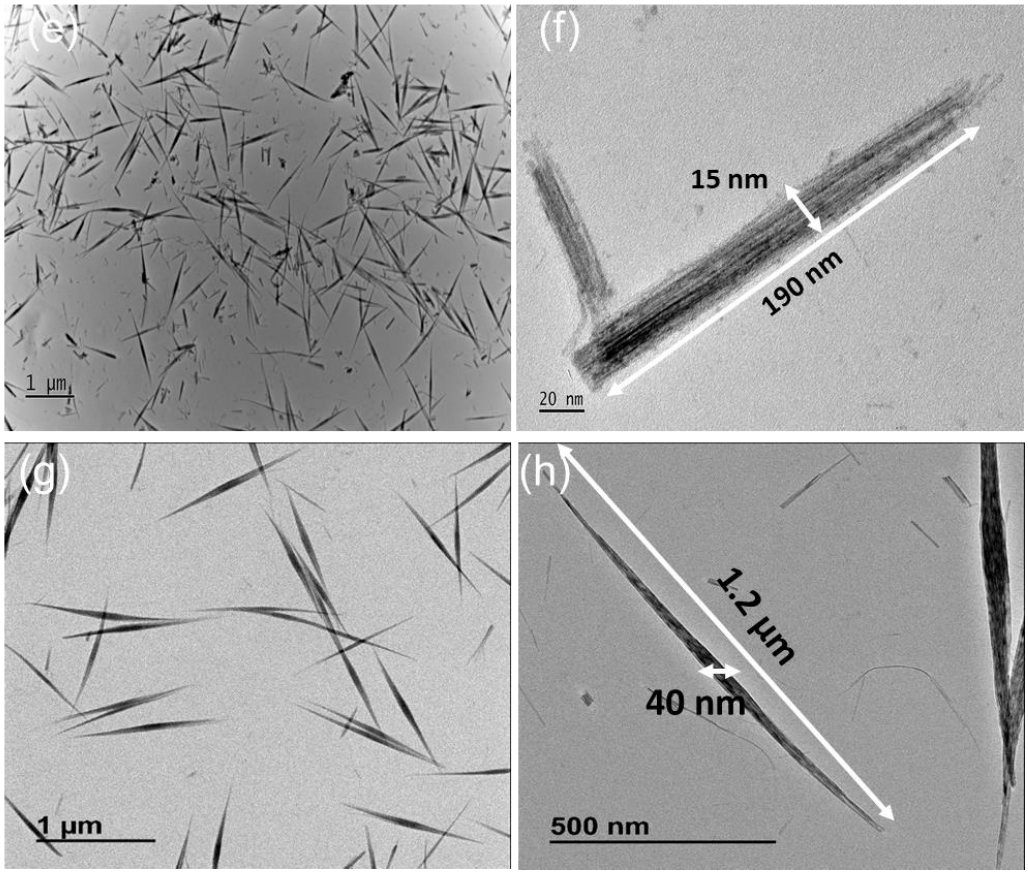

Figure 4.5. TEM images of (a), (b) trial#1: 13.1 mM/propanol/20mL, (c),(d) trial#2: 13.1 mM/propanol/10 mL, (e),(f) trial#3: 10.5 mM/propanol/60 mL and (g),(h) trial#4: 11.6 mM/propanol/60 mL, deposited on a carbon grid in all cases

In Figure 4.5a and b, the synthesis has been done with 13.1 mM of the precursor in 20 mL of propanol (trial #1). We see some dispersed and isolated nanowires with a diameter between 5 and 100 nm and lengths between 100 nm and 1 µm. In Figures 4.3c-d, even if this synthesis differs only by the total volume of the solution (10mL), trial #2, we see a completely different morphology. It looks like "nanopin". All of these nanostructures possess homogeneous form and size, with a width around 200 nm and a length around 360 nm. The two syntheses were done in different size of Teflon box, the pressure inside the autoclave was probably different and explain the difference of morphology. In Figures4.3e-d and Figures4.3g-h, we have used Teflon box with the same size but we have varied the concentration from 10.5 mM (trial #3) to 11.6 mM (trial #4). In Figures4.3e-f, we observe various sizes of nanowires with lengths from 100 nm to 1 µm, similar to the trial #1. In Figures 4.3g-h, we obtain longer nanowires (between 1 and 1.5 µm) with diameters smaller than 100 nm (40-110 nm in the centre and 25-50 nm on the ends) (Figures 4.3g-h). It looks easier to obtain long homogeneous nanowires when the

concentration is not too low. These four synthesis show us that the morphology of this tungsten oxide is very sensitive to the protocol. We have also done synthesis with ethanol where we have obtained very small isolated nano-objects because the bigger ones are entangled (Annexe A4.1).

We took a closer look at their structure by looking at their extremities (Figure 4.6a-b) by TEM at a higher magnification and on the crystal structure with a High Resolution - TEM (Figure 4.6c, see details in annexe A4.1).

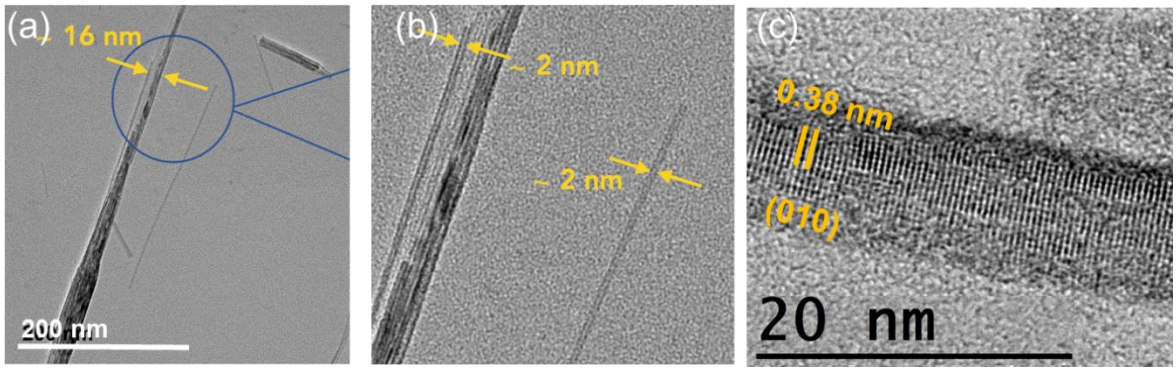

Figure 4.6. TEM images of (a) and (b) the end of nanowires (trial #4) and (c) zoom on a HRTEM image

The first information is that a single NW is a bundle of nanofibers. By looking carefully some small nanofibers (Figure 4.6a-b), we notice that they appear as two parallel dark-grey lines at a constant distance, separated by a lighter-grey zone. These features are the TEM fingerprint of nanotubes (NTs) with the two dark-grey lines representing the walls of the nanotubes. From a statistical analysis of these TEM images (Annexe A4.1), we deduced that the external diameter (d_{nt}) of the nanotubes is 2-3 nm and the internal one (δ_{nt}) is around 1 nm. The HRTEM image (Figure 4.6c) reinforces the nanotube morphology by showing the perpendicular lines and the good crystallinity with the lattice parameter of 0.38 nm. We can thus conclude that the NWs are made of bundles of nanotubes.

- **Why hollow nanofibers and not filled?**

Formation of nanotubes has never been reported on previously works discussing the synthesis and TEM images of tungsten suboxides. To try to propose a growth mechanism, we have transposed the explanation of two main mechanisms about the formation of tellurium nanotubes from solvothermal synthesis reported in the review of Liu et al.:[212]

- Nucleation-Dissolution-Recrystallization Growth (NRDG) (Figure 4.7a).[213] In this case sphere-like seeds are formed. Then, some of the seeds gradually redissolve and get recrystallize under the form of nanorods or nanotubes on undissolved spheres.
- Seed-Induced Growth (SIG) (Figure 4.7b).[214] At the first stage of the reaction, a large number of seeds are formed with an anisotropic cylindrical form. Then the growth occurs along the circumferential edges of the seeds due to their higher free energy than other sites of the surface, forming nanotubes.

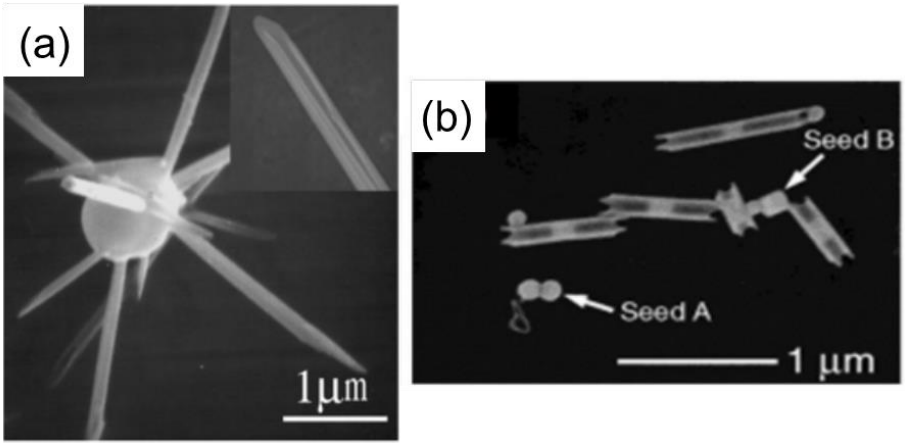

Figure 4.7. (a) NRDG and (b) SIG mechanisms, images from references 213 and 214 respectively.

As we have observed nanotubes along a seed, we do the hypothesis than the SIG mechanism happened in our case. Considering this mechanism, it means that the bundle entity is composed of several nanotubes and seeds stick together.

To complete the observation of the NWs morphology, one sample (trial #4) was dissolved in ethanol and deposited by drop casting on Si/SiO_2 (200 nm thick) and imaged with AFM in tapping mode (Figure 4.8).

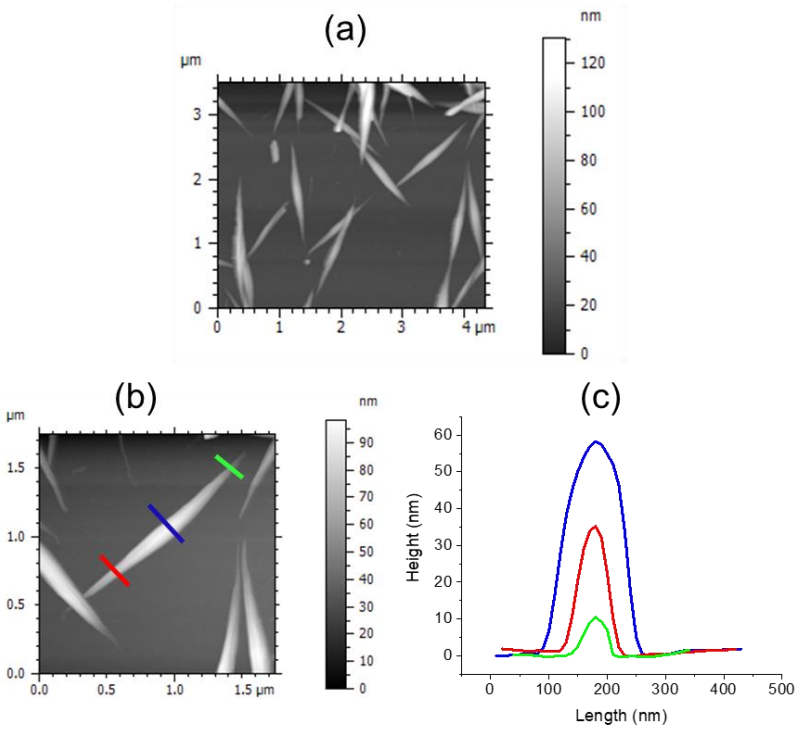

Figure 4.8. (a) Topographic TM-AFM of $W_{18}O_{49}$ NWs deposited on SiO_2; (b) zoom on a NW and (c) profiles at 3 locations along the NW.

Nanowires are bigger in the middle (height ~ 60 nm, Figure 4.8c) and thinner in the extremities (height ~35 and 10 nm, Figure 4.8c). We note that this spindle shape is observed for all NWs whatever the nature of the substrate: TEM grid (Figs. 4.5g-h), SiO_2 (Fig. 4.8 and annexe A4.1) and Au (Annexe A4.1). AFM confirms the observation of bundle with a witdh more important in the centre.

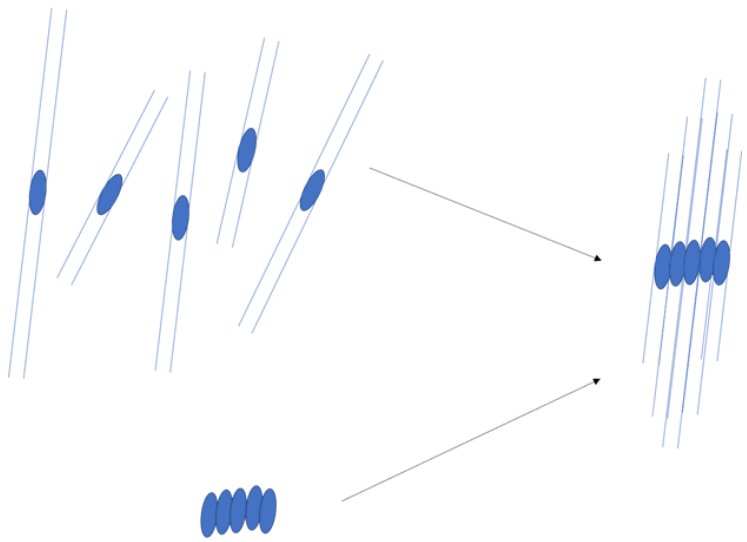

Figure 4.9. Hypothesis of formation of our nanowires

Two different hypotheses can be proposed to explain this bulging bundle form. Either single nanotubes are formed at the very first stage of the reaction and then, they get stick together, or the seeds first stick together then the growth of nanotubes start (Figure 4.9).

In the following, we will use the term nanowire when we talk about the bundle entity, and nanotube by talking about a single nanotube inside the bundle.

III. Conductance of single nanowires

a) Electronic behaviour

To proceed to the electronic measurement, we first prepared the sample in a glovebox. The ^{TS}Au substrate was immersed in a solution of $W_{18}O_{49}$ at 10^{-3}M in ethanol, and then very lightly rinsed with ethanol. The modified surface was directly observed by TM-AFM.

The study has been done using an AFM at RT with an electrostatic force microscopy (EFM) tip. This probe has the particularity of being efficient in the tapping and contact modes. The thickness of each nanowire has been checked using the tapping mode and then, we switched to the TM deflection in order to do electronic measurements in the contact mode. Approximately 10 I-Vs back and forth have been realized on a zoom part of the nanowire (details in annexe A4.2).

Here, we report on the perpendicular conductance for three nanowires synthesized from 12.3 mM/ethanol/10mL (trial #6, annexe A4.1), with a small thickness around 15, 22 and 30 nm respectively (Figure 4.10). The measurements have been done with a loading force ~ 20-25 nN.

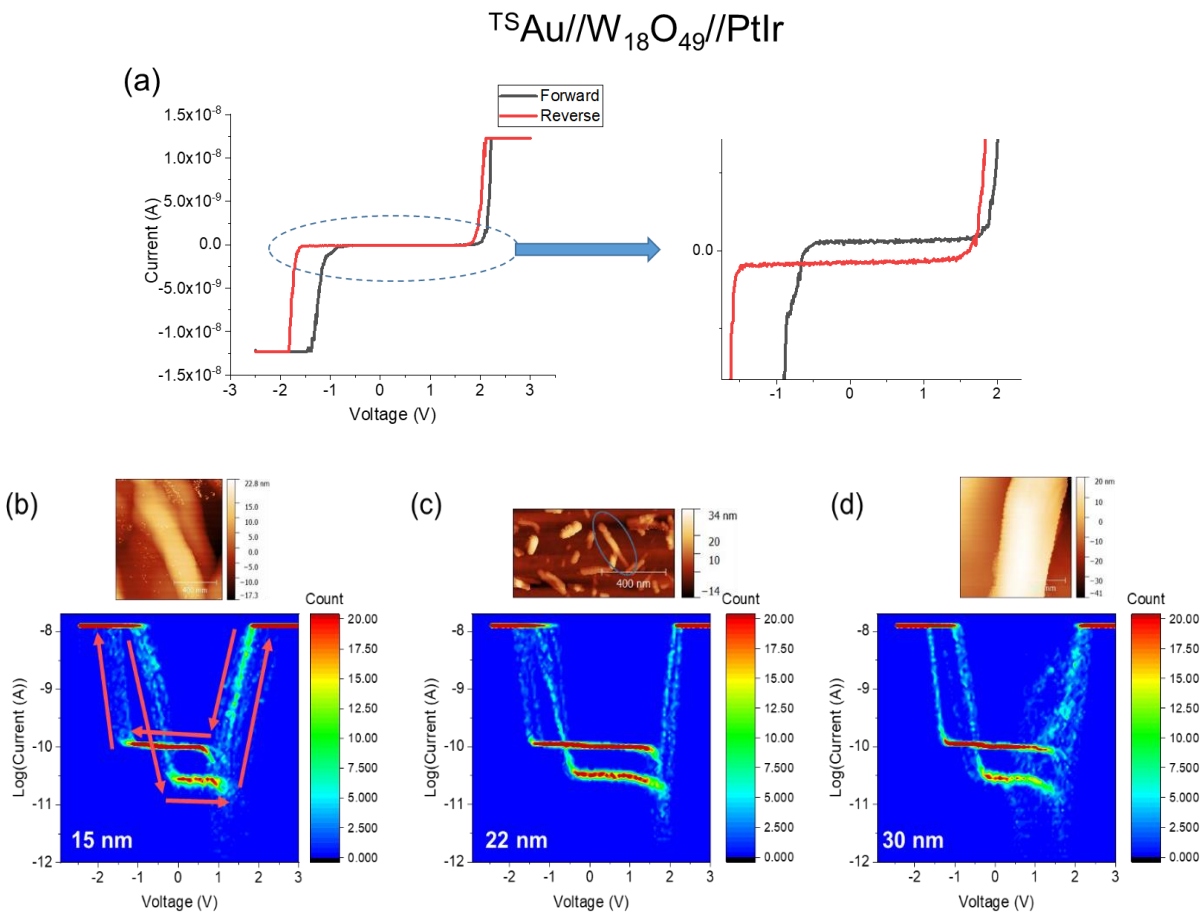

Figure 4.10. Measure on $^{TS}Au//W_{18}O_{49}//PtIr$ (loading force ~ 20-25 nN, trial #6) (a) Typical I-V curve measured on one nanowire (with offset correction). Topographic images and 2D histograms with nanowires of different thicknesses (b) 15 nm (c) 22 nm and (d) 30 nm. The red arrows on (b) indicate the way to read the graph (starting voltage sweep at -3V) and it is the same for (c) and (d) (no offset correction to better distinguish the plateaux)

We notice on the three 2D histograms that we observe two plateaux at slightly different values of the current, I_P, for the back and forth traces. The smaller plateau corresponds to the trace -3V to +3 V at (log(|I_P|) ~ - 10;5) and the longest one to the back trace (log(|I_P|) ~ -10.0). The length of the current plateau is fixed by the voltage at which the current starts to increase and thus this length difference is due to the large hysteresis observed at negative bias. For the 22 and 30 nm thick NWs (Figure 4.10b and c), the behaviours look similar with almost the same I_P values and a large hysteresis at negative voltage. This behaviour can be modelled by a simple equivalent circuit with a resistance (voltage dependent) and a capacitance in parallel (Figure 4.11).

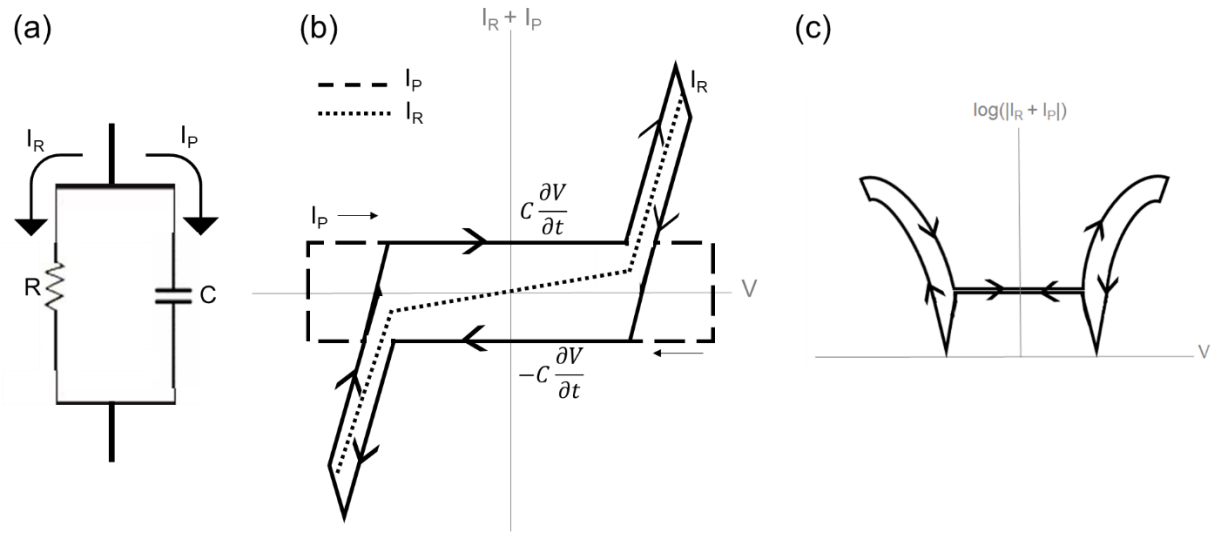

Figure 4.11. (a) Simple equivalent circuit with a resistance (voltage dependent) and a capacitance in parallel. (b) Scheme of the current-voltage behaviour, I_R, for the voltage dependent resistance (large R, weak I_P at low voltages, and lower R at larger voltages) and charging/discharging current, I_P, of the capacitance and (c) same schematic graph in a $\log(|I_R + I_P|)$ scale.

Here, R is the resistance of the nanowire. I_R is its associated linear current, with two branches of low resistances and a much higher R at low voltages. C represents the NW capacitance and I_P its associated current of charge/discharge under an applied varying voltage at a scan rate dV/dt (Figure 4.11 a and b), which is equal to:

$$I_p = C\frac{\partial V}{\partial t} \tag{4.1}$$

At low voltages, I_R is masked by I_P because a thin object possesses a bigger capacitance (per surface unit) than a thick one (typically C scales as 1/thickness). This simple model explains why we have I-V curves with two "branches" at high voltages and plateaus at low voltages (Figure 4.11c). In theory, the two plateaux at positive and negative currents (Fig. 4.10c) are supposed to have the same absolute value. In our experience, we obtained two plateaux (Figure 4.10), likely due to the offset of the AFM (not subtracted here).

To verify this hypothesis, we did some I-Vs at different scan rates, 1.2, 6, 24 and 120 $V.s^{-1}$ (Figure 4.12) selecting a NW with the smallest thickness as possible to maximize the capacitance effect (trial #3, 10.5 mM/propanol/60 mL (Table 4.1)).

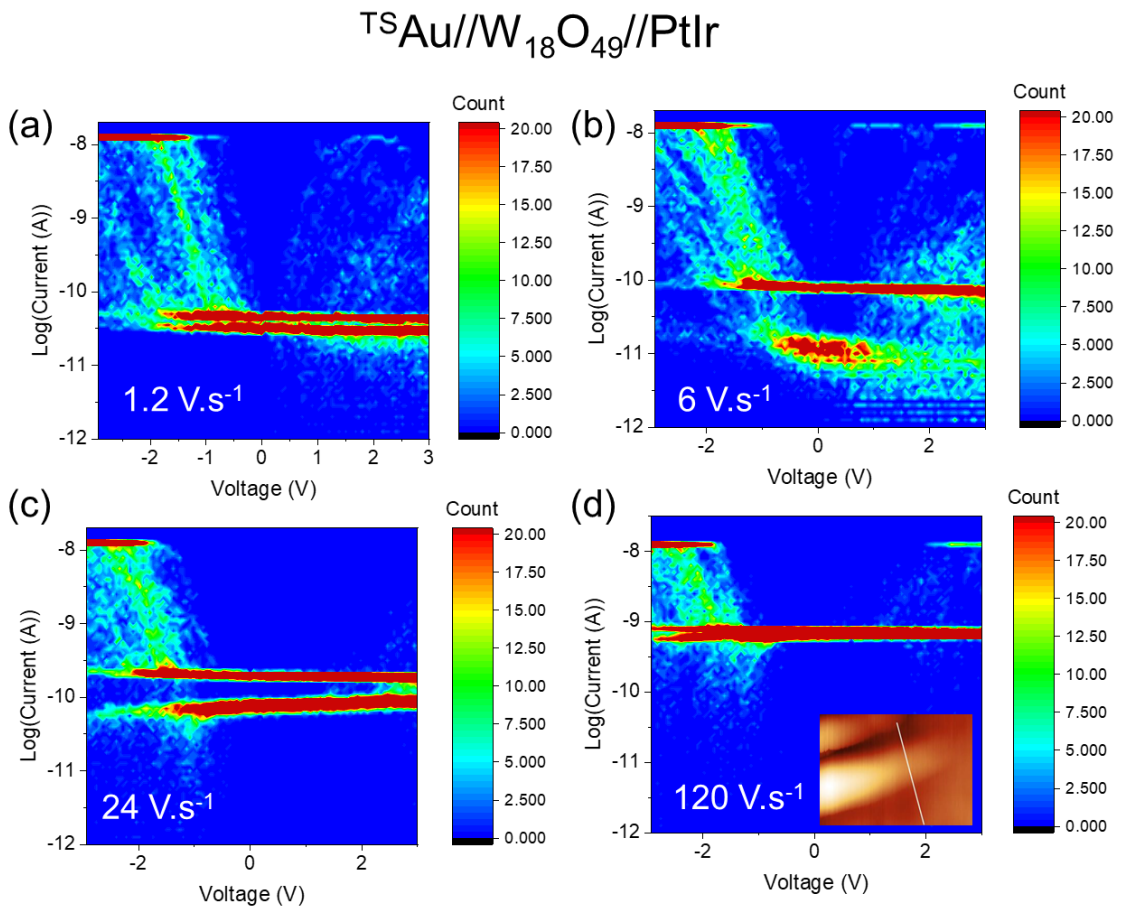

Figure 4.12. 2D histogram of $^{TS}Au//W_{18}O_{49}//PtIr$ (loading force ~ 22nN) on the same NW (12 nm) at different scan rates (a) 1.2 $V.s^{-1}$, (b) 6 $V.s^{-1}$, (c) 24 $V.s^{-1}$ and (d) 120 $V.s^{-1}$.

Here the thickness of the NW is ~ 12 nm. As previously, we observe two plateaux. The current of these plateaux increases with the scan rate. Passing from an average log value around -10.5 at a scan rate of 1.2 V/s to -9 at 120 V/s. We have repeated this experience on five nanowires and plotted the mean curve I_{up} and I_{down} as a function of the scan rate dV/dt (with I_{up} the value of current for the upper plateau, I_{down} the inferior plateau – Figure 4.13).

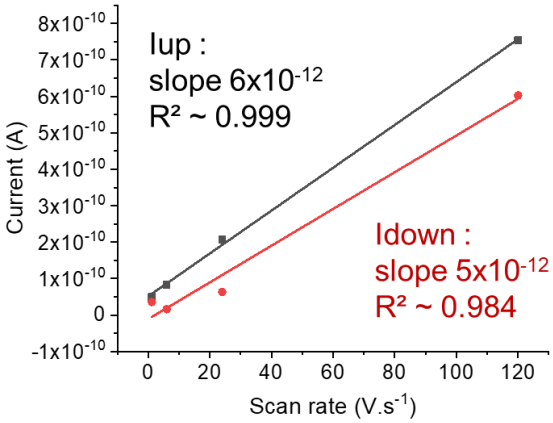

Figure 4.13. Mean I_P versus the voltage scan rate.

These curves confirm the expected linear dependence (Equation 4.1) for a capacitance effect and we can deduce a capacitance of 5-6x10^{-12} F for these NWs.

It is difficult to trace back to a dielectric constant due to the non-conventional geometry of the nanowire (spindle shape). Nevertheless, we can simplify the calculation using the geometry of a cylinder:

$$C \approx r\varepsilon_0\varepsilon_r\left(4.1\left({}^{L}/_{r}\right)^{0.76} + 8\right) \tag{4.2}$$

With C the self-capacitance (6x10^{-12} F), r the radius (6 nm), L the length (1 µm), ε_0 the vacuum permittivity (8.85×10^{-12} F·m^{-1}), we obtained a value of ε_r the dielectric constant of our NW about 5x10^{5} F·m^{-1}. This value is high but already measured for films of nanocrystalline WO_3 particles (size of 100-200 nm) prepared by the team of K. Ivanov.[215] They have also observed that ε_r value decreases when the size of nanostructures increases. We note that the self-capacitance (i.e. C related to the amount of electric charge Q (Q=CV) that must be added to an isolated conductor to raise its electric potential by one unit) is not exactly what has been measured. Indeed, the NW is connected between two asymmetric electrodes, a tiny one (C-AFM tip and a large one (Au surface). Nevertheless, this crude approach allows us to give a consistent order of magnitude for ε_r.

b) Perpendicular conductance

As we wanted to compare the perpendicular and longitudinal conductances (see IIIc), and to avoid the capacitance effect we did a last measurement by C-AFM with the thickest and longest obtained nanowire (trial #4, 11.6 mM/propanol/60 mL (Table 4.1).

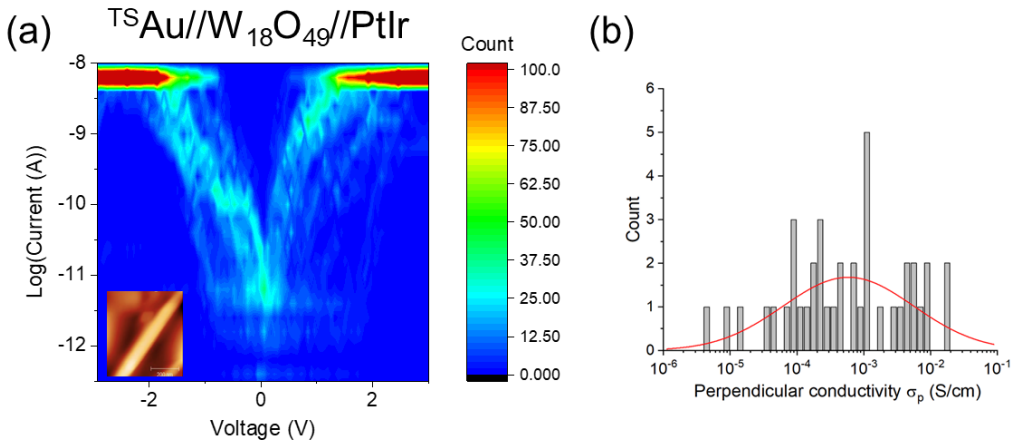

Figure 4.14. (a) 2D I-V histogram of $^{TS}Au//W_{18}O_{49}//PtIr$ at v = 6 V.s^{-1}(trial #4), and (b) histogram of the perpendicular conductivity, σ_P and fit with a log-normal distribution with a mean value $\overline{\sigma_P}$ = 6x10^{-4} S/cm.

From this synthesis, the nanowires are bigger (diameters 50-60 nm). We used a higher loading force to reduce the IV dispersion (60 nN). Figure 4.14a represents the 2D histograms of 41 IVs measured on four different nanowires. In this case, the radius of the NW is five times higher than for the NWs presented in Figure 4.12. We can do the hypothesis (from Eq. 4.2) that the capacitance and current I_p decreases by 5. Log(I_p) becomes -11.5 (I_p ~ 3.2x10^{-12} A) and this current is not measurable. By consequences, no plateau is observed here.

Then, we estimate the conductivity perpendicular to the long axis (σ_p) of the NW thanks to this formula:

$$\sigma_p = G_P * \frac{h}{S_C} \tag{4.3}$$

With G_P the zero-bias conductance (determined from the slope of the I-V curves around 0 V), h the height of the nanowire (~ 50 – 60 nm) and S_C the C-AFM tip surface contact (~ 39 nm² - see annexe A4.2).

Table 4.2. Dataset of the perpendicular conductance of nanowires from the synthesis 11.6mM/propanol/60 mL (trial #4)

#NW	G_P (S)	h (nm)	S_c (nm^2)	σ_P (S/cm)
#3	$7.74x10^{-12}$	50	39	$9.93x10^{-05}$
#3	$3.87x10^{-13}$	50	39	$4.96x10^{-06}$
#3	$2.71x10^{-12}$	50	39	$3.47x10^{-05}$
#3	$9.68x10^{-12}$	50	39	$1.24x10^{-04}$
#3	$1.27x10^{-9}$	50	39	$1.63x10^{-02}$
#3	$9.04x10^{-11}$	50	39	$1.16x10^{-03}$
#3	$5.42x10^{-12}$	50	39	$6.95x10^{-05}$
#3	$3.87x10^{-12}$	50	39	$4.96x10^{-05}$
#3	$7.74x10^{-13}$	50	39	$9.93x10^{-06}$
#3	$1.16x10^{-11}$	50	39	$1.49x10^{-04}$
#3	$1.65x10^{-11}$	50	39	$2.11x10^{-04}$
#3	$1.16x10^{-12}$	50	39	$1.49x10^{-05}$
#6	$4.80x10^{-10}$	60	39	$7.39x10^{-03}$
#6	$1.22x10^{-09}$	60	39	$1.88x10^{-02}$
#6	$5.61x10^{-12}$	60	39	$8.64x10^{-05}$
#6	$2.75x10^{-11}$	60	39	$4.23x10^{-04}$
#6	$7.37x10^{-11}$	60	39	$1.13x10^{-03}$
#6	$8.03x10^{-11}$	60	39	$1.24x10^{-03}$
#6	$1.10x10^{-11}$	60	39	$1.70x10^{-04}$
#6	$1.37x10^{-11}$	60	39	$2.11x10^{-04}$
#6	$6.08x10^{-10}$	60	39	$9.36x10^{-03}$
#6	$5.36x10^{-10}$	60	39	$8.25x10^{-03}$
#6	$4.30x10^{-11}$	60	39	$6.61x10^{-04}$
#6	$4.92x10^{-11}$	60	39	$7.56x10^{-04}$
#12	$1.09x10^{-10}$	60	39	$1.68x10^{-03}$
#12	$3.55x10^{-10}$	60	39	$5.46x10^{-03}$
#12	$2.46x10^{-10}$	60	39	$3.79x10^{-03}$
#12	$1.92x10^{-10}$	60	39	$2.95x10^{-03}$
#12	$1.32x10^{-11}$	60	39	$2.02x10^{-04}$
#12	$3.21x10^{-11}$	60	39	$4.94x10^{-04}$
#1	$2.15x10^{-11}$	60	39	$3.31x10^{-04}$
#1	$1.19x10^{-11}$	60	39	$1.83x10^{-04}$
#1	$3.55x10^{-10}$	60	39	$5.46x10^{-03}$
#1	$5.87x10^{-12}$	60	39	$9.03x10^{-05}$
#1	$3.24x10^{-10}$	60	39	$4.98x10^{-03}$
#1	$2.97x10^{-10}$	60	39	$4.57x10^{-03}$
#1	$5.57x10^{-11}$	60	39	$8.57x10^{-04}$
#1	$6.61x10^{-11}$	60	39	$1.02x10^{-03}$
#1	$1.77x10^{-11}$	60	39	$2.73x10^{-04}$
#1	$7.81x10^{-11}$	60	39	$1.20x10^{-03}$

Table 4.2 recapitulates the whole calculated values and Figure 4.14b illustrates the large dispersion of the conductivity value with a mean value around $6x10^{-4}$ S/cm.

For all the previous experiments, we notice that these values measured are stable over several hours (time of the experiments) and not sensitive to degradation upon air exposure.

c) Longitudinal conductance

The electron transport properties of the same nanowires (trial #4, 11.6 mM/propanol/60 mL) have been measured with a 4-probe STM coupled with a SEM in ultra-high vacuum (UHV,

~10^{-9}-10^{-10} mbar) (annexe A4.3), with the help of Maxime Berthe at IEMN. The NWs were deposited on a Si n^+/SiO_2 (highly doped Si resistivity of 1-3x10^{-3} Ω.cm, 200 nm thick thermally grown SiO_2) substrate (Figure 4.15).

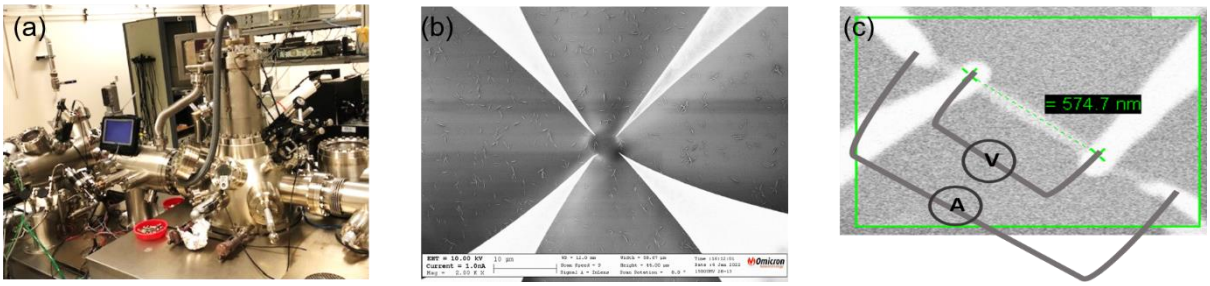

Figure 4.15. (a) Photo of the 4-probe STM, (b) SEM image of the substrate modified with nanowires and (c) zoom of the 4 probes connecting a single NW and the indication of the electrical set-up.

The advantage of this equipment is that we can precisely position the tips on a single nanowire thanks to the SEM. Four tips are connected on the NW, two at the extremity (from which we inject a known current) and two inside (where we measure the voltage). In this configuration, we trace V-I curves. By using four probes, the contact resistances (e.g. at the tip/NW interface) are cancelled and we are sure to measure the intrinsic electronic properties of the NW. On each NW, three V-I curves were acquired. During the measurement, the e-beam of the SEM is turned off (see details in annexe A4.3).

- **At 300K**

We did several experiences at 300K. In total, 52 V-I curves on 29 NWs were acquired.

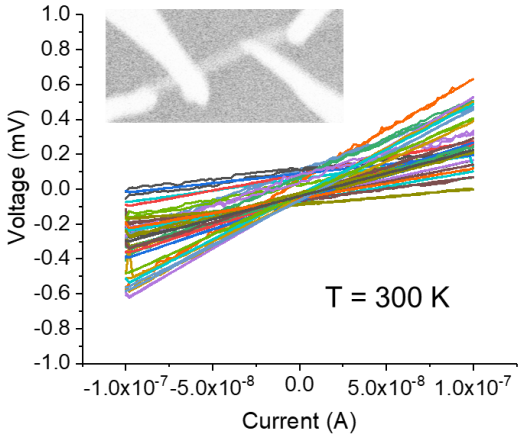

Figure 4.16. V-I curves of 4-probe STM for all series of measurements at 300K (voltage offsets on V-I curves are not corrected as it does not impact the value of the slope that interests us here).

Figure 4.16 shows the three series of data measured at 300K and Table 4.3 gives the dataset of one of them (complete datasets in annexe A4.3). The results are repeatable. We observed a linear behaviour with the applied current from $-1x10^{-7}$ to $+1x10^{-7}$ A. From each curve, we isolated the electrical conductivity along a single NW, i.e. the longitudinal conductance σ_{Lnw} using $\sigma_{Lnw}=G_L(L/S_{nw})$, with G_L the longitudinal conductance (slope of the V-I curve), L the inner-probe distance and S_{nw} the cross section area of the NW (systematically estimated for each NW by measuring the NW diameter, d_{nw}, with the scanning electron microscope (SEM) in the 4P-STM). In this case, we hypothesis that the NWs are homogeneously filled with $W_{18}O_{49}$, and not a bundle of NTs, neglecting voids inside the nanotube and between adjacent NTs, thus these conductivity values can be considered as "effective".

Moreover, we calculated the longitudinal conductivity of a single NT inside the NW, $\sigma_{L,nt}$ with this equation:

$$\sigma_{L,nt} = G_L * \frac{L}{S_{nt}} * \frac{1}{N} \tag{4.4}$$

With S_{nt} the cross-section surface of the NT with an external diameter d_{nt} (~2.7nm) and an internal one δ_{nt} (~1 nm), $S_{nt} = \pi(d_{nt}^2-\delta_{nt}^2)/4$ and N the number of single NT in the bundle. N is estimated for each bundle from the NW diameter (d_{nw}) and the NT diameter d_{nt} by $N\approx (d_{nw}/d_{nt})^2$ (assuming a cylindrical NW). We get values of σ_{Lnt} of the same order of magnitude, but 15-20% larger than above (on average).

Table 4.3. Dataset of the V-I curves from one series of measurements. All the other datasets are given in annexe A4.3. Zero-bias NW longitudinal conductance (G_L), inner-probe distance (L), NW diameter and surface (d_{nw} and S_{nw}), longitudinal NW conductance σ_{Lnw}, N number of NTs in the NW and longitudinal individual NT conductivity σ_{Lnt}.

#NW	G_L (µS)	L (nm)	d_{nw} (nm)	S_{nw} (nm^2)	σ_{Lnw} (S/cm)	N	σ_{Lnt} (S/cm)
#1	442	380	72	4072	413	711	479
#2	108	500	66	3421	157	598	182
#3	415	450	64	3217	580	562	673
#4	67	574	58	2642	147	461	170
#15	365	619	96	7238	312	1264	362
#16	93	428	61	2922	137	510	158
#17	181	624	80	5027	225	878	261
#18	223	474	81	5153	205	900	237
#19	105	528	86	5809	96	1015	111

Figure 4.17 shows the distributions of σ_{Lnw} and σ_{Lnt} deduced from the complete datasets (see annexe A4.3).

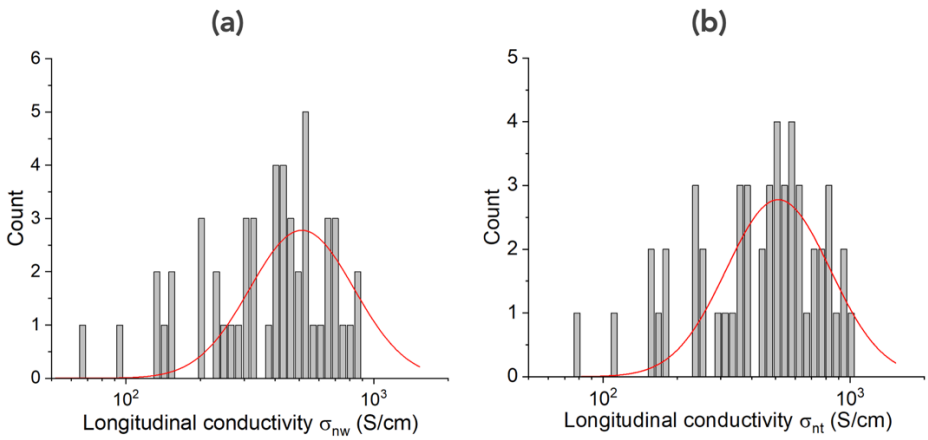

Figure 4.17. Histograms of longitudinal conductivity of (a) nanowire and (b) nanotube, fit with a log-normal distribution.

At 300K, we observed a distribution of single NT conductivity values σ_{Lnt} between ≈ 10^2 and 10^3 S/cm with a majority of values (>95%) above 100 S/cm. We obtained (log-normal fits) mean value $\overline{\sigma_{Lnt}}$ ≈ 510 S/cm, $\overline{\sigma_{Lnw}}$ ≈ 440 S/cm (Figure 4.17).

These values are really high compared to previous reports in the literature for tungsten oxide NWs (WO_3) yet obtained by different fabrication processes (CVD growth, pyrolysis-reduction process, thermal evaporation,…),[103,202–204] with values of electrical conductivity at RT between ~2 and ~15 S/cm, the highest value reported in the paper of Ji Zhang[206] on nanorod crystal. As the synthesis and so the morphologies of our nanowires/nanotubes are different, it is difficult to rationalise these differences, we just mention that our results out-perform the previously reported results for this class of tungsten suboxide nanostructures. Our results are on the part with those of NWs of the archetype conducting polymers. The RT conductivity of organic NWs based on conducting polymers (*e.g.* poly(3,4-ethylene dioxythiophene) (PEDOT), polyaniline (PANI), polypyrrole (PPY)) were reported between 10^{-1} and 10^{3} S/cm depending on doping level, polymer structure, presence of disorder and defects, diameter.[2, 3]

We compare the longitudinal and the perpendicular conductivities. As the measurements in both configuration have not been done in the same condition (UHV and e-beam exposure for the longitudinal conductivity and classical RT for the perpendicular one), we try to adjust the longitudinal values by considering the effect of the e-beam exposure. By doing an electrical measurement of a planar network of NWs before and after SEM exposure, we estimated that the longitudinal conductivity after SEM exposure is over-evaluated by a factor ~ 1.5 (annexe A4.4). The mean anisotropy factor is then given by $\overline{(\sigma_{Ln}/1.5)/\sigma_P}$ and we obtained ~ 10^5.

This corresponds to a large expected anisotropy. Indeed, in the C-AFM configuration, the electron transport across the NWs is hopping between neighbouring NTs. In this case, the large dispersion (Figure 4.17) seems to be caused by a large sensitivity of the electron transport to the precise organization of adjacent NTs. Whereas in the longitudinal transport, electrons are transported along individual NTs in parallel, probably without the needs of strong interaction between them.

- **Semi-conductor or metal-like behaviour?**

To examine whether the NWs have a metallic behaviour or a semiconducting one, we proceed to two experiments, still using the 4-probe STM. Firstly, we did the same experiment as before but at lower temperatures (Figure 4.18). Secondly, we use this time only two probes and put the NW in a transistor configuration by applying different gate voltages on the underlying Si substrate (Figure 4.20).

We did measurements at 120, 170, 210 and 250K. We cooled the sample holder stage with liquid nitrogen and we wait around one hour that the temperature is stabilized. By cooling the sample, we observed some drifts of the sample holder, thus the probes are far away of the surface until the complete stabilization of the system (see annexe A4.3).

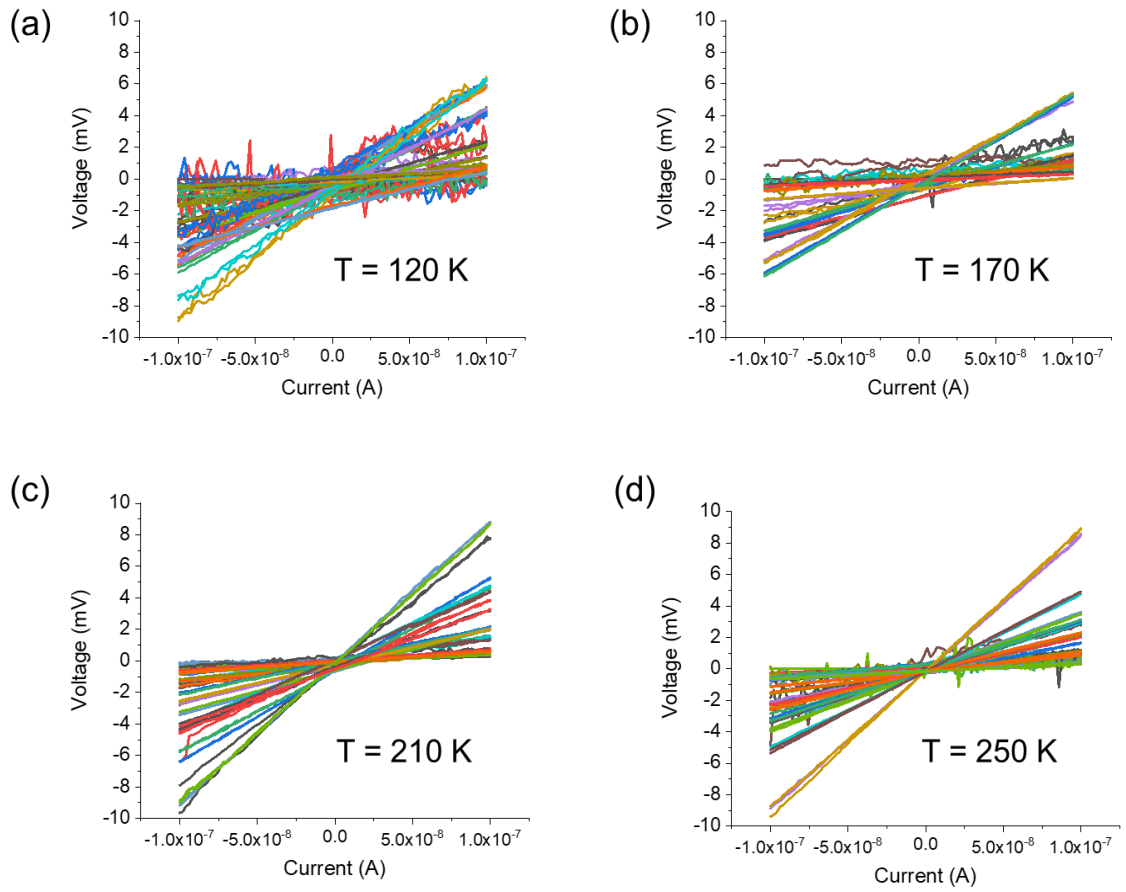

Figure 4.18. V-I curves of 4-probe measurements at (a) 120, (b) 170, (c) 210 and (d) 250 K (voltage offsets on V-I curves are not corrected here as it does not impact the value of the slope that interests us here).

19 V-Is at 120K, 13 V-Is at 170K, 16 V-Is at 210K and 19 V-Is at 250K are plotted in the Figure 4.15 (datasets in annexe A4.3), one V-I trace per NW. At 120K, the curves are noisy because it becomes hard to contact the nanowire properly, which can easily break during or after the measurement (annexe A4.3). The majority of the measured voltages at each temperature are in the range |0; 0.06|V and no significant difference is found as function of the temperature. Then, all the calculated longitudinal NT conductivity values, σ_{Lnt}, are plotted as a 3D histogram listing all the NT conductivity values for each temperature, and at 300K for comparison (Figure 4.19a).

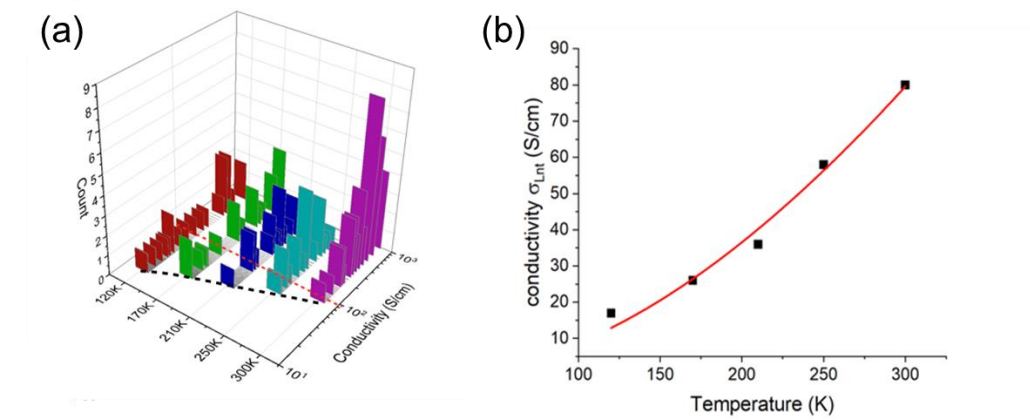

Figure 4.19. (a) Histogram of the temperature dependent conductivity σ_{Lnt} measurements and (b) Plot of the lowest conductivity (black dashed line in Figure 13a) versus temperature and fit with a VRH model (r^2=0.98).

More the temperature decreases, more the conductivity values are broadening, now between 10 and 10^3 S/cm. Still, the majority of values (65-85%) are superior to 100 S/cm, as observed at 300K. This first result allows us to suppose that overall, a large part of the nanotubes present an activation-less temperature behaviour. For the other NTs, if we take the lowest conductivity at each temperature (black dashed line Figure 4.19a), these values follow the Mott Variable Range Hopping (VRH) law. As shown in Figure 4.19b, we plot the conductivity as a function of the temperature and we fit with the equation:

$$\sigma_{L,nt} = \sigma_0 * \ exp\left(-\left(\frac{T_M}{T}\right)^{1/4}\right) \tag{4.5}$$

with T_M the Mott temperature (fitted value ~ 8.5×10^5 K). This model characterizes ET in disordered semiconductors and amorphous solids.[216,217] We conclude that a small part of the NTs have a semiconductor behaviour. Other temperature-dependent mechanisms, *e.g.* thermally activated (Arrhenius) or polaron hopping transport as suggested for $W_{18}O_{49}$ nanowires synthesized by a high temperature (600°C) furnace process,[7] were discarded because they gave a poor fit of the data (see annexe A4.3).

Then, we have measured a NW in a field-effect transistor configuration (Figure 4.20).

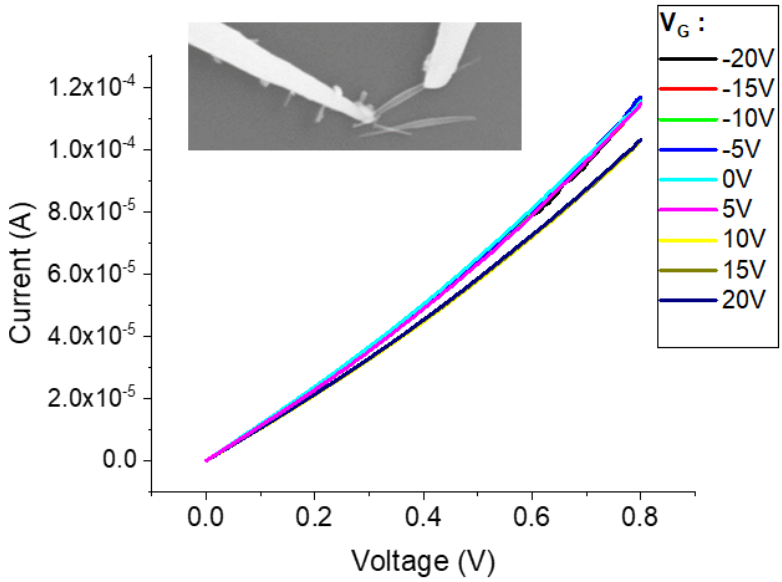

Figure 4.20. I_d-V_d curves in two-probe configuration at different gate voltages.

We connected a nanowire with two probes (as source and drain electrodes) and then, we applied a gate voltage (V_g) on the underlying highly doped Si and we measured the drain current between the two probes as function of the drain voltage (source grounded). No significant variation is observed on the I_d-Vd curves when V_g varies from -20V to +20V. It means there is no field effect on the electron transport in the NW. It confirms the metallic like behaviour of our $W_{18}O_{49}$ NW.

It is known (DFT) that a semiconducting-to-metal transition exits when increasing the oxygen vacancy (V_O) in WO_{3-x} from 2 to 4% (i.e. $0.06 < x < 0.12$).[218] Thus, the observed coexistence of metallic-like and semiconducting-like $W_{18}O_{49}$ NWs can be rationalized assuming a dispersion of the concentration of V_O in the synthesized NWs. Here, from the stoichiometry determined by XPS (see section II), we deduce a V_O concentration of about 3%, thus consistent with the experimental observation of a large fraction of metallic-like NTs.

IV. Conductance of a two-dimensional network of nanowires

As we noticed a large dispersion of V-I curves by connecting the four probes in one single nanowire and it is not possible to stay connected on the same NW during the temperature scan, we have tried to reproduce this temperature-dependent experiment with a dense 2D network of nanowires, connected by lithographed electrodes, which make the contact easier.

By drop casting (few amount of powder diluted in ethanol), we deposited a dense 2D network on a Si/SiO_2 (200 nm thick) wafer with 4 e-beam lithographed electrodes (designed for 4-probe measurements) and a pattern for transmission line method (TLM) (Figures 4.20 and 4.21).

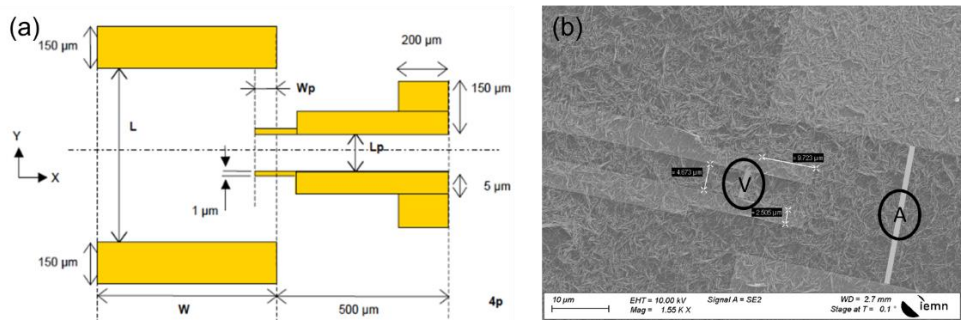

Figure 4.21 (a) Scheme of the 4 probes with 4 gold lithographed electrodes and (b) SEM image of the device with 2D network of NWs.

Here (Fig. 4.21), the inner-probe distance L_p is 5 µm, Wp = 10 µm, and we consider the thickness of the network close to the thickness of one nanowire i.e. 60 nm. We used the same configuration as for the 4-probe STM, applying a known current on the outer electrodes (the range of current is limited by the compliance of the set-up) and measuring the voltage between the inner electrodes.

At the same time, we also have measured the network conductivity with the TLM pattern, the inter-electrode distances ranging between 5 and 30µm (Fig. 4.22).

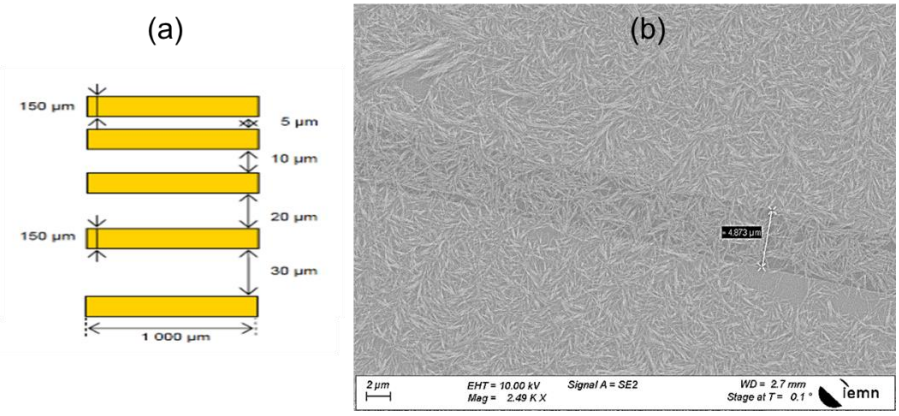

Figure 4.22. (a) Scheme of the TLM pattern with 5 gold lithographed electrodes and (b) SEM image of the deposited NW network.

In this configuration, the current is very sensitive to the exposure to air (Figure 4.23).

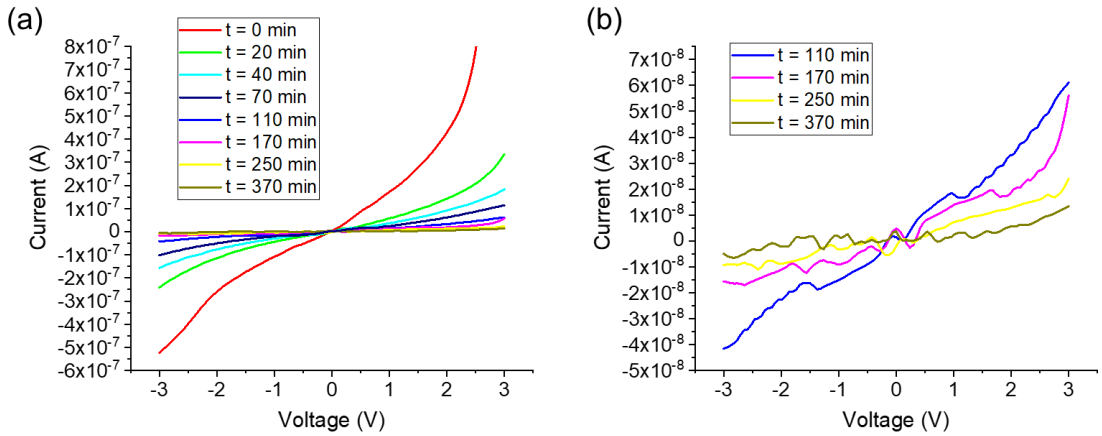

Figure 4.23. (a) I-V of a 2D network of NWs after exposition to air during 370 min, (b) zoom from 110 min.

After only 20 minutes, the current decreases considerably by a factor 2, and a factor around 100 after 370 minutes (Fig. 4.23, Table 4.4 recapitulates the current at -3V).

Table 4.4. Current and factor decrease at -3V in function of time exposition to RT

Time (min)	Current (A) at -3V	Factor decrease
0	-5.24×10^{-7}	-
20	-2.42×10^{-7}	2.2
40	-1.57×10^{-7}	3.3
70	-1.02×10^{-7}	5.1
110	-4.15×10^{-8}	12.6
170	-1.56×10^{-8}	33.6
250	-9.30×10^{-9}	56.3
370	-4.95×10^{-9}	105.9

Thus, all the following measurements have been done in vacuum to avoid the fast kinetics of oxidation. All the measures were done from 120 to 300 K in a cryogenic probe station (Lakeshore) with a pressure of around 10^{-6} mbar in the sample chamber with the help of Sylvie Lépilliet and Etienne Okada (IEMN).

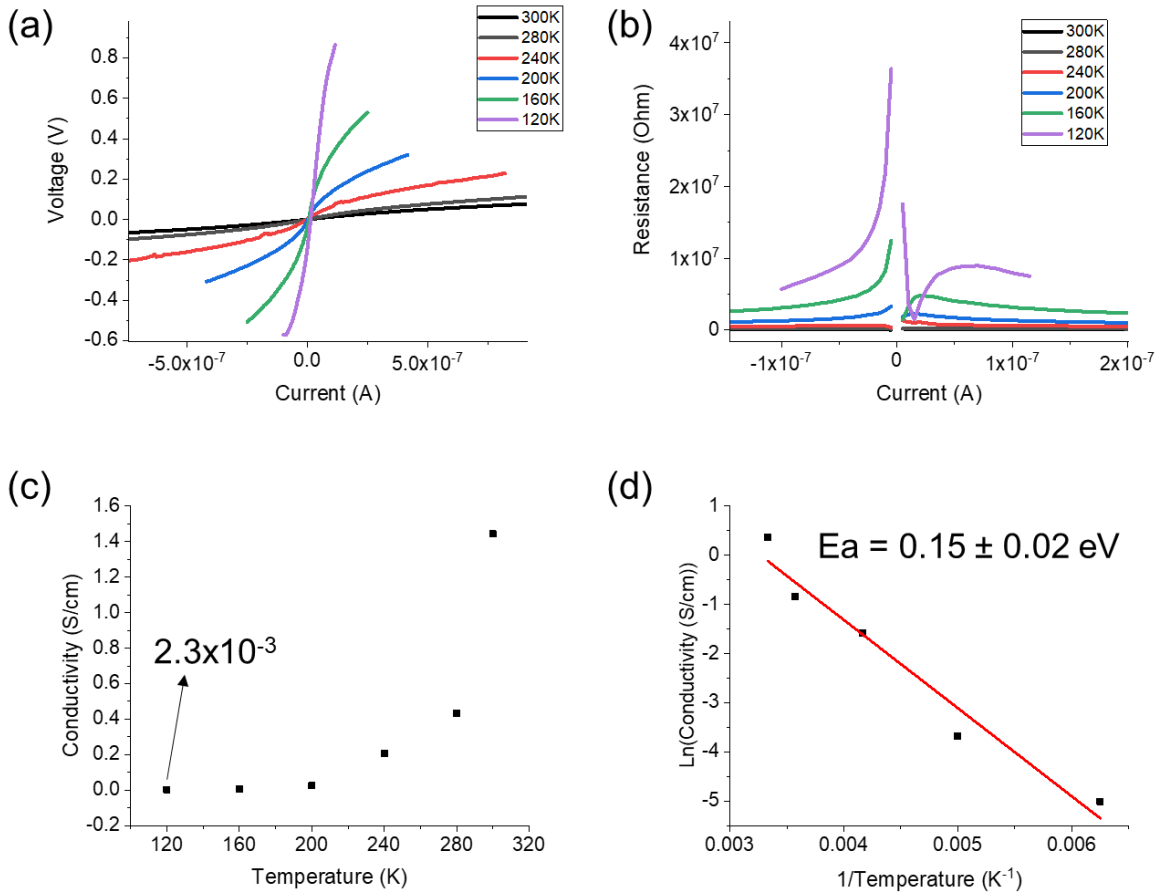

Figure 4.24. (a) V-I curves (b) R-I curves at different temperatures, (c) conductivity plot versus temperature and (d) plot of Arrhenius law.

Figure 4.24a shows the temperature dependence on these V-I curves (4 electrodes devices). In Figure 4.24b, we plotted R-I curves (resistance – current, R obtained by the ratio of V/I point by point). It is clear that the resistance increases when the temperature decreases. Figure 4.24c confirms this comment. The calculated value of the 2D network conductivity increases with the temperature, passing from $2.3x10^{-3}$ S/cm at 120 K to 1.4 S/cm at 300 K, increasing by a factor around $6x10^{2}$. In this configuration, we have deduced (Arrhenius plot: Ln(conductivity) vs. 1/T) that there is a temperature activated behaviour with an activation energy (E_a) value of 0.15 ± 0.02 eV (Figure 4.24d).

With the TLM motif, standard I-V measurements have been done between 120 and 300 K at six different distances between two electrodes.

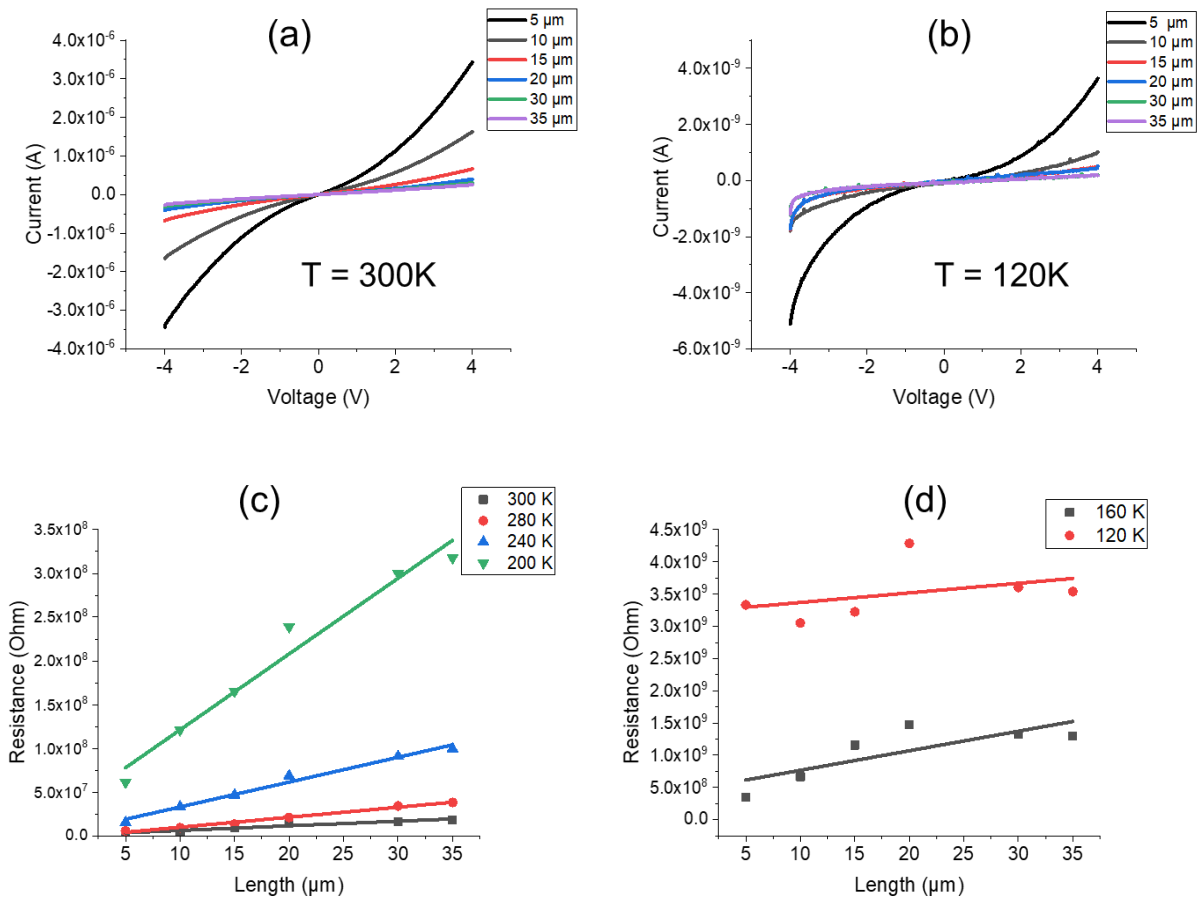

Figure 4.25. I-V curves at (a) 300K, (b) 120K and plot of resistance as a function of the length between two electrodes (c) from 300 to 200 K and (d) at 160 and 120 K.

As expected, the current decreases when the distance between the two electrodes increases. Moreover, we still clearly see the decrease of the current when the temperature decreases (Figure 4.25 a and b). For example, at -4V, for a 5 µm length, we are around -3.5×10^{-6} A at 300 K and -5.0×10^{-9} A at 120 K, which correspond to 7×10^{2} factor (coherent with the one observed in the 4-probe configuration). These values of resistance also increase when temperature decrease (Figure 4.25c and d).

The dependence of the measured resistance R_M versus the length L can be written according to this equation:

$$R_M = R_{C1} + \frac{\rho L}{S} + R_{C2} \tag{4.6}$$

with $R_{C1} + R_{C2}$ the two contact resistances, ρ the resistivity of the 2D network and S the section (with a width of the electrodes of 1 mm and the thickness of the network ~ size of one nanowire 60 nm). So we can extract the contact resistance ($R_{c1}+R_{c2}$) by taking the y-intercept value of each Resistance-Length curves and the conductivity from the slope of data shown in the Figures 4.25c and d and we have listed them in the Table 4.5 below:

Table 4.5. Contact resistance and 2D network conductivity determined at each temperature.

Temperature (K)	Contact Resistance $R_{c1}+R_{c2}$ (Ohm)	Conductivity (S/cm)
300	$4.5x10^5$	0.0032
280	$9.0x10^5$	0.0015
240	$4.7x10^6$	$5.9x10^{-4}$
200	$3.5x10^7$	$1.9x10^{-4}$
160	$4.6x10^8$	$5.5x10^{-5}$
120	$3.2x10^9$	$1.3x10^{-5}$

From the temperature-dependent conductivity, the activation energy E_a has been calculated as previously (Arrhenius law) and we obtained 0.12 ± 0.01 eV (annexe A4.5), close to the value deduced from the 4-probe configuration measurements. In addition, R_C also decreases with the temperature with E_a about 0.16 ± 0.02 eV (annexe A4.5).

With a dense network of NWs, we observe a temperature activated electron transport with an activation energy of the order of 0.12-0.15 eV, in contrast to the behaviour with a single nanowire. As this network is very dense and disordered, there are lots of intersection between the nanowires, generating lots of mechanical junction resistance. We do the hypothesis that these junction resistance values are larger than the resistance of one single NW and electrons hopping across these NW-NW contacts dominate the behaviour of the whole network. By consequences, we cannot use this study to confirm the metal-like behaviour of one single nanowire.

Conclusion

To conclude this chapter, we have synthesized nanowires with less oxygen vacancies than expected. The $W_{18}O_{49}$ nanowires synthesis is very sensitive to the precursor concentration, the solvent or to the air. The composition of the final product is not obvious and, as it exits lots of suboxide of WO_3, we can easily synthesize another one. However, all the characterizations show us that we have one phase with a non-conventional structure of a bundle of nanotubes with a seed inside.

Concerning the perpendicular electronic measurement of one single nanowire, the measured current is dominated by a capacitance effect when the thickness of a NW is weak (<30 nm) and we do not observe it anymore when the thickness increases (e.g. 50-60 nm). For the longitudinal measurement, we notice a high conductance (up to 10^3 S/cm), not reported for other tungsten suboxide NWs in the literature. We have obtained a large anisotropy factor ~ 10^5 between the longitudinal and perpendicular conductivities, likely explained by different electron transport mechanisms: hopping mechanism between adjacent nanotubes in the bundle for the perpendicular conductivity and a dominant metal-like behaviour for the longitudinal conductivity.

General Conclusion and outlook

General Conclusion

The use of conductive-AFM and polyoxometalates are technique and molecules that have been extensively investigated in different research areas. This thesis works brought these elements together to focus on polyoxometalates in the field of molecular nanoelectronics. We worked on several POMs grouped in two structures Keggin and Preyssler.

The **chapter 1** was resituated the context of the thesis in three parts, the field of molecular nanoelectronics, some generalities about polyoxometalates and the development of reconfigurable and unconventional computing devices.

In the **chapter 2**, we have started by presenting a study of molecular junctions with a monolayer of $TBAPMo_{12}$ in the pristine or reduced to one electron state, stable enough in both states to do measurements. In the first case, when the MJ is composed of a SAM with a short alkyl chain (2 carbon atoms), no relevant difference was observed with the oxidized POM or the reduced one. With a longer chain (6 carbon atoms), the reduced PMo_{12} molecular junction is characterized by an increase of the conductance (a factor ~ 10) and asymmetric current-voltage curves (asymmetric ratio ~ 5.5). As electrical differences were observed, we have tried to reduce in-situ the POM by UV-irradiation. The kinetic reduction is slow, few hours are needed and the same to reoxidize the POM. However, we have succeeded in switching states three times, meaning we have a reversible redox switching thanks to UV irradiation. As important dispersion of the level of currents were observed in both cases, we have completed the analysis with the help of an unsupervised machine learning and clustering algorithms and divided the data in five clusters. We have demonstrated that a portion of POMs are already reduced in the as-fabricated MJs with the oxidized POM. Moreover, using simple analytical models, we have concluded that electron transport in PMo_{12}(0) junctions is controlled by the LUMO located at ~ 0.6-0.7 eV above the Fermi energy of the electrodes, with 25% of the junction dataset are characterized by a better electronic coupling to the electrodes. The electron transport in PMo_{12}(I) junctions and the asymmetric current-voltage behaviour are ascribed to a combined electron transmission through energetically closed (0.3-0.4 eV) SOMO and SUMO levels near resonance with the Fermi energy of the electrodes.

The second part of the **chapter 2** was about another POM, P_5W_{30}. In order to do similar study with P_5W_{30}, we proceed to the reduction of this one, first in-situ by UV irradiation. After the in-situ reduction of KP_5W_{30}, a weak effect was observed on the level of current. We have investigated further by proceeding to the chemistry reduction of $TBAP_5W_{30}(0)$. We have reduced this POM in an aqueous media with sodium dithionite. After elementary analysis, we have figured out we reduced this POM to $TBANaP_5W_{30}(III)$, so a P_5W_{30} reduced to 3 electrons. Interestingly, we have found almost the same level of current but with different parameters of the electronic structure (MO energy levels and electronic coupling to the electrodes defined by TVS method) for the molecular junction with these oxidized and reduced POMs. Unlike PMo_{12}, the kinetic of oxidation/reduction is fast with P_5W_{30} and despite the precautions taken to measure their electrical properties, we were probably confronted to stability issues.

To synthetize $TBAP_5W_{30}(0)$, we have proceeded to an exchange of counterions, passing to K, then H and finally TBA. The ePOM team has already synthesized another P_5W_{30} with NH_4. At this point, we had four different P_5W_{30} so we did a study of the effect of the counterions on the electron transport properties. Approximately same level of currents are observed with the four molecular junctions. As with the redox conductance, using TVS method, we have distinguished these POMs by different LUMO level from 0.46 to 0.85 eV and different electrode couplings from 0.14 to 3.7 meV, respectively, in the order K, NH_4, H, TBA.

To conclude this chapter, whether for the electronic transport properties with reduction or with counterion, we notice no relevant difference in the value of currents but a more important one for the electronic structure.

Concerning the **chapter 3**, we have presented results of 2D POM network. The first part was about the implementation of this network called NPSAN inside a lithographed pattern with six electrodes. After the deposition of a homogeneous film of gold nanoparticles with hexagonal arrangement surrounded by oleylamine, we proceed to an exchange of ligands by POMs. $HPMo_{12}$ was physisorbed around the NPs while $TBAPW_{11}SH$ was chemisorbed. We have succeeded in reducing $HPMo_{12}$ NPSAN by UV irradiation and obtained the same factor (~ 10) of increase of current observed with the $TBAPMo_{12}$ MJ described in chapter 2. Nevertheless, this current increase has disrupted the NPSAN and we could not do other measurements. Reducing $TBAPW_{11}SH$ is harder and despite the precaution, we have observed only a slight increase factor (~ 1.1). As the NPSANs were stable after irradiation, we have still tried to continue the electronic measurement to see if there is an effect before and after irradiation. Low-frequency noise and HHG measurements were done before (on the two POMs) and after

irradiation (only with $TBAPW_{11}SH$). The variability and rich ET dynamic in these devices observed from DC current-voltage, low-frequency noise and HHG measurements let us think these POMs are not prone for reconfigurable Reservoir Computing (no effect of irradiation) but for classical RC.

To conclude on the **chapter 4**, we have synthesized another metal oxide, some suboxide of WO_3 following solvothermal protocol to obtain $W_{18}O_{49}$ nanowires. Thanks to the characterization of these nanomaterials, we concluded to a $W_{18}O_{52.4}$ structure, so a $W_{18}O_{49}$ with less oxygen vacancies, probably due to slight differences during the whole synthesis. We have done several trials and obtained different morphologies in function of concentration, solvent or size of precursor but all the characterizations show us that we have one monoclinic phase with a non-conventional structure of a bundle of hundreds of nanotubes that we called nanowires, with a seed inside. We did perpendicular electronic measurement using RT-AFM in conducting mode and observed a capacitance on small nanowires (diameter < 30 nm) and no effect on bigger one (diameter ~ 60nm). Longitudinal electronic measurements have been done with a UHV STM, where four probes were contacted one nanowire. Comparing perpendicular and longitudinal conductances, we have obtained a large anisotropy factor ~ 10^5 (taking in account the difference of the two methods). It was likely explained by a hopping mechanism between adjacent nanotubes in the bundle for the perpendicular conductivity whereas electrons are transported along individual NTs in parallel for the longitudinal one. We have noticed a high conductance (up to 10^3 S/cm), not reported for other tungsten suboxide NWs in the literature and a dominant metal-like behaviour. In dense networks of nanowires, the opposite behaviour was dominated, i.e. semi-conductor like behaviour, because of the contact resistance between two nanowires.

Outlook

The work on redox-controlled conductance of $TBAPMo_{12}$ molecular junctions is the work the most accomplished among those of my thesis. There is no need to do supplementary experimentations but we are waiting for the results of the density functional theory (DFT) calculations to reinforce our study. After taking into account the organic linker, the difficulties are i) two different metals for the two electrodes, ii) many configurations possible to contact

the layer with the tip: is it with PMo_{12} or TBA, where are the counterions inside the junction? iii) how many molecules contact the surface of the tip?

Concerning the similar study with P_5W_{30}, we have results with the RT-AFM. However, due to its fast kinetic of oxidation/reduction in ambient air, it is preferable to use an UHV-AFM. Indeed, this new experiment will allow us to measure the electronic transport of the reduced POM. Electric measurements should be done with both samples (in pristine and reduced state). The second study about the influence of counterions in the electron transport properties does not need UHV condition. More theory works are needed to understand our results.

With the elements of response for the use of POMs in RC, we have finished this experiment with NPSANs with $HPMo_{12}$. Indeed, they are not stable once the POM is reduced. Concerning those with $TBAPW_{11}SH$, they are too hard to reduce and we can find a new protocol to do it. Nevertheless, we have succeeded to synthetize $TBAPW_{11}SH$ Au-NPs directly without the step of ligand exchanges but for the moment, we could not find a subphase to deposit some drops and form a film. A simple drop casting is not working. A perspective of this work is to find out how to do a homogeneous with hexagonal arrangements of Au-POM without exchange method, to facilitate the protocol and be sure of the presence of the POM all along the gold nanoparticles. As we also demonstrated that all the POMs can react differently after irradiation, we can extend these electric measurements to another POM susceptible to reduce after UV exposure and find another one prone for reconfigurable Reservoir Computing.

Regarding the tungsten suboxide nanowires, we have done a study about their conductance. We can prepare a nano-component with a 2D network of nanowires, a film as presented in the chapter 3. The link can be the nanowires and the nodes the contact between two of them. Then, we see if these networks of nanowires are prone for Reservoir Computing by doing IV, PSD and HHG measurements.

Annexes

Annexes of Chapter 2

Annexe A2.1. Fabrication of the molecular junctions

- **Bottom electrode**

Ultraflat template-stripped gold surfaces (^{TS}Au), with rms roughness of ~0.4 nm were prepared according to the method already reported.[111,112] In brief, a 300−500 nm thick Au and 40 nm thick Ti film was evaporated by sputtering on a very flat silicon wafer covered by its native SiO_2 (rms roughness of ~0.4 nm), which was previously carefully cleaned by piranha solution, i.e 15 min in 7:3 H_2SO_4/H_2O_2 (v/v). ***Caution***: Piranha solution is a strong oxidizer and reacts exothermically with organics. The wafer is rinsed with deionized (DI) water, and dried under a stream of nitrogen. Then, the wafer is exposed few minutes under UV-ozone to oxidize the surface of Ti. Clean 10x10 mm pieces of glass slide (ultrasonicated in acetone for 5 min, ultrasonicated in 2-propanol for 5 min, and UV irradiated in ozone for 10 min) were glued on the evaporated Au/Ti/TiO_2 film (UV-polymerizable glue, NOA61 from Epotecny), then mechanically peeled off providing the ^{TS}Au film attached on the glass side (Au film is cut with a razor blade around the glass piece).

- **Monolayers**

The self-assembled monolayers (SAMs) of 2-aminoethane-1-thiol (HS-$(CH_2)_2$-NH_2) and 6-aminohexane-1-thiol (HS-$(CH_2)_6$-NH_2) were prepared following a protocol optimized and described in a previous work for the electrostatic immobilization of POMs on amine-terminated SAMs.[76] The freshly prepared ^{TS}Au substrates were dipped in a solution of 2-aminoethane-1-thiol hydrochloride or 6-aminohexane-1-thiol hydrochloride (Sigma-Aldrich) at a concentration of 10^{-3} M in ethanol overnight in the dark. The samples were rinsed in ethanol for 5 min and then ultrasonically cleaned 5 min in deionized (DI) water. These SAMs were treated by a PBS (phosphate-buffered saline, pH=7.4) solution for 2 hours, followed by ultra-sonication in DI water for 5 minutes. The substrates were finally washed with ethanol and dried under nitrogen

flow. It was found that the PBS treatment removes the formation of aggregates on the aminoalkylthiol SAMs as well as avoids clustering of POMs during the electrostatic deposition, likely because this treatment optimizes the ratio of NH_3^+/NH_2 on the surface.[7] The electrostatic deposition of POM was done by immersion of these SAMs in a solution of POM at a concentration of 10^{-3} M in acetonitrile or H_2O for one to few hours. We checked by ellipsometry that the thickness of the POM layer was independent of the immersion time when the immersion time is longer than 1h.

- **Spectroscopic ellipsometry**

We recorded spectroscopic ellipsometry data (on *ca.* 1 cm^2 samples) in the visible range using a UVISEL (Horiba Jobin Yvon) spectroscopic ellipsometer equipped with DeltaPsi 2 data analysis software. The system acquired a spectrum ranging from 2 to 4.5 eV (corresponding to 300−750 nm) with intervals of 0.1 eV (or 15 nm). The data were taken at an angle of incidence of 70°, and the compensator was set at 45°. We fit the data by a regression analysis to a film-on-substrate model as described by their thickness and their complex refractive indexes. First, a background for the substrate before monolayer deposition was recorded. We acquired three reference spectra at three different places of the surface spaced of few mm. Secondly, after the monolayer deposition, we acquired once again three spectra at three different places of the surface and we used a 2-layer model (substrate/SAM) to fit the measured data and to determine the SAM thickness. We employed the previously measured optical properties of the substrate (background), and we fixed the refractive index of the organic monolayer at 1.50.[17] We note that a change from 1.50 to 1.55 would result in less than a 1 Å error for a thickness less than 30 Å. The three spectra measured on the sample were fitted separately using each of the three reference spectra, giving nine values for the SAM thickness. We calculated the mean value from this nine thickness values and the thickness incertitude corresponding to the standard deviation. Overall, we estimated the accuracy of the SAM thickness measurements at ± 2 Å.[219]

- ***TM-AFM.***

Topographic images were acquired in tapping mode (TM) on an ICON (Bruker) microscope using a silicon tip (NCHV-A from Bruker, 42 N/m spring constant, resonance frequency 320 kHz) at room temperature and in ambient condition. The AFM images were treated with the Gwyddion software.[220]

- **Top electrode**

The top electrode is Pt coated tip (RMN-12PT400B from Bruker, 0.3 N/m spring constant). The load force was set at ≈6-8 nN for all the I-V measurements. A lower value leading to too many contact instabilities during the I-V measurements. Albeit larger than the usual loading force (2-5 nN) used for C-AFM on SAMs, this value is below the limit of about 60-70 nN at which the SAMs start to suffer from severe degradations. For example, a detailed study[121] showed a limited strain-induced deformation of the monolayer (≲ 0.3 nm) at this used load force. The same conclusion was confirmed by our own study comparing mechanical and electrical properties of alkylthiol SAMs on flat Au surfaces and tiny Au nanodots.[120] To form the molecular junction, the conductive tip was located at a stationary contact point on the SAM surface at controlled loading force (~ 6-8 nN).

Annexe A2.2. Methods of electrical measurements

- **C-AFM**

Current−voltage characteristics were measured by conductive atomic force microscopy (Icon, Bruker). The voltage was applied on the substrate, the tip is grounded via the input of the current-voltage preamplifier. The C-AFM tip is located at different places on the sample (typically on an array - 10x10 grid - of stationary contact points spaced of 50-100 nm), at a fixed loading force and the I−V characteristics were acquired directly by varying voltage from –1.5V to +1.5V and from +1.5V to –1.5V for each contact point. The I-V characteristics were not averaged between successive measurements and typically up to 600 I-V measurements were acquired on each sample.

- **Data analysis**

Before to construct the current histograms and analyze the I-V curves with the one energy-level model and the transition voltage spectroscopy (TVS) method, the raw set of I-V data is scanned and some I-V curves were discarded from the analysis:

- At high current, the I-V traces that reached the saturating current during the voltage scan (the compliance level of the trans-impedance amplifier, typically $5x10^{-9}$ A in Fig. A2.1, depending

on the gain of the amplifier) and/or I-V traces displaying large and abrupt steps during the scan (contact instabilities).

- At low currents, the I-V traces that reached the sensitivity limit (almost flat I-V traces and noisy I-Vs) and displayed random staircase behavior (due to the sensitivity limit - typically 0.1-1 pA depending on the used gain of the trans-impedance amplifier and the resolution of the ADC (analog-digital converter), Fig. A2.1.

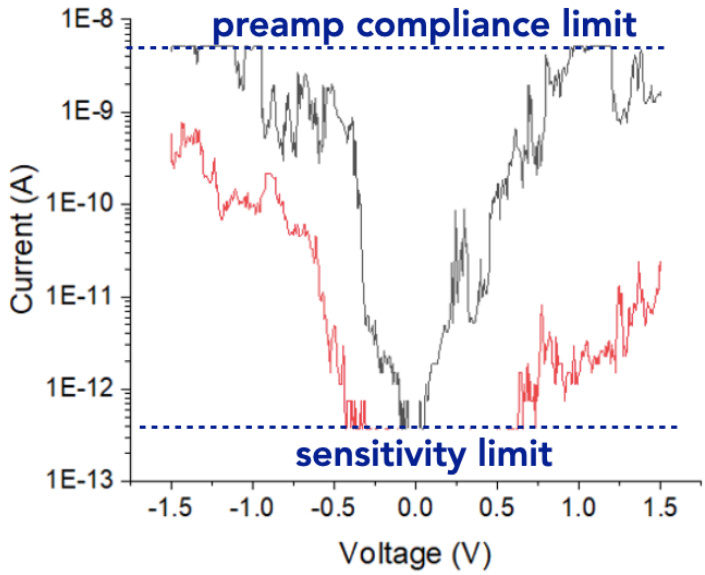

Figure A2.1. *Typical examples of I-V curves discarded from the data analysis.*

- **Fit of the single energy level (SEL) model**

The mean Ī-V curves and all the I-V traces were fitted individually with the single energy-level (SEL) model (Eq. 3, chapter 1_Ic) with 3 fit parameters: $\varepsilon_{0\text{-SEL}}$ the energy position (with respect to the Fermi energy of electrodes) of the molecular orbital involved in the electron transport, Γ_1 and Γ_2 the electronic coupling energy between the molecules and the two electrodes. The fits were done with the routine included in ORIGIN software, using the method of least squares and the Levenberg Marquardt iteration algorithm for the mean Ī-V curve and using Python algorithm for the complete dataset.

The SEL model is a low temperature approximation albeit it can be used at room temperature for voltages below the resonant transport conditions[39,49] since the temperature broadening of the Fermi function is not taken into account. Moreover, a possible voltage dependence of $\varepsilon_{0\text{-SEL}}$ is also neglected.[221] It is known that the value of $\varepsilon_{0\text{-SEL}}$ given by the fit of the SEL model

depends on the voltage window used for the fit.[39,49,221] This feature is confirmed (Fig. A2.2) showing that unreliable values are obtained with a too low voltage range (i.e. the SEL model is not reliable in the linear regime of the I-V curves) and not applicable when the voltage is high enough to bring the electrode Fermi energy close to molecular orbital (near resonant transport), here for a voltage window larger than -1.2 V /1.2 V where the fits are bad and the values of $\varepsilon_{0\text{-SEL}}$ collapse. For voltage windows below -1V/1V we clearly see the lowering of $\varepsilon_{0\text{-SEL}}$ by about 0.15-0.2 eV after reduction of the POMs. For comparison, the same mean $\bar{I}$-V curves are also analyzed by TVS (Fig. 2.15, main text). For example, we obtain a good agreement with the SEL model limiting the fit in the voltage window -1V/1V with the C6-PMo_{12} MJs. For these reasons, we limited the fits to a voltage window -1 V to 1 V to analyze the complete datasets shown in Fig. 2.15 (Chapter2_IId). To construct the histograms of the values of $\varepsilon_{0\text{-SEL}}$, Γ_1 and Γ_2 (Fig. 2.16 and 2.17 in Chapter2_IId, we discarded the cases for which the fits were not converging of not accurate enough (i.e. R-squared < 0.95). In the case of the reduced PMo_{12}(I), the SEL model does not fit the data whatever the voltage window considered (Fig. A2.2), likely because the OM involved in the transport is too close to the Fermi energy (≈0.3 eV determined by TVS, Fig. 2.15), a situation where the model is not valid. Thus only the TVS method was used to analyze the I-V dataset in this latter case.

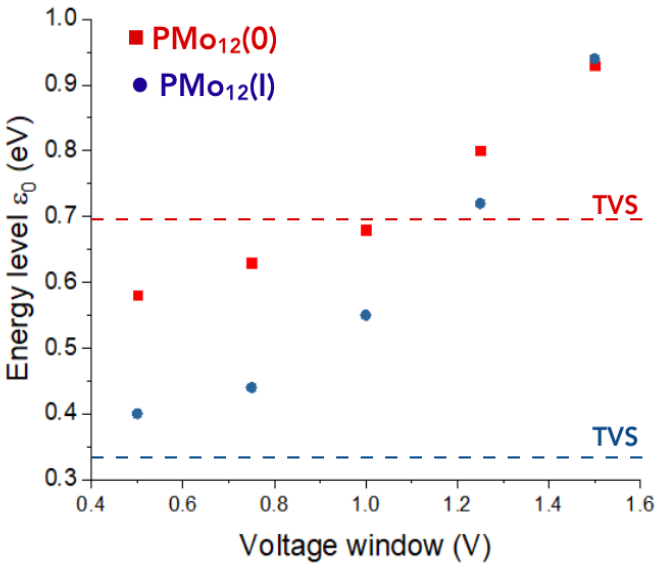

Figure A2.2. *Values of $\varepsilon_{0\text{-SEL}}$ obtained with the SEL model fitted on the mean $\bar{I}$-V curves (Figs. 2.15 in Ch. 2_IId) for the ^{TS}Au-C6/PMo_{12}(0)//Pt and ^{TS}Au-C6/PMo_{12}(I)//Pt with increasing voltage windows (-0.5/0.5 V to -1.5/1.5 V) for the fits. The dashed lines indicate the value obtained by the TVS method (Fig. 2.15 in Ch. 2).*

Annexe A2.3. POM characterization

- **Nuclear magnetic resonance (NMR)**

^{31}P NMR spectra were obtained at room temperature in 5 mm o.d. tubes in a Bruker Avance II 300 spectrometer equipped with a QNP (Quattro Nuclear Probe for H,C,F,P elements) probe head.

- **Ultraviolet–visible (UV/VIS) Spectrometer**

UV-VIS absorption spectra were recorded using Perkin Elmer - Lambda800 spectrometer. The solutions are placed in a quartz tube and one scan is done from 800 to 200 nm.

- **X-ray photoelectron spectroscopy (XPS)**

High resolution XPS spectra were recorded with a monochromatic $Al_{K\alpha}$ X-ray source ($h\upsilon$ = 1486.6 eV), a detection angle of 45° as referenced to the sample surface, an analyzer entrance slit width of 400 µm and with an analyzer pass energy of 12 eV. In these conditions, the overall resolution as measured from the full-width half-maximum (FWHM) of the Ag $3d_{5/2}$ line is 0.55 eV. Background was subtracted by the Shirley method.[222] The peaks were decomposed using Voigt functions and a least squares minimization procedure. Binding energies (BE) were referenced to the C 1s BE, set at 284.8 eV.

- **Infrared (IR)**

Some grains of POM were mixed within a KBR tablet and IR spectra were then recorded in transmission from 250 to 4000 cm^{-1} on a Jasco FT/IR 4100 spectrometer (Resolution 4 cm^{-1}) in ePOM laboratory.

Annexe A2.4. Illumination setup

We used a UV lamp from analytikjena lamp with a power ~ 0.5mW/cm² measured at a distance of ~1cm. This lamp has a wavelength centered at 302 nm (close to the absorbance peak of PMo_{12}, see Fig. 2.4). We put the lamp above the sample in the C-AFM setup at a distance ~1cm.

Annexe A2.5. Color switching of PMo12

A film of $PMo_{12}(0)$ formed by drop casting on a glass substrate (Fig A2.3 (a)) was irradiated in the same condition as the POM monolayer (Fig A2.3 (b)). Then, it was exposure to RT during few days (Fig A2.3 (c)). We observed a color change from yellow to green and reversibly to yellow again after exposure to air. It supports the reversibility of redox switching.

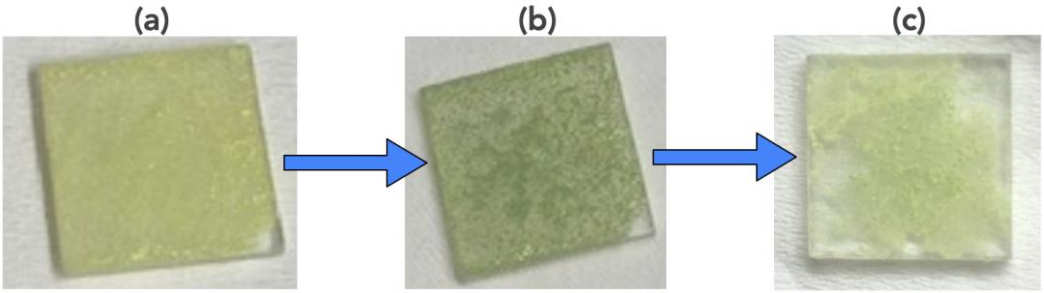

Figure A2.3. *Pictures of a drop cast films (a) before, (b) after UV irradiation for 6 h and (c) after few days exposed at air.*

Annexe A2.6. Machine learning and clustering

Machine learning and clustering have been done tailor-made for this request with MatLab from routines available online on https://github.com/MickaelPerrin74/ClusteringBenchmark and https://github.com/MickaelPerrin74/DataClustering.

- **Rationalized choice of the number of clusters**

To set the optimised number of clusters, we analysed the same dataset with different numbers of clusters from 2 to 6. Figure A2.4 shows the average Ī-Vs obtained for the ^{TS}Au-C6/PMo_{12}(0)//Pt junction dataset for 4, 5 and 6 clusters (clusters are labelled cN/M, with N the cluster number in decreasing order of current amplitude and M the total number of clusters). In all cases, cluster 1 corresponds to saturating I-Vs (current-voltage preamplifier compliance) during the measurements and this cluster is not considered further in the analysis. The average Ī-V curve of each cluster was analysed with the SEL model and the TVS method and the obtained MO energy levels are given in Table A2.1. It is clear that the solution with 4 clusters (and less, not shown) is not satisfactory because the c3/4 cluster can be decomposed (see feature spaces in panels (a) and (b) of Fig. A2.4) into two clusters (c3/5 and c4/5) with significant differences: i) the average Ī-V curve of c3/5 shows a negative asymmetric, while the c4/5 cluster shows an almost symmetric average Ī-V curve (panel (e) of Fig. A2.4); (ii) the ε_0 values (SEL and TVS) are different for c3/5 than for c4/5 (see Table A2.1 and Table A2.2), as well as the electronic coupling to the electrodes (Γ values, see Table 3 in chapt2_IId), while the values for the c3/4 cluster are intermediate between those of the c3/5 and c4/5 clusters. Thus, the analysis with 5 clusters is more relevant. The 6-cluster extension splits the c2/5 cluster into two (c2/6 and c3/6, see characteristic spaces in panels (b) and (c) of Figure A2.4, but the inferred ε_0 values (SEL and TVS) are similar (see Table A2.1), while the other clusters are not changed by the 6-cluster extension (Figures A2.4 and Table A2.1: c3/5 ≡ c4/6, c4/5 ≡ c5/6 and c5/5 ≡ c6/6). Thus, using 6 clusters does not add more relevant information and we conclude that the analysis with 5 clusters is the optimised approach.

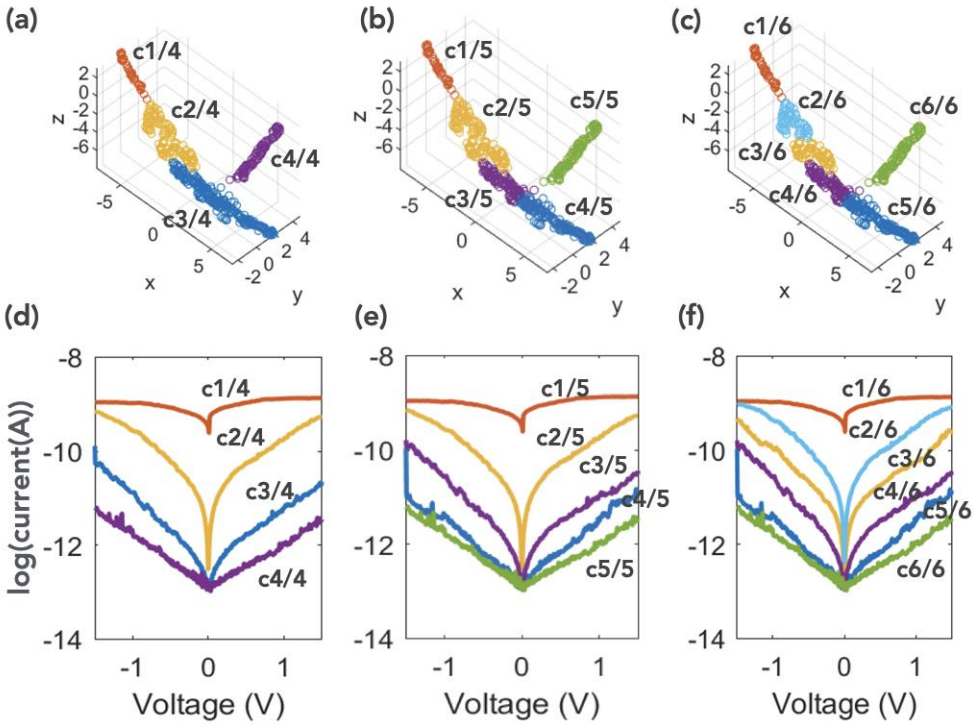

Figure A2.4. *^{TS}Au-C6/PMo$_{12}$(0)//Pt junction dataset. (a-c) feature spaces for 4, 5 and 6 clusters, respectively. (d-f) Mean abs(Ī-V) for 4, 5 and 6 clusters, respectively.*

Table A2.1. *Energy of the MO determined by the SEL model and the TVS method (on the mean Ī-V, Fig. A2.4 and Figs. 2.19 and 2.20 in the chapt2_IId for the clustering analysis with 4, 5 and 6 clusters. The light grey lines highlight the pertinent clusters.*

4 clusters	ε0-SEL (eV)	ε0-TVS (eV)	5 clusters	ε0-SEL (eV)	ε0-TVS (eV)	6 clusters	ε0-SEL (eV)	ε0-TVS (eV)
c2/4	0.69	0.65	c2/5	0.69	0.61	c2/6	0.69	0.65
						c3/6	0.70	0.64
c3/4	0.64	0.57	c3/5	0.67	0.60	c4/6	0.66	0.60
			c4/5	0.60	0.55	c5/6	0.60	0.54
c4/4	0.80	0.68	c5/5	0.81	0.72	c6/6	0.80	0.70

The same analysis conducted with the ^{TS}Au-C$_6$/PMo$_{12}$(I)//Pt junction dataset (Fig. A2.5and Table A2.2) leads to the same conclusion. The c2/M and c3/M clusters are identical regardless of the total number M of clusters (Fig. A2.5 and Table A2.2) and the c3/6 and c4/6 clusters

(analysis with 6 clusters) are identical and therefore this division is not useful. Comparing the analysis with 4 and 5 clusters, the cluster c4/4 can be decomposed into two clusters c4/5 and c5/5 (Fig. A2.5) with slightly different parameters (Table A2.2 and Table 2.3 in Ch.2, section IId). Thus, we also keep an optimised number of 5 clusters for the analysis of the ^{TS}Au-C6/PMo12(I)//Pt junction data set. This is also consistent for the comparison with the analysis of the TSAu-C6-PMo12(0)//Pt junction data set.

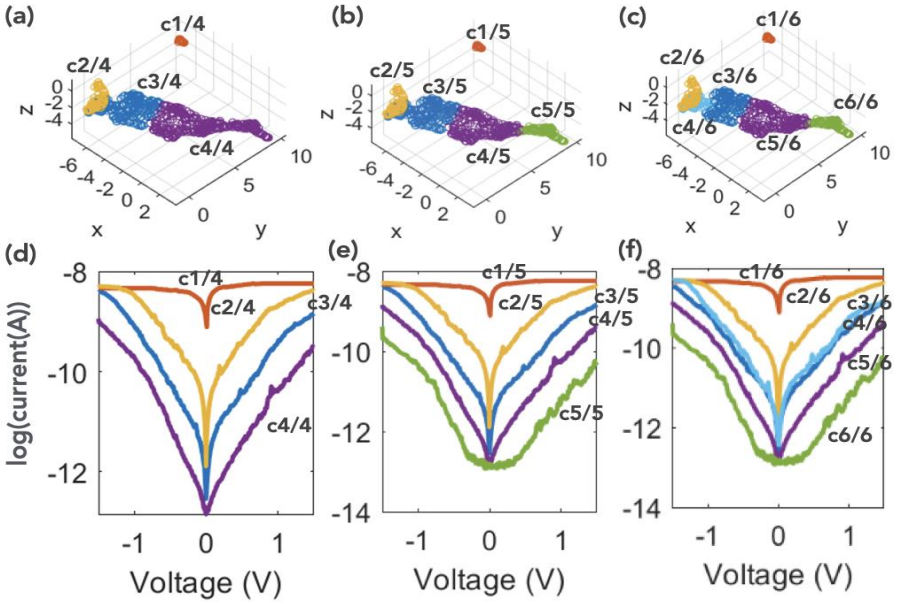

Figure A2.5. *^{TS}Au-C6/PMo$_{12}$(I)//Pt junction dataset. (a-c) feature spaces for 4, 5 and 6 clusters, respectively. (d-f) Mean Ī-V for 4, 5 and 6 clusters, respectively.*

Table A2.2. *Energy of the MO determined by the TVS method (on the mean Ī-V, Figs. A2.5, 2.24 and 2.25 in Ch. 2 section) for the clustering analysis with 4, 5 and 6 clusters. The light grey lines highlight the pertinent clusters.*

4 clusters	$\varepsilon_{0\text{-TVS}}$ (eV)	5 clusters	$\varepsilon_{0\text{-TVS}}$ (eV)	6 clusters	$\varepsilon_{0\text{-TVS}}$ (eV)
c2/4	0.41	c2/5	0.43	c2/6	0.41
c3/4	0.36	c3/5	0.38	c3/6	0.37
				c4/6	0.38
c4/4	0.29	c4/5	0.33	c5/6	0.28
		c5/5	0.28	c6/6	0.26

Annexes of Chapter 3

Annexe A3.1. Device fabrication

First, a ⟨100⟩ oriented silicon wafer was covered with a thermally grown, 200 nm thick, silicon dioxide, formed at 1100 °C during 135 min in a dry oxygen flow (2 L/min) and followed by a postoxidation annealing at 900 °C during 30 min under a nitrogen flow (2 L/min) in order to reduce the presence of defects into the oxide. Second, the e-beam lithography has been optimized by using a 45 nm-thick PMMA (4% 950 K, diluted with anisole with a 5:3 ratio), with an acceleration voltage of 100 keV and an optimized electron beam dose of 370 µC/cm 2 for the writing. After the conventional resist development (MIBK:IPA 1:3 during 1 min and rinsed with IPA), a metallic layer (2 nm of titanium and 12 nm of gold) were deposited by e-beam evaporation. Finally, after the lift-off process using remover SVCTM14 during 5 h at 80 °C, well-defined coplanar electrodes arranged around a ring with a diameter between 80 to 120 nm were realized.

Annexe A3.2. NPSAN characterization

- **Imaging**

Scanning Electron Microscopy (Zeiss ULTRA55) was used to inspect the electrodes and NPSANs (parameters: EHT = 10.00kV and signalA=InLens). The SEM images of NPSANs were treated with ImageJ[170] to measure the size of the NPs and the inter-nanoparticle distance using the function analyze particles and the plugins NND (nearest neighbor diameter).

- **Infrared**

IR spectra were done with a Perkin Elmer – spectrum 2000 instrument, 50 scans are accumulated from 700 to 3500 cm^{-1} to improve the signal/noise ratio with a resolution of 4 cm^{-}

[1]. For the $HPMo_{12}$ NPSANs, the exchange of ligands was directly done on the crystal of germanium instead of a silicon wafer (Figure A3.1) in ATR mode. The same protocol on Ge as SiO_2 was used. For the $TBAPW_{11}SH$ NPSANs, specular reflection mode (using 80Spec accessory from Pike technologies, fixed at 80-degree angle of incidence) was used, doing the exchange of ligands on a gold wafer following the same protocol as with SiO_2. This difference is mainly due to the difficulty to clean the Ge crystal.

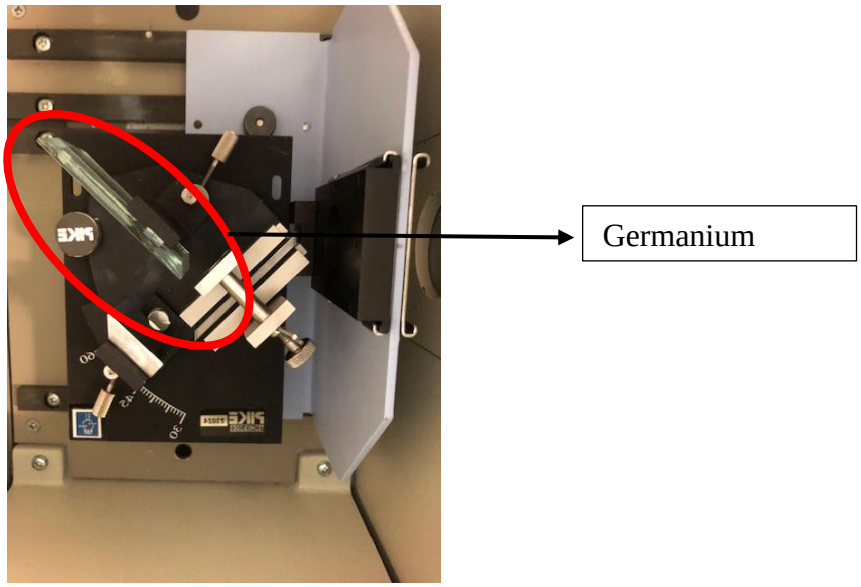

Figure A3.1. *Feature of measurement for* $HPMo_{12}$ NPSANs.

Annexe A3.3. NPSAN electronic measurements

- **IV: Current-Voltage**

The electrodes were contacted with a micromanipulator probe station (Suss Microtec PM-5) placed inside a glove box (MBRAUN) with a strictly controlled nitrogen ambient (less than 0.1 ppm of water vapor and oxygen). IVs were measured using a SMU (source/measure unit) Keysight B2901A.

- **LFN: low-frequency noise**

For LFN measurements, a low noise voltage source (Yokagawa 7651 or battery) was used to apply a DC voltage on one of the electrodes of the NPSAN (Figure 3.20, Chapter3_IIb) and the

output currents were simultaneously probed on two others electrodes and converted to voltage signals by two low-noise current-voltage transimpedance amplifiers (gain between 10^{-9} – 10^{-7} A/V) - DL instruments model 1211). The FFT was performed with a two-channel dynamic signal analyzer Agilent 35670A. An average was done on 50 scans from 1 to 100 Hz.

- **HHG: high harmonic generation**

For HHG measurement, a rather similar equipment was used (Figure 3.25a, see Chapter 3_IIc) but two pure sinusoidal signals (8.5 Hz and 18.5 Hz, peak to peak amplitude of 2V) were applied on two electrodes with a 2-channel Tabor waveform generator WW5062 sources. The AC output current on a third electrode was again amplified and converted to a voltage and analysed with the Agilent 35670A. An average of 10 scans was done from 5 to 805 Hz. From the FFT of sources, no harmonic is registered as illustrated in Figure A3.2.

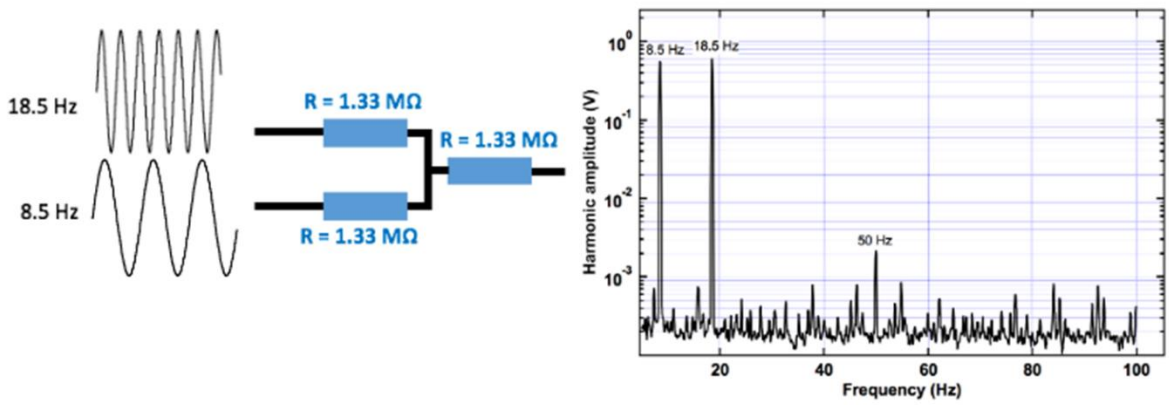

Figure A3.2. *Control experiment with calibrated resistors. Image from reference*[109]

Annexe A3.4. NPSAN fragility

To check the stability of the network, SEM images were done before and after the measurements. Sometimes, we figure out that after the measurements, the pattern (the electrodes or the NPSAN or both) has been damaged (Figure A3.3). It happened randomly but to limit the risk we first optimize the quality of the NPSAN and then, we did only 10 IVs from 0 to 1V (no return) with glovebox connected to a grounded outlet. With this precaution, the damages happened less frequently and we have succeeded in doing all the electronic measurements at each step, except with $HPMo_{12}$, where the patterns were automatically

damaged after irradiation. This phenomenon can be caused by the electromigration for the destruction of electrodes and the disorganization and fusion of NPs, as already seen by the team for NPSANs with other ligands.[110,223] In Figure A3.4, we have estimated at 1 V a density of current ~ 8.3×10^{6} A.cm^{-2} once the POM is reduced while the limit of electromigration of gold electrode is about 10^{5} A.cm^{-2}.

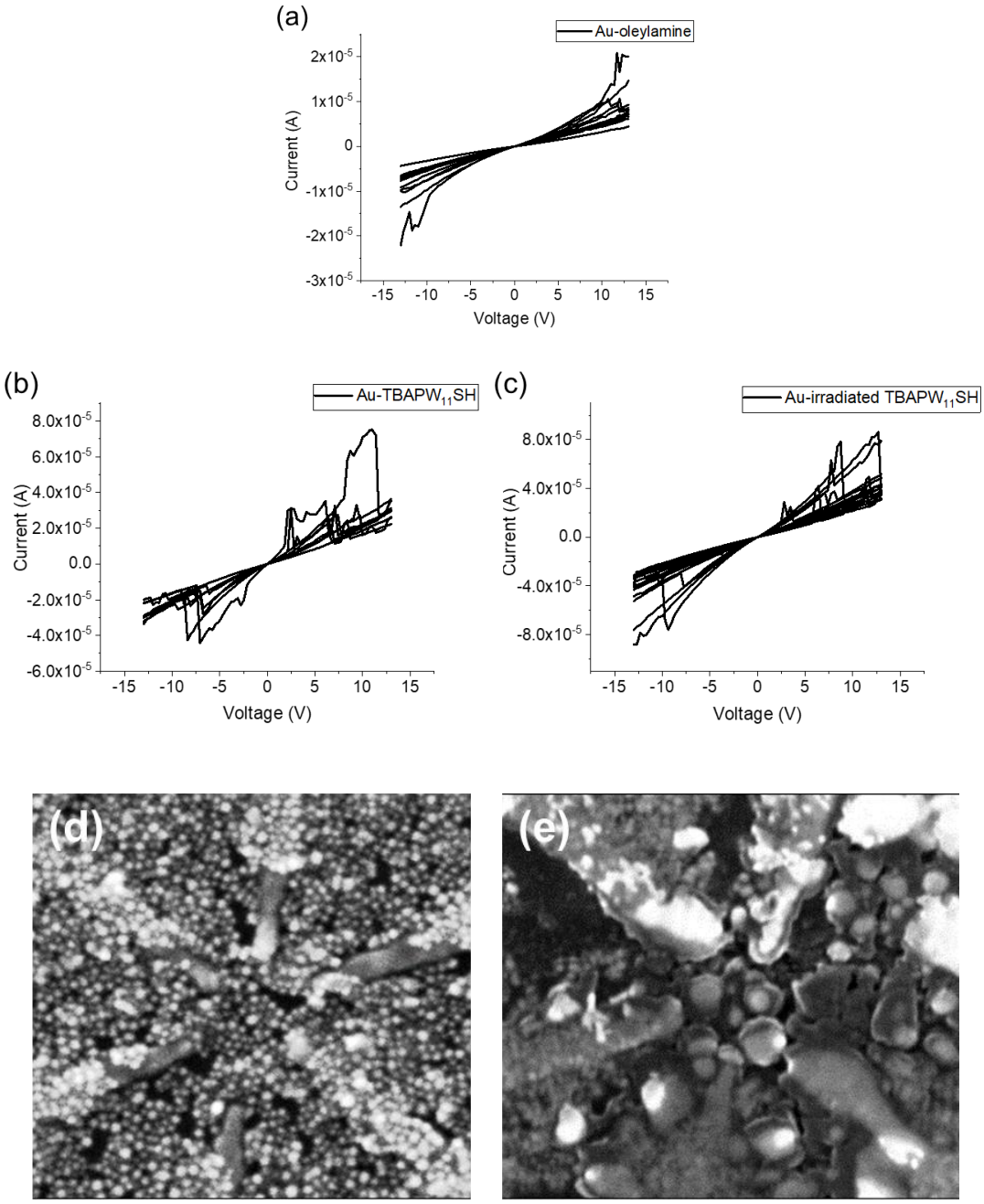

Figure A3.3. *15 IVs curves from -15V to + 15V for NPSAN with (a) oleylamine (b) TBAPW$_{11}$SH and (c) irradiated TBAPW$_{11}$SH. After the exchange of ligands, we directly see the electrical instability during measurement. SEM images (d) before measurement and (e) at the end of all the measurements. We observe huge fusion of NPs.*

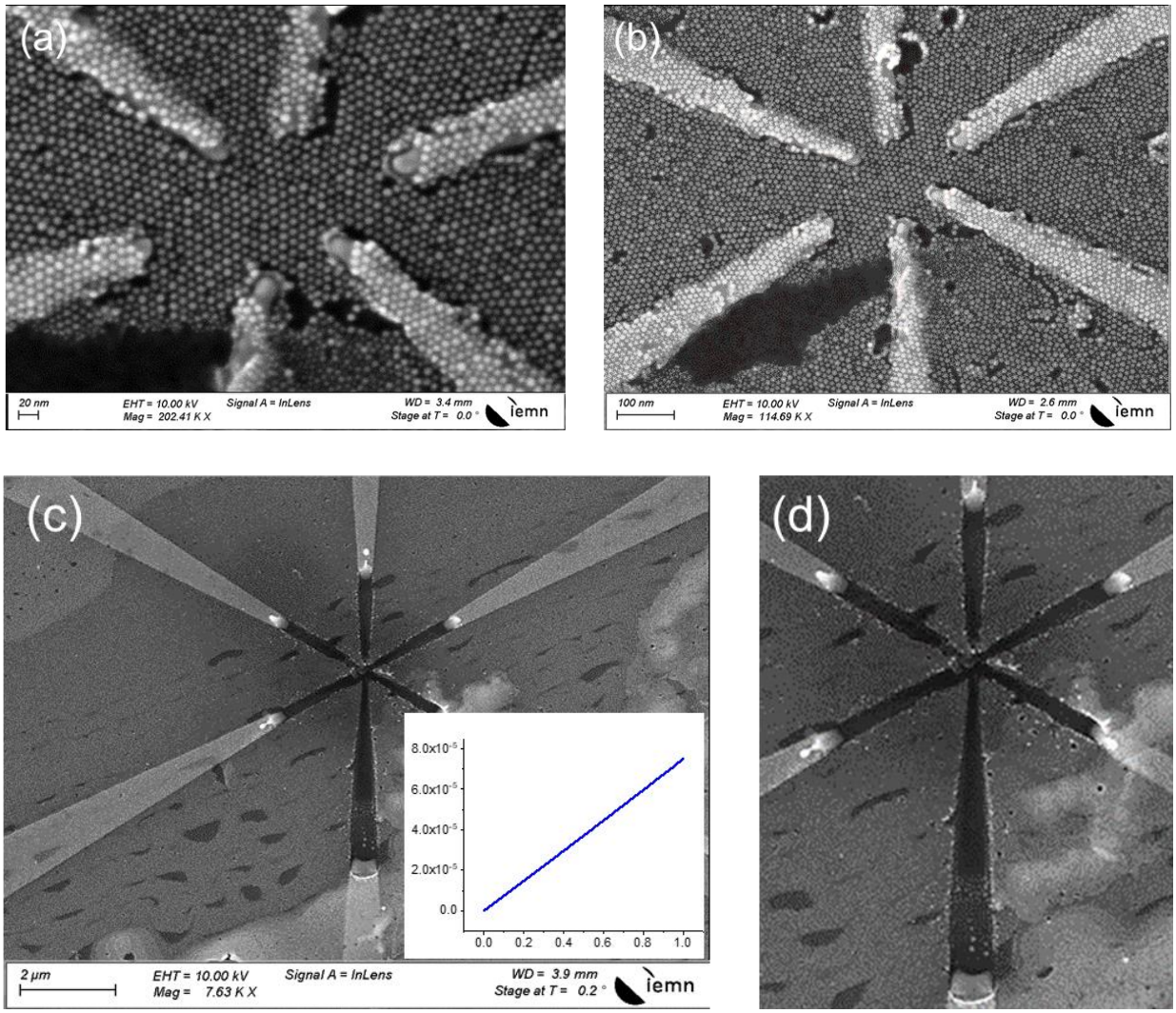

Figure A3.4. *(a) Initial NPSAN with oleylamine, (b) same NPSAN after exchange of ligands by* $HPMo_{12}$ *and measurements and (c) same NPSAN after irradiation of the POM and measurements, inset: mean IV curves obtained for NPSAN with reduced POM (d) zoom on the damaged electrodes.*

Annexe A3.5. LFN measurements with octanethiol and oleylamine at higher voltages

- **Reference with octanethiol**

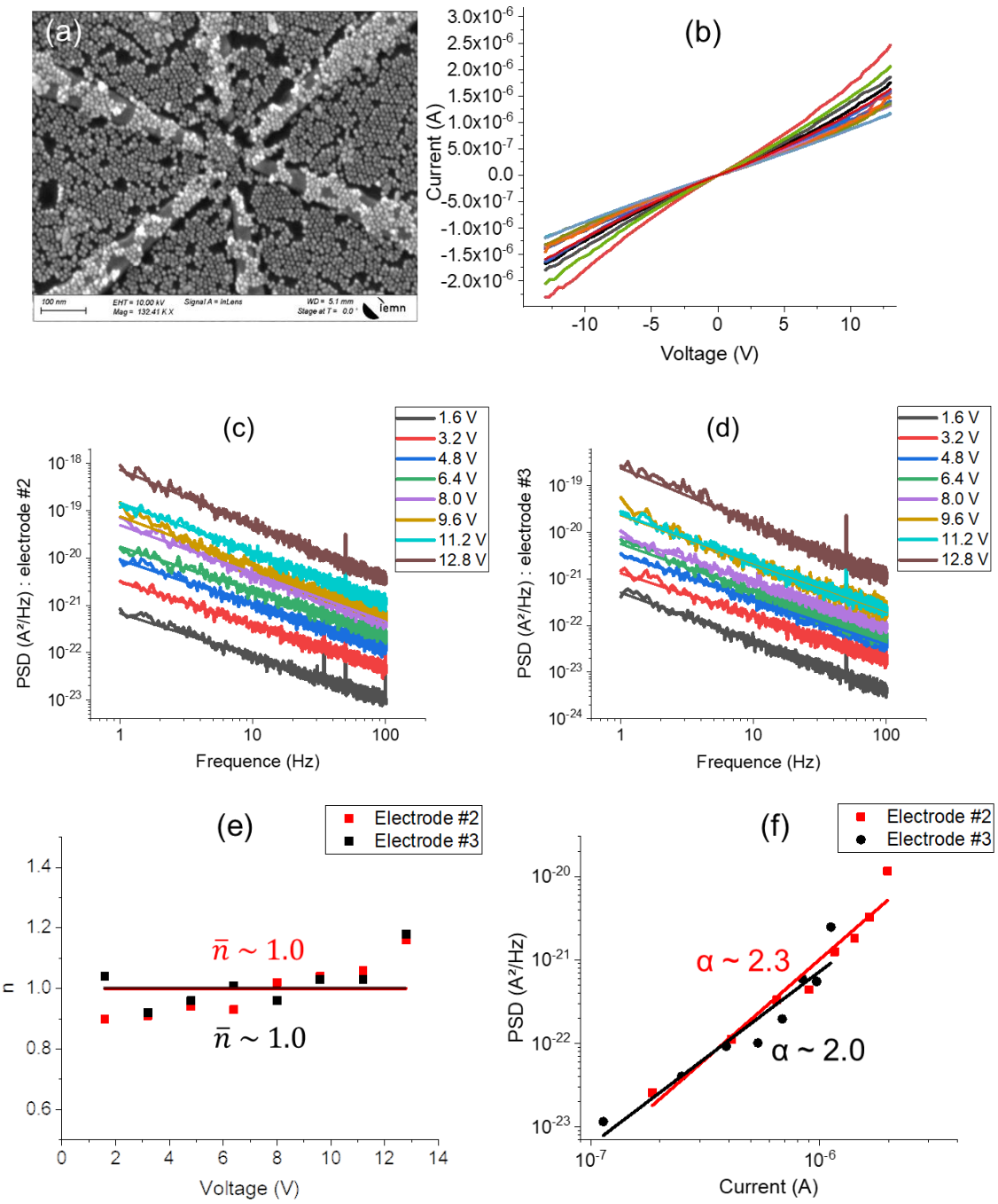

Figure A3.4. *(a) SEM image of NPSAN with octanethiol, (b) 10 IV curves of the pattern with octanethiol, (c) Graph of PSD at different voltages versus frequency, (d) graph of the frequency exponent at each voltage with $\bar{n}$ the mean value of n and (d) graph of PSD (at 40 Hz) versus DC current for NPSAN with octanethiol*

- **Reference with oleylamine**

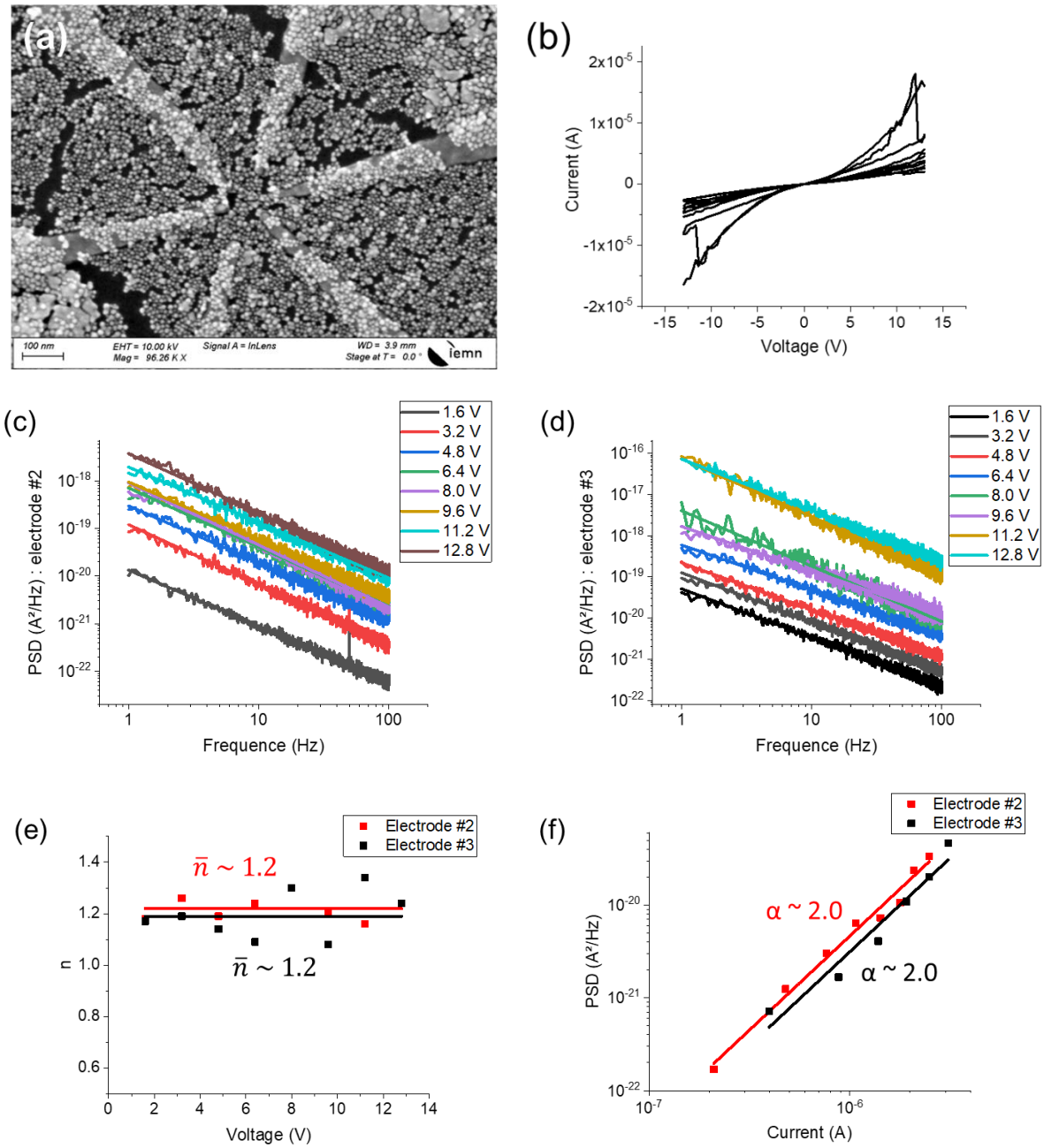

Figure A3.5. *(a) SEM image of NPSAN with oleylamine, (b) 10 IV curves of the pattern with oleylamine, (c-d) Graphs of PSD at different voltages versus frequency, (e) graph of the frequency exponent at each voltage with $\bar{n}$ the mean value of n and (f) graph of PSD (at 40 Hz) versus DC current for NPSAN with oleylamine*

- **Reference with azobenzene derivatives**[224]

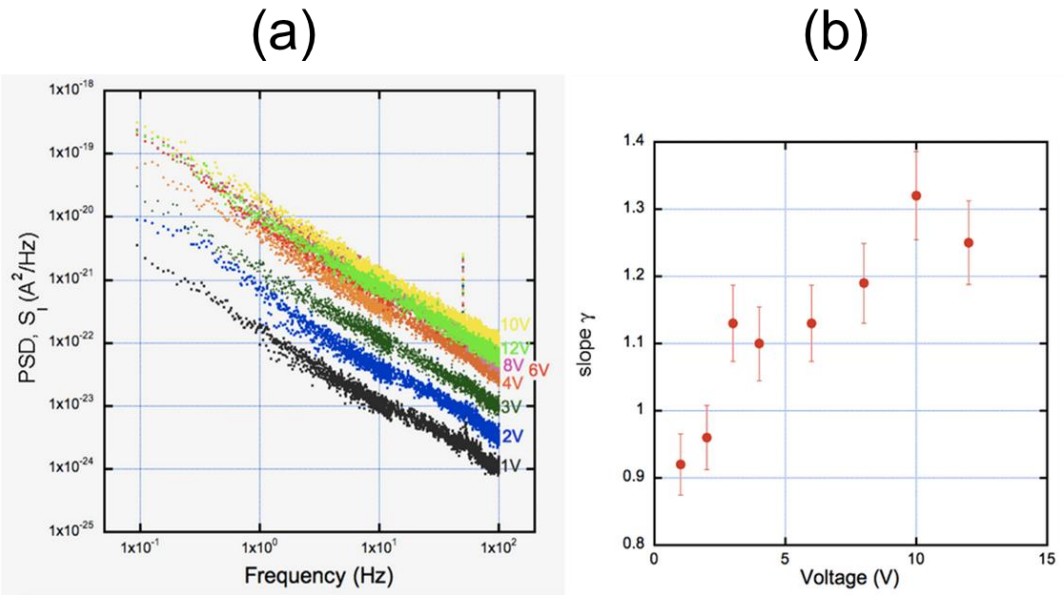

Figure A3.6. *(a) Graph of PSD at different voltages versus frequency and (b) graph of the frequency exponent at each voltage with n increasing with the voltage. AzBT in the trans form.*

Annexe A3.6. High harmonic generation of $HPMo_{12}$

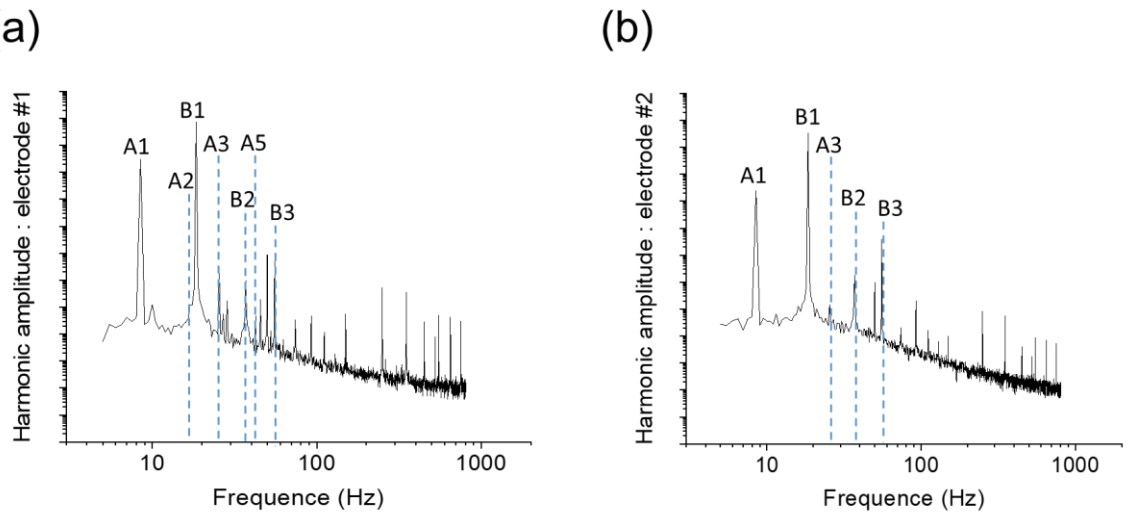

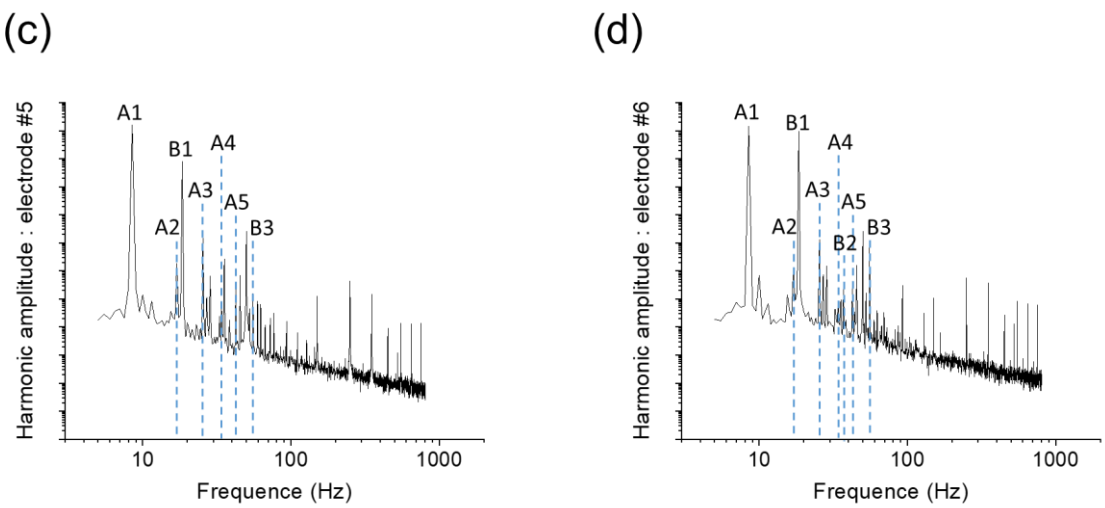

Figure A3.7. *Two sinusoidal signals, signal A at 8.5 Hz and signal B at 18.5 Hz (peak-to-peak amplitude VPP = 2 V for both) are applied at electrodes 3 and 4, respectively. (a–d) The four output currents are measured by the dynamic signal analyzer (FFT). HHG peaks are normalized. The HHG peaks are labeled as Ai (i = 1 for the fundamental, i = 2 for the second harmonic, etc.) and Bi for harmonics corresponding to the A and B input signals, respectively.*

Annexes of Chapter 4

Annexe A4.1. Synthesis and characterization of $W_{18}O_{49}$

Table A4.1. *Others examples of synthesis of $W_{18}O_{49}$.*

Trials	Mass WCl_6 (mg)	Solvent	Volume (mL)	Concentration (mM)	Mass final product $W_{18}O_{49}$ (mg)	Colour
#5	41.6	Ethanol	10	10.5	12	Verdigris
#6	40.7	Ethanol	10	12.3	14.8	Blue - grey

- **RAMAN**

We used a LabRAM HR confocal system from Horiba Jobin-Yvon with a 0.473 µm laser source. A few mg of $W_{18}O_{49}$ NWs were deposited on a glass substrate. A 473 nm excitation laser (≈1 mW) focused with a 100× objective was used for confocal Raman spectroscopy measurements in air at room temperature. Raman data were treated with Labspec5 software from Bruker.

- **X-ray powder diffraction (XRD)**

All the samples were analyzed by X-ray diffraction at the X-ray diffraction platform of the Institut de Minéralogie, de Physique des Matériaux et Cosmochimie (IMPMC), Sorbonne Université (Paris, France).

We used a Rigaku MM007HF diffractometer equipped with Varimax focusing optics, a RAXIS4++ image plate detector and a Mo rotating anode ($\lambda K\alpha_1$ = 0.709319 Å and $\lambda K\alpha_2$ = 0.713609 Å) at 50 KeV and 24 mA. The samples were placed in a 0.25 mm cryoloop and data were collected with a scan range of 3 to 45 º2Θ and an acquisition time of 10 minutes in transmission geometry. The Fit2D program (Hammersley, 2016) was used for the azimuthal integration of 2D images into 1D patterns (from 3 to 45 º2Θ) after a calibration with a LaB6 standard. Lebail refinements[211] were performed with the FullProf suite of programs.[225] The starting unit cell parameters were taken from ICSD-15254, the crystal structure of $W_{18}O_{49}$. The large unit cell parameters and the low symmetry of $W_{18}O_{49}$ and WO_3 compounds lead to a large number of Bragg peak positions, which do not allow affirming which crystal structure is the correct one.

- **TEM (transmission electron microscopy)**

All the samples were analysed by TEM at IMPMC, Sorbonne Université (Paris, France).

One Jeol 1011 microscope and two Jeol 2100 Plus microscopes were used (one with high resolution), with an accelerating voltage of 100 and 200 kV respectively, equipped with a LaB6 filament, with a point resolution of 1.8 Å and 1.4 Å in fringe. It is equipped with an X-ray detector (for X-EDS (Xray Energy Dispersive Spectroscopy): chemical analysis).

A small amount of powder was diluted in purged ethanol and then deposited in a carbon grid by drop casting. Then, the acquisition of the images is done thanks to a Gatan Orius camera.

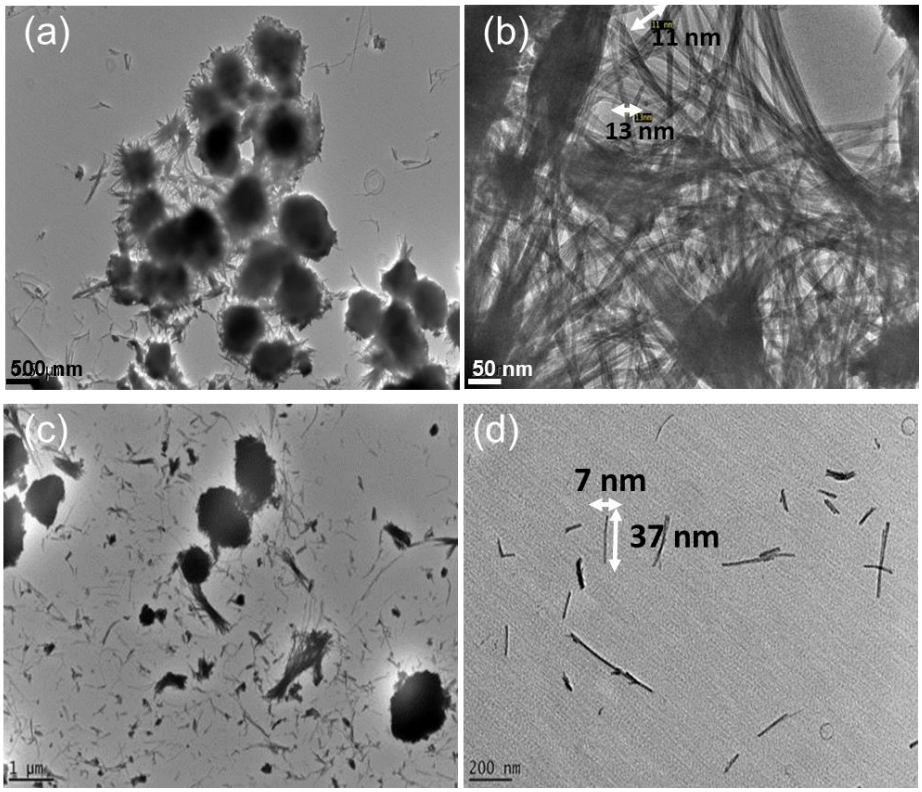

Figure A4.1. *TEM images of trials 5 and 6.*

- **Statistical analysis to extract mean diameters**

28 NWs were analysed using ImageJ to extract mean values of external diameter (d_{nt}) and internal one (δ_{nt}). All the measured values are presented in the dataset below (Table A4.2):

Table A4.2. *Dataset for the analysis of external and internal diameters of the nanotubes.*

#NT	d_{int} (nm)	d_{ext} (nm)
#1	1.0	3.1
#2	1.1	2.5
#3	0.7	2.5
#4	0.9	2.0
#5	0.9	2.4
#6	0.8	2.5
#7	2.2	4.1
#8	1.8	3.5
#9	1.2	3.7
#10	1.7	5.3
#11	1.1	2.7
#12	0.9	2.7
#13	0.6	2.2
#14	0.7	2.2
#15	0.9	2.9
#16	1.0	2.3

#NT	d_{int} (nm)	d_{ext} (nm)
#17	0.9	2.9
#18	1.0	2.1
#19	1.0	2.3
#20	1.1	2.8
#21	1.0	2.5
#22	0.9	2.9
#23	0.8	2.5
#24	0.9	2.7
#25	0.9	2.8
#26	0.6	2.0
#27	0.9	2.8
#28	0.9	2.2
$Value_{max}$	**2.2**	**5.3**
$Value_{min}$	**0.6**	**2**
Mean	**1.0 ± 0.35**	**2.7 ± 0.7**

- **Additional TM-AFM images**

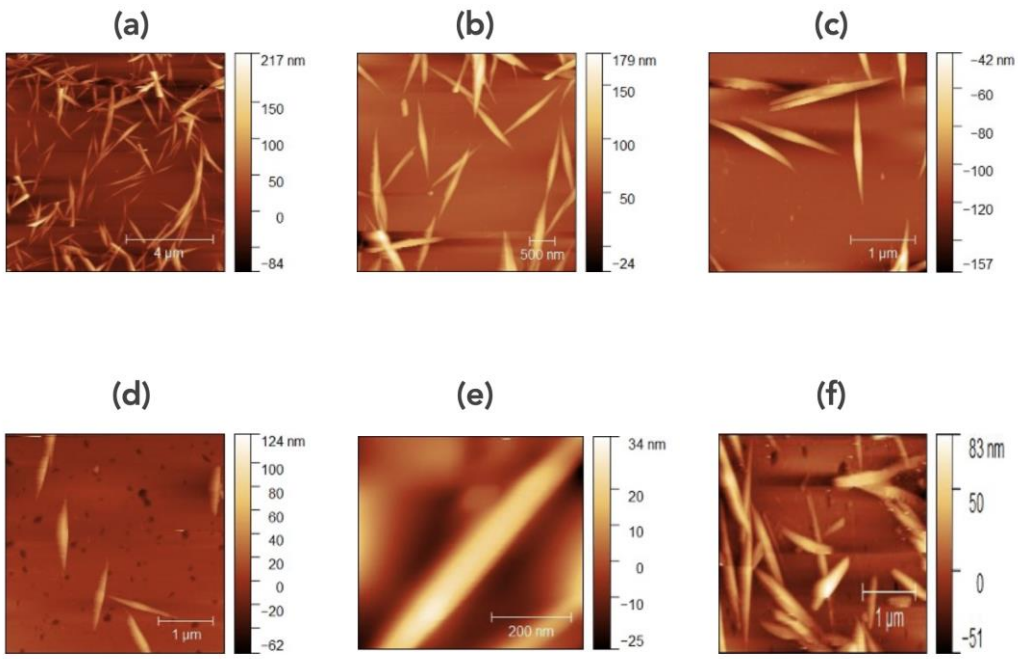

Figure A4.2. *Additional TM-AFM images of the NWs (trial #4) on SiO_2 (a) 10 µm x 10 µm, (b) and (c) 3 µm x 3 µm 2 zones from (a). TM-AFM images of the NWs on template-stripped Au surface (d-e) at various magnifications.*

Annexe A4.2. Perpendicular conductance

- **AFM measurements**

All the topographic and conductive AFM measurements were done with an ICON (Bruker) microscope operated in an air-conditioned laboratory (T_{amb} = 22.5 °C, relative humidity of 35-40 %). The AFM images were treated with the Gwyddion software[220] or with Mountains lab premium 9.0.9878 software®.

Topographic images were acquired in tapping mode (TM) using a silicon tip (42 N/m spring constant, resonance frequency 320 kHz).

Current−voltage characteristics were measured by conductive atomic force microscopy using a PtIr coated tip (SCM-PIT-V2 from Bruker, 3.0 N/m spring constant). We first focused on the middle of the nanowires by imaging an area 40x40 nm² in the TM mode with the C-AFM tip, and then we switched to a stationary C-AFM mode on the center of the NWs (no scan) to measure the I-V curve at a loading force of ~ few tens nN. Around 10 IVs have been measured on each nanowire. The voltage was applied from –3 V to +3 V and from +3 V to –3 V on the substrate and the tip is grounded via the input of the transimpedance preamplifier.

- **C-AFM contact area**

The loading force was set at ~ 60 nN for all the I-V measurements, a lower value leading to too many contact instabilities during the I-V measurements. As usually reported in literature[121,226–228] the contact radius, r_c, between the C-AFM tip and the sample surface, and the film elastic deformation, δ, are estimated from a Hertzian model:[229]

$$r_c^2 = \left(\frac{3RF}{4E^*}\right)^{2/3} \quad \text{(A4.1)}$$

$$\delta = \left(\frac{9}{16R}\right)^{1/3}\left(\frac{F}{E^*}\right)^{2/3} \quad \text{(A4.2)}$$

with F the tip loading force (~60 nN), R the tip radius (25 nm) and E* the reduced effective Young modulus defined as:

[redacted] (A4.3)

In this equation, $E_{nw/tip}$ and $\nu_{nw/tip}$ are the Young modulus and the Poisson ratio of the NWs and C-AFM tip, respectively. For the Pt/Ir (90%/10%) tip, we have E_{tip} = 204 GPa and ν_{tip} = 0.37 using a rule of mixture with the known material data.[13] For the $W_{18}O_{49}$ nanostructures, we consider a mean value of an effective Young modulus $E^*_{nw} = E_{nw}$ = 28 GPa from a series of mechanical measurements (3 points contact on suspended NWs using contact mode AFM) on tungsten oxide nanowires with a diameter of ~ 100 nm (the Poisson ratio is not known).[230] With these parameters, we estimate $r_c \approx 3.6$ nm (contact area ≈ 40 nm^2) and $\delta \approx 0.5$ nm.

Annexe A4.3. Longitudinal conductance

- **4-probe STM instrument**

The electrical resistance of the NWs was measured in an ultrahigh vacuum (UHV) system that can be described in three parts: i) a SEM (UHV-Carl Zeiss Gemini) with a resolution of the order of 5 nm to view and precisely position the STM tips on the sample. The SEM images are acquired from the top of the sample and probes; ii) a multiple-probe STM (Nanoprobe, Scienta-Omicron) with four independent STM scanners for imaging and contacting nanostructures under SEM monitoring; iii) the third part is the control system which is the key component required to operate the system. It combines SPECS-Zürich Nanonis STM controllers to operate the STM probes at the nanoscale with Keithley Source-Measure Units (SMU) to perform the electrical measurements.

As the use of good electrical contacts is essential to inject and extract charge carriers into the NWs, tungsten tips were prepared by an electrochemical etching in NaOH and thoroughly annealed in the UHV preparation chamber to remove the thin oxide layer covering the tips.

The NWs were lying flat on the 200 nm SiO_2/Si sample and the STM tips were approached under the supervision of the SEM. As the SiO_2 surface is insulating, the distance regulation of the STM control system could not be used for the approach of the first tip. A high bias was applied on this tip (typically -8 V) and it was manually approached close to a NW until a

charging hollow effect was visible on the SEM image around the NW. After setting the bias back to 0V on the first tip kept in contact with the NW, the approach of the three other STM tips was controlled by monitoring the tunneling current between the tip and the NW. The contact is detected at the crossover of the exponential distance-dependent tunnel current and the weak distance-dependent contact regime. Stable electrical contacts were obtained by further pushing each tip with feedback regulation off until saturating the preamplifiers. However, great care must be taken to avoid any significant deformation of the NW, as a mechanical stress applied to a NW can degrade its properties.

The tips were positioned with an in-line four-point geometry along the NW and the electrical measurements were always performed with the electron beam of the SEM turned off. Injection of the current I through the outer tips and measurement of the voltage drop V between the two inner tips give access to the four-point resistance $R_{4p}=V/I$. While it is important to maintain steady contacts during the transport measurements, the four-point resistance R_{4p} is, however, independent of the contact resistance.

- **At T< 300K**

The same measurements were performed as a function of temperature thanks to the variable temperature sample stage: a nitrogen flow was kept constant to cool down the sample stage whose temperature could be regulated by an integrated heater and a Lakeshore temperature controller. During cooling down, the tips are far enough from the sample because of the sample and system drift that can damage them. Once the temperature is reached, we wait half an hour to stabilize the system before contacting the NWs and start again the measurements.

- **Transistor configuration**

For the transistor configuration, only two tips are necessary. We applied a fixed voltage gate V_G on the underlying silicon substrate and measured the drain current I_D versus the drain voltage V_D (the source is grounded) between the two tips connected on one nanowire. The measurements have been done at 300 K.

- **Fragility of nanowires during measurement**

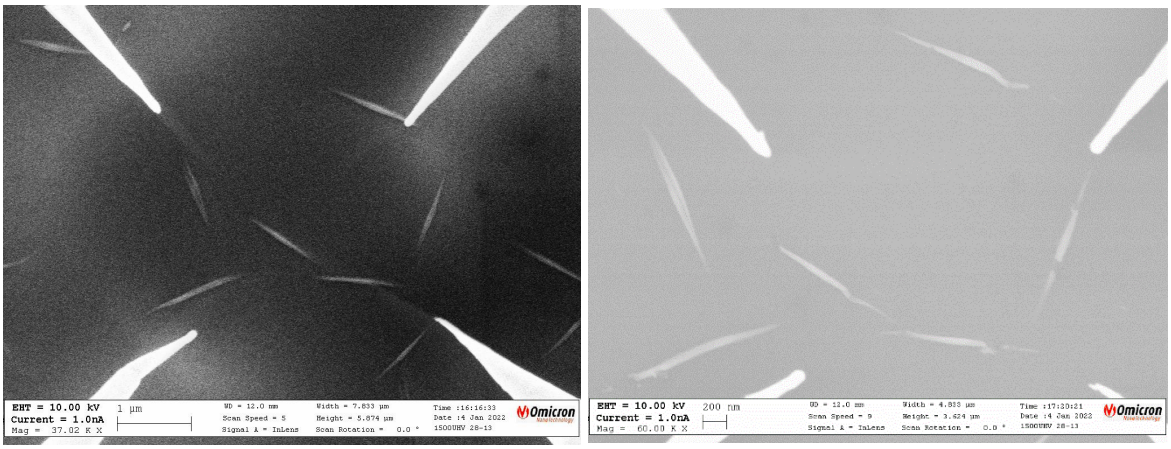

Figure A4.2. *TEM images of nanowires before and after measurements. This phenomenon sometimes happened when nanowires have overheated. Moreover, at low temperature, it happened almost after each measurement because of the drift of the tips which caused them to press harder on the nanowire.*

- **Full dataset at 300K**

In all the following tables, the following data are given: zero-bias NW longitudinal conductance (G_L) from data in Fig.4.13 (Chapter4_ IIc), inner-probe distance (L), NW diameter and surface (d_{nw} and S_{nw}), longitudinal NW conductance ($\sigma_{Lnw}=G_L(L/S_{nw})$), number of NTs in the NW ($N\approx(d_{nw}/d_{nt})^2$ with d_{nt}=2.7 nm (± 0.7 nm), see Chapter4_ IIc) and longitudinal individual NT conductivity ($\sigma_{Lnt}=G_L(L/S_{nt})/N$ with S_{nt} the cross-section surface of the NT, see Chapter4_ IIc).

Table A4.2. *Second series of measurements at 300K*

#NW	G_L (µS)	L (nm)	d_{nw} (nm)	S_{nw} (nm^2)	σ_{Lnw} (S/cm)	N	σ_{Lnt} (S/cm)
#1	741	175	70	3848	337	672	390
#2	500	245	46	1662	737	290	854
#3	455	400	75	4418	412	772	477
#4	303	300	50	1963	463	343	537
#5	370	350	50	1963	660	343	765
#6	444	500	80	5027	442	878	512
#7	345	660	75	4418	515	772	597
#8	370	300	60	2827	393	494	455
#9	741	310	66	3421	671	598	778
#10	286	640	66	3421	534	598	619
#10	588	420	66	3421	722	598	837
#10	117.6	230	66	3421	791	598	917
#11	320	730	77	4657	502	813	581

Table A4.3. *Third series of measurements at 300K*

#NW	G_L (µS)	L (nm)	d_{nw} (nm)	S_{nw} (nm^2)	σ_{Lnw} (S/cm)	N	σ_{Lnt} (S/cm)
#1	167	850	65	3318	427	580	495
#1	277	650	65	3318	543	580	629
#1	532	450	65	3318	721	580	836
#1	820	250	65	3318	618	580	716
#3	226	574	64	3217	403	562	467
#3	346	400	64	3217	430	562	499
#3	455	200	64	3217	283	562	328
#5	221	725	67	3526	454	616	526
#5	588	500	67	3526	834	616	967
#5	746	300	67	3526	635	616	736
#5	116.3	150	67	3526	495	616	573
#6	40	816	45	1590	207	278	240
#6	54	600	45	1590	203	278	236
#6	61	400	45	1590	152	278	177
#6	55	200	45	1590	69	278	80
#7	301	412	60	2827	439	494	509
#7	318	300	60	2827	338	494	392
#7	345	200	60	2827	244	494	283
#8	173	490	60	2827	300	494	348
#8	183	350	60	2827	226	494	262
#8	194	200	60	2827	137	494	159
#9	385	528	55	2376	855	415	991
#9	556	300	55	2376	702	415	813
#9	855	150	55	2376	540	415	625
#10	315	595	68	3632	517	634	599
#10	417	400	68	3632	459	634	532
#10	585	200	68	3632	322	634	373
#11	192	550	60	2827	374	494	434
#11	224	400	60	2827	316	494	367
#11	380	200	60	2827	269	494	312

- **Dataset at lower temperatures**

  - **At 120K**

Table A4.3. *Series of measurements at 120K from data in Fig.4.15a (Chapter4_ IIc)*

#NW	G_L (µS)	L (nm)	d_{nw} (nm)	S_{nw} (nm^2)	σ_{Lnw} (S/cm)	N	σ_{Lnt} (S/cm)
#1	19	411	72	4072	19	711	23
#1	15	417	72	4072	15	711	17
#1	277	417	72	4072	284	711	329
#3	78	440	64	3217	106	562	123
#4	76	283	58	2642	82	461	95
#7	238	503	80	5027	238	878	275
#9	19	480	60	2827	32	494	37
#20	26	615	75	4418	37	772	42
#21	20	350	55	2376	29	415	34
#22	13	470	57	2552	24	446	28
#23	77	638	69	3739	132	653	153
#24	10	490	66	3421	15	598	17
#25	155	496	62	3019	255	527	295
#26	39	505	73	4185	47	731	55
#27	121	673	62	3019	270	527	313
#28	232	520	62	3019	400	527	463
#29	48	420	83	5411	37	945	43
#30	18	522	79	4902	19	856	22
#31	36	562	65	3318	61	580	70

- **At 170K**

Table A4.4. *Series of measurements at 170K from data in Fig.4.15b (Chapter4_ IIc)*

#NW	G_L (µS)	L (nm)	d_{nw} (nm)	S_{nw} (nm^2)	σ_{Lnw} (S/cm)	N	σ_{Lnt} (S/cm)
#3	37	350	64	3217	40	562	47
#7	187	419	78	4778	164	835	190
#9	54	346	60	2827	67	494	77
#10	145	516	56	2463	304	430	352
#10	130	516	56	2463	272	430	315
#10	60	516	56	2463	126	430	146
#32	37	393	75	4418	33	772	38
#33	35	328	61	2922	39	510	45
#34	20	487	73	4185	23	731	27
#35	119	585	56	2463	282	430	327
#36	233	479	63	3117	357	544	414
#37	18	433	66	3421	23	598	26
#38	147	392	76	4536	127	792	147

- **At 210K**

Table A4.5. *Series of measurements at 210K from data in Fig.4.15c (Chapter4_ IIc)*

#NW	G_L (µS)	L (nm)	d_{nw} (nm)	S_{nw} (nm^2)	σ_{Lnw} (S/cm)	N	σ_{Lnt} (S/cm)
#2	23	321	66	3421	22	598	26
#7	280	250	78	4778	147	835	170
#9	158	272	60	2827	152	494	176
#10	67	237	56	2463	65	430	75
#11	68	658	57	2552	177	446	205
#12	96	492	57	2552	185	446	215
#13	244	487	66	3421	347	598	402
#39	165	508	68	3632	230	634	267
#41	43	378	57	2552	64	446	74
#42	36	397	51	2043	70	357	82
#43	148	517	68	3632	211	634	245
#44	47	524	48	1810	136	316	158
#45	42	629	66	3421	77	598	89
#46	22	506	68	3632	31	634	36
#47	154	637	75	4418	222	772	257
#49	27	688	58	2642	69	461	80

- **At 250K**

Table A4.6. *Series of measurements at 250K from data in Fig.4.15d (Chapter4_ IIc)*

#NW	G_L (µS)	L (nm)	d_{nw} (nm)	S_{nw} (nm^2)	σ_{Lnw} (S/cm)	N	σ_{Lnt} (S/cm)
#7	198	312	78	4778	129	835	150
#9	128	221	60	2827	100	494	116
#10	169	212	56	2463	145	430	168
#11	262	285	57	2552	293	446	340
#13	162	556	66	3421	263	598	305
#13	127	598	66	3421	222	598	257
#14	120	570	77	4657	147	813	170
#50	60	701	61	2922	144	510	167
#51	100	619	72	4072	153	711	177
#52	195	481	66	3421	274	598	318
#53	41	580	69	3739	64	653	74
#54	32	599	70	3848	50	672	58
#55	73	574	71	3959	105	691	122

#NW	G_L (µS)	L (nm)	d_{nw} (nm)	S_{nw} (nm^2)	σ_{Lnw} (S/cm)	N	σ_{Lnt} (S/cm)
#56	27	663	66	3421	52	598	60
#57	42	646	72	4072	66	711	77
#58	32	629	63	3117	64	544	75
#60	20	562	62	3019	38	527	44
#61	42	728	71	3959	77	691	89
#62	201	588	76	4536	261	792	302

- **Other electron transport mechanism**

We tested a classical temperature-activated transport mechanism for the samples with the lowest conductivity (Fig. 4.16, see Chapter4_IIc). Figure A4.3 shows the Arrhenius plot ($\ln(\sigma_L)$ vs. 1000/T) of the same data as in Fig. 4.16 These data of σ_L clearly badly follow an Arrhenius plot, moreover, the activation energy deduced from a linear fit of these data gives a physically insignificant low value of 26 ± 4 meV. We also tested a polaron hopping transport as suggested for $W_{18}O_{49}$ nanowires synthesized by a low temperature (600°C) furnace process.[205] Figure A4.3 shows the plot of $\ln(\sigma_L T)$ vs. 1000/T with the same data. Again, we obtain a poor linear behavior with a low activation energy (42 ± 6 meV) compared to ~0.25 eV as previously reported.[205]

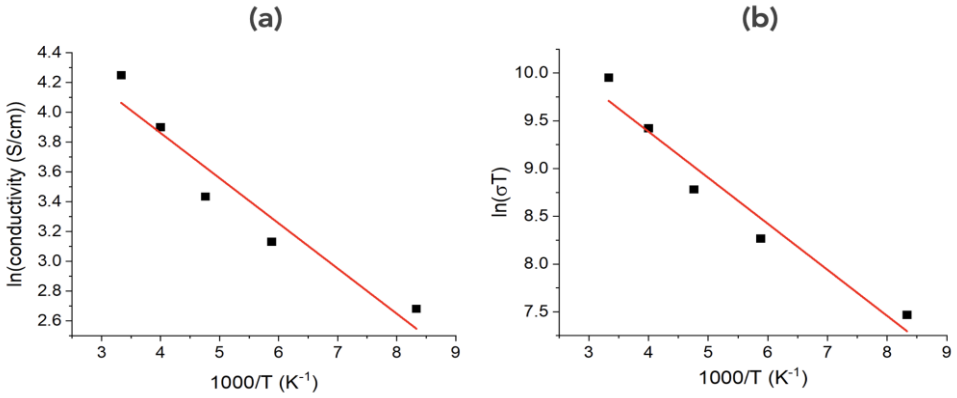

***Figure A4.3**. (a) Plot of $\ln(\sigma_L)$ vs. 1000/T and (b) plot of $\ln(\sigma_L T)$ vs. 1000/T with the same data as in Fig. 4.16 (Chapter4_IIc) The red lines are the fits by a linear regression (bad fits with r^2 = 0.92 and 0.94, respectively).*

Annexe A4.4. Effect of e-beam exposure

The NWs are imaged by the SEM embodied in the 4-probe STM machine to visualize them for a precise positioning of the 4 STM tips. As nanostructure properties can be influenced by e-beam exposure, we need to evaluate this effect on $W_{18}O_{49}$, that could be reduced under e-beam.[231] To do so, we fabricated a 2-dimensional (2D) percolated network of NWs on lithographed Au electrodes (Fig. A4.4). The electrodes were fabricated on a Si/SiO_2 (200 nm thick) substrate

by a standard lithography process. The electrodes, Ti (2 nm, adhesion layer) and Au (12 nm), are 1 mm long and spaced by 5 µm. The NWs are deposited by drop casting. Figure A4.4shows the I-V curve measured on the same 2D networks before and after exposure to the e-beam of the SEM in the same conditions as in the 4-probe STM (e-beam at 10 kV during ~ 20 min). To prevent any influence of ambient air, the I-Vs were measured in a glove box (under dry N_2, < 1ppm of oxygen and water vapor). We note a slight increase of the current by a factor ~ 1.5, and such a correction factor was taken into account to determine the NW conductivity from the V-I measurements with the 4-probe STM.

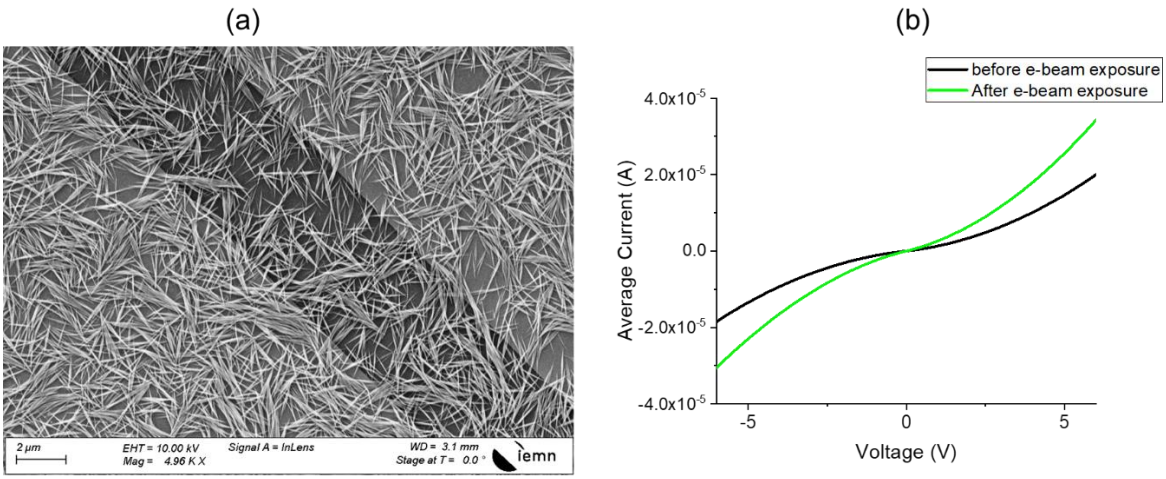

***Figure A4.4**. SEM image of a percolating 2D network of NWs between two Au electrodes. Average I-V (from measurements on 5 different 2D networks) before (dark line) and after (green line) e-beam exposure.*

Annexe A4.5. Activation energy calculated from TLM method

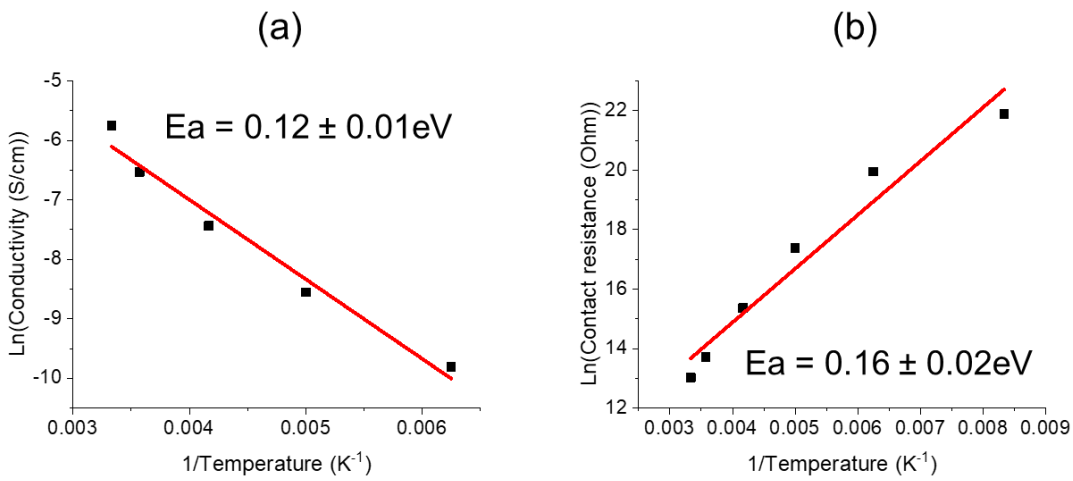

***Figure A4.5**. Determination of activation energy for the dense network using TLM method with (a) the conductivity and (b) the resistance.*

Publications & Oral communications

Publications

- **On the role of counterions in the electron transport properties of polyoxometalate nanodevices.** ***(in preparation)***

Huez, C.; Volatron, F.; Proust, A.; Vuillaume, D.

- **Highly conductive tungsten suboxide nanotubes.** ***(in progress)***

Huez, C.; Berthe, M. ; Volatron, F.; Proust, A.; Vuillaume, D.

- **Redox-controlled conductance of polyoxometalate molecular junctions.**

Huez, C.; Guerin, D.; Lenfant, S.; Volatron, F.; Calame, M.; Perrin, M.; Proust, A.; Vuillaume, D. Redox-Controlled Conductance of Polyoxometalate Molecular Junctions. *Nanoscale* **2022,** 14 (37), 13790–13800. https://doi.org/10.1039/D2NR03457C.

Oral communications

- **Electron transport properties of metal-oxides nanostructures.**

Huez, C.; Guerin, D.; Berthe, M. ; Lenfant, S.; Volatron, F.; Proust, A.; Vuillaume, D.
Forum des microscopies à sondes locales – Saint-Valéry-sur-Somme, France (2022).

- **Redox state-modulated electron transport properties of polyoxometalates at the nanoscale.**

Huez, C.; Guerin, D.; Lenfant, S.; Volatron, F.; Proust, A.; Vuillaume, D.
International conference on molecular electronics (ElecMol) – Lyon, France (2021).

- **Redox state-modulated electron transport properties of polyoxometalates at the nanoscale.**

Huez, C.; Guerin, D.; Lenfant, S.; Volatron, F.; Proust, A.; Vuillaume, D.
Symposium of International Research Network - polyoxometalates (IRN-POM), Smart Molecular Oxides – Paris, France (2021).

- **Evolutive nanodevices based on polyoxometalates for non-conventional computing.**

Huez, C.; Guerin, D.; Lenfant, S.; Volatron, F.; Proust, A.; Vuillaume, D.
European school on molecular nanoscience (EsMolNa) – Benidorm, Spain (2021).

Bibliography

(1) Mann, B.; Kuhn, H.; Szentpály, L. v. Tunnelling through Fatty Acid Monolayers and Its Relevance to Photographic Sensitization. *Chem. Phys. Lett.* **1971**, *8* (1), 82–84. https://doi.org/10.1016/0009-2614(71)80582-1.

(2) Aviram, A.; Ratner, M. A. Molecular Rectifiers. *Chem. Phys. Lett.* **1974**, *29* (2), 277–283. https://doi.org/10.1016/0009-2614(74)85031-1.

(3) Shirakawa, H.; Louis, E. J.; MacDiarmid, A. G.; Chiang, C. K.; Heeger, A. J. Synthesis of Electrically Conducting Organic Polymers: Halogen Derivatives of Polyacetylene, (CH). *J Chem Soc Chem Commun* **1977**, No. 16, 578–580. https://doi.org/10.1039/C39770000578.

(4) Binnig, G.; Rohrer, H.; Gerber, Ch.; Weibel, E. Surface Studies by Scanning Tunneling Microscopy. *Phys. Rev. Lett.* **1982**, *49* (1), 57–61. https://doi.org/10.1103/PhysRevLett.49.57.

(5) Binnig, G.; Rohrer, H. Scanning Tunneling Microscopy---from Birth to Adolescence. *Rev. Mod. Phys.* **1987**, *59* (3), 615–625. https://doi.org/10.1103/RevModPhys.59.615.

(6) Chau, R.; Doyle, B.; Datta, S.; Kavalieros, J.; Zhang, K. Integrated Nanoelectronics for the Future. *Nat. Mater.* **2007**, *6* (11), 810–812. https://doi.org/10.1038/nmat2014.

(7) Vuillaume, D. Molecular Electronics: Electron, Spin and Thermal Transport through Molecules. 42. https://doi.org/10.48550/arXiv.2111.10616.

(8) Akkerman, H. B.; Blom, P. W. M.; de Leeuw, D. M.; de Boer, B. Towards Molecular Electronics with Large-Area Molecular Junctions. *Nature* **2006**, *441* (7089), 69–72. https://doi.org/10.1038/nature04699.

(9) Loo, Y.-L.; Lang, D. V.; Rogers, J. A.; Hsu, J. W. P. Electrical Contacts to Molecular Layers by Nanotransfer Printing. *Nano Lett.* **2003**, *3* (7), 913–917. https://doi.org/10.1021/nl034207c.

(10) Vilan, A.; Cahen, D. Soft Contact Deposition onto Molecularly Modified GaAs. Thin Metal Film Flotation: Principles and Electrical Effects. *Adv. Funct. Mater.* **2002**, *12* (11–12), 795–807. https://doi.org/10.1002/adfm.200290009.

(11) Jeong, H.; Kim, D.; Xiang, D.; Lee, T. High-Yield Functional Molecular Electronic Devices. *ACS Nano* **2017**, *11* (7), 6511–6548. https://doi.org/10.1021/acsnano.7b02967.

(12) Holmlin, R. E.; Haag, R.; Chabinyc, M. L.; Ismagilov, R. F.; Cohen, A. E.; Terfort, A.; Rampi, M. A.; Whitesides, G. M. Electron Transport through Thin Organic Films in Metal−Insulator−Metal Junctions Based on Self-Assembled Monolayers. *J. Am. Chem. Soc.* **2001**, *123* (21), 5075–5085. https://doi.org/10.1021/ja004055c.

(13) Chiechi, R. C.; Weiss, E. A.; Dickey, M. D.; Whitesides, G. M. Eutectic Gallium–Indium (EGaIn): A Moldable Liquid Metal for Electrical Characterization of Self-Assembled Monolayers. *Angew. Chem. Int. Ed.* **2008**, *47* (1), 142–144. https://doi.org/10.1002/anie.200703642.

(14) McCreery, R. L.; Yan, H.; Bergren, A. J. A Critical Perspective on Molecular Electronic Junctions: There Is Plenty of Room in the Middle. *Phys. Chem. Chem. Phys.* **2012**, *15* (4), 1065–1081. https://doi.org/10.1039/C2CP43516K.

(15) Karuppannan, S. K.; Hongting, H.; Troadec, C.; Vilan, A.; Nijhuis, C. A. Ultrasmooth and Photoresist-Free Micropore-Based EGaIn Molecular Junctions: Fabrication and How Roughness Determines Voltage Response. *Adv. Funct. Mater.* **2019**, *29* (38), 1904452. https://doi.org/10.1002/adfm.201904452.

(16) Rinfray, C. Greffage de polyoxométallates hybrides sur surfaces planes. PhD, 2014.

(17) Ulman, A. *An Introduction to Ultrathin Organic Films: From Langmuir--Blodgett to Self--Assembly*; Academic Press, 2013.

(18) Langmuir, I. The Mechanism of the Surface Phenomena of Flotation. *Trans. Faraday Soc.* **1920**, *15* (June), 62–74. https://doi.org/10.1039/TF9201500062.

(19) Delamar, M.; Hitmi, R.; Pinson, J.; Saveant, J. M. Covalent Modification of Carbon Surfaces by Grafting of Functionalized Aryl Radicals Produced from Electrochemical Reduction of Diazonium Salts. *J. Am. Chem. Soc.* **1992**, *114* (14), 5883–5884. https://doi.org/10.1021/ja00040a074.

(20) Maoz, R.; Sagiv, J. On the Formation and Structure of Self-Assembling Monolayers. I. A Comparative Atr-Wettability Study of Langmuir—Blodgett and Adsorbed Films on Flat Substrates and Glass Microbeads. *J. Colloid Interface Sci.* **1984**, *100* (2), 465–496. https://doi.org/10.1016/0021-9797(84)90452-1.
(21) Love, J. C.; Estroff, L. A.; Kriebel, J. K.; Nuzzo, R. G.; Whitesides, G. M. Self-Assembled Monolayers of Thiolates on Metals as a Form of Nanotechnology. *Chem. Rev.* **2005**, *105* (4), 1103–1170. https://doi.org/10.1021/cr0300789.
(22) Nuzzo, R. G.; Allara, D. L. Adsorption of Bifunctional Organic Disulfides on Gold Surfaces. *J. Am. Chem. Soc.* **1983**, *105* (13), 4481–4483. https://doi.org/10.1021/ja00351a063.
(23) Lehn, J.-M. Supramolecular Chemistry. *Science* **1993**, *260* (5115), 1762–1763. https://doi.org/10.1126/science.8511582.
(24) Hnid, I. Surfaces et Jonctions Moléculaires Photo-Actives : Organisations, Fonctionnalisations et Caractérisations Par Microscopie à Effet Tunnel et Microscopie à Force Atomique et Pointe Conductrice. PhD, 2021.
(25) Aswal, D. K.; Lenfant, S.; Guerin, D.; Yakhmi, J. V.; Vuillaume, D. Self Assembled Monolayers on Silicon for Molecular Electronics. *Anal. Chim. Acta* **2006**, *568* (1–2), 84–108. https://doi.org/10.1016/j.aca.2005.10.027.
(26) Kluth, G. J.; Sung, M. M.; Maboudian, R. Thermal Behavior of Alkylsiloxane Self-Assembled Monolayers on the Oxidized Si(100) Surface. *Langmuir* **1997**, *13* (14), 3775–3780. https://doi.org/10.1021/la970135r.
(27) Poirier, G. E.; Pylant, E. D. The Self-Assembly Mechanism of Alkanethiols on Au(111). *Science* **1996**, *272* (5265), 1145–1148.
(28) Kojio, K.; Ge, S.; Takahara, A.; Kajiyama, T. Molecular Aggregation State of N-Octadecyltrichlorosilane Monolayer Prepared at an Air/Water Interface. *Langmuir* **1998**, *14* (5), 971–974. https://doi.org/10.1021/la970040p.
(29) Oelhafen, P. Practical Surface Analysis by Auger and X-Ray Photoelectron Spectroscopy. *J. Electron Spectrosc. Relat. Phenom.* **1984**, *34* (2), 203. https://doi.org/10.1016/0368-2048(84)80044-4.
(30) Wasserman, S. R.; Tao, Y. T.; Whitesides, G. M. Structure and Reactivity of Alkylsiloxane Monolayers Formed by Reaction of Alkyltrichlorosilanes on Silicon Substrates. *Langmuir* **1989**, *5* (4), 1074–1087. https://doi.org/10.1021/la00088a035.
(31) Fontaine, P.; Goguenheim, D.; Deresmes, D.; Vuillaume, D.; Garet, M.; Rondelez, F. Octadecyltrichlorosilane Monolayers as Ultrathin Gate Insulating Films in Metal-insulator-semiconductor Devices. *Appl. Phys. Lett.* **1993**, *62* (18), 2256–2258. https://doi.org/10.1063/1.109433.
(32) Karthäuser, S. Control of Molecule-Based Transport for Future Molecular Devices. *J. Phys. Condens. Matter* **2011**, *23* (1), 013001. https://doi.org/10.1088/0953-8984/23/1/013001.
(33) Moth-Poulsen, K.; Bjørnholm, T. Molecular Electronics with Single Molecules in Solid-State Devices. *Nat. Nanotechnol.* **2009**, *4* (9), 551–556. https://doi.org/10.1038/nnano.2009.176.
(34) Barth, J. V. Molecular Architectonic on Metal Surfaces. *Annu. Rev. Phys. Chem.* **2007**, *58* (1), 375–407. https://doi.org/10.1146/annurev.physchem.56.092503.141259.
(35) Jia, C.; Guo, X. Molecule–Electrode Interfaces in Molecular Electronic Devices. *Chem. Soc. Rev.* **2013**, *42* (13), 5642. https://doi.org/10.1039/c3cs35527f.
(36) Davies, P. C. W.; Betts, D. S. *Quantum Mechanics*; Physics and Its Applications; Springer US, 1994.
(37) Simmons, J. G. Electric Tunnel Effect between Dissimilar Electrodes Separated by a Thin Insulating Film. *J. Appl. Phys.* **1963**, *34* (9), 2581–2590. https://doi.org/10.1063/1.1729774.
(38) Vilan, A. Analyzing Molecular Current-Voltage Characteristics with the Simmons Tunneling Model: Scaling and Linearization. *J. Phys. Chem. C* **2007**, *111* (11), 4431–4444. https://doi.org/10.1021/jp066846s.
(39) Grüter, L.; Cheng, F.; Heikkilä, T. T.; González, M. T.; Diederich, F.; Schönenberger, C.; Calame, M. Resonant Tunnelling through a C_{60} Molecular Junction in a Liquid Environment. *Nanotechnology* **2005**, *16* (10), 2143–2148. https://doi.org/10.1088/0957-4484/16/10/029.

(40) Zotti, L. A.; Kirchner, T.; Cuevas, J.-C.; Pauly, F.; Huhn, T.; Scheer, E.; Erbe, A. Revealing the Role of Anchoring Groups in the Electrical Conduction Through Single-Molecule Junctions. *Small* **2010**, *6* (14), 1529–1535. https://doi.org/10.1002/smll.200902227.
(41) Beebe, J. M.; Kim, B.; Frisbie, C. D.; Kushmerick, J. G. Measuring Relative Barrier Heights in Molecular Electronic Junctions with Transition Voltage Spectroscopy. *ACS Nano* **2008**, *2* (5), 827–832. https://doi.org/10.1021/nn700424u.
(42) Beebe, J. M.; Kim, B.; Gadzuk, J. W.; Daniel Frisbie, C.; Kushmerick, J. G. Transition from Direct Tunneling to Field Emission in Metal-Molecule-Metal Junctions. *Phys. Rev. Lett.* **2006**, *97* (2), 026801. https://doi.org/10.1103/PhysRevLett.97.026801.
(43) Ricœur, G.; Lenfant, S.; Guérin, D.; Vuillaume, D. Molecule/Electrode Interface Energetics in Molecular Junction: A "Transition Voltage Spectroscopy" Study. *J. Phys. Chem. C* **2012**, *116* (39), 20722–20730. https://doi.org/10.1021/jp305739c.
(44) Huisman, E. H.; Guédon, C. M.; van Wees, B. J.; van der Molen, S. J. Interpretation of Transition Voltage Spectroscopy. *Nano Lett.* **2009**, *9* (11), 3909–3913. https://doi.org/10.1021/nl9021094.
(45) Bâldea, I. Ambipolar Transition Voltage Spectroscopy: Analytical Results and Experimental Agreement. *Phys. Rev. B* **2012**, *85* (3), 035442. https://doi.org/10.1103/PhysRevB.85.035442.
(46) Magoga, M.; Joachim, C. Conductance of Molecular Wires Connected or Bonded in Parallel. *Phys. Rev. B* **1999**, *59* (24), 16011–16021. https://doi.org/10.1103/PhysRevB.59.16011.
(47) Reuter, M. G.; Hersam, M. C.; Seideman, T.; Ratner, M. A. Signatures of Cooperative Effects and Transport Mechanisms in Conductance Histograms. *Nano Lett.* **2012**, *12* (5), 2243–2248. https://doi.org/10.1021/nl204379j.
(48) Trasobares, J.; Rech, J.; Jonckheere, T.; Martin, T.; Aleveque, O.; Levillain, E.; Diez-Cabanes, V.; Olivier, Y.; Cornil, J.; Nys, J. P.; Sivakumarasamy, R.; Smaali, K.; Leclere, P.; Fujiwara, A.; Théron, D.; Vuillaume, D.; Clément, N. Estimation of π–π Electronic Couplings from Current Measurements. *Nano Lett.* **2017**, *17* (5), 3215–3224. https://doi.org/10.1021/acs.nanolett.7b00804.
(49) Brunner, J. G. Gaining Microscopic Insight into Molecular Junctions by Transport Experiments. PhD, Basel University, 2013.
(50) Bâldea, I. Important Issues Facing Model-Based Approaches to Tunneling Transport in Molecular Junctions. *Phys. Chem. Chem. Phys.* **2015**, *17* (31), 20217–20230. https://doi.org/10.1039/C5CP02595H.
(51) Bâldea, I. Transition Voltage Spectroscopy Reveals Significant Solvent Effects on Molecular Transport and Settles an Important Issue in Bipyridine -Based Junctions. *Nanoscale* **2013**, *5* (19), 9222–9230. https://doi.org/10.1039/C3NR51290H.
(52) Xie, Z.; Bâldea, I.; Frisbie, C. D. Energy Level Alignment in Molecular Tunnel Junctions by Transport and Spectroscopy: Self-Consistency for the Case of Alkyl Thiols and Dithiols on Ag, Au, and Pt Electrodes. *J. Am. Chem. Soc.* **2019**, *141* (45), 18182–18192. https://doi.org/10.1021/jacs.9b08905.
(53) MT Pope; A Müller. Polyoxometalate Chemistry : An Old Field with New Dimensions in Several Disciplines. *Angew. Chem. Int. Ed. Engl*, **1991**. https://doi.org/insis.bib.cnrs.fr/10.1002/anie.199100341.
(54) Moeller, C. W. Gmelins Handbuch Der Anorganischen Chemie. *J. Am. Chem. Soc.* **1959**, *81* (16), 4440–4440. https://doi.org/10.1021/ja01525a094.
(55) Gleu. Chemische Koordinationslehre, von F. Hein. S. Hirzel Verlag, Leipzig. 1. Aufl. 1950. 683 S., 41 Abb., halbln. DM 41.–. *Angew. Chem.* **1951**, *63* (19), 474–474. https://doi.org/10.1002/ange.19510631912.
(56) Keggin, J. F. Structure of the Molecule of 12-Phosphotungstic Acid. *Nature* **1933**, *131* (3321), 908–909. https://doi.org/10.1038/131908b0.
(57) Bijelic, A.; Aureliano, M.; Rompel, A. Polyoxometalates as Potential Next-Generation Metallodrugs in the Combat Against Cancer. *Angew. Chem. Int. Ed.* **2019**, *58* (10), 2980–2999. https://doi.org/10.1002/anie.201803868.
(58) Alizadeh, M. H.; Harmalker, S. P.; Jeannin, Y.; Martin-Frere, J.; Pope, M. T. A Heteropolyanion with Fivefold Molecular Symmetry That Contains a Nonlabile Encapsulated Sodium Ion. The Structure and Chemistry of [NaP5W30O110]14-. *J. Am. Chem. Soc.* **1985**, *107* (9), 2662–2669. https://doi.org/10.1021/ja00295a019.

(59) M. T. Pope. Heteropoly and Isopoly Oxometalates. (Vol. 8). Berlin: Springer-Verlag.**1983**.
(60) Yaqub, M.; Walsh, J. J.; Keyes, T. E.; Proust, A.; Rinfray, C.; Izzet, G.; McCormac, T.; Forster, R. J. Electron Transfer to Covalently Immobilized Keggin Polyoxotungstates on Gold. *Langmuir* **2014**, *30* (15), 4509–4516. https://doi.org/10.1021/la4048648.
(61) Godin, B.; Vaissermann, J.; Herson, P.; Ruhlmann, L.; Verdaguer, M.; Gouzerh, P. Coordination Chemistry of the Hexavacant Tungstophosphate [H 2 P 2 W 12 O 48] 12− : Synthesis and Characterization of Iron(Iii) Complexes Derived from the Unprecedented {P 2 W 14 O 54 } Fragment. *Chem. Commun.* **2005**, *0* (45), 5624–5626. https://doi.org/10.1039/B510434C.
(62) Müller, A.; Meyer, J.; Krickemeyer, E.; Diemann, E. Molybdenum Blue: A 200 Year Old Mystery Unveiled. *Angew. Chem. Int. Ed. Engl.* **1996**, *35* (11), 1206–1208. https://doi.org/10.1002/anie.199612061.
(63) Sadakane, M.; Steckhan, E. Electrochemical Properties of Polyoxometalates as Electrocatalysts. *Chem. Rev.* **1998**, *98* (1), 219–238. https://doi.org/10.1021/cr960403a.
(64) Poblet, J. M.; López, X.; Bo, C. Ab Initio and DFT Modelling of Complex Materials: Towards the Understanding of Electronic and Magnetic Properties of Polyoxometalates. *Chem Soc Rev* **2003**, *32* (5), 297–308. https://doi.org/10.1039/B109928K.
(65) Hill, C. L. Progress and Challenges in Polyoxometalate-Based Catalysis and Catalytic Materials Chemistry. *J. Mol. Catal. Chem.* **2007**, *262* (1–2), 2–6. https://doi.org/10.1016/j.molcata.2006.08.042.
(66) Katsoulis, D. E. A Survey of Applications of Polyoxometalates. *Chem. Rev.* **1998**, *98* (1), 359–388. https://doi.org/10.1021/cr960398a.
(67) Yang, L.; Lei, J.; Fan, J.-M.; Yuan, R.-M.; Zheng, M.-S.; Chen, J.-J.; Dong, Q.-F. The Intrinsic Charge Carrier Behaviors and Applications of Polyoxometalate Clusters Based Materials. *Adv. Mater.* **2021**, *33* (50), 2005019. https://doi.org/10.1002/adma.202005019.
(68) Velessiotis, D.; Glezos, N.; Ioannou-Sougleridis, V. Tungstate Polyoxometalates as Active Components of Molecular Devices. *J. Appl. Phys.* **2005**, *98* (8), 084503. https://doi.org/10.1063/1.2103416.
(69) Coronado, E.; Mingotaud, C. Hybrid Organic/Inorganic Langmuir–Blodgett Films. A Supramolecular Approach to Ultrathin Magnetic Films. *Adv. Mater.* **1999**, *11* (10), 869–872. https://doi.org/10.1002/(SICI)1521-4095(199907)11:10%3c869::AID-ADMA869%3e3.0.CO;2-W.
(70) Oh, S.-Y.; Yun, Y.-J.; Kim, D.-Y.; Han, S.-H. Formation of a Self-Assembled Monolayer of Diaminododecane and a Heteropolyacid Monolayer on the ITO Surface. *Langmuir* **1999**, *15* (14), 4690–4692. https://doi.org/10.1021/la9900268.
(71) Balliou, A.; Skarlatos, D.; Papadimitropoulos, G.; Vouroutzis, N. Z.; Boukos, N.; Glezos, N. Molecular/Nanostructured Functional Metal Oxide Stacks for Nanoscale Nanosecond Information Storage. *Adv. Funct. Mater.* **2019**, *29* (51), 1902642. https://doi.org/10.1002/adfm.201902642.
(72) Busche, C.; Vilà-Nadal, L.; Yan, J.; Miras, H. N.; Long, D.-L.; Georgiev, V. P.; Asenov, A.; Pedersen, R. H.; Gadegaard, N.; Mirza, M. M.; Paul, D. J.; Poblet, J. M.; Cronin, L. Design and Fabrication of Memory Devices Based on Nanoscale Polyoxometalate Clusters. *Nature* **2014**, *515* (7528), 545–549. https://doi.org/10.1038/nature13951.
(73) Balliou, A.; Bouroushian, M.; Douvas, A. M.; Skoulatakis, G.; Kennou, S.; Glezos, N. Size-Dependent Single Electron Transfer and Semi-Metal-to-Insulator Transitions in Molecular Metal Oxide Electronics. *Nanotechnology* **2018**, *29* (27), 275204. https://doi.org/10.1088/1361-6528/aabdc3.
(74) Decher, G.; Eckle, M.; Schmitt, J.; Struth, B. Layer-by-Layer Assembled Multicomposite Films. *Curr. Opin. Colloid Interface Sci.* **1998**, *3* (1), 32–39. https://doi.org/10.1016/S1359-0294(98)80039-3.
(75) Douvas, A. M.; Makarona, E.; Glezos, N.; Argitis, P.; Mielczarski, J. A.; Mielczarski, E. Polyoxometalate-Based Layered Structures for Charge Transport Control in Molecular Devices. *ACS Nano* **2008**, *2* (4), 733–742. https://doi.org/10.1021/nn700333j.
(76) Dalla Francesca, K.; Lenfant, S.; Laurans, M.; Volatron, F.; Izzet, G.; Humblot, V.; Methivier, C.; Guerin, D.; Proust, A.; Vuillaume, D. Charge Transport through Redox Active [$H_7P_8W_{48}$

$O_{184}]^{33-}$ Polyoxometalates Self-Assembled onto Gold Surfaces and Gold Nanodots. *Nanoscale* **2019**, *11* (4), 1863–1878. https://doi.org/10.1039/C8NR09377F.

(77) Laurans, M.; Dalla Francesca, K.; Volatron, F.; Izzet, G.; Guerin, D.; Vuillaume, D.; Lenfant, S.; Proust, A. Molecular Signature of Polyoxometalates in Electron Transport of Silicon-Based Molecular Junctions. *Nanoscale* **2018**, *10* (36), 17156–17165. https://doi.org/10.1039/C8NR04946G.

(78) Turo, M. J.; Chen, L.; Moore, C. E.; Schimpf, A. M. Co^{2+} -Linked $[NaP_5W_{30}O_{110}]^{14-}$: A Redox-Active Metal Oxide Framework with High Electron Density. *J. Am. Chem. Soc.* **2019**, *141* (11), 4553–4557. https://doi.org/10.1021/jacs.9b00866.

(79) Linnenberg, O.; Moors, M.; Notario-Estévez, A.; López, X.; de Graaf, C.; Peter, S.; Baeumer, C.; Waser, R.; Monakhov, K. Yu. Addressing Multiple Resistive States of Polyoxovanadates: Conductivity as a Function of Individual Molecular Redox States. *J. Am. Chem. Soc.* **2018**, *140* (48), 16635–16640. https://doi.org/10.1021/jacs.8b08780.

(80) Notario-Estévez, A.; López, X.; de Graaf, C. Computational Study of the Staircase Molecular Conductivity of Polyoxovanadates Adsorbed on Au(111). *Dalton Trans.* **2021**, *50* (16), 5540–5551. https://doi.org/10.1039/D1DT00731A.

(81) Demis, E. C.; Aguilera, R.; Sillin, H. O.; Scharnhorst, K.; Sandouk, E. J.; Aono, M.; Stieg, A. Z.; Gimzewski, J. K. Atomic Switch Networks—Nanoarchitectonic Design of a Complex System for Natural Computing. *Nanotechnology* **2015**, *26* (20), 204003. https://doi.org/10.1088/0957-4484/26/20/204003.

(82) Chicca, E.; Stefanini, F.; Bartolozzi, C.; Indiveri, G. Neuromorphic Electronic Circuits for Building Autonomous Cognitive Systems. *Proc. IEEE* **2014**, *102* (9), 1367–1388. https://doi.org/10.1109/JPROC.2014.2313954.

(83) Burr, G. W.; Shelby, R. M.; Sebastian, A.; Kim, S.; Kim, S.; Sidler, S.; Virwani, K.; Ishii, M.; Narayanan, P.; Fumarola, A.; Sanches, L. L.; Boybat, I.; Le Gallo, M.; Moon, K.; Woo, J.; Hwang, H.; Leblebici, Y. Neuromorphic Computing Using Non-Volatile Memory. *Adv. Phys. X* **2017**, *2* (1), 89–124. https://doi.org/10.1080/23746149.2016.1259585.

(84) Pecqueur, S.; Vuillaume, D.; Alibart, F. Perspective: Organic Electronic Materials and Devices for Neuromorphic Engineering. *J. Appl. Phys.* **2018**, *124* (15), 151902. https://doi.org/10.1063/1.5042419.

(85) *Jaeger H 2002 Tutorial on Training Recurrent Neural Networks, Covering BPPT, RTRL, EKF and the' Echo State Network' Approach GMD-Forschungszentrum Informationstechnik.*

(86) Verstraeten, D.; Schrauwen, B.; D'Haene, M.; Stroobandt, D. An Experimental Unification of Reservoir Computing Methods. *Neural Netw.* **2007**, *20* (3), 391–403. https://doi.org/10.1016/j.neunet.2007.04.003.

(87) Jaeger, H. The "Echo State" Approach to Analysing and Training Recurrent Neural Networks – with an Erratum Note. 47.

(88) Maass, W.; Natschläger, T.; Markram, H. Real-Time Computing Without Stable States: A New Framework for Neural Computation Based on Perturbations. *Neural Comput.* **2002**, *14* (11), 2531–2560. https://doi.org/10.1162/089976602760407955.

(89) Jaeger, H. Harnessing Nonlinearity: Predicting Chaotic Systems and Saving Energy in Wireless Communication. *Science* **2004**, *304* (5667), 78–80. https://doi.org/10.1126/science.1091277.

(90) Tanaka, G.; Yamane, T.; Héroux, J. B.; Nakane, R.; Kanazawa, N.; Takeda, S.; Numata, H.; Nakano, D.; Hirose, A. Recent Advances in Physical Reservoir Computing: A Review. *Neural Netw.* **2019**, *115*, 100–123. https://doi.org/10.1016/j.neunet.2019.03.005.

(91) Rosenblatt, F. The Perceptron: A Probabilistic Model for Information Storage and Organization in the Brain. *Psychol. Rev.* **1958**, *65* (6), 386–408. https://doi.org/10.1037/h0042519.

(92) Verstraeten, D. Reservoir Computing : Computation with Dynamical Systems. PhD, 2009.

(93) Pecqueur, S.; Mastropasqua Talamo, M.; Guérin, D.; Blanchard, P.; Roncali, J.; Vuillaume, D.; Alibart, F. Neuromorphic Time-Dependent Pattern Classification with Organic Electrochemical Transistor Arrays. *Adv. Electron. Mater.* **2018**, *4* (9), 1800166. https://doi.org/10.1002/aelm.201800166.

(94) van de Burgt, Y.; Melianas, A.; Keene, S. T.; Malliaras, G.; Salleo, A. Organic Electronics for Neuromorphic Computing. *Nat. Electron.* **2018**, *1* (7), 386–397. https://doi.org/10.1038/s41928-018-0103-3.

(95) Gkoupidenis, P.; Schaefer, N.; Garlan, B.; Malliaras, G. G. Neuromorphic Functions in PEDOT:PSS Organic Electrochemical Transistors. *Adv. Mater.* **2015**, *27* (44), 7176–7180. https://doi.org/10.1002/adma.201503674.
(96) van de Burgt, Y.; Lubberman, E.; Fuller, E. J.; Keene, S. T.; Faria, G. C.; Agarwal, S.; Marinella, M. J.; Alec Talin, A.; Salleo, A. A Non-Volatile Organic Electrochemical Device as a Low-Voltage Artificial Synapse for Neuromorphic Computing. *Nat. Mater.* **2017**, *16* (4), 414–418. https://doi.org/10.1038/nmat4856.
(97) Miller, J. F.; Harding, S. L.; Tufte, G. Evolution-in-Materio: Evolving Computation in Materials. *Evol. Intell.* **2014**, *7* (1), 49–67. https://doi.org/10.1007/s12065-014-0106-6.
(98) Miller, J. F.; Downing, K. Evolution in Materio: Looking beyond the Silicon Box. In *Proceedings 2002 NASA/DoD Conference on Evolvable Hardware*; 2002; pp 167–176. https://doi.org/10.1109/EH.2002.1029882.
(99) Bose, S. K.; Lawrence, C. P.; Liu, Z.; Makarenko, K. S.; van Damme, R. M. J.; Broersma, H. J.; van der Wiel, W. G. Evolution of a Designless Nanoparticle Network into Reconfigurable Boolean Logic. *Nat. Nanotechnol.* **2015**, *10* (12), 1048–1052. https://doi.org/10.1038/nnano.2015.207.
(100) Bose, S. K.; Mallinson, J. B.; Gazoni, R. M.; Brown, S. A. Stable Self-Assembled Atomic-Switch Networks for Neuromorphic Applications. *IEEE Trans. Electron Devices* **2017**, *64* (12), 5194–5201. https://doi.org/10.1109/TED.2017.2766063.
(101) Mallinson, J. B.; Shirai, S.; Acharya, S. K.; Bose, S. K.; Galli, E.; Brown, S. A. Avalanches and Criticality in Self-Organized Nanoscale Networks. *Sci. Adv.* **2019**, *5* (11), eaaw8438. https://doi.org/10.1126/sciadv.aaw8438.
(102) Pike, M. D.; Bose, S. K.; Mallinson, J. B.; Acharya, S. K.; Shirai, S.; Galli, E.; Weddell, S. J.; Bones, P. J.; Arnold, M. D.; Brown, S. A. Atomic Scale Dynamics Drive Brain-like Avalanches in Percolating Nanostructured Networks. *Nano Lett.* **2020**, *20* (5), 3935–3942. https://doi.org/10.1021/acs.nanolett.0c01096.
(103) Avizienis, A. V.; Sillin, H. O.; Martin-Olmos, C.; Shieh, H. H.; Aono, M.; Stieg, A. Z.; Gimzewski, J. K. Neuromorphic Atomic Switch Networks. *PLoS ONE* **2012**, *7* (8), e42772. https://doi.org/10.1371/journal.pone.0042772.
(104) Sillin, H. O.; Aguilera, R.; Shieh, H.-H.; Avizienis, A. V.; Aono, M.; Stieg, A. Z.; Gimzewski, J. K. A Theoretical and Experimental Study of Neuromorphic Atomic Switch Networks for Reservoir Computing. *Nanotechnology* **2013**, *24* (38), 384004. https://doi.org/10.1088/0957-4484/24/38/384004.
(105) Stieg, A. Z.; Avizienis, A. V.; Sillin, H. O.; Martin-Olmos, C.; Aono, M.; Gimzewski, J. K. Emergent Criticality in Complex Turing B-Type Atomic Switch Networks. *Adv. Mater.* **2012**, *24* (2), 286–293. https://doi.org/10.1002/adma.201103053.
(106) Tanaka, H.; Akai-Kasaya, M.; TermehYousefi, A.; Hong, L.; Fu, L.; Tamukoh, H.; Tanaka, D.; Asai, T.; Ogawa, T. A Molecular Neuromorphic Network Device Consisting of Single-Walled Carbon Nanotubes Complexed with Polyoxometalate. *Nat. Commun.* **2018**, *9* (1), 2693. https://doi.org/10.1038/s41467-018-04886-2.
(107) Banerjee, D.; Azhari, S.; Usami, Y.; Tanaka, H. Room Temperature Demonstration of In-Materio Reservoir Computing for Optimizing Boolean Function with Single-Walled Carbon Nanotube/Porphyrin-Polyoxometalate Composite. *Appl. Phys. Express* **2021**, *14* (10), 105003. https://doi.org/10.35848/1882-0786/ac24db.
(108) Banerjee, D.; Kotooka, T.; Azhari, S.; Usami, Y.; Ogawa, T.; Gimzewski, J. K.; Tamukoh, H.; Tanaka, H. Emergence of In-Materio Intelligence from an Incidental Structure of a Single-Walled Carbon Nanotube–Porphyrin Polyoxometalate Random Network. *Adv. Intell. Syst.* **2022**, *4* (4), 2100145. https://doi.org/10.1002/aisy.202100145.
(109) Viero, Y.; Guérin, D.; Vladyka, A.; Alibart, F.; Lenfant, S.; Calame, M.; Vuillaume, D. Light-Stimulatable Molecules/Nanoparticles Networks for Switchable Logical Functions and Reservoir Computing. *Adv. Funct. Mater.* **2018**, *28* (39), 1801506. https://doi.org/10.1002/adfm.201801506.
(110) Zhang, T.; Guérin, D.; Alibart, F.; Vuillaume, D.; Lmimouni, K.; Lenfant, S.; Yassin, A.; Oçafrain, M.; Blanchard, P.; Roncali, J. Negative Differential Resistance, Memory, and Reconfigurable Logic Functions Based on Monolayer Devices Derived from Gold Nanoparticles

Functionalized with Electropolymerizable TEDOT Units. *J. Phys. Chem. C* **2017**, *121* (18), 10131–10139. https://doi.org/10.1021/acs.jpcc.7b00056.

(111) Weiss, E. A.; Chiechi, R. C.; Kaufman, G. K.; Kriebel, J. K.; Li, Z.; Duati, M.; Rampi, M. A.; Whitesides, G. M. Influence of Defects on the Electrical Characteristics of Mercury-Drop Junctions: Self-Assembled Monolayers of *n* -Alkanethiolates on Rough and Smooth Silver. *J. Am. Chem. Soc.* **2007**, *129* (14), 4336–4349. https://doi.org/10.1021/ja0677261.

(112) Weiss, E. A.; Kaufman, G. K.; Kriebel, J. K.; Li, Z.; Schalek, R.; Whitesides, G. M. Si/SiO $_2$ -Templated Formation of Ultraflat Metal Surfaces on Glass, Polymer, and Solder Supports: Their Use as Substrates for Self-Assembled Monolayers. *Langmuir* **2007**, *23* (19), 9686–9694. https://doi.org/10.1021/la701919r.

(113) Whitesides, G. M.; Biebuyck, H. A.; Folkers, J. P.; Prime, K. L. Acid-Base Interactions in Wetting. *J. Adhes. Sci. Technol.* **1991**, *5* (1), 57–69. https://doi.org/10.1163/156856191X00828.

(114) Vezenov, D. V.; Noy, A.; Rozsnyai, L. F.; Lieber, C. M. Force Titrations and Ionization State Sensitive Imaging of Functional Groups in Aqueous Solutions by Chemical Force Microscopy. *J. Am. Chem. Soc.* **1997**, *119* (8), 2006–2015. https://doi.org/10.1021/ja963375m.

(115) Nishiyama, K.; Kubo, A.; Ueda, A.; Taniguchi, I. Surface PKa of Amine-Terminated Self-Assembled Monolayers Evaluated by Direct Observation of Counter Anion by FT-Surface Enhanced Raman Spectroscopy. *Chem. Lett.* **2002**, *31* (1), 80–81. https://doi.org/10.1246/cl.2002.80.

(116) Marmisollé, W. A.; Capdevila, D. A.; de la Llave, E.; Williams, F. J.; Murgida, D. H. Self-Assembled Monolayers of NH2-Terminated Thiolates: Order, PKa, and Specific Adsorption. *Langmuir* **2013**, *29* (17), 5351–5359. https://doi.org/10.1021/la304730q.

(117) Cui, X. D.; Primak, A.; Zarate, X.; Tomfohr, J.; Sankey, O. F.; Moore, A. L.; Moore, T. A.; Gust, D.; Harris, G.; Lindsay, S. M. Reproducible Measurement of Single-Molecule Conductivity. *Science* **2001**, *294* (5542), 571–574. https://doi.org/10.1126/science.1064354.

(118) Cui, X. D.; Zarate, X.; Tomfohr, J.; Sankey, O. F.; Primak, A.; Moore, A. L.; Moore, T. A.; Gust, D.; Harris, G.; Lindsay, S. M. Making Electrical Contacts to Molecular Monolayers. *Nanotechnology* **2001**, *13* (1), 5–14. https://doi.org/10.1088/0957-4484/13/1/302.

(119) Morita, T.; Lindsay, S. Determination of Single Molecule Conductances of Alkanedithiols by Conducting-Atomic Force Microscopy with Large Gold Nanoparticles. *J. Am. Chem. Soc.* **2007**, *129* (23), 7262–7263. https://doi.org/10.1021/ja072040+.

(120) Smaali, K.; Desbief, S.; Foti, G.; Frederiksen, T.; Sanchez-Portal, D.; Arnau, A.; P. Nys, J.; Leclère, P.; Vuillaume, D.; Clément, N. On the Mechanical and Electronic Properties of Thiolated Gold Nanocrystals. *Nanoscale* **2015**, *7* (5), 1809–1819. https://doi.org/10.1039/C4NR06180B.

(121) Engelkes, V. B.; Frisbie, C. D. Simultaneous Nanoindentation and Electron Tunneling through Alkanethiol Self-Assembled Monolayers. *J. Phys. Chem. B* **2006**, *110* (20), 10011–10020. https://doi.org/10.1021/jp055567m.

(122) Rocchiccioli-Deltcheff, C.; Fournier, M.; Franck, R.; Thouvenot, R. Vibrational Investigations of Polyoxometalates. 2. Evidence for Anion-Anion Interactions in Molybdenum(VI) and Tungsten(VI) Compounds Related to the Keggin Structure. *Inorg. Chem.* **1983**, *22* (2), 207–216. https://doi.org/10.1021/ic00144a006.

(123) Artero, V.; Proust, A. Reduction of the Phosphododecamolybdate Ion by Phosphonium Ylides and Phosphanes. *Eur. J. Inorg. Chem.* **2000**, *2000* (11), 2393–2400. https://doi.org/10.1002/1099-0682(200011)2000:11%3c2393::AID-EJIC2393%3e3.0.CO;2-G.

(124) Trasatti, S. The Absolute Electrode Potential: An Explanatory Note (Recommendations 1986). *Pure Appl. Chem.* **1986**, *58* (7), 955–966. https://doi.org/10.1351/pac198658070955.

(125) Kurth, D. G.; Volkmer, D.; Ruttorf, M.; Richter, B.; Müller, A. Ultrathin Composite Films Incorporating the Nanoporous Isopolyoxomolybdate "Keplerate" (NH4)42[Mo132O372(CH3COO)30(H2O)72]. *Chem. Mater.* **2000**, *12* (10), 2829–2831. https://doi.org/10.1021/cm001032o.

(126) Salomon, A.; Cahen, D.; Lindsay, S.; Tomfohr, J.; Engelkes, V. b.; Frisbie, C. d. Comparison of Electronic Transport Measurements on Organic Molecules. *Adv. Mater.* **2003**, *15* (22), 1881–1890. https://doi.org/10.1002/adma.200306091.

(127) Sun, H.-R.; Zhang, S.-Y.; Xu, J.-Q.; Yang, G.-Y.; Shi, T.-S. Electrochemical and In-Situ UV-Visible-near-IR and FTIR Spectroelectrochemical Characterisation of the Mixed-Valence Heteropolyanion PMo12O40n− (N=4, 5, 6, 7) in Aprotic Media. *J. Electroanal. Chem.* **1998**, *455* (1–2), 57–68. https://doi.org/10.1016/S0022-0728(98)00150-8.
(128) Troupis, A.; Hiskia, A.; Papaconstantinou, E. Photocatalytic Reduction—Recovery of Silver Using Polyoxometalates. *Appl. Catal. B Environ.* **2003**, *42* (3), 305–315. https://doi.org/10.1016/S0926-3373(02)00264-3.
(129) Yamase, T. Photo- and Electrochromism of Polyoxometalates and Related Materials. *Chem. Rev.* **1998**, *98* (1), 307–326. https://doi.org/10.1021/cr9604043.
(130) Cabosart, D.; El Abbassi, M.; Stefani, D.; Frisenda, R.; Calame, M.; van der Zant, H. S. J.; Perrin, M. L. A Reference-Free Clustering Method for the Analysis of Molecular Break-Junction Measurements. *Appl. Phys. Lett.* **2019**, *114* (14), 143102. https://doi.org/10.1063/1.5089198.
(131) El Abbassi, M.; Overbeck, J.; Braun, O.; Calame, M.; van der Zant, H. S. J.; Perrin, M. L. Benchmark and Application of Unsupervised Classification Approaches for Univariate Data. *Commun. Phys.* **2021**, *4* (1), 1–9. https://doi.org/10.1038/s42005-021-00549-9.
(132) Hamill, J. M.; Zhao, X. T.; Mészáros, G.; Bryce, M. R.; Arenz, M. Fast Data Sorting with Modified Principal Component Analysis to Distinguish Unique Single Molecular Break Junction Trajectories. *Phys. Rev. Lett.* **2018**, *120* (1), 016601. https://doi.org/10.1103/PhysRevLett.120.016601.
(133) Lemmer, M.; Inkpen, M. S.; Kornysheva, K.; Long, N. J.; Albrecht, T. Unsupervised Vector-Based Classification of Single-Molecule Charge Transport Data. *Nat. Commun.* **2016**, *7* (1), 12922. https://doi.org/10.1038/ncomms12922.
(134) Karcz, R.; Niemiec, P.; Pamin, K.; Połtowicz, J.; Kryściak-Czerwenka, J.; Napruszewska, B. D.; Michalik-Zym, A.; Witko, M.; Tokarz-Sobieraj, R.; Serwicka, E. M. Effect of Cobalt Location in Keggin-Type Heteropoly Catalysts on Aerobic Oxidation of Cyclooctane: Experimental and Theoretical Study. *Appl. Catal. Gen.* **2017**, *542*, 317–326. https://doi.org/10.1016/j.apcata.2017.05.035.
(135) Beljonne, D.; Cornil, J.; Muccioli, L.; Zannoni, C.; Brédas, J.-L.; Castet, F. Electronic Processes at Organic−Organic Interfaces: Insight from Modeling and Implications for Opto-Electronic Devices. *Chem. Mater.* **2011**, *23* (3), 591–609. https://doi.org/10.1021/cm1023426.
(136) Cornil, D.; Li, H.; Wood, C.; Pourtois, G.; Brédas, J.-L.; Cornil, J. Work-Function Modification of Au and Ag Surfaces upon Deposition of Self-Assembled Monolayers: Influence of the Choice of the Theoretical Approach and the Thiol Decomposition Scheme. *ChemPhysChem* **2013**, *14* (13), 2939–2946. https://doi.org/10.1002/cphc.201300450.
(137) Crivillers, N.; Osella, S.; Van Dyck, C.; Lazzerini, G. M.; Cornil, D.; Liscio, A.; Di Stasio, F.; Mian, S.; Fenwick, O.; Reinders, F.; Neuburger, M.; Treossi, E.; Mayor, M.; Palermo, V.; Cacialli, F.; Cornil, J.; Samorì, P. Large Work Function Shift of Gold Induced by a Novel Perfluorinated Azobenzene-Based Self-Assembled Monolayer. *Adv. Mater.* **2013**, *25* (3), 432–436. https://doi.org/10.1002/adma.201201737.
(138) Vila-Nadal, L.; Georgiev, V. P. Ab-Initio Calculations, Private Communication. **2022**.
(139) Maestre, J. M.; Lopez, X.; Bo, C.; Poblet, J.-M.; Casañ-Pastor, N. Electronic and Magnetic Properties of α-Keggin Anions: A DFT Study of [XM12O40]n-, (M = W, Mo; X = AlIII, SiIV, PV, FeIII, CoII, CoIII) and [SiM11VO40]m- (M = Mo and W). *J. Am. Chem. Soc.* **2001**, *123* (16), 3749–3758. https://doi.org/10.1021/ja003563j.
(140) Yuan, L.; Franco, C.; Crivillers, N.; Mas-Torrent, M.; Cao, L.; Sangeeth, C. S. S.; Rovira, C.; Veciana, J.; Nijhuis, C. A. Chemical Control over the Energy-Level Alignment in a Two-Terminal Junction. *Nat. Commun.* **2016**, *7* (1), 12066. https://doi.org/10.1038/ncomms12066.
(141) Heimel, G.; Zojer, E.; Romaner, L.; Brédas, J.-L.; Stellacci, F. Doping Molecular Wires. *Nano Lett.* **2009**, *9* (7), 2559–2564. https://doi.org/10.1021/nl9006613.
(142) Crivillers, N.; Munuera, C.; Mas-Torrent, M.; Simão, C.; Bromley, S. T.; Ocal, C.; Rovira, C.; Veciana, J. Dramatic Influence of the Electronic Structure on the Conductivity through Open- and Closed-Shell Molecules. *Adv. Mater.* **2009**, *21* (10–11), 1177–1181. https://doi.org/10.1002/adma.200801707.
(143) Naghibi, S.; Sangtarash, S.; Kumar, V. J.; Wu, J.-Z.; Judd, M. M.; Qiao, X.; Gorenskaia, E.; Higgins, S. J.; Cox, N.; Nichols, R. J.; Sadeghi, H.; Low, P. J.; Vezzoli, A. Redox-Addressable

Single-Molecule Junctions Incorporating a Persistent Organic Radical. **2021**. https://doi.org/10.26434/chemrxiv-2021-3lqf7.
(144) Low, J. Z.; Kladnik, G.; Patera, L. L.; Sokolov, S.; Lovat, G.; Kumarasamy, E.; Repp, J.; Campos, L. M.; Cvetko, D.; Morgante, A.; Venkataraman, L. The Environment-Dependent Behavior of the Blatter Radical at the Metal–Molecule Interface. *Nano Lett.* **2019**, *19* (4), 2543–2548. https://doi.org/10.1021/acs.nanolett.9b00275.
(145) Souto, M.; Yuan, L.; Morales, D. C.; Jiang, L.; Ratera, I.; Nijhuis, C. A.; Veciana, J. Tuning the Rectification Ratio by Changing the Electronic Nature (Open-Shell and Closed-Shell) in Donor–Acceptor Self-Assembled Monolayers. *J. Am. Chem. Soc.* **2017**, *139* (12), 4262–4265. https://doi.org/10.1021/jacs.6b12601.
(146) Qi, Y.; Yaffe, O.; Tirosh, E.; Vilan, A.; Cahen, D.; Kahn, A. Filled and Empty States of Alkanethiol Monolayer on Au (111): Fermi Level Asymmetry and Implications for Electron Transport. *Chem. Phys. Lett.* **2011**, *511* (4), 344–347. https://doi.org/10.1016/j.cplett.2011.06.050.
(147) Lenfant, S.; Krzeminski, C.; Delerue, C.; Allan, G.; Vuillaume, D. Molecular Rectifying Diodes from Self-Assembly on Silicon. *Nano Lett.* **2003**, *3* (6), 741–746. https://doi.org/10.1021/nl034162f.
(148) Nijhuis, C. A.; Reus, W. F.; Whitesides, G. M. Molecular Rectification in Metal−SAM−Metal Oxide−Metal Junctions. *J. Am. Chem. Soc.* **2009**, *131* (49), 17814–17827. https://doi.org/10.1021/ja9048898.
(149) Chen, X.; Roemer, M.; Yuan, L.; Du, W.; Thompson, D.; del Barco, E.; Nijhuis, C. A. Molecular Diodes with Rectification Ratios Exceeding 105 Driven by Electrostatic Interactions. *Nat. Nanotechnol.* **2017**, *12* (8), 797–803. https://doi.org/10.1038/nnano.2017.110.
(150) Vilan, A.; Aswal, D.; Cahen, D. Large-Area, Ensemble Molecular Electronics: Motivation and Challenges. *Chem Rev* **2017**, 39.
(151) Van Dyck, C.; Bergren, A. J. Large Built-In Fields Control the Electronic Properties of Nanoscale Molecular Devices with Dipolar Structures. *Adv. Electron. Mater.* **2018**, *4* (5), 1700656. https://doi.org/10.1002/aelm.201700656.
(152) Huez, C.; Guerin, D.; Lenfant, S.; Volatron, F.; Calame, M.; Perrin, M.; Proust, A.; Vuillaume, D. Redox-Controlled Conductance of Polyoxometalate Molecular Junctions. *Nanoscale* **2022**. https://doi.org/10.1039/D2NR03457C.
(153) Liu, S.; Möhwald, H.; Volkmer, D.; Kurth, D. G. Polyoxometalate-Based Electro- and Photochromic Dual-Mode Devices. *Langmuir* **2006**, *22* (5), 1949–1951. https://doi.org/10.1021/la0523863.
(154) Han, Y.; Nickle, C.; Zhang, Z.; Astier, H. P. A. G.; Duffin, T. J.; Qi, D.; Wang, Z.; del Barco, E.; Thompson, D.; Nijhuis, C. A. Electric-Field-Driven Dual-Functional Molecular Switches in Tunnel Junctions. *Nat. Mater.* **2020**, *19* (8), 843–848. https://doi.org/10.1038/s41563-020-0697-5.
(155) Lapham, P.; Vilà-Nadal, L.; Cronin, L.; Georgiev, V. P. Influence of the Contact Geometry and Counterions on the Current Flow and Charge Transfer in Polyoxometalate Molecular Junctions: A Density Functional Theory Study. *J. Phys. Chem. C* **2021**, *125* (6), 3599–3610. https://doi.org/10.1021/acs.jpcc.0c11038.
(156) Creaser, I.; Heckel, M. C.; Neitz, R. J. Rigid Nonlabile Polyoxometalate Cryptates [ZP~W300110](~T~-Ha"t)E-Xhibit Unprecedented Selectivity for Certain Lanthanide and Other Multivalent Cations. 6.
(157) Sadakane, M.; Ichi, Y.; Ide, Y.; Sano, T. Thermal Stability and Acidic Strength of Preyssler-Type Phosphotungstic Acid, H14[P5W30O110Na] and It's Catalytic Activity for Hydrolysis of Alkyl Acetates. *Z. Für Anorg. Allg. Chem.* **2011**, *637* (14–15), 2120–2124. https://doi.org/10.1002/zaac.201100427.
(158) Cantwell, F. F.; Nielsen, J. S.; Hrudey, S. E. Free Nickel Ion Concentration in Sewage by an Ion Exchange Column-Equilibration Method. *Anal. Chem.* **1982**, *54* (9), 1498–1503. https://doi.org/10.1021/ac00246a012.
(159) Jeannin, Y.; Martin-Frere, J.; Choi, D. J.; Pope, M. T. The Sodium Pentaphosphato(V)-Triacontatungstate Anion Isolated as the Ammonium Salt. In *Inorganic Syntheses*; Ginsberg, A.

P., Ed.; John Wiley & Sons, Inc.: Hoboken, NJ, USA, 2007; pp 115–118. https://doi.org/10.1002/9780470132586.ch20.
(160) Viero, Y.; Copie, G.; Guérin, D.; Krzeminski, C.; Vuillaume, D.; Lenfant, S.; Cleri, F. High Conductance Ratio in Molecular Optical Switching of Functionalized Nanoparticle Self-Assembled Nanodevices. *J. Phys. Chem. C* **2015**, *119* (36), 21173–21183. https://doi.org/10.1021/acs.jpcc.5b05839.
(161) Turkevich, J.; Stevenson, P. C.; Hillier, J. A Study of the Nucleation and Growth Processes in the Synthesis of Colloidal Gold. *Discuss. Faraday Soc.* **1951**, *11*, 55. https://doi.org/10.1039/df9511100055.
(162) Enustun, B. V.; Turkevich, J. Coagulation of Colloidal Gold. *J. Am. Chem. Soc.* **1963**, *85* (21), 3317–3328. https://doi.org/10.1021/ja00904a001.
(163) Wang, F.; He, C.; Han, M.-Y.; Wu, J. H.; Xu, G. Q. Chemical Controlled Reversible Gold Nanoparticles Dissolution and Reconstruction at Room-Temperature. *Chem. Commun.* **2012**, *48* (49), 6136. https://doi.org/10.1039/c2cc31319g.
(164) Adegoke, O.; Takemura, K.; Park, E. Y. Plasmonic Oleylamine-Capped Gold and Silver Nanoparticle-Assisted Synthesis of Luminescent Alloyed CdZnSeS Quantum Dots. *ACS Omega* **2018**, *3* (2), 1357–1366. https://doi.org/10.1021/acsomega.7b01724.
(165) Yang, G. A Convenient Phase Transfer Protocol to Functionalize Gold Nanoparticles with Short Alkylamine Ligands. *J. Colloid Interface Sci.* **2015**, 9. https://doi.org/10.1016/j.jcis.2015.08.054.
(166) Zhang, H.; Junaid, M.; Liu, K.; Ras, R. H. A.; Ikkala, O. Light-Induced Reversible Hydrophobization of Cationic Gold Nanoparticles *via* Electrostatic Adsorption of a Photoacid. *Nanoscale* **2019**, *11* (30), 14118–14122. https://doi.org/10.1039/C9NR05416B.
(167) Bernard, L.; Kamdzhilov, Y.; Calame, M.; van der Molen, S. J.; Liao, J.; Schönenberger, C. Spectroscopy of Molecular Junction Networks Obtained by Place Exchange in 2D Nanoparticle Arrays. *J. Phys. Chem. C* **2007**, *111* (50), 18445–18450. https://doi.org/10.1021/jp077095c.
(168) Santhanam, V.; Liu, J.; Agarwal, R.; Andres, R. P. Self-Assembly of Uniform Monolayer Arrays of Nanoparticles. *Langmuir* **2003**, *19* (19), 7881–7887. https://doi.org/10.1021/la0341761.
(169) Santhanam, V.; Andres, R. P. Microcontact Printing of Uniform Nanoparticle Arrays. *Nano Lett.* **2004**, *4* (1), 41–44. https://doi.org/10.1021/nl034851r.
(170) Schindelin, J.; Arganda-Carreras, I.; Frise, E.; Kaynig, V.; Longair, M.; Pietzsch, T.; Preibisch, S.; Rueden, C.; Saalfeld, S.; Schmid, B.; Tinevez, J.-Y.; White, D. J.; Hartenstein, V.; Eliceiri, K.; Tomancak, P.; Cardona, A. Fiji: An Open-Source Platform for Biological-Image Analysis. *Nat. Methods* **2012**, *9* (7), 676–682. https://doi.org/10.1038/nmeth.2019.
(171) Borges, J.; Ribeiro, J. A.; Pereira, E. M.; Carreira, C. A.; Pereira, C. M.; Silva, F. Preparation and Characterization of DNA Films Using Oleylamine Modified Au Surfaces. *J. Colloid Interface Sci.* **2011**, *358* (2), 626–634. https://doi.org/10.1016/j.jcis.2011.03.039.
(172) Martinez, B.; Livache, C.; Meriggio, E.; Xu, X. Z.; Cruguel, H.; Lacaze, E.; Proust, A.; Ithurria, S.; Silly, M. G.; Cabailh, G.; Volatron, F.; Lhuillier, E. Polyoxometalate as Control Agent for the Doping in HgSe Self-Doped Nanocrystals. *J. Phys. Chem. C* **2018**, *122* (46), 26680–26685. https://doi.org/10.1021/acs.jpcc.8b07190.
(173) Wang, Y.; Weinstock, I. A. Polyoxometalate-Decorated Nanoparticles. *Chem. Soc. Rev.* **2012**, *41* (22), 7479. https://doi.org/10.1039/c2cs35126a.
(174) Ernst, A. Z.; Sun, L.; Wiaderek, K.; Kolary, A.; Zoladek, S.; Kulesza, P. J.; Cox, J. A. Synthesis of Polyoxometalate-Protected Gold Nanoparticles by a Ligand-Exchange Method: Application to the Electrocatalytic Reduction of Bromate. *Electroanalysis* **2007**, *19* (19–20), 2103–2109. https://doi.org/10.1002/elan.200703925.
(175) Mayer, C. R.; Neveu, S.; Cabuil, V. A Nanoscale Hybrid System Based on Gold Nanoparticles and Heteropolyanions. *Angew. Chem. Int. Ed.* **2002**, *41* (3), 501–503. https://doi.org/10.1002/1521-3773(20020201)41:3%3c501::AID-ANIE501%3e3.0.CO;2-Z.
(176) Hegde, S.; Joshi, S.; Mukherjee, T.; Kapoor, S. Formation of Gold Nanoparticles via a Thiol Functionalized Polyoxometalate. *Mater. Sci. Eng. C* **2013**, *33* (4), 2332–2337. https://doi.org/10.1016/j.msec.2013.01.065.
(177) *Table Infra-rouge : interprétation des spectres IR*. https://www.lachimie.fr/analytique/infrarouge/table-infra rouge.php%20(accessed%202022-09-08).

(178) Kluenker, M.; Mondeshki, M.; Nawaz Tahir, M.; Tremel, W. Monitoring Thiol–Ligand Exchange on Au Nanoparticle Surfaces. *Langmuir* **2018**, *34* (4), 1700–1710. https://doi.org/10.1021/acs.langmuir.7b04015.
(179) Yang, Y.; Serrano, L. A.; Guldin, S. A Versatile AuNP Synthetic Platform for Decoupled Control of Size and Surface Composition. *Langmuir* **2018**, *34* (23), 6820–6826. https://doi.org/10.1021/acs.langmuir.8b00353.
(180) Batalha, D. C.; Ferreira, S. O.; Silva, R. C. da; Silva, M. J. da. Cesium-Exchanged Lacunar Keggin Heteropolyacid Salts: Efficient Solid Catalysts for the Green Oxidation of Terpenic Alcohols with Hydrogen Peroxide. *ChemistrySelect* **2020**, *5* (6), 1976–1986. https://doi.org/10.1002/slct.201903437.
(181) Kim, Y.; Song, H. Noise Spectroscopy of Molecular Electronic Junctions. *Appl. Phys. Rev.* **2021**, *8* (1), 011303. https://doi.org/10.1063/5.0027602.
(182) Ambrózy, A. *Electronic Noise*; Mcgraw-Hill College, 1982.
(183) Briaire, J.; Vandamme, L. K. J. Uncertainty in Gaussian Noise Generalized for Cross-Correlation Spectra. *J. Appl. Phys.* **1998**, *84* (8), 4370–4374. https://doi.org/; https://doi.org/10.1063/1.368657.
(184) Hooge, F. N. 1/f Noise. *Phys. B C* **1976**, *83* (1), 14–23. https://doi.org/10.1016/0378-4363(76)90089-9.
(185) Hooge, F. N. 1/*f* Noise Is No Surface Effect. *Phys. Lett. A* **1969**, *29* (3), 139–140. https://doi.org/10.1016/0375-9601(69)90076-0.
(186) Donhauser, Z. J.; Mantooth, B. A.; Kelly, K. F.; Bumm, L. A.; Monnell, J. D.; Stapleton, J. J.; Price, D. W.; Rawlett, A. M.; Allara, D. L.; Tour, J. M.; Weiss, P. S. Conductance Switching in Single Molecules through Conformational Changes. *Science* **2001**, *292* (5525), 2303–2307. https://doi.org/10.1126/science.1060294.
(187) Xiang, D.; Lee, T.; Kim, Y.; Mei, T.; Wang, Q. Origin of Discrete Current FLuctuations in a Single Molecule Junction. **2014**, 6. https://doi-org.insis.bib.cnrs.fr/10.1039/C4NR03480E.
(188) Adak, O.; Rosenthal, E.; Nuckolls, C.; Hybertsen, M. S.; Venkataraman, L. Flicker Noise as a Probe of Electronic Interaction at Metal−Single Molecule Interfaces. *Nano Lett* **2015**, 7. https://doi-org.insis.bib.cnrs.fr/10.1021/acs.nanolett.5b01270.
(189) Brunner, J.; González, M. T.; Schönenberger, C.; Calame, M. Random Telegraph Signals in Molecular Junctions. *J. Phys. Condens. Matter* **2014**, *26* (47), 474202. https://doi.org/10.1088/0953-8984/26/47/474202.
(190) Clément, N.; Pleutin, S.; Seitz, O.; Lenfant, S.; Vuillaume, D. 1 ⁄ f γ Tunnel Current Noise through Si-Bound Alkyl Monolayers. *Phys. Rev. B* **2007**, *76* (20), 205407. https://doi.org/10.1103/PhysRevB.76.205407.
(191) Kim, Y.; Song, H.; Kim, D.; Lee, T.; Jeong, H. Noise Characteristics of Charge Tunneling *via* Localized States in Metal−Molecule−Metal Junctions. *ACS Nano* **2010**, *4* (8), 4426–4430. https://doi.org/10.1021/nn100255b.
(192) Nitzan, A. Electron Transmission through Molecules and Molecular Interfaces. *Tel Aviv* 109. https://doi.org/10.1146/annurev.physchem.52.1.681.
(193) Kurdak, C.; Kim, J.; Kuo, A.; Lucido, J. J.; Farina, L. A.; Bai, X.; Rowe, M. P.; Matzger, A. J. 1⁄f Noise in Gold Nanoparticle Chemosensors. *Appl Phys Lett* 4. https://doi-org.ressources-electroniques.univ-lille.fr/10.1063/1.1865324.
(194) Marz, M. B. Interharmonics: What They Are, Where They Come From and What They Do. **2016**, 8.
(195) Horowitz, P.; Hill, W. *The Art of Electronics*, Third edition, 19th printing with corrections.; Cambridge University Press: New York, 2022.
(196) Xia, Y.; Yang, P.; Sun, Y.; Wu, Y.; Mayers, B.; Gates, B.; Yin, Y.; Kim, F.; Yan, H. One-Dimensional Nanostructures: Synthesis, Characterization, and Applications. *Adv. Mater.* **2003**, *15* (5), 353–389. https://doi.org/10.1002/adma.200390087.
(197) Yang, P.; Yan, R.; Fardy, M. Semiconductor Nanowire: What's Next? *Nano Lett.* **2010**, *10* (5), 1529–1536. https://doi.org/10.1021/nl100665r.
(198) Appenzeller, J.; Knoch, J.; Bjork, M. T.; Riel, H.; Schmid, H.; Riess, W. Toward Nanowire Electronics. *IEEE Trans. Electron Devices* **2008**, *55* (11), 2827–2845. https://doi.org/10.1109/TED.2008.2008011.

(199) Deb, S. K. Opportunities and Challenges in Science and Technology of WO3 for Electrochromic and Related Applications. *Sol. Energy Mater. Sol. Cells* **2008**, *92* (2), 245–258. https://doi.org/10.1016/j.solmat.2007.01.026.
(200) Kim, D.; Shin, J.; Kim, S. Implementation of Reservoir Computing Using Volatile WOx-Based Memristor. *Appl. Surf. Sci.* **2022**, *599*, 153876. https://doi.org/10.1016/j.apsusc.2022.153876.
(201) Du, C.; Cai, F.; Zidan, M. A.; Ma, W.; Lee, S. H.; Lu, W. D. Reservoir Computing Using Dynamic Memristors for Temporal Information Processing. *Nat. Commun.* **2017**, *8* (1), 2204. https://doi.org/10.1038/s41467-017-02337-y.
(202) Shen, Z.; Peng, Z.; Zhao, Z.; Fu, X. Nonlinear Current-Voltage Characteristics of WO3-x Nano-/Micro-Rods. *Solid State Sci.* **2018**, *78*, 126–132. https://doi.org/10.1016/j.solidstatesciences.2018.03.002.
(203) Migas, D. B.; Shaposhnikov, V. L.; Borisenko, V. E. Tungsten Oxides. II. The Metallic Nature of Magnéli Phases. *J. Appl. Phys.* **2010**, *108* (9), 093714. https://doi.org/10.1063/1.3505689.
(204) Hai, G.; Huang, J.; Jie, Y.; Cao, L.; Wang, L.; Fu, C.; Xiao, T.; Niu, M.; Feng, L. Unveiling the Relationships between (010) Facets-Orientation Growth and Photocatalytic Activity in W18O49 Nanowires. *J. Alloys Compd.* **2020**, *820*, 153127. https://doi.org/10.1016/j.jallcom.2019.153127.
(205) Shi, S.; Xue, X.; Feng, P.; Liu, Y.; Zhao, H.; Wang, T. Low-Temperature Synthesis and Electrical Transport Properties of W18O49 Nanowires. *J. Cryst. Growth* **2008**, *310* (2), 462–466. https://doi.org/10.1016/j.jcrysgro.2007.10.038.
(206) Zhang, J.; Zhang, H.; Liu, L.; Li, F.; Wang, S. W18O49 Nanorods: Controlled Preparation, Structural Refinement, and Electric Conductivity. *Chem. Phys. Lett.* **2018**, *706*, 243–246. https://doi.org/10.1016/j.cplett.2018.06.002.
(207) Guo, C.; Yin, S.; Yan, M.; Kobayashi, M.; Kakihana, M.; Sato, T. Morphology-Controlled Synthesis of $W_{18}O_{49}$ Nanostructures and Their Near-Infrared Absorption Properties. *Inorg. Chem.* **2012**, *51* (8), 4763–4771. https://doi.org/10.1021/ic300049j.
(208) Li, G.; Zhang, S.; Guo, C.; Liu, S. Absorption and Electrochromic Modulation of Near-Infrared Light: Realized by Tungsten Suboxide. *Nanoscale* **2016**, *8* (18), 9861–9868. https://doi.org/10.1039/C5NR09147K.
(209) Xi, G.; Ouyang, S.; Li, P.; Ye, J.; Ma, Q.; Su, N.; Bai, H.; Wang, C. Ultrathin W18O49 Nanowires with Diameters below 1 Nm: Synthesis, Near-Infrared Absorption, Photoluminescence, and Photochemical Reduction of Carbon Dioxide. *Angew. Chem. Int. Ed.* **2012**, *51* (10), 2395–2399. https://doi.org/10.1002/anie.201107681.
(210) Lu, D. Y.; Chen, J.; Zhou, J.; Deng, S. Z.; Xu, N. S.; Xu, J. B. Raman Spectroscopic Study of Oxidation and Phase Transition in W18O49 Nanowires. *J. Raman Spectrosc.* **2007**, *38* (2), 176–180. https://doi.org/10.1002/jrs.1620.
(211) Le Bail, A. Whole Powder Pattern Decomposition Methods and Applications: A Retrospection. *Powder Diffr.* **2005**, *20* (4), 316–326. https://doi.org/10.1154/1.2135315.
(212) Liu, C.; Wang, R.; Zhang, Y. Tellurium Nanotubes and Chemical Analogues from Preparation to Applications: A Minor Review. *Nanomaterials* **2022**, *12* (13), 2151. https://doi.org/10.3390/nano12132151.
(213) Xi, G.; Peng, Y.; Yu, W.; Qian, Y. Synthesis, Characterization, and Growth Mechanism of Tellurium Nanotubes. *Cryst. Growth Des.* **2005**, *5* (1), 325–328. https://doi.org/10.1021/cg049867p.
(214) Mayers, B.; Xia, Y. Formation of Tellurium Nanotubes Through Concentration Depletion at the Surfaces of Seeds. *Adv. Mater.* **2002**, *14* (4), 279–282. https://doi.org/10.1002/1521-4095(20020219)14:4%3c279::AID-ADMA279%3e3.0.CO;2-2.
(215) Kozyukhin, S. A.; Bedin, S. A.; Rudakovskaya, P. G.; Ivanova, O. S.; Ivanov, V. K. Dielectric Properties of Nanocrystalline Tungsten Oxide in the Temperature Range of 223–293 K. *Semiconductors* **2018**, *52* (7), 885–890. https://doi.org/10.1134/S1063782618070114.
(216) Mott, N. F. Conduction in Glasses Containing Transition Metal Ions. *J. Non-Cryst. Solids* **1968**, *1* (1), 1–17. https://doi.org/10.1016/0022-3093(68)90002-1.
(217) Hill, R. M. Variable-Range Hopping. *Phys. Status Solidi A* **1976**, *34* (2), 601–613. https://doi.org/10.1002/pssa.2210340223.

(218) Wang, F.; Di Valentin, C.; Pacchioni, G. Semiconductor-to-Metal Transition in WO 3 − X : Nature of the Oxygen Vacancy. *Phys. Rev. B* **2011**, *84* (7), 073103. https://doi.org/10.1103/PhysRevB.84.073103.
(219) Rabe, J. P.; Knoll, W. An Ellipsometric Method for the Characterization of Macroscopically Heterogeneous Films. *Opt. Commun.* **1986**, *57* (3), 189–192. https://doi.org/10.1016/0030-4018(86)90415-3.
(220) Nečas, D.; Klapetek, P. Gwyddion: An Open-Source Software for SPM Data Analysis. *Open Phys.* **2012**, *10* (1). https://doi.org/10.2478/s11534-011-0096-2.
(221) Delmas, V.; Diez-Cabanes, V.; Dyck, C. van; Scheer, E.; Costuas, K.; Cornil, J. On the Reliability of Acquiring Molecular Junction Parameters by Lorentzian Fitting of I / V Curves. *Phys. Chem. Chem. Phys.* **2020**, *22* (46), 26702–26706. https://doi.org/10.1039/D0CP05372D.
(222) Shirley, D. A. High-Resolution X-Ray Photoemission Spectrum of the Valence Bands of Gold. *Phys. Rev. B* **1972**, *5* (12), 4709–4714. https://doi.org/10.1103/PhysRevB.5.4709.
(223) Zhang, T.; Guérin, D.; Alibart, F.; Troadec, D.; Hourlier, D.; Patriarche, G.; Yassin, A.; Oçafrain, M.; Blanchard, P.; Roncali, J.; Vuillaume, D.; Lmimouni, K.; Lenfant, S. Physical Mechanisms Involved in the Formation and Operation of Memory Devices Based on a Monolayer of Gold Nanoparticle-Polythiophene Hybrid Materials. *Nanoscale Adv.* **2019**, *1* (7), 2718–2726. https://doi.org/10.1039/C9NA00285E.
(224) Viero, Y.; Guérin, D.; Vladyka, A.; Alibart, F.; Lenfant, S.; Calame, M.; Vuillaume, D. Unpublished.
(225) Rodríguez-Carvajal, J. Recent Advances in Magnetic Structure Determination by Neutron Powder Diffraction. *Phys. B Condens. Matter* **1993**, *192* (1–2), 55–69. https://doi.org/10.1016/0921-4526(93)90108-I.
(226) Morita, T.; Lindsay, S. Determination of Single Molecule Conductances of Alkanedithiols by Conducting-Atomic Force Microscopy with Large Gold Nanoparticles. *J. Am. Chem. Soc.* **2007**, *129* (23), 7262–7263. https://doi.org/10.1021/ja072040+.
(227) Cui, X. D.; Zarate, X.; Tomfohr, J.; Sankey, O. F.; Primak, A.; Moore, A. L.; Moore, T. A.; Gust, D.; Harris, G.; Lindsay, S. M. Making Electrical Contacts to Molecular Monolayers. *Nanotechnology* **2002**, *13* (1), 5–14. https://doi.org/10.1088/0957-4484/13/1/302.
(228) Cui, X. D.; Primak, A.; Zarate, X.; Tomfohr, J.; Sankey, O. F.; Moore, A. L.; Moore, T. A.; Gust, D.; Harris, G.; Lindsay, S. M. Reproducible Measurement of Single-Molecule Conductivity. *Science* **2001**, *294* (5542), 571–574. https://doi.org/10.1126/science.1064354.
(229) Johnson, K. L.; Johnson, K. L. *Contact Mechanics*; Cambridge University Press, 1987.
(230) Zhu, Y.; Zhang, Y.; Cheong, F.-C.; Sow, C.-H.; Lim, C.-T. Annealing Effects on the Elastic Modulus of Tungsten Oxide Nanowires. *J. Mater. Res.* **2008**, *23* (8), 2149–2156. https://doi.org/10.1557/JMR.2008.0277.
(231) Durand, C.; Berthe, M.; Makoudi, Y.; Nys, J.-P.; Leturcq, R.; Caroff, P.; Grandidier, B. Persistent Enhancement of the Carrier Density in Electron Irradiated InAs Nanowires. *Nanotechnology* **2013**, *24* (27), 275706. https://doi.org/10.1088/0957-4484/24/27/275706.

Résumé Les polyoxométallates (POMs) sont des oxydes moléculaires nanométriques aux propriétés redox remarquables qui peuvent être explorées dans le cadre de composants avancés. Nous proposons de développer des fonctionnalités évolutives dans des nanomatériaux 2D à base de POMs (2D POM Network, 2D-PN) "programmables/switchables" à la demande grâce aux propriétés multifonctionnelles de ces molécules (par exemple, états redox multiples). Le premier objectif est de préparer une monocouche compacte et dense de POMs sur un substrat métallique afin d'évaluer leurs propriétés de transport d'électrons (ET). Ici, nous rapportons les propriétés de transport d'électrons de deux POMs dans leurs différents états redox en utilisant des monocouches auto-assemblées (SAM) et le C-AFM. Pour les deux molécules, nous avons clairement observé une augmentation d'un facteur 10 de la conductance pour les états réduits qui est liée à une diminution d'environ 0.3eV de l'énergie de l'orbitale moléculaire impliquée dans le transport à travers le métal/POM/métal. Ensuite, nous avons fabriqué un 2D-PN hybride multi-connecté (6 électrodes) avec deux POMs et des nanoparticules d'or et nous avons mesuré leur ET révélant une grande variabilité dans le 2D-PN. Des mesures de bruit à basse fréquence et de génération de hautes harmoniques sont utilisées pour discuter de l'utilisation possible de ces 2D-PN dans le cadre global de l'implémentation physique d'un système de calcul à réservoir neuromorphique avec des nano-objets (nanotubes de carbone nanoparticules, molécules, commutateurs atomiques). Nous synthétisons également des nanofils de $W_{18}O_{49}$ (environ quelques µm de long et quelques dizaines de nanomètres de diamètre) et nous mesurons leur conductivité avec un STM UHV 4 probes. Nous démontrons une conductivité très élevée allant jusqu'à 10^3S/cm le long du nanofil, qui surpasse les données de la littérature et une grande anisotropie de conductivité.

Mots clés: polyoxométallates ; jonction moléculaire ; C-AFM ; Reservoir Computing ; Nanofils $W_{18}O_{49}$

Abstract Polyoxometalates (POMs) are nanometric molecular oxides with remarkable redox properties that can be explored in the context of advanced components. We propose to develop scalable functionalities in 2D nanomaterials based on POMs (2D POM Network, 2D-PN) "programmable/switchable" on demand thanks to the multifunctional properties of these molecules (e.g. multiredox states). The first objective is to prepare compact and dense monolayers of POMs on a metal substrate to assess their electron transport (ET) properties. Here, we report the ET properties of two POMs in their different redox states using self-assembled monolayers (SAM) and conductive-AFM. For both molecules, we clearly observed an increase of the conductance of a factor of 10 for the reduced states which is related to a decrease of the energy of about 0.3eV of the molecular orbital involved in the transport though the metal/POM/metal. Then, we successfully fabricated multi-connected (6 electrodes) hybrid 2D-PN with two POMs and Au nanoparticles and we measured their ET revealing large variability in the 2D-PN. Low-frequency noise and high-harmonic generation measurements will be used to discuss the possible use of these 2D-PN within the global framework of the physical implementation of a neuromorphic reservoir computing system with nano-objects (Carbon nanotubes, nanoparticles, molecules, atomic switches). We also synthesize $W_{18}O_{49}$ nanowires (about µm long and few tens of nanometers in diameter) and we measure their conductivity with a 4-probe UHV STM. We demonstrate a very high conductivity up to 10^3S/cm along the nanowire, which outperforms the literature data and a large conductivity anisotropy.

Key words: polyoxometalates; molecular junction; C-AFM; Reservoir Computing; $W_{18}O_{49}$ nanowires